1 2 9 0

UNIVERSIDADE Ð
COIMBRA

Margarida Machado Cordeiro

Permeation of weak acids and bases through lipid bilayers
Modelling and validation of a pH variation assay

Fevereiro de 2022

Faculdade de Ciências e Tecnologia da Universidade de Coimbra

Permeation of weak acids and bases through lipid bilayers
Modelling and validation of a pH variation assay

Margarida Machado Cordeiro

Dissertação no âmbito do Mestrado em Química, na área de especialização em Química Avançada e Industrial, variante Química-Física Experimental e Teórica, orientada pelo Professor Doutor Armindo José Alves da Silva Salvador e pela Professora Doutora Maria João Pedrosa Ferreira Moreno Silvestre e apresentada ao Departamento de Química da Faculdade de Ciências e Tecnologia da Universidade de Coimbra.

Fevereiro de 2022

1 2 9 0

UNIVERSIDADE Đ
COIMBRA

Agradecimentos

Chegando ao fim desta importante etapa é tempo de agradecer a algumas pessoas que tornaram tudo isto possível e que contribuíram para o meu desenvolvimento pessoal e académico. A todas elas, quero deixar um profundo e sincero agradecimento.

Ao professor Armindo Salvador agradeço a total disponibilidade para me explicar questões tão simples e que me pareciam, à primeira vista, complicadíssimas. Agradeço ainda o esforço para me introduzir ao software com o qual desenvolvi este trabalho, a bagagem científica e o pensamento crítico transmitidos durante as aulas do Mestrado em Biologia Computacional e durante o último ano.

À professora Maria João Moreno gostaria de agradecer o auxílio, ensinamentos, esclarecimentos, compreensão, rigor, exigência e orientação científica dos últimos três anos. Tem sido um percurso muito prazeroso, especialmente neste último ano com a proposta para participar no desafiante e apaixonante projeto que deu origem a esta tese. Agradeço ainda as longas reuniões e discussões em torno deste trabalho e todo o apoio emocional.

À professora Stefanie Krämer agradeço pela excelência do seu trabalho e pelo debate em torno deste trabalho.

Aos colegas e amigos do grupo de Química Biológica, Cristiana Pires, Cristiana Ramos, Alexandre Oliveira, Jaime Samelo, Inês Silva, Joana Brás, Rui Santos e Carlos Coelho, agradeço o bom ambiente de laboratório, o companheirismo, a preocupação, os conselhos e todos os bons momentos e conversas científicas ou não tão científicas. Foram sempre muito prestáveis e tornaram muito melhor o trabalho no laboratório. Não posso deixar de agradecer à Elsa Loureiro e à Anaísa Simões que acompanharam parte deste trabalho e com quem também pude aprender muito.

Aos colegas e amigos da Licenciatura e do Mestrado em Química agradeço pelo companheirismo, a amizade e as aventuras. Agradeço ainda a todos aqueles com quem trabalhei enquanto membro e dirigente do Núcleo de Estudantes de Química e com quem trabalho, mais recentemente, no projeto da Molecular JE. Em equipa somos capazes de fazer coisas tão boas e juntos potenciamos as melhores qualidades de cada um. Um especial agradecimento à Ana Marques que me acompanha desde o início e com quem venci tantas e difíceis batalhas e passei tão bons momentos.

Aos meus pais e irmão, agradeço pelo amor, a constante preocupação e pelas palavras de incentivo. Sei que compreenderão todas as minhas falhas e sinto-me uma felizarda pelo orgulho que têm em mim. Aos meus avós agradeço os valores transmitidos e o grande contributo na minha educação. Uma gratidão que manifesto com amor e atenção.

Ao João não posso deixar de expressar o mais profundo agradecimento, pela amizade e carinho, por toda a paciência, pelo esclarecimento de todas as dúvidas, por sempre debater tão assertivamente comigo, por ouvir e compreender sempre as minhas frustrações e nunca me deixar desistir. Desculpa ainda pela atenção que não te consegui dar. Espero conseguir retribuir toda a ajuda.

Funding

I can't change the direction of the wind,

but I can adjust my sails to always reach my destination.

Jimmy Dean

Index

x

List of Figures

Supplementary Material:

List of Tables

Supplementary Material:

Abbreviations

ADMET	Absorption, Distribution, Metabolism, Excretion and Toxicity
AIC	Akaike's Information Criterion
AS	Apical Side
ATP	Adenosine TriPhoshate
BBB	Blood-Brain Barrier
BS	Basolateral Side
BSA	Bovine Serum Albumin
EDTA	EthyleneDiamine TetraAcetic acid
EMA	European Medicines Agency
FDA	Food and Drug Administration
HPLC-UV/Flu	High-Performance Liquid Chromatography coupled to an absorption (UV) or a fluorescence (Flu) detector
HPTS	8-HydroxyPyrene-1,3,6-TriSulfonic acid
LC-MS	Liquid Chromatography - Mass Spectrometry
LUVs	Large Unilamellar Vesicles
MDCK	Madin−Darby Canine Kidney
MS	Mass Spectrometry
PAMPA	Parallel Artificial Membrane Permeability Assay
POPC	1-Palmitoyl-2-Oleoyl-sn-glycero-3-Phosphocholine
POPS	1-Palmitoyl-2-Oleoyl-sn-glycero-3-Phospho-L-Serine
PR	Plate Reader
SF	Stopped-Flow
SUVs	Small Unilamellar Vesicles
T_m	Melting point temperature

Symbols

1. Notation

$n\mathrm{X}$	Number of moles of the species X*
X	Notation for the species X* or concentration of the species X*, regarding to the volume of the compartment where it is (depending on the context)

<div align="right">* X can be any species described in the list below</div>

BD_{wo}	Deprotonated form of the buffer in the outer aqueous compartment
BH_{wo}	Protonated form of the buffer in the outer aqueous compartment
$\boldsymbol{H_i}$	Aggregated variable of inner protons and species carrying a proton (includes the species H_{wi}, SH_{wi}, PH_{wi} and SH_{li} and PSH_{wi} if it is present; considers the volume V_{wi})
$\boldsymbol{H_o}$	Aggregated variable of external protons and species carrying a proton (includes the species H_{wo}, SH_{wo}, BH_{wo} and SH_{lo}; considers the volume V_{wo})
H_{wi}	Free protons in the inner aqueous compartment
H_{wo}	Free protons in the outer aqueous compartment
PD_{wi}	Base form of the pH-sensitive probe in the inner aqueous compartment
PD_{wi}^{*}	Concentration of the fluorescent probe, with respect to the total volume
PH_{wi}	Weak acid form of the pH-sensitive probe in the inner aqueous compartment
PSD_{wi}	Conjugated base bonded to the protein in the inner aqueous compartment
PSH_{wi}	Weak acid bonded to the protein in the inner aqueous compartment
P_{wi}	Unbonded entrapped protein
SD	Weak base
SD_{li}	Solute base form in the inner membrane leaflet
SD_{lo}	Solute base form in the outer membrane leaflet
SD_{wi}	Solute base form in the inner aqueous compartment
SD_{wo}	Solute base form in the outer aqueous compartment
SH	Weak acid
SH_{li}	Solute acid form in the inner membrane leaflet
SH_{lo}	Solute acid form in the outer membrane leaflet
SH_{wi}	Solute acid form in the inner aqueous compartment
SH_{wo}	Solute acid form in the outer aqueous compartment
$\boldsymbol{S_i}$	Aggregated variable of solute species (includes SH_{wi}, SD_{wi}, SH_{li} and SD_{li} and PSH_{wi} and PSD_{wi} if they are present; considers the volume V_{wi})
$\boldsymbol{S_o}$	Aggregated variable of solute species (includes SH_{wo}, SD_{wo}, SH_{lo} and SD_{lo}; considers the volume V_{wo})
K_{wi}	Potassium ion in the inner aqueous compartment
K_{wo}	Potassium ions in the outer aqueous compartment

A^i	Area of the internal surface (at the lipid head groups of the bilayer inner leaflet)
A^{io}	Area of the section that separates the outer and inner leaflets in a lipid bilayer
A^o	Area of the external surface (at the lipid head groups of the bilayer outer leaflet)
a_L	Surface area *per* lipid
A_T^i	Total area of the internal surface of the vesicles
A_T^{io}	Total area of the section that separates the outer and inner leaflets
A_T^o	Total area of the outer surface of the vesicles
B_T	Total concentration of buffer outside the vesicles
c_L	Lipid concentration
h	Membrane thickness
H_T	Total concentration of protons (bonded and free, considers the total volume)
K_a^B	Acidity constant of the buffer
k_a^B	Rate constant for the association of BD_{wo} with a proton
K_a^P	Acidity constant of the pH-sensitive probe
k_a^P	Rate constant for the association of PD_{wi} with a proton
K_a^{Sli}	Acidity constant of the weak acid in the inner leaflet
k_a^{Sli}	Rate constant for the association of SH_{li} with a proton
K_a^{Slo}	Acidity constant of the weak acid in the outer leaflet
k_a^{Slo}	Rate constant for the association of SH_{lo} with a proton
K_a^{Sw}	Acidity constant of the weak acid in the aqueous media
k_a^{Sw}	Rate constant for the association of SD_{wo} or SD_{wi} with a proton
k_d^B	Rate constant for the dissociation of BH_{wo}
k_d^P	Rate constant for the dissociation of PH_{wi}
k_d^{Sli}	Rate constant for the dissociation of SH_{li}
k_d^{Slo}	Rate constant for the dissociation of SH_{lo}
k_d^{Sw}	Rate constant for the dissociation of SH_{wo} or SH_{wi}
K_d^{PSD}	Equilibrium constant for the dissociation of the complex protein-deprotonated solute (PSD_{wi})
K_d^{PSH}	Equilibrium constant for the dissociation of the complex protein-protonated solute (PSH_{wi})
κ_H	Permeability coefficient of the proton
κ_K	Permeability coefficient of the potassium ion
k_{lio}^{SD}	Translocation rate constant of the base towards the outer leaflet
k_{lio}^{SH}	Translocation rate constant of the acid towards the outer leaflet
κ_{lwo}^{SD}	Permeability coefficient of the base between the outer leaflet and the water
κ_{lwo}^{SH}	Permeability coefficient of the acid between the outer leaflet and the water
k_{loi}^{SD}	Translocation rate constant of the base towards the inner leaflet
k_{loi}^{SH}	Translocation rate constant of the acid towards the inner leaflet
K_{lwi}^{SD}	Partition coefficient of the base between the inner leaflet and the water

κ_{lwi}^{SD}	Permeability coefficient of the base between the inner leaflet and the water
K_{lwi}^{SH}	Partition coefficient of the acid between the inner leaflet and the water
κ_{lwi}^{SH}	Permeability coefficient of the acid between the inner leaflet and the water
κ_{wli}^{SD}	Permeability coefficient of the base between the water and the inner leaflet
κ_{wli}^{SH}	Permeability coefficient of the acid between the water and the inner leaflet
K_{wlo}^{SD}	Partition coefficient of the base between the water and the outer leaflet
κ_{wlo}^{SD}	Permeability coefficient of the base between the water and the outer leaflet
K_{wlo}^{SH}	Partition coefficient of the acid between the water and the outer leaflet
κ_{wlo}^{SH}	Permeability coefficient of the acid between the water and the outer leaflet
$N_{lipids\ per\ LUV}$	Number of lipids *per* vesicle
n_{LUVs}	Moles of LUVs
$N_{vesicles}$	Total number of vesicles
P_{app}	Apparent membrane permeability
pHi	pH in the inner aqueous compartment (vesicle lumen)
pHo	pH in the outer aqueous compartment
pK_a^{Sw}	Logarithm of the acidity constant in water
pK_b^{Sw}	Logarithm of the basicity constant in water
P_T	Total concentration of the pH-sensitive probe inside the vesicles
P_{wi_T}	Total concentration of the protein (free and associated with the solute) encapsulated in the vesicles
r	Radius of the vesicle
S_T	Total concentration of solute (considers the total volume)
V_{li}	Total volume of the inner leaflets of the vesicles
$V_{lipids\ per\ LUV}$	Volume occupied by each lipid molecule when associated to form a vesicle
$V_{li\ vesicle}$	Volume of the inner leaflet of each vesicle
$\overline{V_L}$	Molar volume of the lipid
V_{lo}	Total volume of the outer leaflets of the vesicles
$V_{lo\ vesicle}$	Volume of the outer leaflet of each vesicle
V_T	Total volume
V_{wi}	Total volume of the aqueous medium encapsulated by the vesicles
$V_{wi\ vesicle}$	Volume of the aqueous medium encapsulated by each vesicle
V_{wo}	Volume of the aqueous compartment outside the vesicles
z_H	Valency of the proton
z_K	Valency of the potassium
z_{SD}	Valency of the base
z_{SH}	Valency of the acid

2. Physical constants

e	Unit charge	1.6022×10^{-19} C
ε_0	Permittivity of vacuum	8.85×10^{-12} F m^{-1}
F	Faraday's constant	96485 C mol^{-1}
k_B	Boltzmann's constant	1.3807×10^{-23} J K^{-1}
N_A	Avogadro's number	6.0221×10^{23}
R	Gas constant	8.3145 J mol^{-1} K^{-1}

Abstract

Drug discovery and development is an iterative and very complex process. The poor absorption, distribution, clearance, efficiency, and safety of drug candidates are the major pitfall in the development of new therapies. Lipid membranes represent the main barrier to the free diffusion of solutes and determine the availability of these compounds in the tissues. Predicting the rate at which solutes permeate *in vivo* barriers is crucial, and there are several *in vitro* studies valuable for this goal. The pH-variation assay is particularly relevant because it allows following the permeation of weak acids and bases even when they do not exhibit optical properties. However, there are some artefacts, its validity is not widely accepted, and the permeability coefficients are not always consistent with those from other methods.

In this work, a kinetic model was developed for the permeation of weak acids and bases through lipid membrane barriers that considers explicitly the two membrane leaflets. The simulations of these processes were able to identify some experiment design principles to not compromise the accuracy of the method in the prediction of permeability coefficients. The assay must be employed with larger vesicles, and the pH variation must be under 0.25 units. These conclusions were achieved by analysing the effect of the topology of the system, solute lipophilicity, and solute and fluorescent pH probe concentrations on the occupancy numbers *per* vesicle and by comparing the dynamics of solute accumulation and fluorescence variation. When analysing the effect of these parameters on the permeability coefficient it was found that the widely used equation $P_{app} = \beta \times r/3$ is inappropriate to assess the permeability coefficient of drug-like weak acids and bases. This results from the failure of several assumptions and approximations considered in the derivation of this equation.

This work also examined the effect of several parameters (flip-flop rate constant, solute's pK_a, proton, and potassium permeabilities) on the kinetics of solute permeation and the resulting pH variation inside the vesicles. The permeation of weak acids leads to a fast decrease of the pH, which is followed by a slow recovery to the initial pH value, and a symmetric effect is observed for the permeation of weak bases. If only the neutral solute species may permeate the membrane, the solute equilibration is well described by a mono-exponential function. However, if permeation of charged species is included (albeit as a slower process), the accumulation of solute may follow a biphasic kinetics. In this case, the solute apparent permeability should be calculated from a weighted characteristic constant ($\alpha_1 \beta_1 + \alpha_2 \beta_2$). However, when using the fluorescence dynamics, this is not possible to perform accurately due to a non-direct relationship between the characteristic constants and pre-exponential terms. When using only the characteristic constants of the fast process, the solute permeability coefficient is overestimated. It was observed that the slow phase in solute accumulation is not influenced only by the permeability of the charged solute species, but also by the permeability

of other charged species in solution such as H^+/OH^- and the ions responsible for the dissipation of electrostatic potentials generated by charge unbalance.

Some pH equilibration experiments were performed to estimate the permeability of H^+/OH^- and assess the effect of valinomycin, an ionophore with high specificity for K^+. However, our objectives were not successfully achieved as the experimental results obtained were quite different from the time courses predicted by our kinetic model. We concluded that the main reason for the discrepancies was the additional pH buffer capacity present inside the vesicles, possibly due to the presence of carbonic acid. The increased buffer capacity leads to a higher amount of H^+/OH^- required to achieve pH equilibration, which in turn leads to the development of a larger charge unbalance between the aqueous media inside and outside the vesicles. The electrostatic potential thus generated hinders the movement of additional H^+/OH^- and prevents pH equalisation. The full equalization requires the countermovement of additional charges, such as K^+ in the presence of valinomycin, which explains the strong effect of valinomycin observed experimentally.

Resumo

A descoberta e desenvolvimento de fármacos é um processo iterativo e muito complexo. A insuficiente absorção, distribuição, eliminação, eficácia e segurança dos candidatos a fármacos são os principais obstáculos no desenvolvimento de novas terapias. As membranas lipídicas são a principal barreira à difusão dos solutos e determinam a disponibilidade destes compostos nos tecidos. Prever a velocidade de permeação de solutos *in vivo* é crucial, e existem vários estudos *in vitro* para entender e quantificar esse processo. O ensaio de variação de pH é particularmente relevante porque permite seguir a permeação de ácidos e bases fracas, mesmo quando estes não apresentam propriedades óticas. No entanto, existem alguns artefactos, a validade deste ensaio não é amplamente aceite e os coeficientes de permeabilidade nem sempre são consistentes com aqueles obtidos por outros métodos.

Neste trabalho foi desenvolvido um modelo cinético para a permeação de ácidos e bases fracos através de membranas lipídicas que considera explicitamente os dois folhetos da membrana. As simulações desses processos permitiram identificar alguns princípios do desenho experimental necessários para não comprometer a precisão do método na previsão dos coeficientes de permeabilidade. Devem ser utilizadas vesículas lipídicas de grandes dimensões e a variação de pH deve ser inferior a 0.25 unidades. Estas conclusões resultaram da análise do efeito da topologia do sistema, da lipofilicidade do soluto e das concentrações do soluto e da sonda de fluorescência nos números de ocupação por vesícula e da comparação da dinâmica de permeação do soluto e da variação da fluorescência. Ao analisar o efeito destes parâmetros no coeficiente de permeabilidade, verificou-se que a equação comummente utilizada $P_{app} = \beta \times r/3$ é inadequada para avaliar o coeficiente de permeabilidade de ácidos e bases fracas. Isso resulta do facto de vários pressupostos e aproximações considerados na derivação desta equação não serem válidos nas condições do ensaio.

Este trabalho também se focou na análise do efeito de vários parâmetros (constante de velocidade de translocação, pK_a do soluto, permeabilidades de protão e do potássio) na cinética de permeação do soluto e na variação do pH interno resultante. A permeação de ácidos fracos resulta numa rápida diminuição do pH, seguida de uma recuperação mais lenta do seu valor inicial. Na permeação de bases fracas é observado um efeito simétrico. Se apenas a espécie neutra permear a membrana, a dinâmica do soluto é bem descrita por uma função monoexponencial. No entanto, se a permeação das espécies carregadas for incluída (ainda que num processo mais lento), a acumulação de soluto pode seguir uma cinética bifásica. Neste caso, a permeabilidade aparente do soluto deve ser calculada a partir de uma constante característica média ($\alpha_1 \beta_1 + \alpha_2 \beta_2$). Porém, não é possível calculá-la com precisão a partir da dinâmica de fluorescência, uma vez que não existe uma relação direta entre as constantes

características e os termos pré-exponenciais. Usar apenas a constante característica do processo rápido resultará numa sobrestimação do coeficiente de permeabilidade ao soluto. A fase lenta da permeação do soluto não é influenciada apenas pela permeabilidade das espécies de soluto carregadas, mas também pela permeabilidade de outras espécies carregadas em solução como H^+/OH^- e os outros iões responsáveis pela dissipação do potencial eletrostático, gerado pelo desequilíbrio de carga.

Foram realizadas algumas experiências de equilíbrio de pH para estimar a permeabilidade dos iões H^+/OH^- e avaliar o efeito da valinomicina, um ionóforo com alta especificidade para K^+. No entanto, estes objetivos não foram alcançados com sucesso, uma vez que os resultados experimentais obtidos eram bastante diferentes das variações previstas pelo nosso modelo cinético. Concluiu-se que as discrepâncias se devem principalmente à capacidade tampão de pH adicional presente no interior das vesículas, possivelmente devido à presença de ácido carbónico. O aumento da capacidade tampão resulta na necessidade de permeação de uma maior quantidade de iões H^+/OH^- para reestabelecer o equilíbrio de pH, o que, por sua vez, leva ao desenvolvimento de um maior desequilíbrio de cargas entre os meíos aquosos externo e interno das vesículas. Assim, o potencial eletrostático gerado opõe-se ao movimento dos iões H^+/OH^- e impede o reequilibrar do pH. O completo reequilíbrio requer o movimento adicional de cargas, como K^+ na presença de valinomicina, o que explica o forte efeito da valinomicina observado experimentalmente.

Palavras-Chave: Permeabilidade; Ácidos fracos; Bases fracas; Bicamada lipídica; Modelação cinética; Ensaio de variação de pH.

Chapter 1

Introduction

1.1. <u>Biological membranes</u>

Membranes are the basic structure of cells. They surround prokaryotic and eukaryotic cells and the organelles of the former, delimit their intracellular content, forming a barrier that controls selectively the passage of species between the intra and extracellular media, keep ionic gradients responsible for the maintenance of transmembrane potentials, the accumulation of different chemical species inside the organelles and essential for electrical signalling, store and transmit energy, and receive and amplify signals.[1,2]

After some rudimentary models and almost fifty years since Gorter and Grendel[3] found that biological membranes are bilayers structures, Singer and Nicolson[4] proposed, in 1972, a new way of thinking about biologic membranes, the Fluid Mosaic Model. According to this model, membranes look like a mosaic, made of different pieces. Lipids in the fluid state form a bilayer and create a matrix where some proteins are adsorbed (peripheral proteins) or randomly embedded (integral proteins) minimising their free energy by hiding their non-polar residues inside the membrane and keeping the hydrophilic ones at the surface in contact with the lipid polar head groups and water. The ability of lipids and proteins to diffuse laterally is responsible for the dynamic and fluid behaviour of the biomembranes.[4] Moreover, the configurational isomerism is responsible for the rotational movements of lipid chains and head groups.[5] Lipids can also move vertically, between layers, however, the rate is considerably slow because of thermodynamic constraints which in addiction with the role of some specific and unspecific enzymes are responsible for maintaining lipidic asymmetries, underlying in cell operation such us in apoptosis and signalling processes.[1,4,6,7]

In biological membranes, one can find three types of lipids: phospholipids, derived from diacylglycerol or sphingosine, sterols, and glycolipids, with the first being the main component and the ones responsible for making the lipid bilayer a highly anisotropic structure.[5] Phospholipids are amphiphilic molecules with a hydrophobic skeleton made of fatty acids and a hydrophilic head group. In solution, amphiphilic molecules self-assembly forming micelles or bilayers, depending on their packing constraints and as a consequence of hydrophobic interactions that allow the exclusion of their long aliphatic tails from water. Additionally, van der Waals, hydrophilic and electrostatic interactions also play a role in membrane stability. Sterols, such as cholesterol in mammalian cells, have a small head group (hydroxyl group) bonded to a tetra-cyclic structure and influence considerably the fluidity and permeation across membranes. On the other hand, glycolipids, as glycoproteins, are

carbohydrates covalently attached to lipids and proteins, respectively, localized at the outer side of all cell plasma membranes and are essential in recognising functions and signalling pathways. Proteins can associate with membranes in distinct ways depending on their molecular features. They transport different species into and out of the cell, acting as carriers, channels and pumps. Membrane proteins also behave as receptors that allow the cell to respond to external stimuli, or as enzymes, catalysing specific reactions at the membrane.

One of the most relevant physical properties of the membrane is its physical state. Membrane lipids can exhibit an assortment of organized structures, depending on the structure of the lipid itself, degree of hydration, temperature, pressure, ionic strength and pH. The gel or crystalline phase (temperature lower than the melting point, T_m) is characterised by an ordered and packed structure as the hydrocarbon chains exist predominantly in their rigid, extended, all-trans conformation. On the other hand, when in the liquid-crystalline phase (temperatures above T_m) the lipids conformational, rotational, and translational degrees of freedom are considerably higher. The increase in mobility leads to a decrease in the thickness of the bilayer and a small increase in the total volume occupied by the molecules.[5] Under physiological conditions, membranes exist usually in the liquid phase and may exhibit stable domains which segregate specific components. These domains, also named rafts, result from the non-uniformly lipid distribution and present higher levels of cholesterol and sphingolipids, characteristic of liquid-ordered phases.[8]

The fluidity of the membrane depends on the composition as well as the temperature. The length and the number of double bonds in the lipid acyl chains influence the packaging of the lipid membrane, tightening or relaxing the distance between them.[9] However, at the same reduced temperature ($\frac{T-T_m}{T_m}$) the fluidity is not very dependent on acyl chain length.[10] On the other hand, cis unsaturated bonds work in the opposite way, as the kink formed at the double bond tends to maintain the acyl chains (and consequently the lipids) apart from each other decreasing the interaction between them. Bacteria and yeast control membrane fluidity by adjusting membrane composition as a response to temperature variations, decreasing the synthesis and incorporation of lipids with cis-double bonds in the bilayer upon temperature increase.[2,9] In animal cells, fluidity is controlled mainly through the cholesterol content. This lipid is small and rigid, interacts strongly with the hydrophobic acyl chains of phospholipids and forces them into all-trans conformation even at temperatures above the lipid main transition, decreasing membrane fluidity. On the other hand, at temperatures below the lipid main transition, the presence of cholesterol leads to a partial disruption of the regular and highly ordered structure of the lipid bilayer. In this way, the fluidity of the lipid bilayer below and above the phospholipid main transition becomes similar, and no phase transition is observed for cholesterol rich lipid bilayers.[2,5,9]

In this work, the mimetic membranes in the liquid-crystalline phase have 1-palmitoil-2-oleoil-sn-glicero-3-phosphatidilcoline (POPC) and 1-palmitoyl-2-oleoyl-sn-glycero-3-phospho-L-serine (POPS) in their constitution (T_m^{POPC}= -2 °C, T_m^{POPS} = 14 °C).[11] These lipids differ only in the group attached to the phosphate group (a choline in POPC and a serine in POPS). Whilst POPC is a zwitterionic lipid and is the main constituent of animal membranes, POPS is a negatively charged lipid that is also very abundant in animal cells.[12] The inclusion of POPS in the model membranes used in this study serves two purposes: i) to obtain model membranes with a negative surface potential similar to that of biomembranes; and ii) to decrease the favourable interaction between different lipid bilayers, thus decreasing the propensity to form multilamellar vesicles and to avoid aggregation.
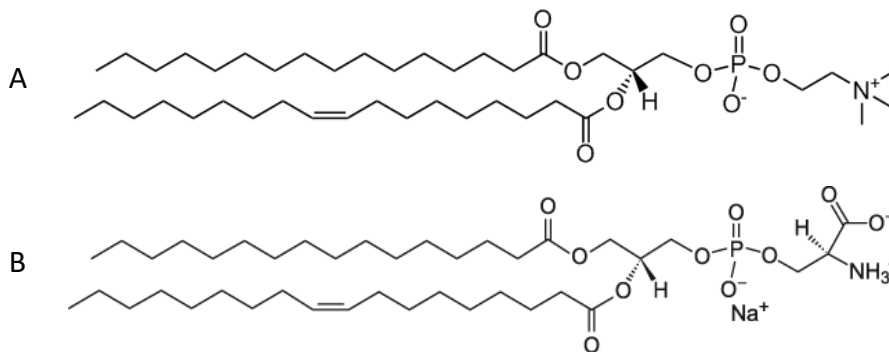
Figure 1. Molecular structures: **A)** 1-Palmitoyl-2-Oleoyl-sn-glycero-3-Phosphocholine or POPC; **B)** 1-Palmitoyl-2-Oleoyl-sn-glycero-3-Phospho-L-Serine or POPS.

1.2. <u>Permeation mechanisms</u>

Biological membranes constitute a selective barrier for the diffusion of solutes based on their size and polarity. The selection based on compound polarity results from the anisotropic nature of membranes, particularly because of the amphiphilic structure of the lipids. Carbon dioxide, oxygen and other non-polar small molecules can diffuse easily across the lipidic membrane, down their concentration gradient. Bigger non-polar molecules can also diffuse passively through the membrane, however, the rate at which it occurs is very low. Water, urea, and other small uncharged polar molecules also diffuse readily across a bilayer. On the other side, membranes are mostly impermeable to large uncharged polar molecules (glucose) and ions (sodium, potassium, calcium and chloride) or charged molecules, regardless their size.[9] Thus, living organisms developed mediated processes, by membrane proteins, capable of transporting bigger or significantly polar compounds, such as ions, sugars, or amino acids, vital for cell functions. Membrane proteins that increase the permeation through the membranes can be classified as channels or transporters. Channels usually cross the entire membrane and let the compounds diffuse through their tiny hydrophilic pores, differentiating compounds not only based on their size but also their electrical charge. On the other hand, the

permeation mediated by transporters is accompanied by a conformational change of the protein, usually but not always accompanied by energy consumption, resulting from adenosine triphosphate (ATP) hydrolysis. When there is no energy consumption the transport occurs only down the concentration gradient of the compound, whilst, in the presence of transporter proteins, permeation can also happen against the concentration gradient with consumption of ATP or being coupled with the transport of another species in favour of its gradient. Transporter proteins are specific and only those compounds with affinity for the binding sites can cross the membrane. The different permeation mechanisms are schematically represented in Figure 2.

Each type of cell membrane and organelle exhibit specific transporter proteins allowing the accumulation or elimination of specific compounds depending on their function and needs. For example, transporters that import protons and export products from the digestive process are abundant in lysosome membranes, those responsible for importing pyruvate and exporting ATP are present in the inner membrane of mitochondria and those that import nutrients are present on the plasma membrane.[9]
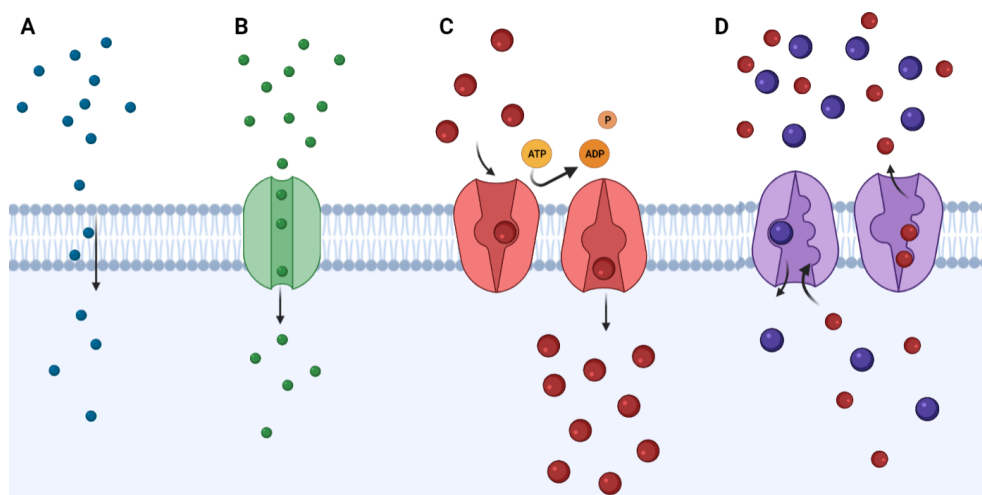
Figure 2. Different membrane permeation mechanisms. **A)** Passive permeation; **B)** Mediated transport through a channel; **C)** Mediated transport through a transmembrane pump with energy consumption; **D)** Mediated transport through a membrane protein of a species down its concentration gradient coupled with the transport of another species against its concentration gradient.

The very small passive permeability of ions through lipid bilayers and the presence of specific channels and/or transporters in the biomembranes allow a fine control of the content inside the cell and cellular organelles. Cells take advantage of this property, with ion gradients being on the basis of a large number of fundamental cell functions. However, there are some molecules that can increase the permeability of ions and thus dissipate their gradients in an uncontrolled way. Because they disturb fundamental functions, they usually lead to cell death, and are thus venoms or antibiotics. For example, gramicidin, a natural antibiotic synthesised by *Brevibacillus brevis,* is a linear peptide with

fifteen alternating D- and L-hydrophobic amino acids that form a transient channel.[13,14] The dimeric helical structure is able to transport univalent cations, such as protons, alkali metals and ammonium, with low selectivity.[14] There are seven different isoforms of gramicidin, one of those being a cyclic decapeptide.[15] On the other hand, valinomycin is a mobile ionophore, synthesised by bacteria of the *Streptomyces* genus, transporting the same ions but with high specificity for potassium.[16] Valinomycin is a macrocyclic molecule consisting of a triple repeating unit with D- and L-valine alternated with carboxylic acids (D-α-hydroxyisovaleric and L-lactic acids) connected by ester linkages (**Figure 3**).[17] The cyclic structure is stabilised by the formation of hydrogen bonds between carbonyl oxygens of the amide groups with NH groups of consecutive residues. Valinomycin hydrophobic surface allows its solubilization in the membrane core and the polar cavity with six oxygen atoms, from the ester groups, enables ions octahedrally coordination and its transport through the membrane dissipating the membrane potential.[18] The size of the cavity, as well as the intramolecular hydrogen bonds, are responsible for the higher affinity of potassium ions in comparison with other metal ions, or even protons.[19] This specificity for potassium ions is explored in the present work, with valinomycin being used to promote the dissipation of transmembrane electrostatic potentials without directly affecting pH gradients.
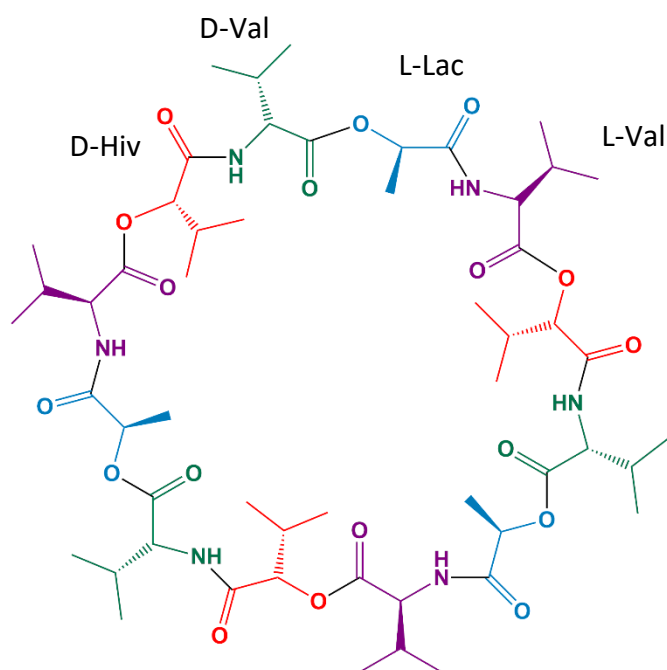
Figure 3. Molecular structure of valinomycin, formed by the repetition of the sequence D-α-hydroxyisovaleric acid (D-Hiv), D-valine (D-Val), L-lactic acid (L-Lac) and L-valine (L-Val).

Despite the large machinery of the cell, drug-like compounds cross the bilayer frequently by passive diffusion as they rarely bind to transporter proteins by themselves. It is therefore of high importance to develop and optimise transporting vectors in conjunction with the pharmacological formulations, to guarantee its efficient entry into the therapeutic target. Once inside the organism the

drug must cross several additional membrane barriers for its distribution, to reach the therapeutic target, and finally for its elimination. Passive permeation through the membrane barriers usually plays a crucial role in the distribution, therapeutic and side effects of a drug.

1.3. <u>**Drug discovery and development**</u>

Drug discovery and development is a complex, risky, expensive and long process, subject to heavy regulation. It takes on average 12 to 15 years and costs more 1 billion dollars to reach the finished product.[20] Drug discovery is driven by the need of medical treatment for diseases or improvement of life quality of patients carrying some clinical conditions. Despite technical and scientific advancements, the pharmaceutical industry is still not able to respond to all disorders, namely those from oncological or central nervous system nature, with high and growing prevalences.[21,22]

Understanding the mechanism of the diseases, what causes them, and the components involved is crucial to identify the best targets for treating or preventing them. Usually, these targets are proteins with essential functions in the pathological mechanism and are identified with the contribution of academia or clinical research.[20] As an example, all the vaccines against SARS-COV-2, authorised for use in the European Union, were developed based on the essential role of the Spike protein, that allows the virus entry into host cells, leading to its replication. They give the immunity system the ability to recognise and fight SARS-COV-2 in a future contact with the virus.[23–26]

In the past, drug discovery was based on the synthesis of many new compounds with a focus on their therapeutic effect and how to optimise their activity over their physicochemical and pharmacokinetic properties. Nowadays, drug discovery is a more rational process, that prioritises both the optimisation of properties and activity, as large libraries of compounds already exist and are available at ease.[27] Virtual screening and high-throughput methods are routinely used to identify chemical compounds or starting structures that are likely to bind and modulate the target. These approaches allow the selection of the best candidates to progress into the preclinical phase.[20,28]

Failure of drug candidates during the clinic stage is mostly because they exhibit poor pharmacokinetic profiles (poor absorption, distribution and clearance), are inefficient, or are not safe.[20] To achieve a therapeutic effect, orally administered drugs need to pass through multiple tissues until reaching the target of interest (**Figure 4**). First, they must be absorbed into the bloodstream, reach the target without suffering relevant modifications, perform their purpose and finally be safely eliminated at the kidney or liver. Pre-clinical studies to predict pharmacokinetic and pharmacodynamic properties are underlying to assess efficacy and safety, increase compounds quality and ensure that compounds that are doomed to failure are excluded thus reducing late-stage attrition.[29]
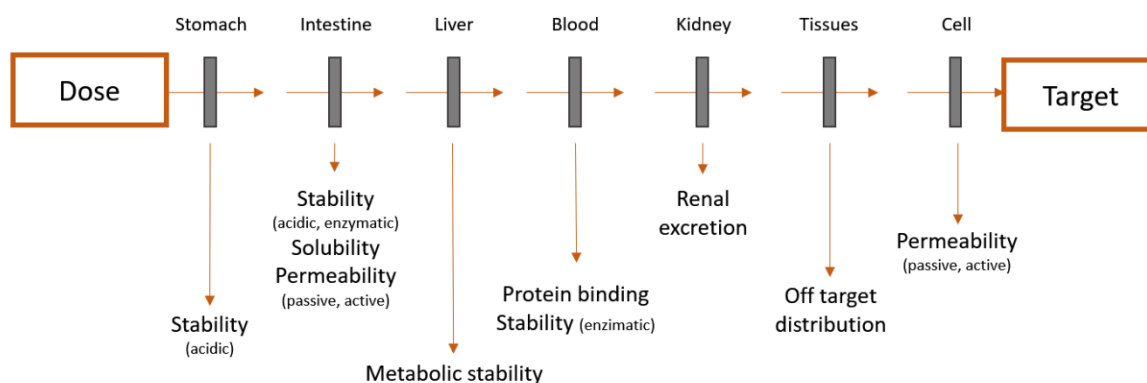
Figure 4. Barriers encountered by orally administered drugs between dosing and the therapeutic target. Studies that must be performed during early drug discovery. (Adapted from reference 28)

Information regarding activity and selectivity against the target allows researcher teams to identify the most promising candidates. However, solubility and permeability are the most critical features in the decision of what compounds can advance into the clinical stage. Candidates with poor solubility or permeability characteristics will hardly be successful regardless of their *in vitro* efficacy, due to the impairment of absorption and distribution.[20,29] During the early stages of drug discovery, studies also focus on the identification of the interaction of drug candidates with plasma proteins, which may reduce the amount of free drug available, and uptake and efflux proteins, that can move the drug into and out of the cells, respectively. In addition, metabolic assays are performed to predict *in vivo* drug stability and the rate of metabolism. Activity and toxicity of the resulting metabolites must be assessed as well.[28] *In vivo* assays using animals play a critical role in drug discovery, as they allow not only the scientists to understand the mechanism of diseases, but also to identify drug metabolites and excretion pathways, access absorption, bioavailability and drug distribution, which provide important information about drug efficacy and safety.[28,29]

The most promising candidates may be structurally modified to improve subtle deficiencies and optimise absorption, distribution, metabolism and elimination (ADME) properties without compromising its potency and selectivity - lead optimisation.[28]

The filtering process results in a reduced number of candidates, that if accepted by regulatory authorities can get into the clinical trials to test them on human volunteers and to evaluate safety and effectiveness. Usually, drug candidates are first tested in a small group of healthy volunteers to assess their safety and pharmacokinetics (Phase I). Studies progress later in patients carrying the disease to evaluate drug efficacy, side effects and determine the optimal dose (Phase II). Then, by subjecting the treatment to a larger patient population, efficacy and safety can be confirmed (Phase III). During this stage, the drug candidates are compared with available therapeutics and if a positive benefit-risk relationship is demonstrated, a marketing authorization is requested. Among a large set of compounds

considered at the beginning, only one or two drug candidates complete these clinical trials and is made available for clinical use after being approved by competent authorities such as the Food and Drug Administration (FDA) in the United States of America, and the European Medicines Agency (EMA) in the European Union. Patients will continue to be monitored to confirm effectiveness, long-term safety and identify less common side effects (Phase IV).[30]

1.3.1. *In silico* models

The importance of *in silico* methods is self-evident, as they can provide an efficient screening of thousands of drug candidates, select molecules that are more likely to succeed and eliminate those that are unlikely to have the desired pharmacokinetic profile, all those advantages without requiring the physical existence of the tested compounds. Thus, when implemented early in the process of drug development, they often reduce the need for an elevated number of experimental studies, allowing a significant reduction in resources and time required for synthesis and selection of promising molecules.[27,31]

Development of predictive and trustworthy methods is supported by *in vitro* and *in vivo* extensive databases and the identification of structural rules that correlate with the desired features. After selecting and analysing a set of 2245 drugs, Lipinski and co-workers identified four molecular parameters deeply associated with solubility and permeability that influenced drug absorption. The "Rule of 5" states that compounds with more than 5 hydrogen-bond donors (OH and NH groups), 10 hydrogen-bond acceptors (N and O atoms), molecular weight greater than 500 Da and LogP greater than 5 are poorly absorbed or permeable.[32] The growing interest in these predictive tools resulted in an assortment of models to estimate the intestinal absorption and blood-brain barrier permeation. These models include the combination of some molecular descriptors such as other lipophilicity parameters (LogD and ΔLogP), the number of rotatable bonds, the number of rings, the total number of atoms, the total surface area, the polar surface area, the molecular volume and intermolecular interactions.[31] Due to the complexity of biological systems, several compounds can fall within the "Rule of 5" or other general rules but have no potential as a drug for the desired purpose, or fall beyond the drug-like chemical space and still be absorbed and efficient after oral administration. This may occur either because of being substrates of biological transporters or because they may diffuse passively across bilayers or present adequate solubility in aqueous media in spite of their unfavourable molecular descriptors.[31–33]

Despite the potential of *in silico* methods, the success in therapeutic research is not assured, it only guides medicinal chemists and pharmaceutics in the correct direction, allowing a more rational and efficient drug design.[32] As the discovery progresses, more robust and reliable tests are used, *in vitro* or

even *in vivo* approaches, and the best candidates among the hundreds of molecules are selected. In this stage, membrane permeability, stability to metabolising processes and binding affinity to relevant biological transporters are some of the most relevant properties in study.[28,32]

1.3.2. *In vitro* models to predict drug permeability

1.3.2.1. Caco-2 permeability assay

The Caco-2 cells were initially isolated in the 70s from an epithelial colorectal adenocarcinoma of a Caucasian male, and exhibit morphological and functional properties of small intestine mature cells.[34–36] Since the introduction of these cells as a model of intestinal absorption in 1989[35], it has become a reference for studies regarding permeability[35,36] and toxicity effects[37] of potential drugs and formulations. With appropriate protocols, the drug's most effective transport pathway may be qualitatively and quantitatively evaluated (passive, paracellular permeation or active influx and efflux) and the drug absorption efficiency at the intestine may be predicted.[38,39] The Caco-2 cell line is also suitable for the study and identification of substrates, inhibitors and inducers of intestinal transporters[40,41], and the study of drug metabolism[42]. In addition, the extensive knowledge about the transport mechanisms and structure-transport relationships allows the identification of optimal physicochemical characteristics and the design of new pharmacological formulations with improved permeability and absorption.[39]

In Caco-2 permeability assays, the cells are seeded on permeable supports, placed at the interface between donor-receiver compartments (**Figure 5**). When cultivated in specific conditions, these cells grow to form a confluent monolayer and differentiate spontaneously, exhibiting microvilli on the apical membrane, tight junctions between cells and expressing proteins involved in uptake and efflux processes and several drug-metabolising enzymes. The confluent polarised monolayer provides a selective barrier, simulating intestinal absorption to the bloodstream. Drug permeability from the apical to the basolateral side (absorptive transport) is usually assessed, although it may also be done from the basolateral to the apical side (secretory transport). In both cases, the drug accumulation in the acceptor compartment is followed over time, using adequate techniques for its quantification (usually chromatographic and spectrometry based methodologies).[43]
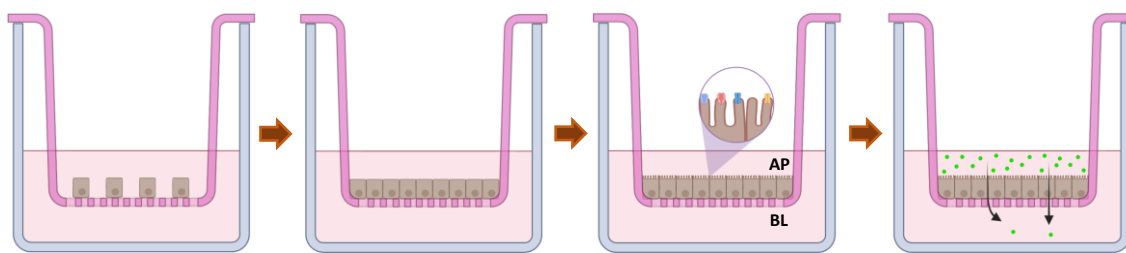
Figure 5. Simple representation of the protocol used to evaluate drug permeability with Caco-2 cell lines. After being seeded on a porous support, Caco-2 cells grow into a confluent cell monolayer and start to differentiate spontaneously, expressing several morphological and functional characteristics of the mature enterocyte. At this point, the cell monolayer exhibits microvilli on the apical membrane, tight junctions between cells and several intestinal transporters and enzymes on the apical and basolateral membrane. The drug solution is typically added to the apical side (AS) and samples from the receiver compartment or basolateral side (BS) are collected and analysed over time.

Caco-2 permeability assay has been recognised by pharmaceutical and regulatory authorities as a standard assay to predict intestinal permeability. The permeability obtained is a sum of different mechanisms (active, passive, endocytose and paracellular pathways) which gives an overall vision about the ability of the compound to cross through the intestinal barrier. This makes it difficult to understand in detail the properties of solutes and identify general rules that control the permeation process. To study and quantify individually each permeation mechanism, several studies under multiple conditions are required. Other disadvantages are the cost, the time required for cell culture and the high probability of contamination. In addition, the variability introduced by culture-related conditions and the *in vivo* variability impose poor reproducibility and inter-laboratory variations, limiting the quantitative comparison between results reported in the literature.[44] Correlation between *in vitro* and *in vivo* data are affected by the expression levels of uptake and efflux transporters as well as the lower or non-existing levels of some intestinal enzymes in Caco-2 cells, with drug absorption being sometimes under- or overstimated.[45]

Similar to Caco-2 cells, when seeded on a porous support, Madin–Darby Canine Kidney (MDCK) cells differentiate into a polarised monolayer of epithelial cells with the apical membrane covered with microvilli and exhibiting tight junctions between adjacent cells. The correlation between permeability data in MDCK cells and human absorption is similar to that encountered in the Caco-2 permeability assay. Additionally, as it is a faster-growing cell line, only 3 days of culture needed, it allows a faster membrane permeability screening (a great limitation of Caco-2 permeability assay) in the early stages of drug discovery and development.[46]

Several assays have been proposed to study permeation across the blood-brain barrier (BBB) but a standard model or assay still does not exist. Due to the specific membrane characteristics of BBB (hydrophobicity and rigidity), prediction of *in vivo* permeability by some of these models may be in general inaccurate.[47] Reported cell-based assays for BBB penetration use primary cultures of brain

capillary endothelial cells, triple cultures with astrocytes and pericytes or use epithelial cell lines (MDCK and Caco-2 cells), with the firsts being considered the best *in vitro* BBB models (similar morphological structure, free of leaks and similar expression of BBB transporters).[48]

An essential factor for good drug bioavailability and efficacy is the ability of a compound to cross the lipidic barrier and be absorbed. For industrial use, given the high number of candidates in the first stages of drug development, it is always preferable to use higher throughput strategies as an alternative to labor, time- and cost-intensive, and sensitive cell-based assays to predict permeability and discard, as soon as possible, those compounds that are prone to failure.

1.3.2.2. <u>Parallel Artificial Membrane Permeability Assay (PAMPA)</u>

Parallel Artificial Membrane Permeability Assay (PAMPA), introduced in the end of the 20th century, is an inexpensive and a moderate throughput method. In this assay, the permeability barrier is an artificial membrane formed by a mixture of lipids and an inert organic solvent, immobilised on a hydrophobic filter.[49] Due to the simple and chemical nature of the barrier, the assays have good reproducibility, small variability and are easy to automate, which has attracted the industry pharmaceutics attention over the years. The PAMPA method easily evaluates the ability of certain compounds to permeate hydrophobic membranes, being useful at an initial stage in drug discovery research by identifying priority and most likely to succeed compounds for more detailed *in vitro* and *in vivo* studies.[49,50]

PAMPA set-up is identical to those of Caco-2 permeability assay. Test compounds are added to the donor wells, carefully placed on the top of the donor multi-well plate, in a sandwich construction (**Figure 6**). During the incubation time, the compounds diffuse across the artificial membrane into the acceptor well and their concentration on the donor and receiver chamber are measured after an incubation time, using chromatographic and spectrographic measurements, depending on the tested compound properties.
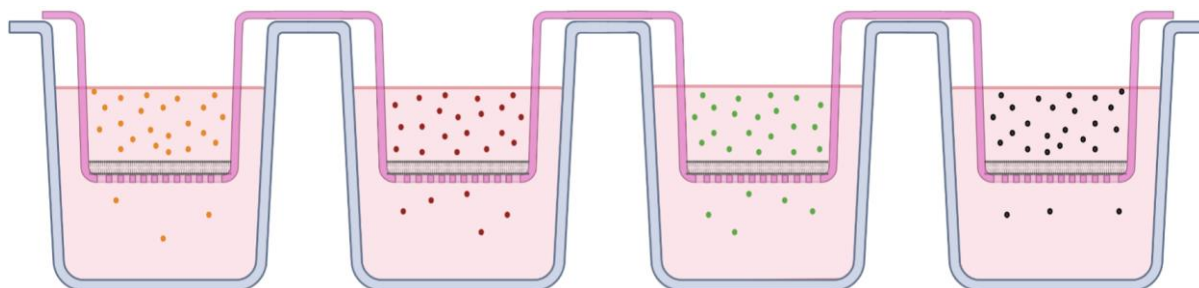
Figure 6. PAMPA sandwich construction, consisting of a donor compartment on the top filled with drug solutions, an artificial membrane on the filter supports in the middle and an acceptor compartment on the bottom.

As PAMPA is a cheap and reproducible method, it supports multidimensional studies and allows numerous experimental designs. The effect of pH and pH gradients, solubilising agents, surfactants and serum proteins are some of the extensive examples of different studies that can be used for *in vivo* prediction.[49] By changing the lipidic composition of the artificial barrier, this assay allows to easily study their effect on permeation and absorption. PAMPA assays variants were used not only to predict the contribution of passive pathways in drug's absorption across the gastro-intestinal epithelium but also across the blood-brain barrier[51] and skin[52].

PAMPA and cell-based permeability assays are not competitive approaches. Both can guide, in a productive way, possible structural modifications on drug candidates and formulations to enhance permeation. Their combination gives a more detailed understanding and is helpful when there is no information about the transport pathway and to determine the role of passive and active permeation.[49,53] Moreover, without the measurement of passive permeation by PAMPA, it would be difficult to decouple passive and active permeation processes. Drugs that exhibit a good correlation between PAMPA and Caco-2 permeabilities have passive diffusion as the predominant permeation mechanism. PAMPA permeabilities lower than that predicted by Caco-2 assay point towards a significant contribution of active and/or paracellular transport, while significantly bigger PAMPA permeabilities suggest that drugs are subjected to secretory transport mechanisms, such as efflux processes.[53]

In spite of the recognised usefulness of PAMPA in the prediction of permeation by passive routes, the results must be interpreted with caution because the properties of the hydrophobic barrier are somewhat different from those of the lipid bilayer of biomembranes.[50] The major limitation is due to the presence of very high amounts of organic solvent (usually dodecane) which is coated with phospholipids to allow wetting by the aqueous transport media used in the permeability assays and may change solute permeability. The typical mass percentage of phospholipids in the PAMPA hydrophobic barrier is around 3 %.[47] Other important limitations, which are somehow a result of the previous one, are the much higher thickness of the hydrophobic barrier (several μm as compared to only a few nm for biomembranes), and the possible formation of non-bilayer structures.

There are several versatile methodologies easily applied that, such as PAMPA, allow different setup experiments to measure passive permeation, being however better mimetic models of biological membranes by presenting similar intrinsic properties.

1.3.2.3. Liposome-based assays

Liposomes have been employed in a broad spectrum of studies about numerous membrane related phenomena including, for example, bilayer permeation. Liposomes are easy to manipulate and allow several possibilities regarding the lipidic composition and different set-up conditions. By allowing a better understanding of the molecular mechanism of membrane permeabilization, liposome-based assays enable the study of the most relevant mechanism of *in vivo* barriers, the gain of detailed insights about the role of the barrier properties, also being useful for drug delivery research. In turn, methodologies using proteoliposomes allow the study of kinetics and transport mechanisms mediated by membrane transporters.

Liposome permeation kinetics can be monitored in real-time by the measurement of the fluorescence of compounds that exhibit self-quenching at higher concentrations. The self-quenching can be used to detect changes in the luminal volume of the liposome upon solute permeation[54] or to evaluate the leakage of compounds such as calcein[55] or carboxyfluorescein[56]. The set-up experiment consists in encapsulate the probe, remove it from the outer aqueous compartment and evaluate the fluorescence over time. To evaluate the permeation of fluorescent compounds that do not exhibit self-quenching the set-up experiment is equivalent to the one described above, however, the measurement of the leakage profile does not occur in real-time and the separation of the liposome from the outer aqueous medium must be performed by size exclusion chromatography or ultrafiltration, and the destruction of lipidic vesicles by a surfactant is required.[57,58] The samples of the external and internal compartments are usually analysed by fluorescence or UV absorption. A different assay that avoids the separation of the inner content from the outer one consists in the placement of a lipid solution, without solute outside, in a dialysis tubing. Liposomes remain inside of the semipermeable tubing while small molecules can diffuse out. During the incubation time, aliquots from the external media are collected at different time points and further analysed based on the test compound properties. Fluorescence quenching and fluorescence enhancing upon labelling with impermeable agents are some examples.[59] One of the limitations of the methods described above, specifically those with the need for separation of internal and external contents and dialysis assays, is that they are only applicable for very slow solute permeation.

Based on specific known interactions, several compounds can be entrapped in liposomes to directly characterise the diffusion across lipidic membranes. For example, the fluorescence of trivalent lanthanide ions, such as Terbium and Europium, increases upon formation of a chelate with aromatic compounds, by energy transfer from the aromatic system to the ion upon excitation at the absorption wavelength of the first. This assay has already been used to measure the permeation of biological relevant entities coupled to carboxylic acids and an aromatic system to gain new insights into their

transport pathways.[60,61] Proteins that enhance the fluorescence properties of their substrates can also be encapsulated and used to access permeability coefficients.[62] A prerequisite for these assays is that the kinetics of these processes must be negligible when compared with the permeation of the compounds.

The methods described above can be divided into two sets of assays: i) the test compound was fluorescent and ii) other components with which the test compound could interact should be entrapped inside the liposomes. In the case of the permeation of weak acids and bases, the concentration of protons inside the liposomes will change and the permeation can be monitored in real-time by the fluorescence of pH-sensitive probes.

1.3.2.4. pH variation assay

pH gradients can be a consequence of the selective permeation of specific cation or anions (Donnan equilibrium)[63] or a consequence of the more favourable permeation of the neutral species of weak acids or bases[64]. They have been extensively studied as a method to increase the loading of weak acids and bases.[57]

Fluorescent probes have firstly been used to estimate pH gradients[65] and monitor the proton-hydroxide flux in response to pH gradients[66]. Methodologies using pH variations have already been used to estimate weak acid permeation simultaneously with monitoring the efflux of the fluorescent probe carboxyfluorescein[56] or, more recently, by measuring the fluorescence of the entrapped fluorescent probe pyranine, using large unilamellar vesicles (LUVs) prepared by extrusion[67].

Permeation kinetic of drug-like compounds across a single lipid bilayer can be measured in real-time by different fluorescence assays as described before. A methodology based on monitoring the pH using a sensitive probe has been recently applied in the measurement of several weak acid and bases permeabilities. The pH variation assay applies to weak acids or bases without a chromo- or fluorophore and is based on the hypothesis that the permeation of the neutral form of these compounds is significantly faster, resulting in the release (acids) or uptake (base) of protons once inside the liposomes (**Figure 7A** and **B**, respectively).[68] This leads to a pH variation in the inner aqueous compartment when the proton equilibration across the lipid bilayer is slower than solute permeation. pH variations are monitored in real-time with an encapsulated or a membrane-anchored pH-sensitive probe. An encapsulated probe is usually preferable as its fluorescence will not report extraluminal processes.
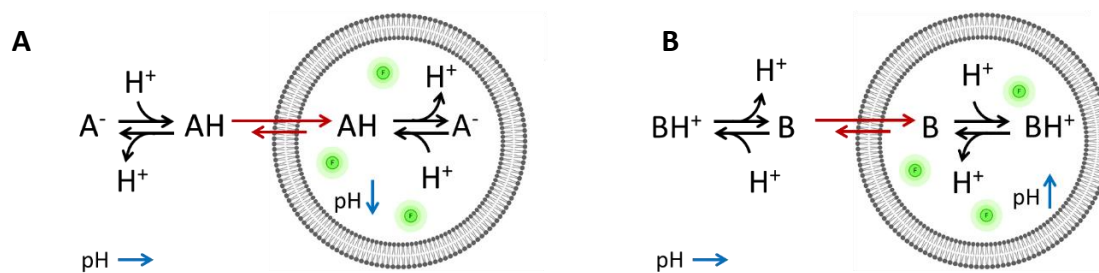
Figure 7. Simple representation of the pH variation assay: **A)** Permeation of a weak acid, AH, with A⁻ being its conjugated base, accompanied by a decrease in the luminal pH. **B)** Permeation of a weak base, BH⁺, with B being its conjugated acid, followed by an increase in the luminal pH. ⊛ denotes the encapsulated fluorescent probe that allows the observation, in real-time, of the pH variation induced by solute permeation. (Adapted from reference 68)

In this liposomal fluorescence assay, the outer medium is buffered while the lumen is not or has a lower buffer capacity (for example from the fluoresce probe only). Thereby, the release or capture of the protons inside the liposome generates a pH gradient between the inner and outer aqueous compartments. The dissipation of the pH gradient proceeds at a slower rate due to the low permeability of H^+/OH^-. In these assays, it is therefore observed a fast variation in fluorescence (assigned to solute permeation), followed by a slow variation in the opposite direction due to the dissipation of the pH gradient.

In studies performed by the Stefanie Krämer group[68,69] for the permeation of weak bases and acids, the fully kinetic profile was fitted with a four-exponential function

$$F[t] = \alpha_1 \, e^{-\beta_1 \, t} + \alpha_2 \, e^{-\beta_2 \, t} + \alpha_3 \, e^{-\beta_3 \, t} + \alpha_4 \, e^{-\beta_4 \, t} + F_0 \tag{1}$$

with α_1, α_2, α_3 and α_4 being weighting coefficients and β_1, β_2, β_3 and β_4 the respective characteristic constants (units of s^{-1}) and F_0 being the fluorescence signal at $t = 0$. For weak acids permeation, the terms $\alpha_1 \, e^{-\beta_1 \, t}$ and $\alpha_2 \, e^{-\beta_2 \, t}$ describe the fast fluorescence decreasing phase (α_1, $\alpha_2 > 0$) while the terms $\alpha_3 \, e^{-\beta_3 \, t}$ and $\alpha_4 \, e^{-\beta_4 \, t}$ describe the slower increasing phase (α_3, $\alpha_4 < 0$), with β_3 and β_4 being solute-independent, $\beta_1 > \beta_2$ and $\beta_3 > \beta_4$. Permeability coefficients for the tested compounds were obtained considering the liposome radius and using the fastest characteristic constant of the first phase (β_1), according to the equation

$$P = \beta_1 \frac{r}{3}. \tag{2}$$

By characterising the kinetics of different weak acids and bases, this assay allows the understanding of general rules that govern passive permeation and guides the development of drugs with improved properties. Despite being applied only to weak bases and acids, it is not a "true" limitation as a significant part of the drugs, toxins and biological ligands have ionisable moieties.[70] This assay was also applied and adapted for high-throughput measurements on a microfluidic chip which denotes its potential in pharmaceutical research.[68]

The pH variation assay has already been used to study the permeability of several drugs. For the compounds tested, those whose intestinal absorption is independent of transporters, permeability coefficients obtained by the Caco-2 permeability assay and the pH variation assay correlate better with human data than the prediction based on octanol/water distribution coefficients or even PAMPA.[69]

However, this assay is prone to some artefacts, and some authors have raised several questions and objections to the work developed by Krämer and co-workers. One of the presented arguments was that protonation kinetics should be considered in the analysis of permeation. The origin of the bi-exponential relationship in the fast fluorescence variation is one of the concerns, questioning whether it may contain information about the ionisation of the solute and/or fluorescent probe in addition to the permeation of the solute.[71,72] Alternative kinetic models were proposed in these works to explore those issues. Both models neglect the permeation of the charged compound, do not consider explicitly the water-membrane partition of the neutral and charged species but consider the kinetics of ionisation processes. Their mathematical description of the pH variation assay is not complete and one of these works does not even include the permeation of the proton. In the most recent paper, it is concluded that the chemical reactions of buffer, probe and solute (ionisation) are not rate-limiting, as they occur much faster than solute permeation.[71]

The present work will explore the origin of the multi-exponentiality in the time evolution of the fluorescence and give a better understanding of the methodology through the development of a complete and detailed kinetic model for the permeation of weak acids and bases. This model will allow the identification of the best experimental practices to make the assay more robust and less fallible.

1.3.2.5. Comparison between the methods

The Caco-2 permeability assay and PAMPA are currently the most relevant methods to assess permeabilities coefficients during the early stages of drug discovery. The most recent method, the pH variation assay, also looks promising. Table **1** resumes some characteristics of the three methods.

Table 1. Comparison between Caco-2 permeability assay, Parallel Artificial Membrane Permeability Assay, and pH variation assay.

Assay	Caco-2	PAMPA	pH variation assay
Configuration	Cell monolayer	Artificial membrane (impregnated filter)	Artificial membrane (vesicle)
Type of permeability	Passive Active uptake Active efflux Paracellular	Passive	Passive
Metabolism	Yes	No	No
Application	Depends on the detection method Virtually applicable to all solutes		Weak acids and bases with or without a chromo- or fluorophore
Analysis method	LC-MS, MS, HPLC-UV/Flu quantification		Kinetic on a Stopped flow apparatus
Permeability estimate	Different time points	One time point	Kinetic measurement (fluorescence of an entrapped probe)
Assay preparation	Requires cell culture, time consuming	Easy, no time consuming, easy to automate	Easy, no time consuming
Cost	High	Low	Low
Throughput	Low	Medium	Medium

1.4. Kinetic models to describe lipid-bilayer permeation

To gain predictive power from the results available and be able to rationally design drugs with improved bioavailability, it is necessary to understand the role of the properties of the solute and lipidic barrier on the rate of solute permeation. For this goal, it is important to understand the mechanism of permeation through the lipid bilayer. Several models have been proposed and the most relevant in passive permeation are presented below.

1.4.1. Solubility-diffusion model

At the end of the 19th century little was known about the structure of the cell membrane. In 1899, Hans Meyer found that the anesthetic potential of a series of compounds is nearly proportional to its oil/water partition coefficient, and the ability of a solute to permeate a biological membrane is ruled by its liposolubility.[73] Independently and at the same time, Ernest Overton reached the same conclusion, by examining the capability of hundreds of substances to diffuse into isolated cells, through the measurement of their plasmolytic effects.[74] These findings led to the solubility-diffusion model also known as Meyer – Overton's Rule. This is a simple approach that considers the bilayer as a static and homogenous phase – an oil-like liquid – separating two aqueous phases.[74] It neglects the permeation of charged compounds because their solvation by the oil-like membrane is prevented.

According to the solubility-diffusion model, membrane permeation is described by the dissolution of the solute in the hydrophobic core of the membrane, followed by the diffusion across the barrier and partition into the aqueous phase. The diffusion process is assumed to be the rate-limiting step while the membrane-water partition is considered close to equilibrium.[75,76]

Diffusion across a barrier with the thickness h can be described based on Fick's first law, which states that in the presence of a membrane concentration gradient ($c_{1m} - c_{2m}$) the flux of matter *per* time interval and *per* area (J) is proportional to the diffusion coefficient of the solute inside this phase (D, with units of area *per* time).[76]

$$J = -D \frac{dc}{dx} = -D \frac{c_{1m} - c_{2m}}{h} \qquad (3)$$

Rewriting equation (3), with the concentration in the membrane expressed in terms of the partition coefficient between the aqueous phase and the membrane (K_P) one gets

$$J = D \frac{K_P (c_{2w} - c_{1w})}{h}, \qquad (4)$$

with the permeability P being equal to $\frac{D\,K_P}{h}$.

Considering the diffusion of a molecule from side 1 to side 2 (**Figure 8**), the rate of appearance of a compound on side 2 is defined by

$$\frac{d\,n_{2w}}{dt} = k_{DA}\,n_{1w} - k_{AD}\,n_{2w}, \qquad (5)$$

where k_{DA} and k_{AD} are the first-order rate constants for the diffusion from the donor to the acceptor and from the acceptor to the donor compartments, respectively.
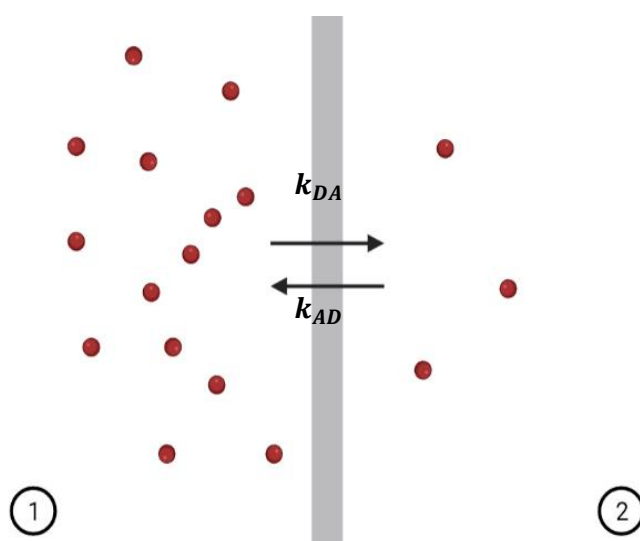
Figure 8. Diffusion across a membrane, from the highly concentrated side 1 to side 2.

Assuming that there are no molecules on side 2 at the beginning, the sum of moles of solute is constant and equal to the number of moles of molecules on side 1 at $t = 0$.

$$n_{1_w}[t] + n_{2_w}[t] = n_{1_w}[0] \tag{6}$$

Considering the above conservation relationship and integrating the equation (5) yields a mono-exponential function

$$n_{2_w}[t] = n_{1_w}[0] \frac{k_{DA}}{k_{DA} + k_{AD}} \left(1 - e^{-(k_{DA}+k_{AD})t}\right), \tag{7}$$

with $k_{DA} + k_{AD}$ being the characteristic constant for the accumulation of the permeable molecule on the side 2.

As the disappearance of a molecule from side 1 and its accumulation on side 2 is proportional to the surface area and permeability, by converting $\frac{d\,n[t]}{dt}$ to $\frac{d\,c[t]}{dt}$ (dividing by the respective compartment volume) and assuming that the permeability is the same in both directions, k_{DA} can be defined by $P \frac{A}{V_D}$ and k_{AD} by $P \frac{A}{V_A}$. The terms V_D and V_A stand for the volume of the donor and acceptor aqueous compartments, respectively. According to the solubility-diffusion model, the rate of solute accumulation is $\frac{D\,K_P}{h} A \left(\frac{1}{V_D} + \frac{1}{V_A}\right)$.

Some of the limitations of the solubility-diffusion model are the assumption of a fast partition in comparison with the transport across the membrane and that the last process occurs by diffusion. Thus, according to this model, permeation across lipid bilayers depends on the membrane thickness, the viscosity of the medium (η), and the solute hydrodynamic radius (R_h) as described by the Stokes-Einstein equation,

$$D_\tau = \frac{k_B\,T}{6\,\pi\,\eta\,R_h}, \tag{8}$$

where k_B is the Boltzmann's constant and T is the absolute temperature.

Although biological membranes are a dynamic and quite heterogeneous medium, this model yields satisfactory predictions for the relative permeability of very small and uncharged solutes. However, the solubility-diffusion model does not always lead to good predictions of solute's permeability coefficient in the case of more complex solutes. In extreme cases, the model may even predict a behaviour opposite to that observed. This is the case when an increase in solutes' hydrophobicity leads to a decrease in the ability to cross the biological barriers. This suggests that for relatively complex molecules permeation occurs with more complicated mechanisms or that a different rate-limiting step is present.[75,77]

1.4.2. Flip-Flop model

Due to the amphiphilic properties of membrane lipids and the ability of electrostatic interaction between the solute and the lipid head groups, membranes can also efficiently solubilise charged compounds. In this case, permeation can be more complex than that predicted from the solubility-diffusion model. According to the Flip-Flop model, the rate of translocation does not depend on the diffusion rate across an isotropic medium, but on the probability of a flip-flop process.[76] Moreover, there are some situations where the rate of interaction of the amphiphilic compound with the membrane (particularly the desorption) may be considerably slow or that a single rate-limiting step is not identified, affecting the overall permeation.[77,78] Thus, insertion and desorption rates, as well as translocation rate, must be considered to describe solute permeation in alternative to the solubility-diffusion model.[77]

Based on the Flip-Flop model the permeation of amphiphilic compounds occurs by a three-step process (**Figure 9**). The amphiphilic solute may insert in the outer monolayer, with the rate constant k_+, translocate between the outer and inner leaflet, with the rate constant k_f, and desorb from the bilayer, with the rate constant k_-.

$$A + L^{out} \underset{k_-}{\overset{k_+}{\rightleftharpoons}} AL^{out} \underset{k_f}{\overset{k_f}{\rightleftharpoons}} AL^{in} \underset{k_+}{\overset{k_-}{\rightleftharpoons}} A$$
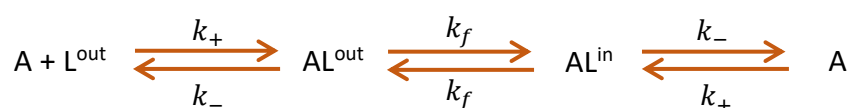
Figure 9. Scheme of the bilayer permeation process of an amphiphile compound A: Partition into the bilayer is described by k_+, translocation between the two leaflets by k_f, and desorption by the rate constant k_-.

If the rate constant of the flip-flop is much smaller than the rate constants for the association/dissociation processes, the permeation kinetics follows a mono-exponential function, as in the solubility-diffusion model. However, the relationship between the rate of permeation observed and the molecular properties of the solute is distinct for both models. While the focus is given on solute size (R_h) and hydrophobicity (K_P) in the case of the solubility-diffusion model, properties such as amphiphilicity, charge and shape are implicit in the flip-flop model. If no single rate-limiting step can be identified the kinetics becomes complicated and deviates from a mono-exponential behaviour. In this case, it may be possible to characterise all the relevant rate constants (insertion, desorption, and flip-flop), as performed for the homologous series of NBD-Cn fluorescent amphiphiles[79], and the drug chlorpromazine[80].

1.5. Permeation of charged compounds

1.5.1. pH-partition hypothesis

Compared to neutral species, the partition of charged compounds into alkanes is not favourable. Therefore, according to the diffusion-solubility model, it is assumed that only the neutral species associates with the membrane with the diffusion of ionised species not contributing to the overall permeation. Based on this belief, membrane permeation (P_{app}) is thus related to the molar fraction of the neutral form of an acid or base in solution (f_{ns}) multiplied by its intrinsic permeability coefficient (P_{ns}), equation (9).[58] Considering a weak acid, the fraction of the neutral species at a specific pH relates with its ionisation constant (K_a) and the concentration of protons.

$$P_{app} = f_{ns}\, P_{ns}, \text{ where } f_{ns} = \frac{[H^+]}{[H^+]+K_a} \tag{9}$$

Under alkaline conditions, the logarithm of the permeability as a function of the pH exhibits a linear dependence with a unitary slope and a plateau is observed at lower pH as the neutral form is dominant in such situations (blue curve in **Figure 10**). Significant deviations from this linear relationship at higher pH may reflect a contribution to transport from the charged species (red curve in **Figure 10**) which prove that as well as hydrophobic interactions, the electrostatic ones may also contribute to the binding of solutes to lipid bilayers, despite their oil-like bulk.[58] In contrast with the pH-partition hypothesis, permeation is better described as a weighted average of the intrinsic permeability of each species in solution accordingly equation (10), where P_i is the intrinsic permeability of each charged compound at a molar fraction f_i. Moreover, the permeation of charged species may not be much slower than that of the uncharged ones, when for example they are able to form intramolecular hydrogen bonds and thus delocalise their charge.[78] In any case, even when the permeability of the charged species is much slower than that of the neutral form, the first will control the overall permeation kinetics through the biological barriers when its fraction is high enough ($[H^+] \ll K_a$).[58,61]
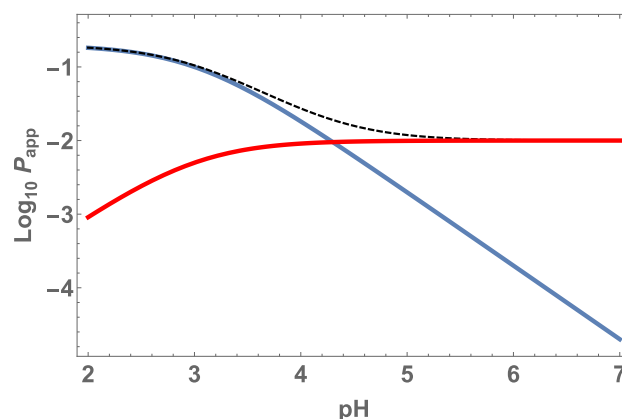
Figure 10. pH-permeation profile of a weak acid with pK_a equal to 3. pH-permeation profiled associated to the permeation of the weak acid (——), its conjugated base (——), and if both species can permeate (- - - - -).

$$P_{app} = f_{ns} P_{ns} + \sum f_i P_i \tag{10}$$

Before reaching the target, the drugs must pass through different barriers. The pH variation along the gastrointestinal tract influences not only the solubility but also the absorption of ionisable drugs. In the stomach, the pH is highly acidic ($\approx$ 2) and increases gradually along the gastrointestinal tract to slightly a basic pH.[81] The knowledge of the intrinsic permeability of the neutral and charged forms is extremely important to evaluate drug delivery and their ability to cross biological membranes.

1.5.2. Mathematical description

Permeation of charged compounds is driven by both a concentration $\left(\frac{dc_1}{dx}\right)$ and an electrical gradient $\left(\frac{d\psi}{dx}\right)$, as described in equation (11), where D is the diffusion coefficient, z is the valency of the ionic compound, R is the ideal gas constant, F is the Faraday constant and T is the absolute temperature.[82]

$$J = -D \left(\frac{dc_1}{dx} + c_1 \frac{z\,F}{R\,T} \frac{d\psi}{dx}\right) \tag{11}$$

Net charge transfer only stops when the electrochemical potential of each species (equation (12)) is equal in both compartments. The dissipation of the concentration gradient may not be observed if the transmembrane potential can compensate for it.[83]

$$\tilde{\mu} = \mu_0 + R\,T \ln c + z\,F\,\psi \tag{12}$$

μ_0 is the standard chemical potential, c is an arbitrary concentration of an ion with valency z and ψ is the local electrostatic potential.

The movement of charged species with different permeabilities results in an accumulation or depletion of charge, which is responsible for the development of an electrical potential that opposes the driving force of the gradient concentration.

When describing the permeation of charged solutes across membranes in the absence of an electrical field, the charge neutrality on both sides of the membrane must be ensured by the simultaneous permeation of an electrolyte (potassium, sodium, chloride), a proton, or a hydroxide ion in response to the developed transmembrane potential. Charge neutrality may also be achieved through the translocation within the lipid bilayer of charged lipids or fatty acids.[76] The direction of this permeation and/or translocation mechanism is defined by the developed potential (positive or negative) and the valency of the ion responsible for its dissipation.

1.6. <u>Mathematical modelling</u>

The increase of the computational power in the last years came to revolutionise biological and pharmaceutical research that requires an efficient analysis of an abundance of data.[84] Modelling is a powerful tool to deal with and analyse complex phenomena involving a set of diverse elements and resulting from multiple interactions at different organization levels. Studying systems as a whole allows understanding and predicting what might happen in some circumstances, creating and assessing new hypotheses, and obtaining explanations for non-intuitive behaviours. Such approach gives greater insights into the inherent complexity of biological systems and processes, allows their control and optimisation, guiding research teams in the development of new therapies and therapeutic compounds for treating human diseases.[38,77,84,85]
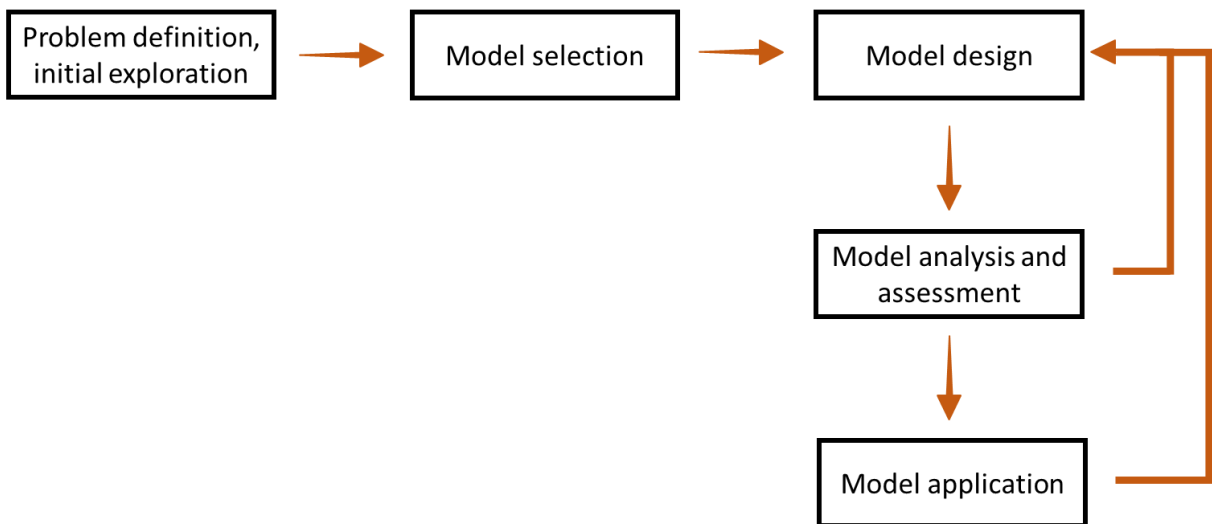
Figure 11. Overview of the typical modelling process.

The modelling process can be divided into five central steps (**Figure 11**). The first one is to study extensively the system of interest and identify specific research questions, define the aim and purpose of the model, and map what is or can be known.[85] At this stage, in order not to compromise the investigation, it is important to identify the aspects that should be integrated into the model, understand if the available information is reliable and sufficient and if the missing information can be accessed.

Based on the key questions and the system behaviours or processes of interest, the following step consists of the decision of the type of model that should be built. The choice falls on mechanistic models if the mechanistic information can attain the goals or if the goal is to identify the mechanism that explains some observations and data. Correlative models are supported by statistical analysis to estimate parameters and identify with which other parameters they correlate. Static models do not consider time and take into account structure, stoichiometry, and the topology of the interaction

network. In opposition, dynamic models consider variations with time, and prediction of the temporal evolution of the system is based on differential equations. Dynamic models can be stochastic if the system exhibits random effects or deterministic when the events depend on the parameter values and initial conditions. In some situations, two of the questions that must be addressed at this stage are if the process takes place on a homogeneous or compartmentalised medium and if any approximation may be done. Models should be simplified as much as possible, as usually complexity difficulties the analysis and can shift focus away from the objectives and goals of the model.[85]

During the design of kinetic models, a diagram that considers all relevant processes and interactions between the variables must be drawn and mathematical equations that rule these interactions are derived. In this phase, parameters are estimated from experimental data.

After model implementation, dimensions, conservation relationships, and system symmetries must be evaluated to identify some inconsistencies. In addition, if the data and the steady-state obtained by the model are not comparable or consistent with the observations or predicted behaviour, imperfections or errors must be detected and corrected in an iterative cycle (**Figure 11**). Some variations of the initial model are frequently developed to determine how discrepancies between computational predictions and experimental observations might be explained and eliminated, or to test different approaches. In this stage, it is common to perform stability and sensitivity analysis to understand the system behaviour after small perturbations and identify whether the results depend critically on uncertain or non-robust parameters. The process of assessment and validation may suggest new experiments, and the cycle repeats.[84,85]

When the model is considered plausible it can be used based on the initial aims. Even during its application and from the analysis of the experimental results, the initial hypothesis can be discarded, and new ones can be addressed. Hence, the work is redirected into the model design stage (**Figure 11**) and a refined and validated version of the model is built. Once the model is validated, several simulations can be carried out to examine the response to several perturbations and evaluate different experimental conditions.[84]

Despite the iterative process, which could be extensive, modelling should be viewed as a heuristic tool to better understand and interpret the behaviour of biological systems. Discrepancies between the predictions and the observable behaviour are a source of knowledge. Improved versions of the initial model can be built to consider other components or interactions that have not been considered or to test new hypotheses and sustain these differences. The modelling process allows more comprehensive pictures of biological systems and how they work.[84,85] The process of modelling the permeation of weak acids through the vesicle membranes is slightly simpler but follows the same guidelines, also giving useful information about the system behaviour.

1.7. **Objectives**

The pH variation assay is prone to some artefacts and interference from other weak acids/bases and charges in the system, justifying its analysis with a fully detailed kinetic model. As far as we know, a complete kinetic model has not yet been developed to describe this methodology. Some limitations of the kinetic models available in literature are the consideration of the lipid membrane as an infinitely thin barrier and the fact that they do not consider explicitly the permeation of charged species, which lead to the development and dissipation of electrostatic potentials. Some of the limitations have been addressed but with focus on specific questions only, such as the effect of pH buffers or the rate of acid/base equilibria.[71,72]

In this work, a complete kinetic model for the permeation of weak acids and bases is developed. The model considers the slow steps involved in the permeation of the solute, the processes responsible for the dissipation of the pH gradient, and the dissipation of the resulting transmembrane potential. Contrary to what has already been published by other authors, this model considers explicitly the volume occupied by the membrane, leading to four compartments: outer and inner aqueous compartments, and outer and inner membrane leaflets.

To implement properly and easily, the model was developed step by step instead of trying to do a complete model at the first attempt. This allows the identification and correction of some errors that prevented numerical integrations or lead to erroneous results. The model uses parameters that are already available for amphiphilic drugs and related compounds or can be easily obtained. By using this model, it is possible to simulate the effect of several parameters on the kinetics of solute accumulation inside the vesicles and their effect on the accuracy of the encapsulated fluorescent probe as a reporter of solute permeation in the pH variation assay. Such insights might provide useful information on how to perform the pH variation assay, avoiding some possible artefacts and thus providing accurate information on the rate of permeation of the molecule of interest.

Additionally, another purpose of this work is to determine proton and potassium permeabilities under different conditions and to evaluate if the ionophore valinomycin can be used in a pH variation assay to ensure the complete equilibration of weak acids and bases. This aspect has been addressed both with the collection of experimental data, and with the analysis of the results using the kinetic model developed.

Chapter 2

Materials and Methods

2.1. Reagents

A list of reagents used in this project is presented, including their manufacturers and CAS number.

Table 2. Reagents, suppliers, and CAS-Numbers.

Reagent	Supplier	CAS-Number
Ammonium molybdate - $(NH_4)_6Mo_7O_{24}$	BDH	12027-67-7
Ascorbic acid - $C_6H_8O_6$	Riedel-de Haën	50-81-7
Ethanol - CH_3CH_2OH	Merk	64-17-5
Ethylenediamine tetraacetic acid (EDTA) - $C_{10}H_{16}N_2O_8$	BDH	60-00-4
Hydrochloric acid at 37 % - HCl	Merk	7647-01-0
LiChroprep® RP-18 (40-63 µm)	Merk	108688-10-4
Methanol - CH_3OH	AppliChem	67-56-1
Perchloric acid at 70 % - $HClO_4$	Sigma Aldrich	7601-90-3
POPC - $C_{42}H_{82}NO_8P$	Avanti	26853-31-6
POPS - $C_{40}H_{75}NO_{10}PNa$	Avanti	321863-21-2
Potassium Chloride - KCl	Sigma-Aldrich	7447-40-7
Potassium hydroxide - KOH	Fluka	1310-58-3
Potassium phosphate monobasic - KH_2PO_4	Sigma-Aldrich	7778-77-0
Sodium phosphate dibasic - Na_2HPO_4	Sigma Aldrich	7558-79-4
Valinomycin - $C_{54}H_{90}N_6O_{18}$	Acros Organics	2001-95-8
8-Hydroxypyrene-1,3,6-trisulfonic acid (HPTS) - $C_{16}H_7Na_3O_{10}S_3$	Sigma-Aldrich	6358-69-6

All aqueous solutions were prepared with deionised water (Arioso Water Purification System).

2.2. <u>Computation</u>

A kinetic model for the permeation of weak acids across the membrane was developed step by step using the software *Mathematica*[TM] (version 12.2).[86] In Model I, it is assumed that only the neutral form, the weak acid, can permeate the membrane. Model II considers binding agents encapsulated in the vesicles. Model III implements independently two modifications in the first model: the permeation of the conjugated base and the permeation of the proton. The final model (Model IV) considers all the steps involved in the permeation of the solute and pH variation inside the vesicles, including the permeation of the proton and the conjugated base. It also includes the dissipation of the transmembrane potential generated by the permeation of the charged species. This process is modelled by the permeation of potassium ions. From this model, some modifications were performed to characterise the permeation of weak bases (Model V). A detailed description of all the models is given in *Chapter 3 – Model Development and Implementation*.

2.3. <u>Preparation of large unilamellar vesicles</u>

Large unilamellar vesicles containing HPTS were prepared by extrusion.[87] The desired amount of POPC and POPS stock solutions in chloroform were mixed (9 : 1) and evaporated under vacuum to form a lipidic film on the walls of a conical flask on a BÜCHI rotavapor R-114 attached to a BÜCHI water bath B-480. To remove the remaining organic solvent the flask was placed into the exicator for at least 1 hour.

Posteriorly, the thin film was hydrated with gentle stirring at 37 °C, with a solution at pH 7.0 containing HPTS, 100 µM, KCl, 150 mM, and EDTA, 1 mM. The multilamellar vesicles formed were then subject to 3 freeze and thaw processes using liquid nitrogen and a water bath, respectively, and passed through two staked polycarbonate filters (Nucleopore) with 2.5 cm diameter and 200 nm pore size in an extruder (Lipex Biomembranes, Vancouver, British Columbia, Canada). The freeze and thaw steps allow to homogenise the lipid composition, increase the entrapped volume and promote the equilibration of compounds inside and outside the vesicles. The procedure freeze-thaw-extrusion was repeated three additional times and, subsequently, ten extrusion cycles were performed. The pression for the extrusion was kept between 5 and 10 bars using nitrogen flow. The resulting LUVs were allowed to equilibrate overnight before use.

2.4. <u>Exchange of the outer aqueous phase</u>

The outer aqueous phase containing HPTS was exchanged with a solution at pH 7.0 with KH_2PO_4 (10 mM), EDTA (1 mM), and KCl (131.7 mM, to maintain the ionic strength) by size exclusion chromatography. The column Pierce Chromatography Cartridge Desalting, 5 mL, (Thermofisher) was previously washed and equilibrated with the desired buffer solution. Liposome solution (0.5 mL) was injected into the column, the LUVs were eluted using a controlled flux lower than 5 mL/min and collected. After this procedure, the outer aqueous phase of the liposome solution becomes buffered by potassium phosphate while the buffer capacity of the inner aqueous phase is very small (HPTS is also a pH buffer but is present at a much smaller concentration, 0.1 mM). The pH-sensitive probe HPTS encapsulated in the vesicles is unable to permeate membranes due to the negatively charged sulfonic substituents. The collected fractions were then analysed using a SpectraMax iD5 microplate reader (Molecular Devices, San José, California, EUA), by detection of HPTS fluorescence around 510 nm to identify those that contain the vesicles (with encapsulated HPTS) but not HPTS in the outer aqueous compartment.

2.5. <u>Dynamic light scattering measurements</u>

Dynamic light scattering is a sensitive technique useful to characterise the size of dispersed particles. In solution, particles collide with solvent molecules resulting in random movements, called Brownian motion. The intensity and frequency of these collisions are dependent on the molecular size, temperature, and solvent viscosity. In a dynamic light-scattering experiment, a monochromatic beam is dispersed in all directions by the particles in solution and the fluctuations of the scattered light intensity are dependent on the time that the particles remain in the laser path. When the particles can only move by Brownian motions (in the absence of flow due to solvent or thermal inhomogeneities or due to particle sedimentation), the frequency of light scatter intensity gives information about the particle diffusion coefficient. From the diffusion coefficient, and assuming that the particles are spheres, the hydrodynamic radius is obtained, based on the Stokes-Einstein (equation (8), Section 1.4.1).[88]

A Malvern Nano ZS (Malvern Instruments, Malvern, UK) was used to measure the intensity of scattered light of liposome solutions to extract their size. The measurement was performed with a zeta potential cell from Malvern because this property was measured as well. The cell has conductive points to receive and transmit an electrical current. When an electric field is applied, particles move in a direction that is dependent on their charge, and the detected intensity of light fluctuates with a frequency that is proportional to the speed of the charged particle. The increase in this speed is accompanied by a raise in the zeta potential.

2.6. <u>Lipid quantification</u>

The quantification of the lipids was made through the quantification of phosphate groups by a colorimetric method.[89] The outer aqueous medium of liposome solutions contain inorganic phosphate in large amounts (the phosphate buffer) that reduce the sensitivity and accuracy of the method for the quantification of phospholipids. It was therefore necessary to first remove the phosphate buffer. This was made by passing the liposome suspension through a column packed with RP-18 resin. The resin was first suspended in ethanol and the column was equilibrated using this solvent. The mobile phase was then changed progressively into water, and after being equilibrated with 1 to 2 mL water the sample was applied. A volume of 1 mL of water was added to allow very polar compounds (such as inorganic phosphate) to elute. Posteriorly, 13 fractions of 1 mL of methanol were added to elute the phospholipids and the elution solution was collected in a round bottom flask. Methanol was evaporated using a rotavapor and the lipid film was resuspended with three aliquots of 1 mL methanol. Each aliquot of resuspended lipid was transferred to a glass tube, to be used in phosphate quantification. Methanol was evaporated directly in the tube by heating and vortex stirring under a flow of nitrogen before the addition of 300 μL water, the first step in the phosphate quantification assay.

Simultaneously, different solutions (with 300 μL total volume) were prepared in duplicate from a stock solution of sodium phosphate dibasic (1 mM) in water. The concentrations of the sodium phosphate standard were selected to cover the expected range of phosphate concentrations in the samples. A volume of 700 μL of perchloric acid was added to each tube and mixing was performed in the vortex. The tubes were placed in a block heater (Stuart Scientific SHT200D) at 190 °C for up to 2 h. After cooling to room temperature, 2 mL of ammonium molybdate 1 % (w/v) and 2 mL of ascorbic acid 4 % (w/v) were added. The tubes were mixed and incubated at 37 °C for 1-2 hours. The coloured phosphate-molybdenum complex formed was then quantified by absorbance at 700 nm using the Unicam UV530 UV/Vis spectrophotometer.

2.7. <u>Stopped-flow fluorescence measurements</u>

Stopped-flow is a powerful technique developed in the 40s by modification of the continuous Hartridge-Roughton flow method.[90] This allows the study of reactions and processes that occurs on a millisecond to minute timescale and in comparison with the continuous flow method, stopped-flow avoids the use of large amounts of samples, being better suited for biochemical applications.[90,91]

Reagents, contained in separated drive syringes, are rapidly mixed and flow into the observation cell, after the movement of a driving platform triggered by gas pressure or motors. Data collection is started by the abrupt stop of the flow imposed by a stop syringe, that collects the previous contents of the spectroscopic cell, also limiting the volume of injected solutions. In the observation cell, the time course of the reaction is monitored, frequently, by UV-Vis or fluorescence spectroscopy (**Figure 12**).[90,91]

Detectors can be placed perpendicular or parallel to the light source, depending on the optical property to be measured, and multiple detections are also available in more advanced apparatus. Several detectors such as circular dichroism[92,93], X-ray scattering[94], neutron scattering[95], light scattering[96], conductivity[97], and nuclear magnetic resonance[98] have been employed, providing not only kinetic information but also complementary knowledge about the structure, reaction mechanisms, and reaction environment, giving useful insights into the system in study.
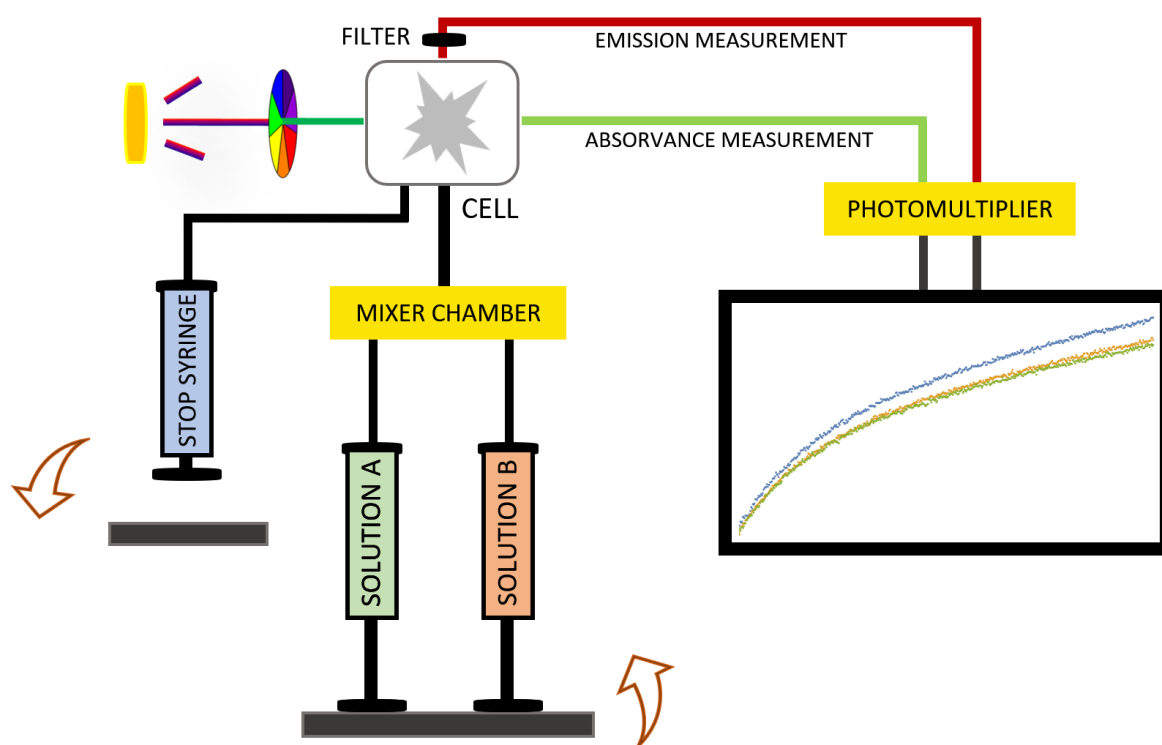
Figure 12. Schematic diagram of a typical stopped-flow apparatus: Two syringes containing the reactants are connected to a mixer chamber, from where they are injected into the observation cell. A light source is coupled to an excitation monochromator to select the excitation wavelength, and after the flow is stopped, the absorbance or fluorescence measurements start. For fluorescence measurements, a filter is used between the cell and the detector to eliminate the scattered and reflected light. The light that reaches the photomultiplier is then converted into an electric signal and recorded.

A thermostated stopped-flow apparatus (Hi-Tech Scientific model SF-61) with a mixing time of 20 ms was used for kinetic experiments, and all the measurements were performed at 25 °C. HPTS was excited at 455 nm and fluorescence was monitored using a cutoff filter OG-530 between the cell and the detector. Measurement duration was 1 s for acid-base equilibration and 250 s in the study of the dissipation of pH gradients. At each condition (acquisition time and pH gradient), the mixing and measurement process was repeated at least three times. The curves from short duration acquisitions were averaged to improve the signal-to-noise ratio while each curve was analysed in the case of long duration acquisitions. Curve-fitting analysis was performed using the software *Mathematica*™.

2.7.1. Determination of the acidity constant of HPTS

To characterise the acidity constant of HPTS in the aqueous solution, several solutions at different pH (adjusted by the addition of KOH or HCl) in the pH range between 2 and 12, were injected and mixed in a 1 ∶ 1 ratio with a HPTS aqueous solution at pH 7, resulting in a final solution of HPTS with pH between $\approx$ 3.5 and $\approx$ 12. The pH resulting from the mixture of the buffers at different pH with the HPTS solution was independently measured using a Jenway 3510 pH metre.

2.7.2. Study of the dissipation of the proton gradient

Liposome solutions containing encapsulated HPTS at pH 7 were incubated with different concentrations of the ionophore valinomycin. The ionophore was added from ethanolic stocks solutions to obtain the final concentrations of 0, 0.01, 0.1, 0.4, 0.7, and 1 µM, and 0.2 % (v/v) of the organic solvent. Lipid concentration is predicted to be approximately 0.66 mM and was confirmed using the phosphate quantification method described in Section 2.6.

Liposome solutions equilibrium was perturbed by changing the pH in the outer aqueous medium due to rapid mixing with buffer solutions at different pH. This allowed the study of the effect of valinomycin on the restoration of the internal pH equilibrium at different pH gradients, by measuring the fluorescence of the entrapped HPTS.

A similar experiment was performed using a SpectraMax iD5 microplate reader. Aliquots of 150 µL from the liposome's samples previously incubated with valinomycin were placed in different plate wells. The buffer solutions at different pH values were then injected, in a 1 ∶ 1 volume ratio, and the kinetics of the fluorescence variation was followed for at least 1.5 hours. Fluorescence was read from the bottom of the plate as the top was lidded to avoid evaporation and pH fluctuations due to air-solution equilibration. The pH at equilibrium was confirmed at the end of the kinetic experiment.

Chapter 3

Model Development and Implementation

3.1. Problem definition and initial exploration

One of the aims of this project is to identify the best conditions for measuring the permeability of weak acids and bases, using the pH variation assay. Permeability is a global parameter that depends on multiple processes, each of which depends on specific properties of the amphiphilic compound. To understand the whole process, a quantitative knowledge about all the important steps is required.[99]

The model developed in this work intends to distinguish the contribution of the partition and translocation processes. By discriminating these processes, the model can give new insights about the permeation of weak acids and bases and a better, deeper, and easier understanding of the general rules. This information can guide the development of drugs with improved properties. The kinetic model considers all the relevant steps as described by the Flip-Flop model, where the permeation of amphiphilic compounds is viewed as a three-step mechanism, involving four different compartments with volumes V_1, V_2, V_3 and V_4 (**Figure 13**). (For more details, see Section 1.4.2).
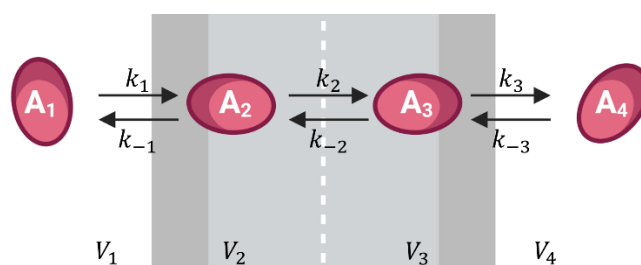
Figure 13. Model of the transport of a small amphiphilic drug across a lipid-bilayer. The lipid bilayer is shown schematically with its polar head group (dark grey) and hydrophobic regions (light grey). First, the drug partitions between the aqueous medium in compartment 1 (volume V_1) and the adjacent lipid leaflet (volume V_2), with k_1 and k_{-1} being the rate constants of insertion into and desorption from the lipid membrane, respectively. It then translocates between the two leaflets, with the rate constants k_2 and k_{-2}, for the forward and backward direction, respectively. The drug can then desorb to the aqueous medium in compartment 4 (volume V_4) with the rate constant k_3, and reinsert into the adjacent lipid leaflet with the rate constant k_{-3}.

The nomenclature used in Figure 13 and in the following mathematical description of the permeation mechanism of an uncharged amphiphilic compound is summarised in Table 3.

Table 3. Nomenclature adopted in Figure 13 and in the mathematical description of the permeation of a neutral amphiphilic drug.

Symbol	Meaning
A_1	Amphiphilic molecule located in the compartment 1
A_2	Amphiphilic molecule located in the compartment 2
A_3	Amphiphilic molecule located in the compartment 3
A_4	Amphiphilic molecule located in the compartment 4
A^i	Surface area of the inner membrane leaflet
A^o	Surface area of the outer membrane leaflet
k_1	Rate of insertion of the amphiphile into the outer membrane leaflet ($1 \rightarrow 2$)
k_{-1}	Rate of desorption of the amphiphile from the outer membrane leaflet ($2 \rightarrow 1$)
k_2	Translocation rate constant ($2 \rightarrow 3$)
k_{-2}	Translocation rate constant ($3 \rightarrow 2$)
k_3	Rate of desorption of the amphiphile from the inner membrane leaflet ($3 \rightarrow 4$)
k_{-3}	Rate of insertion of the amphiphile into the inner membrane leaflet ($4 \rightarrow 3$)
$\kappa_{1 \rightarrow 2}$	Permeability coefficient for the insertion into the outer leaflet
$\kappa_{2 \rightarrow 1}$	Permeability coefficient for the desorption from the outer leaflet
$\kappa_{3 \rightarrow 4}$	Permeability coefficient for the desorption from the inner leaflet
$\kappa_{4 \rightarrow 3}$	Permeability coefficient for the insertion into the inner leaflet
n_{LUVs}	Moles of LUVs
V_1	Volume of the compartment 1
V_2	Volume of the compartment 2
V_3	Volume of the compartment 3
V_4	Volume of the compartment 4
V_T	Total volume

For the implementation of the model, it is necessary to have estimates for the parameters of insertion, desorption, and translocation. There are a few examples in the literature where all those rate constants have been characterised.[7,79,100–102]

Insertion in lipid membranes is frequently treated as a second-order process. This is because the two entities (solute and lipid vesicles) first need to approach each other by diffusion with the formation of an encounter complex.[79,99–101] If the rate of association with the lipid membrane is fast compared with the lifetime of this encounter complex, the solute inserts into the lipid membrane. Otherwise, the solute diffuses back into the aqueous phase. With this approach, the second-order rate constant has a physical meaning, being always smaller than the rate of formation of the encounter complex. The latter is the rate constant for a diffusion-limited process, $\approx 10^{10}$ M^{-1} s^{-1}.[103] The insertion step can also be treated as a permeability coefficient, which has units of length *per* unit of time, and represents the

thickness of the medium adjacent to the membrane that contained the solute molecules inserting in the membrane *per* unit of time. This parameter is more convenient because it is not dependent on the topology of the lipid vesicles. In this project, the rate constant for insertion, k_1 and k_{-3} in Figure 13, will be treated as a permeability coefficient ($\kappa_{1\to2}$ and $\kappa_{4\to3}$), with units of dm s^{-1}.

Insertion in the outer leaflet:

Current model	Literature[79,99–101]
$$\frac{dnA_2}{dt} = \kappa_{1\to2}\, A^o\, \frac{nA_1}{V_1} \qquad (13)$$	$$\frac{d\,\frac{nA_2}{V_T}}{dt} = k_1 \frac{n_{LUVs}}{V_T} \frac{nA_1}{V_T} \qquad (14)$$
Dynamics of the insertion in the outer leaflet in terms of the local concentration of A_1, $\frac{nA_1}{V_1}$.	Dynamics of the insertion as a second-order process, in terms of the concentrations of lipidic vesicles and solute, $\frac{n_{LUVs}}{V_T}$ and $\frac{nA_1}{V_T}$, respectively.

When working with vesicles, the volume of the outer aqueous compartment is always much larger than that of the inner aqueous compartment and thus the external volume is approximately equal to the total volume ($V_1 \approx V_T$). This way, and by comparing equations (13) and (14), one finds that the permeability coefficient $\kappa_{1\to2}$ can be obtained from the literature reported values through equation (15). The equation includes the moles of LUVs and the corresponding surface area of the system where the second-order rate constant has been measured, therefore the topology of that system must be well known.

$$\kappa_{1\to2} = k_1 \frac{n_{LUVs}}{A^o} \qquad (15)$$

To maintain consistency with the insertion process, the rate constants for desorption, k_{-1} and k_3 in Figure 13, will also be treated as permeability coefficients ($\kappa_{2\to1}$ and $\kappa_{3\to4}$), although the parameter measured experimentally is a first-order rate constant, being therefore dependent on the system topology.[79,100,101]

Desorption from the outer leaflet:

Current model	Literature[79,100,101]
$$\frac{dnA_1}{dt} = \kappa_{2\to1}\, A^o\, \frac{nA_2}{V_2} \qquad (16)$$	$$\frac{d\,\frac{nA_1}{V_T}}{dt} = k_{-1} \frac{nA_2}{V_T} \qquad (17)$$
Dynamics of the desorption process in terms of the local concentration of A_2, $\frac{nA_2}{V_2}$.	Dynamics of the desorption as a first-order process, in terms of the global concentration of A_2, $\frac{nA_2}{V_T}$.

The permeability coefficient $\kappa_{2\to1}$ is approximately equal to the desorption rate constant found in literature multiplied by the leaflet thickness, d. The approximation is due to the curvature of the membrane leaflet, and the inaccuracy is smaller than 2 % for vesicles with an outer radius larger than 100 nm and the usual leaflet thickness ($d \approx 2$ nm). An equivalent relationship is obtained for $\kappa_{3\to4}$, with the surface area being that of the inner leaflet, equation (19).

$$\kappa_{2\to1} = k_{-1}\,\frac{V_2}{A^o} \approx k_{-1}\,d \tag{18}$$

$$\kappa_{3\to4} = k_3\,\frac{V_3}{A^i} \approx k_3\,d \tag{19}$$

The rate constant for translocation, k_2 and k_{-2} in Figure 13, will be treated as a first-order rate constant, the same way as it is measured experimentally.[6,79] For symmetric membranes with negligible curvature, the interleaflet partition coefficient equilibrium should be 1. If the vesicles have a radius much smaller than 50 nm (SUVs – small unilamellar vesicles), the curvature is significant and leads to distinct properties for both leaflets. In this case, the interleaflet partition coefficient may deviate from unity and depends on the geometric properties of the solute. Because this is solute dependent and there is little quantitative data available in the literature, in this work it is considered that the interleaflet partition coefficient is always equal to 1. However, the different volumes of both leaflets (V_3 and V_2 for the inner and outer, respectively) will be taken into consideration. So that the equilibrium local concentration of the solute is the same in both compartments, the translocation rate constants must obey:

$$k_{-2} = k_2\,\frac{V_2}{V_3}. \tag{20}$$

Depending on the method used for the characterisation of the translocation rate constant, the reported value may correspond only to the direction from the outer to the inner leaflet of the vesicles (k_2), from the inner to the outer leaflet (k_{-2}), or to the rate constant at which equilibrium is attained ($k_2 + k_{-2}$).[99]

The experimental parameter most commonly available for the interaction of drug-like molecules with lipid membranes is the water/membrane partition coefficient. When there are no partition coefficients available, their determination is relatively simple and easy to attain. This parameter is usually larger than 10^2 for solutes with moderate to high lipophilicity, being typically between 10^3 and 10^4 for small drugs. The partition coefficient may also be calculated from the equilibrium affinity given by the ratio between the insertion and desorption rate constants.[100] However, those rate constants are only available for a small number of molecules.[7,79,99–102,104,105] This limitation does not compromise the development of a complex kinetic model for the pH variation assay taking into consideration all four compartments, which will be described in the next sections.

3.2. Model design

3.2.1. Geometric parameters

To simulate the permeation of weak acids and bases through the lipid bilayers of vesicles, the thickness of the bilayer will not be neglected. This is a major difference in comparison with previous models for the pH variation assay[71,72] where the membrane was considered as a surface only, without volume. Thus, four compartments are considered: the outer aqueous medium and membrane leaflet (subscripts wo and lo, respectively), and the corresponding internal compartments (wi and li). The areas of the surfaces separating different compartments and the volume of each compartment can be obtained through equations (21) to (23) and (24) to (27), respectively. Here r is the outer radius of the vesicle, h is the bilayer thickness, V_T is the total volume and $N_{vesicles}$ is the number of vesicles.

$$A^o = 4\,\pi\,r^2 \tag{21}$$

$$A^{io} = 4\,\pi\left(r - \frac{h}{2}\right)^2 \tag{22}$$

$$A^i = 4\,\pi\,(r - h)^2 \tag{23}$$

$$V_{wo} = V_T - \frac{4}{3}\pi\,r^3\,N_{vesicles} \tag{24}$$

$$V_{wi\,vesicle} = \frac{4}{3}\pi\,(r - h)^3 \tag{25}$$

$$V_{lo\,vesicle} = \frac{4}{3}\pi\left[r^3 - \left(r - \frac{h}{2}\right)^3\right] \tag{26}$$

$$V_{li\,vesicle} = \frac{4}{3}\pi\left[\left(r - \frac{h}{2}\right)^3 - (r - h)^3\right] \tag{27}$$
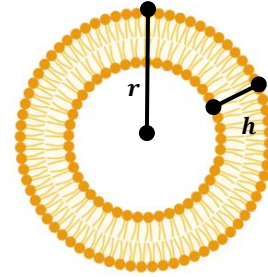
Figure 14. Schematic cross-sectional representation of a lipid vesicle.

Nomenclature:
A^o: area of the outer surface of a vesicle; A^{io}: area of the surface between the lipid chains of the inner and outer leaflets; A^i: area of the inner surface of a vesicle;
V_{wo}: volume of the outer aqueous compartment; $V_{wi\,vesicle}$: volume of the lumen of each vesicle;
$V_{lo\,vesicle}$: volume of the outer leaflet of each vesicle; $V_{li\,vesicle}$: volume of the inner leaflet of each vesicle.

The bilayer thickness was estimated by considering that the volume of the lipid bilayer in each vesicle with radius r matches that calculated from the number of lipid molecules *per* vesicle and the lipid molecular volume. This calculation proceeds as follows. First, considering the area *per* lipid (a_L), it is estimated how many lipid molecules fit in the surface area of the outer and inner leaflets of a vesicle membrane, equation (28). Then the volume occupied by that number of lipid molecules is calculated based on the known molar volume of the lipid ($\overline{V_L}$), according to equation (29), where N_A is the Avogadro's number.

$$N_{lipids\,per\,vesicle} = \frac{A^o + A^i}{a_L} \tag{28}$$

$$V_{lipids\,per\,vesicle} = \frac{N_{lipids\,per\,vesicle}}{N_A}\,\overline{V_L} \tag{29}$$

The volume of the lipid bilayer is given by the difference between the volume of the sphere with the outer vesicle radius and that of a sphere with the inner radius, which is equal to the outer radius minus the bilayer thickness $(r - h)$, equation (30).

$$V_{lipids \, per \, vesicle} = \frac{4}{3} \pi \left[r^3 - (r - h)^3 \right] \tag{30}$$

The thickness of the bilayer is the value of h that leads to the same volume of lipid as calculated by equation (29).

In all the kinetic models considered in this work, the compartments of each vesicle will not be considered individually. Instead, the total volume of each compartment type is considered, which is calculated from the geometrical parameters of each vesicle and the number of vesicles in solution. This is calculated from the lipid concentration (c_L), and the total volume of the solution, equation (31). The total surfaces and the total volume of each compartment are then calculated from equations (32) to (34) and equations (35) to (36), respectively.

$$N_{vesicles} = \frac{c_L \, V_T \, N_A}{N_{lipids \, per \, vesicle}} \tag{31}$$

$$A_T^o = A^o \, N_{vesicles} \quad (32) \qquad A_T^{io} = A^{io} \, N_{vesicles} \quad (33) \qquad A_T^i = A^i \, N_{vesicles} \quad (34)$$

$$V_{wi} = V_{wi \, vesicle} \, N_{vesicles} \quad (35) \quad V_{lo} = V_{lo \, vesicle} \, N_{vesicles} \quad (36) \quad V_{li} = V_{li \, vesicle} \, N_{vesicles} \quad (37)$$

3.2.2. Model I – Permeation of uncharged species only

The permeation mechanism described in Figure 13 is only valid for the case of molecules that are globally neutral and do not change their ionisation state. When the permeation of ionisable molecules is considered, it is necessary to take their acid-base equilibria into account as well, both in the aqueous compartments and when associated with both membrane leaflets. The kinetic scheme of Model I includes a pH-buffer in the aqueous compartment outside the vesicles, a pH-sensitive probe inside the vesicles, and all the transformations between the protonated and deprotonated species of the buffer, probe, and solute (**Figure 15**). The model also considers the interaction of the solute with the membrane, and the permeation of the uncharged species.
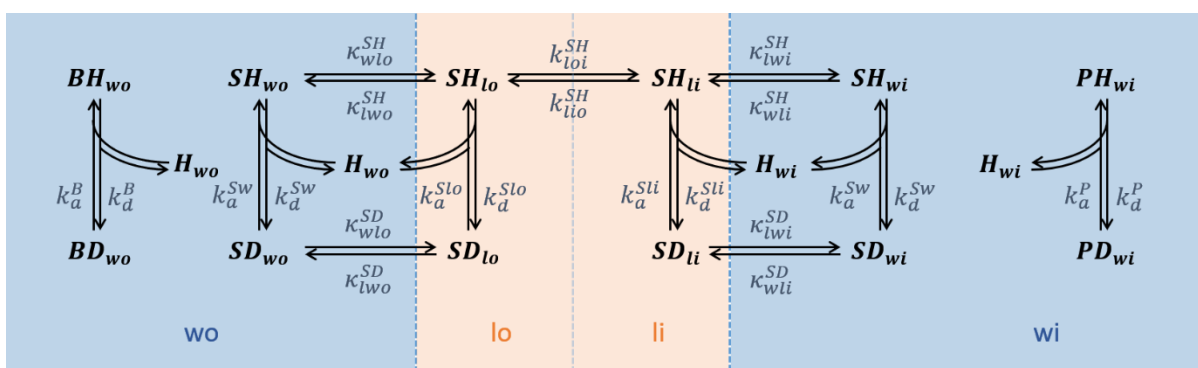
Figure 15. Reaction scheme for the permeation of a weak acid through lipid membranes. Only the protonated (uncharged) species can permeate.

The presence of the buffer in the external aqueous medium (wo) maintains the pH in this compartment unchanged. The weak acid BH_{wo} dissociates to form its conjugated base (BD_{wo}), and H_{wo} with the rate constant k_d^B. The protonation of the conjugated base occurs with the second-order rate constant k_a^B.

In the outer aqueous compartment, the protonated solute (SH_{wo}) releases a proton and converts into SD_{wo} with the rate constant k_d^{Sw} and the reverse occurs with the rate constant k_a^{Sw}. The protonated and deprotonated solute species can enter the membrane outer leaflet (lo), with the rate constants κ_{wlo}^{SH} and κ_{wlo}^{SD}, respectively. The solute in the membrane may move back to the outer aqueous compartment with the rate constants κ_{lwo}^{SH} and κ_{lwo}^{SD}, for SH_{lo} and SD_{lo}, respectively.

Once in the outer leaflet, the solute can change its protonation state with the rate constants of dissociation and association k_d^{Slo} and k_a^{Slo}, respectively. The neutral drug is allowed to flip-flop across the hydrophobic core of the membrane with the rate constants k_{loi}^{SH} and k_{lio}^{SH}, when the molecule moves from the outer leaflet into the inner leaflet (li) and the reverse way, respectively.

When the protonated solute is located near the surface of the inner membrane leaflets, it can release a proton into the internal aqueous medium (wi) with the rate constant k_d^{Sli}, generating the conjugated base which equilibrates back with the association rate constant k_a^{Sli}. Finally, the weak acid and its conjugated base may move from the inner membrane leaflet into the inner aqueous compartment, with the rate constants κ_{lwi}^{SH} and κ_{lwi}^{SD}. Once in this aqueous compartment, the two forms of the solute equilibrate with each other, with the rate constants k_d^{Sw} and k_a^{Sw}. Note that while the acid-base equilibrium of the solute in the inner aqueous compartment is assumed equal to that in the outer aqueous compartment, the acid-base equilibria of the solute in the membrane are allowed to proceed with different rate and equilibrium constants.

The protons released in the inner aqueous compartment, due to the equilibration of the weak acid with the conjugated base, can associate with the deprotonated form of the fluorescent pH probe PD_{wi}

to form PH_{wi}. The rate constants for transformation between the two forms are k_a^P and k_d^P. The fluorescence quantum yield of the deprotonated form is usually higher, and thus, the decrease in pH generated by the permeation of the weak acid leads to a decrease in the fluorescence intensity.

This model was designed for the permeation of weak acids, but it may very easily be altered to describe the permeation of weak bases. The only difference is that the uncharged solute species would be the deprotonated one, and this would be the species allowed to translocate between the two membrane leaflets.

The simulation results obtained with this model are described in Section 4.2.1.

3.2.2.1. Notation used for the different species and rate constants

The notation used in this work was defined with the intention of being simple, logical, and intuitive for easy interpretation.

SH is a weak acid and SD is the conjugated base. BH and BD are the buffer components, PH and PD are the weak acid and the conjugated base of the pH-sensitive probe, respectively, and H represents protons. All the species in the model are defined in terms of the compartment where they are (**Table 4**). The subscript wo and wi denote that the species is in the outer and inner aqueous medium, respectively, and the subscript lo and li imply that the species is in the outer and inner membrane leaflet, respectively.

Table 4. Notation adopted in the kinetic model for the different species.

Variable	Description
BH_{wo}	Buffer (weak acid) in the outer aqueous compartment
BD_{wo}	Buffer (conjugated base of BH_{wo})
H_{wo}	Proton in the outer aqueous compartment
SH_{wo}	Weak acid in the outer aqueous compartment
SD_{wo}	Conjugated base of SH_{wo}
SH_{lo}	Weak acid in the outer membrane leaflet
SD_{lo}	Conjugated base of SH_{lo}
H_{wi}	Proton in the inner aqueous compartment
SH_{wi}	Weak acid in the inner aqueous compartment
SD_{wi}	Conjugated base of SH_{wi}
SH_{li}	Weak acid in the inner membrane leaflet
SD_{li}	Conjugated base of SH_{li}
PH_{wi}	pH-sensitive probe (weak acid) in the inner aqueous compartment
PD_{wi}	pH-sensitive probe (conjugated base of PH_{wi})

The rate constants also follow a logic notation (**Table 5**). Association and dissociation rate constants include in their symbology the identification of the species to which they refer. Permeability coefficients and translocation rate constants also include an identification of the charged or uncharged forms to which they refer and were defined with the purpose of identifying explicitly the direction of the process. For example, the coefficient κ_{wlo}^{SH} defines the rate of transfer process of the weak acid (SH) from the outer aqueous media (wo) to the outer leaflet (lo).

Table 5. Notation adopted in the kinetic model for the different rate constants.

Symbol	Description	Units
k_a^{X}	Rate constant for the association of the deprotonated species BD_{wo}, SD_{wo}, SD_{lo}, SD_{li}, SD_{wi}, and PD_{wi} with protons, where X may be B, Sw, Slo, Sli, Sw, and P, respectively.	dm^3 mol^{-1} s^{-1}
k_d^{X}	Rate constant for the dissociation of the weak acids (BH_{wo}, SH_{wo}, SH_{lo}, SH_{li}, SH_{wi} and PH_{wi}), where X may be B, Sw, Slo, Sli, Sw, and P, respectively.	s^{-1}
κ_{wlo}^{SX}	Permeability coefficient between water and the external leaflet for SH or SD, where X may be H or D for the protonated and deprotonated species, respectively.	dm s^{-1}
κ_{lwo}^{SX}	Permeability coefficient between the external leaflet and water for SH or SD, where X may be H or D for the protonated and deprotonated species, respectively.	dm s^{-1}
κ_{wli}^{SX}	Permeability coefficient between water and the internal leaflet for SH or SD, where X may be H or D for the protonated and deprotonated species, respectively.	dm s^{-1}
κ_{lwi}^{SX}	Permeability coefficient between the internal leaflet and water for SH or SD, where X may be H or D for the protonated and deprotonated species, respectively.	dm s^{-1}
k_{loi}^{SH}	Rate constant for the translocation of SH from the outer to the inner membrane leaflets.	s^{-1}
k_{lio}^{SH}	Rate constant for the translocation of SH from the inner to the outer membrane leaflets.	s^{-1}

3.2.2.2. Differential equations

The differential equations below describe the dynamics of the amount of each species for the kinetic scheme represented in Figure 15.

$$nSH'_{wo}[t] = \kappa^{SH}_{lwo}\, A^o_T\, \frac{nSH_{lo}[t]}{V_{lo}} + k^{Sw}_a\, nSD_{wo}[t]\, \frac{nH_{wo}}{V_{wo}} - \kappa^{SH}_{wlo}\, A^o_T\, \frac{nSH_{wo}[t]}{V_{wo}} - k^{Sw}_d\, nSH_{wo}[t] \tag{38}$$

$$nSD'_{wo}[t] = \kappa^{SD}_{lwo}\, A^o_T\, \frac{nSD_{lo}[t]}{V_{lo}} + k^{Sw}_d\, nSH_{wo}[t] - \kappa^{SD}_{wlo}\, A^o_T\, \frac{nSD_{wo}[t]}{V_{wo}} - k^{Sw}_a\, nSD_{wo}[t]\, \frac{nH_{wo}[t]}{V_{wo}} \tag{39}$$

$$nSH'_{lo}[t] = \kappa^{SH}_{wlo}\, A^o_T\, \frac{nSH_{wo}[t]}{V_{wo}} + k^{Slo}_a\, nSD_{lo}[t]\, \frac{nH_{wo}}{V_{wo}} + k^{SH}_{lio}\, nSH_{li}[t] - \kappa^{SH}_{lwo}\, A^o_T\, \frac{nSH_{lo}[t]}{V_{lo}} - k^{Slo}_d nSH_{lo}[t] - k^{SH}_{loi}\, nSH_{lo}[t] \tag{40}$$

$$nSD'_{lo}[t] = \kappa^{SD}_{wlo}\, A^o_T\, \frac{nSD_{wo}[t]}{V_{wo}} + k^{Slo}_d\, nSH_{lo}[t] - \kappa^{SD}_{lwo}\, A^o_T\, \frac{nSD_{lo}[t]}{V_{lo}} - k^{Slo}_a\, nSD_{lo}[t]\, \frac{nH_{wo}[t]}{V_{wo}} \tag{41}$$

$$nBH'_{wo}[t] = k^{B}_a\, nBD_{wo}[t]\, \frac{nH_{wo}[t]}{V_{wo}} - k^{B}_d\, nBH_{wo}[t] \tag{42}$$

$$nBD'_{wo}[t] = k^{B}_d\, nBH_{wo}[t] - k^{B}_a\, nBD_{wo}[t]\, \frac{nH_{wo}[t]}{V_{wo}} \tag{43}$$

$$nH'_{wo}[t] = k^{Sw}_d\, nSH_{wo}[t] + k^{Slo}_d\, nSH_{lo}[t] + k^{B}_d\, nBH_{wo}[t] - k^{Sw}_a\, nSD_{wo}[t]\, \frac{nH_{wo}[t]}{V_{wo}} - k^{Slo}_a\, nSD_{lo}[t]\, \frac{nH_{wo}[t]}{V_{wo}} - k^{B}_a\, nBD_{wo}[t]\, \frac{nH_{wo}[t]}{V_{wo}} \tag{44}$$

$$nSH'_{li}[t] = \kappa^{SH}_{wli}\, A^i_T\, \frac{nSH_{wi}[t]}{V_{wi}} + k^{Sli}_a\, nSD_{li}[t]\, \frac{nH_{wi}[t]}{V_{wi}} + k^{SH}_{loi}\, nSH_{lo}[t] - \kappa^{SH}_{lwi} A^i_T\, \frac{nSH_{li}[t]}{V_{li}} - k^{Sli}_d\, nSH_{li}[t] - k^{SH}_{lio}\, nSH_{li}[t] \tag{45}$$

$$nSD'_{li}[t] = \kappa^{SD}_{wli}\, A^i_T\, \frac{nSD_{wi}[t]}{V_{wi}} + k^{Sli}_d\, nSH_{li}[t] - \kappa^{SD}_{lwi}\, A^i_T\, \frac{nSD_{li}[t]}{V_{li}} - k^{Sli}_a\, nSD_{li}[t]\, \frac{nH_{wi}[t]}{V_{wi}} \tag{46}$$

$$nSH'_{wi}[t] = \kappa^{SH}_{lwi}\, A^i_T\, \frac{nSH_{li}[t]}{V_{li}} + k^{Sw}_a\, nSD_{wi}[t]\, \frac{nH_{wi}[t]}{V_{wi}} - \kappa^{SH}_{wli}\, A^i_T\, \frac{nSH_{wi}[t]}{V_{wi}} - k^{Sw}_d\, nSH_{wi}[t] \tag{47}$$

$$nSD'_{wi}[t] = \kappa^{SD}_{lwi}\, A^i_T\, \frac{nSD_{li}[t]}{V_{li}} + k^{Sw}_d\, nSH_{wi}[t] - \kappa^{SD}_{wli}\, A^i_T\, \frac{nSD_{wi}[t]}{V_{wi}} - k^{Sw}_a\, nSD_{wi}[t]\, \frac{nH_{wi}[t]}{V_{wi}} \tag{48}$$

$$nPH'_{wi}[t] = k^{P}_a\, nPD_{wi}[t]\, \frac{nH_{wi}[t]}{V_{wi}} - k^{P}_d\, nPH_{wi}[t] \tag{49}$$

$$nPD'_{wi}[t] = k^{P}_d\, nPH_{wi}[t] - k^{P}_a\, nPD_{wi}[t]\, \frac{nH_{wi}[t]}{V_{wi}} \tag{50}$$

$$nH'_{wi}[t] = k^{Sw}_d\, nSH_{wi}[t] + k^{Sli}_d\, nSH_{li}[t] + k^{P}_d\, nPH_{wi}[t] - k^{Sw}_a nSD_{wi}[t]\, \frac{nH_{wi}[t]}{V_{wi}} - k^{Sli}_a\, nSD_{li}[t]\, \frac{nH_{wi}[t]}{V_{wi}} - k^{P}_a\, nPD_{wi}[t]\, \frac{nH_{wi}[t]}{V_{wi}} \tag{51}$$

3.2.2.3. Model considerations

In this work, the aqueous medium outside the vesicles has a high buffer capacity, and therefore the concentration of protons in the external aqueous medium could be considered constant for simplicity. However, for future refinements of the model, it may be relevant to consider pH variations in the external aqueous medium. This variable has therefore been included (equation (44)), even in this simplest model.

The rate constants for the protonation and deprotonation processes are usually not known, only the equilibrium constants. Where those rate constants have been characterised, they were shown to be quite fast, both in bulk water and at the lipid bilayer surface.[106] The inclusion of this fast step would lead to some variables varying much faster than others, and can cause problems to the numerical integration. It is therefore more effective to make a quasi-equilibrium approximation. This approximation consists in identifying the fast subsystems and assuming that these rapidly approach an equilibrium that is slowly shifting due to the slow processes. In this model it is assumed that translocation is the single rate-limiting step therefore not only protonation and deprotonation are in quasi-equilibrium, but also partition for and from the membrane.

The kinetic scheme considered in this model is shown in Figure 16, where all steps with thick arrows are considered in fast equilibrium. Therefore, the system can be subdivided into two quasi-equilibrium subsystems: the subsystem concerning the outer species, on the left side of the figure, and the subsystem that includes the inner species, on the right side. K_{wlo}^{SH} and K_{lwi}^{SH} are the water-membrane and membrane-water partition coefficient of the neutral solute, respectively, and K_{wlo}^{SD} and K_{lwi}^{SD} are the partition coefficient of the charged solute. K_a^{Sw}, K_a^{Slo} and K_a^{Sli} are the acidity constants of the solute in the aqueous media, in the inner and outer leaflet. K_a^{B} and K_a^{P} stand for the acidity constant of the buffer and the probe.
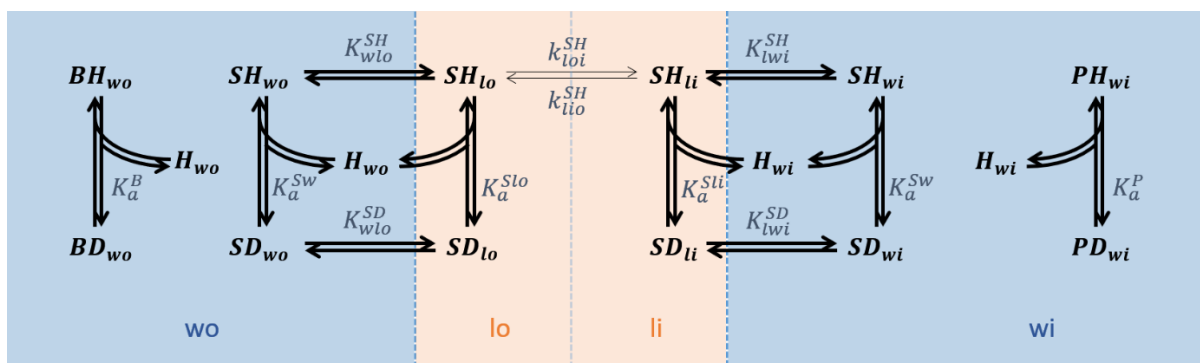
Figure 16. Reaction scheme for the permeation of a weak acid, considering the translocation between the membrane leaflets as the single rate-limiting step (thin arrows), with protonation/deprotonation and aqueous/membrane partition processes being at quasi-equilibrium (thick arrows).

can only enter the inner compartment associated with the solute, the dynamics of internal protons is equal to the dynamics of the internal solute ($S'_o[t] = H'_o[t]$ and $S'_i[t] = H'_i[t]$). Therefore, the variation of the concentration of all the species in the system is defined by a single differential equation. Because the objective of this study is to model the permeation of the solute into the inner compartment, the dynamics of this system is described based on the differential equation for S_i, equation (58), with all other variables being calculated from their relationships with $S_i[t]$.

The time dependent concentration of the total solute in the outer media ($S_o[t]$) is obtained from that of $S_i[t]$ considering the conservation of solute molecules in the system. The distribution of solute molecules among the different species (SH_{wo}, SH_{lo}, SD_{wo} and SD_{lo}) is then calculated from the conservation and equilibrium relationships between them, equations (60) to (63). The buffer concentrations in the protonated and deprotonated forms are calculated from the ionisation equilibrium and mass conservation equation, equations (64) and (65), respectively.

$$S_T \frac{V_T}{V_{wo}} - S_i[t] \frac{V_{wi}}{V_{wo}} = SH_{wo}[t] + SH_{lo}[t] \frac{V_{lo}}{V_{wo}} + SD_{wo}[t] + SD_{lo}[t] \frac{V_{lo}}{V_{wo}} \tag{60}$$

$$K_{wlo}^{SH} = \frac{SH_{lo}[t]}{SH_{wo}[t]} \tag{61} \qquad K_a^{Sw} = \frac{SD_{wo}[t]\,H_{wo}[t]}{SH_{wo}[t]} \tag{62} \qquad K_{wlo}^{SD} = \frac{SD_{lo}[t]}{SD_{wo}[t]} \tag{63}$$

$$K_a^B = \frac{BD_{wo}[t]\,H_{wo}[t]}{BH_{wo}[t]} \tag{64} \qquad\qquad BD_{wo}[t] + BH_{wo}[t] = B_T \tag{65}$$

The system of equations above (equations (60) to (65)) has a simple analytical solution for the concentrations of the fast-changing variables as a function of the slow-changing one ($S_i[t]$), given by equations (66) to (71). As mentioned before, the concentration of the proton in the outer aqueous compartment was not considered as a fixed independent variable, and it will be calculated during the numerical integration. But due to the high buffering capacity outside the vesicles, the external pH will remain constant.

$$SH_{wo}[t] = \frac{H_{wo}[t]\,(S_T\,V_T - V_{wi}\,S_i[t])}{K_a^{Sw}(K_{wlo}^{SD}\,V_{lo} + V_{wo}) + H_{wo}[t]\,(K_{wlo}^{SH}\,V_{lo} + V_{wo})} \tag{66}$$

$$SD_{wo}[t] = \frac{K_a^{Sw}\,(S_T\,V_T - V_{wi}\,S_i[t])}{K_a^{Sw}(K_{wlo}^{SD}\,V_{lo} + V_{wo}) + H_{wo}[t]\,(K_{wlo}^{SH}\,V_{lo} + V_{wo})} \tag{67}$$

$$SH_{lo}[t] = \frac{H_{wo}[t]\,K_{wlo}^{SH}\,(S_T\,V_T - V_{wi}\,S_i[t])}{K_a^{Sw}(K_{wlo}^{SD}\,V_{lo} + V_{wo}) + H_{wo}[t]\,(K_{wlo}^{SH}\,V_{lo} + V_{wo})} \tag{68}$$

$$SD_{lo}[t] = \frac{K_a^{Sw}\,K_{wlo}^{SD}\,(S_T\,V_T - V_{wi}\,S_i[t])}{K_a^{Sw}(K_{wlo}^{SD}\,V_{lo} + V_{wo}) + H_{wo}[t]\,(K_{wlo}^{SH}\,V_{lo} + V_{wo})} \tag{69}$$

$$BH_{wo}[t] = \frac{B_T\,H_{wo}[t]}{K_a^B + H_{wo}[t]} \tag{70}$$

$$BD_{wo}[t] = \frac{B_T\,K_a^B}{K_a^B + H_{wo}[t]} \tag{71}$$

The analytical solution for the system of equations (72) to (78) for the species in the inner compartments is so complicated, that it is preferable to solve the differential equations numerically.

$$S_i[t] = SH_{li}[t]\frac{V_{li}}{V_{wi}} + SH_{wi}[t] + SD_{wi}[t] + SD_{li}[t]\frac{V_{li}}{V_{wi}} \tag{72}$$

$$H_{wi}[t] + PH_{wi}[t] = H_i[0] + SD_{wi}[t] + SD_{li}[t]\frac{V_{li}}{V_{wi}} \tag{73}$$

$$K_{wli}^{SH} = \frac{SH_{li}[t]}{SH_{wi}[t]} \tag{74} \qquad K_a^{Sw} = \frac{SD_{wi}[t]\,H_{wi}[t]}{SH_{wi}[t]} \tag{75} \qquad K_{wli}^{SD} = \frac{SD_{li}[t]}{SD_{wi}[t]} \tag{76}$$

$$K_a^P = \frac{PD_{wi}[t]\,H_{wi}[t]}{PH_{wi}[t]} \tag{77} \qquad\qquad PD_{wi}[t] + PH_{wi}[t] = P_T \tag{78}$$

Two thermodynamic cycles can be identified in this system, involving all the solute species in the outer compartments and all the solute species in the inner ones. Therefore, the equilibrium constants associated with the solute are not independent and they must obey the micro-reversibility constraints according to equations (79) and (80).

$$K_{wlo}^{SH}\ K_a^{Slo}\ K_{wlo}^{SD}{}^{-1}\ K_a^{Sw}{}^{-1} = 1 \tag{79}$$

$$K_{wli}^{SH}\ K_a^{Sli}\ K_{wli}^{SD}{}^{-1}\ K_a^{Sw}{}^{-1} = 1 \tag{80}$$

The equations required to calculate the initial concentration of all species are given below, for the species in the outer compartments, equation (81) to (87), and in the inner compartments, equations (88) to (95). In the simulation performed in this work, it is assumed as initial conditions that the solute is all in the outer compartments, equations (88) to (92). It is also assumed that the solute species in the outer compartments are at equilibrium, equations (82) to (87), and that the species in the inner aqueous compartment (H_{wi}, PH_{wi} and PD_{wi}) are also at equilibrium, equations (94) and (95).

$$S_T = SH_{wo}[0]\frac{V_{wo}}{V_T} + SH_{lo}[0]\frac{V_{lo}}{V_T} + SD_{wo}[0]\frac{V_{wo}}{V_T} + SD_{lo}[0]\frac{V_{lo}}{V_T} + S_i[0]\frac{V_{wi}}{V_T} \tag{81}$$

$$SH_{wo}[0] = \frac{H_{wo}[0]\,S_T\,V_T}{K_a^{Sw}(K_{wlo}^{SD}\,V_{lo} + V_{wo}) + H_{wo}[0]\,(K_{wlo}^{SH}\,V_{lo} + V_{wo})} \tag{82}$$

$$SD_{wo}[0] = \frac{K_a^{Sw}\,S_T\,V_T}{K_a^{Sw}(K_{wlo}^{SD}\,V_{lo} + V_{wo}) + H_{wo}[0]\,(K_{wlo}^{SH}\,V_{lo} + V_{wo})} \tag{83}$$

$$SH_{lo}[0] = \frac{H_{wo}[0]\,K_{wlo}^{SH}\,S_T\,V_T}{K_a^{Sw}(K_{wlo}^{SD}\,V_{lo} + V_{wo}) + H_{wo}[0]\,(K_{wlo}^{SH}\,V_{lo} + V_{wo})} \tag{84}$$

$$SD_{lo}[0] = \frac{K_a^{Sw}\,K_{wlo}^{SD}\,S_T\,V_T}{K_a^{Sw}(K_{wlo}^{SD}\,V_{lo} + V_{wo}) + H_{wo}[0](K_{wlo}^{SH}\,V_{lo} + V_{wo})} \tag{85}$$

$$BH_{wo}[0] = \frac{B_T\,H_{wo}[0]}{K_a^B + H_{wo}[0]} \tag{86} \qquad\qquad BD_{wo}[0] = \frac{B_T\,K_a^B}{K_a^B + H_{wo}[0]} \tag{87}$$

$$SH_{wi}[0] = 0 \quad \text{(88)} \qquad SD_{wi}[0] = 0 \quad \text{(89)} \qquad SH_{li}[0] = 0 \quad \text{(90)} \qquad SD_{li}[0] = 0 \quad \text{(91)}$$

$$\boldsymbol{S_i}[0] = 0 \quad \text{(92)} \qquad \boldsymbol{H_i}[0] = H_{wi}[0] + PH_{wi}[0] + SH_{wi}[0] + SH_{li}[0]\frac{V_{li}}{V_{wi}} \quad \text{(93)}$$

$$PH_{wi}[0] = \frac{H_{wi}[0]\, P_T}{H_{wi}[0] + K_a^P} \quad \text{(94)} \qquad\qquad PD_{wi}[0] = \frac{K_a^P\, P_T}{H_{wi}[0] + K_a^P} \quad \text{(95)}$$

It is also helpful to define the initial condition for the time derivative of the solute in the inner compartments, $\boldsymbol{S_i'}[0]$.

$$\boldsymbol{S_i'}[0] = \frac{H_{wo}[0]\, k_{loi}^{SH}\, K_{wlo}^{SH}\, S_T\, V_T\, V_{lo}}{V_{wi}\,[K_a^{Sw}\,(K_{wlo}^{SD}\, V_{lo} + V_{wo}) + H_{wo}[0](K_{wlo}^{SH}\, V_{lo} + V_{wo})]} \quad \text{(96)}$$

After defining all the parameters, the differential equations, equilibrium relations, and initial conditions, it is possible to calculate the time course of all the dependent variables using a software able to solve numerically a differential-algebraic system of equations. In the present work this is done using the software *Mathematica*[TM].

3.2.3. Model II – Inclusion of an entrapped solute binder

This model extends Model I by considering the presence of a membrane-impermeable binding agent such as a protein in the inner aqueous medium. This may be done in practice to increase the amount of solute that permeates into the inner compartments, and to shift its location towards the inner aqueous compartment. Three new variables must be considered: P_{wi}, PSH_{wi}, and PSD_{wi}, which are the free protein encapsulated in the inner aqueous compartment, and the protein associated with the protonated and deprotonated solutes, respectively. It is assumed that the association and dissociation between solute and protein are fast[100] relative to solute permeation, and thus, the quasi-equilibrium approximation was also applied for this step. Therefore, the kinetic scheme, shown in Figure 17, considers the association/dissociation processes (acid-base and ligand-protein reactions) at quasi-equilibrium and the translocation of the uncharged species as the only rate-limiting process.
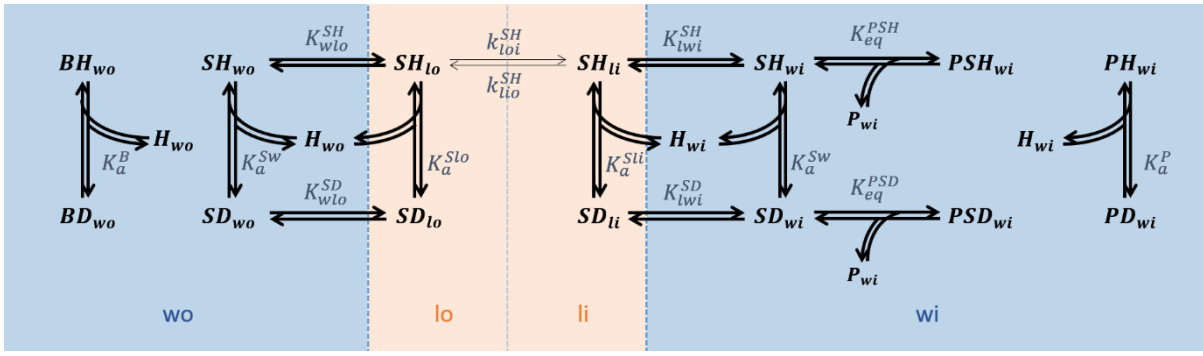
Figure 17. Reaction scheme for the permeation of a weak acid with an entrapped protein. The translocation between the membrane leaflets is the single rate-limiting step (thin arrows) and protonation/deprotonation, aqueous/membrane partition and solute-protein association/dissociation processes are at quasi-equilibrium (thick arrows).

To simulate the permeation of a weak acid in the presence of an entrapped binding agent, the equation that defines the mass conservation for the solute in the inner compartments becomes

$$S_i[t] = SH_{wi}[t] + SD_{wi}[t] + SH_{li}[t]\frac{V_{li}}{V_{wi}} + SD_{li}[t]\frac{V_{li}}{V_{wi}} + PSH_{wi}[t] + PSD_{wi}[t]. \tag{97}$$

The model also accounts for the mass conservation of the binding agent, equation (98), and the affinities of the SH_{wi} and SD_{wi}, defined by the respective dissociation constants K_d^{PSH} and K_d^{PSD} (reciprocal of K_{eq}^{PSH} and K_{eq}^{PSD}, respectively), equations (99) and (100).

$$PSD_{wi}[t] + PSH_{wi}[t] + P_{wi}[t] = P_{wi_T} \tag{98}$$

$$K_d^{PSH} = \frac{SH_{wi}[t]\, P_{wi}[t]}{PSH_{wi}[t]} \tag{99} \qquad\qquad K_d^{PSD} = \frac{SD_{wi}[t]\, P_{wi}[t]}{PSD_{wi}[t]} \tag{100}$$

As considered above for Model I, it is considered as initial conditions that the solute is only present in the outer compartments. Therefore, the initial conditions involving the encapsulated binding agent are

$$PSD_{wi}[0] = 0 \tag{101} \qquad PSH_{wi}[0] = 0 \tag{102} \qquad P_{wi}[0] = P_{wi_T}. \tag{103}$$

3.2.4. Model III – pH equilibration

The models described before do not include all the processes underlying the pH variation assay. The restoration of the internal pH is not modelled and, as a consequence, the concentrations of the same species in the distinct media of the same nature (water and lipid) do not equalise at equilibrium. There are two possible mechanisms to re-equilibrate the pH: i) the permeation of the conjugated base (Model IIIa), and ii) the permeation of H⁺/OH⁻ (Model IIIb, where for simplicity only the permeation of the proton is considered).

3.2.4.1. Model IIIa – Permeation of the conjugated base

The present model considers the permeation of the conjugated base. After partition into the outer leaflet and/or as the result of the dissociation of the weak acid in the membrane, the conjugated base (SD_{lo}) can translocate between the outer and inner leaflets, with the rate constant k_{loi}^{SD} for the forward direction, and k_{lio}^{SD} for the reverse direction (**Figure 18**). Once in the inner membrane leaflet and in the inner aqueous compartment, the conjugated base can capture a proton originating the weak acid and decreasing the pH gradient.
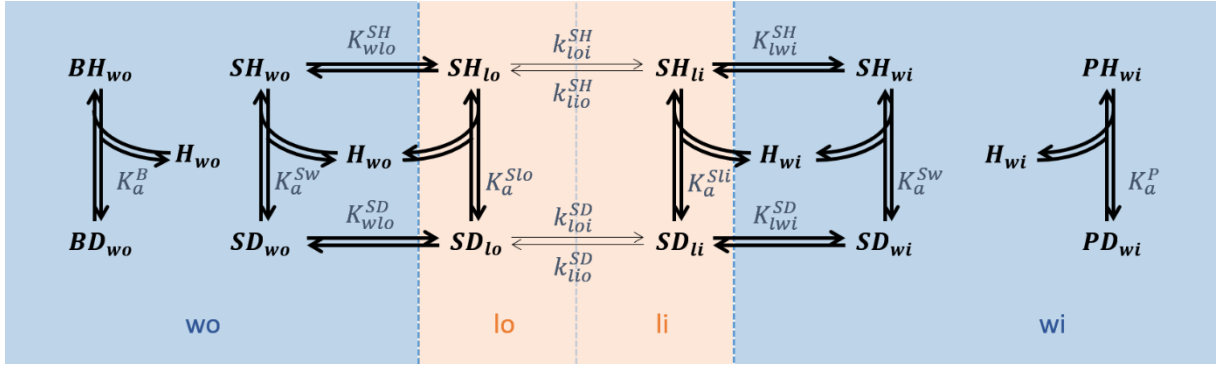
Figure 18. Reaction scheme for the permeation of a weak acid, considering the permeation of the acid form (*SH*) and the conjugated base (*SD*). The translocation of the weak acid and the conjugated base between the membrane leaflets are both considered the rate-limiting steps (thin arrows), while protonation/deprotonation and aqueous/membrane partition processes are at quasi-equilibrium (thick arrows).

The differential equations for SD_{lo} and SD_{li}, equations (41) and (46), were modified to take into account the translocation of *SD*, equation (104). The translocation rate constants k_{loi}^{SD} and k_{lio}^{SD} are related by equation (105) (for more details see Section 3.1, equation (20)).

$$J_{SD} = k_{loi}^{SD}\, SD_{lo}[t]\, V_{lo} - k_{lio}^{SD}\, SD_{li}[t]\, V_{li} \tag{104}$$

$$k_{lio}^{SD} = k_{loi}^{SD}\,\frac{V_{lo}}{V_{li}} \tag{105}$$

In this case, the differential equations of the aggregated slow variables $\boldsymbol{S_i}$ and $\boldsymbol{H_i}$ are not equal and both are needed, equations (106) and (107).

$$\boldsymbol{S_i'}[t] = k_{loi}^{SH}\, SH_{lo}[t]\,\frac{V_{lo}}{V_{wi}} + k_{loi}^{SD}\, SD_{lo}[t]\,\frac{V_{lo}}{V_{wi}} - k_{lio}^{SH}\, SH_{li}[t]\,\frac{V_{li}}{V_{wi}} - k_{lio}^{SD}\, SD_{li}[t]\,\frac{V_{li}}{V_{wi}} \tag{106}$$

$$\boldsymbol{H_i'}[t] = k_{loi}^{SH}\, SH_{lo}[t]\,\frac{V_{lo}}{V_{wi}} - k_{lio}^{SH}\, SH_{li}[t]\,\frac{V_{li}}{V_{wi}} \tag{107}$$

The initial conditions are the same as defined in Model I, except for the time derivative of the slow variables S_i and H_i, which are given by equations (108) and (109).

$$S_i'[0] = \frac{\left(K_a^{Sw} k_{loi}^{SD} K_{wlo}^{SD} + H_{wo}[0] k_{loi}^{SH} K_{wlo}^{SH}\right) S_T V_T V_{lo}}{V_{wi} \left[K_a^{Sw} \left(K_{wlo}^{SD} V_{lo} + V_{wo}\right) + H_{wo}[0]\left(K_{wlo}^{SH} V_{lo} + V_{wo}\right)\right]} \tag{108}$$

$$H_i'[0] = \frac{H_{wo}[0] k_{loi}^{SH} K_{wlo}^{SH} S_T V_T V_{lo}}{V_{wi} \left[K_a^{Sw} \left(K_{wlo}^{SD} V_{lo} + V_{wo}\right) + H_{wo}[0]\left(K_{wlo}^{SH} V_{lo} + V_{wo}\right)\right]} \tag{109}$$

3.2.4.2. Model IIIb – Permeation of the proton

The permeation of the weak acid into the inner compartments and its equilibration with the conjugated base decreases the pH in the inner aqueous compartment. The re-equilibration of the pH between the outer and inner compartments can also proceed through the efflux of protons or the influx of hydroxide ions. The experimental distinction between both processes is not straightforward and their relative contribution depends on the pH value.[107] For simplicity, in this model only the permeation of protons will be considered (**Figure 19**), its flow representing the net H^+/OH^- transport across the membrane. As the inner pH increases to approach the pH outside the vesicles, the ratio of protonated/deprotonated species changes, and the local concentration of both species becomes equal to those in the corresponding outer compartments (aqueous compartment and membrane leaflet).
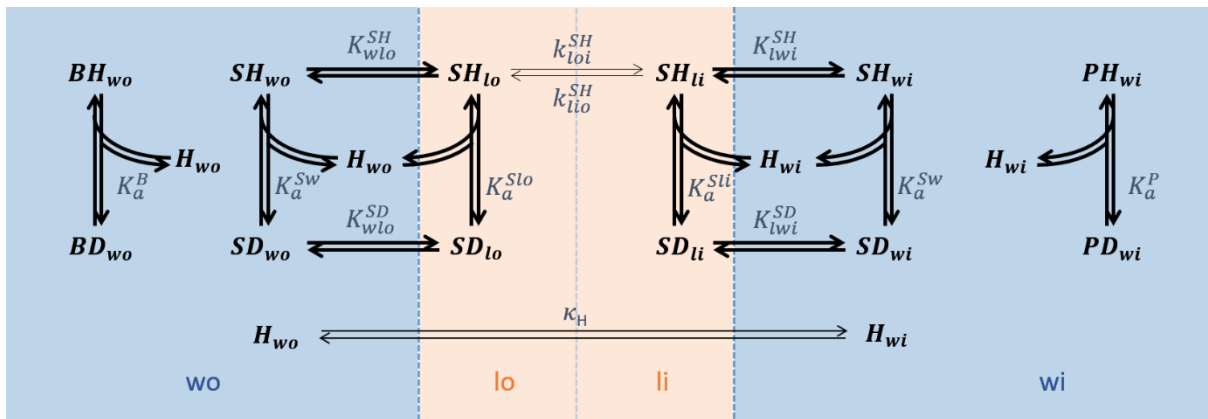
Figure 19. Reaction scheme for the permeation of a weak acid, considering the permeation of the acid form (*SH*) and that of the proton (H). The translocation of the weak acid between the membrane leaflets and the permeation of the proton are both considered the rate-limiting steps (thin arrows), while protonation/deprotonation and aqueous/membrane partition processes are at quasi-equilibrium (thick arrows).

Analogously to Model IIIa, the differential equations of H_{wo} and H_{wi}, equations (44) and (51), were modified to take into account the flux of protons, equation (110).

$$J_H = A_T^{io} \kappa_H \left(H_{wo}[t] - H_{wi}[t]\right) \tag{110}$$

The dynamics of the aggregated slow variable $\boldsymbol{S_i}$ is defined as in equation (58) (Section 3.2.2.3) and the dynamics of the total concentration of protons $\boldsymbol{H_i}$ is described by the following equation:

$$\boldsymbol{H_i'}[t] = k_{loi}^{SH}\, SH_{lo}[t]\frac{V_{lo}}{V_{wi}} - k_{lio}^{SH}\, SH_{li}[t]\frac{V_{li}}{V_{wi}} + \frac{A_T^{io}\,\kappa_H}{V_{wi}}(H_{wo}[t] - H_{wi}[t]). \tag{111}$$

In this model, all the other initial conditions remain as defined in Section 3.2.2.3, except for the time derivative of the slow variable $\boldsymbol{H_i}$ which is now given by equation (112):

$$\boldsymbol{H_i'}[0] = \frac{H_{wo}[0]\, k_{loi}^{SH}\, K_{wlo}^{SH}\, S_T\, V_T\, V_{lo}}{V_{wi}\,[K_a^{Sw}\,(K_{wlo}^{SD}\, V_{lo} + V_{wo}) + H_{wo}[0](K_{wlo}^{SH}\, V_{lo} + V_{wo})]} + \frac{A_T^{io}\,\kappa_H(H_{wo}[0] - H_{wi}[0])}{V_{wi}}. \tag{112}$$

The dissipation of the pH gradient through the permeation of the charged base (Model IIIa) or the proton (Model IIIb) generates a charge unbalance between the outer and inner compartments. The transmembrane potential generated by this charge unbalance must be dissipated to achieve the full equilibrium. The final model (Model IV) extends the previous ones by considering this process.

3.2.5. Model IV – Dissipation of the transmembrane potential

The transmembrane potential generated by the proton and base concentration gradients can be dissipated through the permeation of another much more abundant ion, such as a salt or buffer component. The high relative abundance of this ion avoids that the dissipation of the potential is counteracted by a significant concentration gradient. As the permeation of weak acids into the lipid vesicles being considered creates a negative electrostatic potential inside the vesicle, the dissipation of this potential requires the influx of a positive charge or the efflux of a negative charge. In the system considered in this work, the species that may exist in mM concentrations are the buffer (usually phosphate when pH $\approx$ 7) and salts (usually sodium and/or potassium, chloride) in the outer aqueous compartment, and only the salts in the inner aqueous compartment. Reported permeability coefficients are around 10^{-12} cm s^{-1} or lower[108–110] for sodium and potassium, in the range of 10^{-12} to 10^{-13} cm s^{-1} for phosphate[59], and nearly three orders of magnitude higher for chloride[110]. Thus, from the relative permeabilities and the localization of the ions, the electrostatic potential would most probably be dissipated due to the efflux of the chloride anion. However, in this model it is assumed that it is the influx of potassium that leads to the dissipation of the charge unbalance. This is because the permeability of this cation may be selectively increased by the ionophore valinomycin.[16]

Equation (113) stands for the mass conservation of potassium ions, with $K_{wo}[0]$ and $K_{wi}[0]$ being the local concentrations of these ions at $t = 0$.

$$K_{wo}[t]\, V_{wo} + K_{wi}[t]\, V_{wi} = K_{wo}[0]\, V_{wo} + K_{wi}[0]\, V_{wi} \tag{113}$$

Lipid membranes behave like an insulating matrix that separates two conducting solutions, acting as a capacitor. Membrane capacitance, C (in Farad), equation (114), characterises the excess of charge, Q (in Coulomb), needed to induce a potential difference, $\Delta\psi$ (in Volt), between two electrolytic solutions.[83] Membrane specific capacitance is about 1 µF cm^{-2}, and the total membrane capacitance is calculated through equation (115), where A_T^{io} and h are the surface area and the thickness of the vesicles, respectively (Section 3.2.1), ε_r is the membrane dielectric constant (≈ 2.1) and ε_0 is the vacuum permittivity.[83,111]

$$C = \frac{Q}{\Delta\psi} \tag{114}$$

$$C = \frac{A_T^{io}\,\varepsilon_r\,\varepsilon_0}{h} \tag{115}$$

Although the previous models consider only a concentration gradient as the driving force for permeation and flux of ions, those processes are also driven by an electrical gradient (Section 1.5.2). Therefore, when considering the equilibrium of charged species, it is necessary to consider both the concentration gradient (chemical potential), and the electrostatic potential, both being accounted for in the gradient of the electrochemical potential, equation (116). In equation (116), C_o and C_i are the concentrations of the ion with valency z in the outer and inner compartments, respectively, and, $\psi_o - \psi_i$ is the transmembrane potential, F is the Faraday constant, R is the ideal gas constant and T is the absolute temperature.

$$\Delta\tilde{\mu} = R\,T\,\ln C_o + z\,F\,\psi_o - R\,T\,\ln C_i - z\,F\,\psi_i = R\,T\,ln\frac{C_o}{C_i} + z\,F\,(\psi_o - \psi_i) \tag{116}$$

The net flux of an ion will become zero when its $\Delta\tilde{\mu}$ is zero, which may occur at different ion concentrations if balanced by the corresponding electrochemical potential.

At equilibrium, equation (116) yields the relationships described by equations (117) to (119) for the concentrations of the permeating charged species, the conjugated base, the proton, and the potassium. Other equivalent relationships are also valid but these ones can simplify integration.[112]

$$SD_{lo}[t] = SD_{li}[t]\,e^{\frac{z_{SD}\,F\,(\psi_o - \psi_i)}{R\,T}} \tag{117}$$

$$H_{wo}[t] = H_{wi}[t]\,e^{\frac{z_H\,F\,(\psi_o - \psi_i)}{R\,T}} \tag{118}$$

$$K_{wo}[t] = K_{wi}[t]\,e^{\frac{z_K\,F\,(\psi_o - \psi_i)}{R\,T}} \tag{119}$$

Model IV includes the permeation of both the conjugated base and the proton, presented separately in Sections 3.2.4.1 and 3.2.4.2, as well as the permeation of potassium, occurring with the permeability coefficient κ_H. The differential equations $S_i'[t]$ and $H_i'[t]$ have to be replaced by

equations (120) and (121) to include the relationships described in equations (117) and (118). Additionally, a new dynamic equation is required, equation (122), to describe the permeation of potassium ions, that also considers the relationship derived from the electrochemical neutrality, equation (119).

$$\boldsymbol{S_i'}[t] = k_{loi}^{SH}\, SH_{lo}[t]\frac{V_{lo}}{V_{wi}} + k_{loi}^{SD}\, SD_{lo}[t]\frac{V_{lo}}{V_{wi}} - k_{lio}^{SH}\, SH_{li}[t]\frac{V_{li}}{V_{wi}} - k_{lio}^{SD}\, SD_{li}[t]\frac{V_{li}}{V_{wi}}\, e^{\, z_{SD}\frac{F\,\Delta\psi[t]}{R\,T}} \tag{120}$$

$$\boldsymbol{H_i'}[t] = \frac{A_T^{io}\,\kappa_H}{V_{wi}}\left(H_{wo}[t] - H_{wi}[t]\, e^{z_H\frac{F\,\Delta\psi[t]}{R\,T}}\right) - k_{lio}^{SH}\, SH_{li}[t]\frac{V_{li}}{V_{wi}} + k_{loi}^{SH}\, SH_{lo}[t]\frac{V_{lo}}{V_{wi}} \tag{121}$$

$$K_{wi}'[t] = \frac{A_T^{io}\,\kappa_K}{V_{wi}}\left(K_{wo}[t] - K_{wi}[t]\, e^{z_K\frac{F\,\Delta\psi[t]}{R\,T}}\right) \tag{122}$$

The electrostatic potential difference at time t ($\Delta\psi[t]$) is related to the accumulated charge inside the vesicles through equation (114), and the accumulated charge may be calculated by the variation in the amount of all charged species

$$Q = \left(\Delta nH_{wi}[t] + \Delta nK_{wi}[t] - \Delta nPD_{wi}[t] - nSD_{li}[t] - nSD_{wi}[t]\right) N_A\, e, \tag{123}$$

where ΔnH_{wi}, ΔnK_{wi} and ΔnPD_{wi} denote the variation in the number of moles of protons, potassium, and deprotonated probe in the aqueous medium inside the vesicles, $nSD_{li}[t]$ and $nSD_{wi}[t]$ are the number of moles of the charged solute in the inner leaflet and vesicles lumen, respectively, and e is the charge of the electron. The equation above can be written in terms of the cumulative variables ($\boldsymbol{S_i}$ and $\boldsymbol{H_i}$):

$$Q = \frac{4}{3}\pi\,(r - h)^3\left[z_H\left(\boldsymbol{H_i}[t] - H_{wi}[0] - \frac{H_{wi}[0]\,P_T}{H_{wi}[0] + K_a^P}\right) - \boldsymbol{S_i}[t]\right.$$
$$\left. + z_K\,(K_{wi}[t] - K_{wi}[0])\right] N_A\, e. \tag{124}$$

3.2.6. Model V – Permeation of a weak base (complete model)

As the pH variation assay can be applied in the measurement of the permeability of weak bases, it is also relevant to adapt the model for the permeation of this type of compounds and make additional simulations.

The permeation of weak acids through lipidic membranes was modelled step by step but, considering the similarities between both systems, the permeation of weak bases is most straightforwardly modelled by adapting Model IV. The necessary changes are very subtle: i) the base has no electrical charge ($z_{SD} = 0$) while the conjugated acid is now positively charged ($z_{SH} = +1$) and ii) the base permeates faster than its conjugated acid ($k_{loi}^{SD} > k_{loi}^{SH}$ and $k_{lio}^{SD} > k_{lio}^{SH}$). The nomenclature is the same (see Symbols section) and the kinetic scheme is as represented in Figure 20.
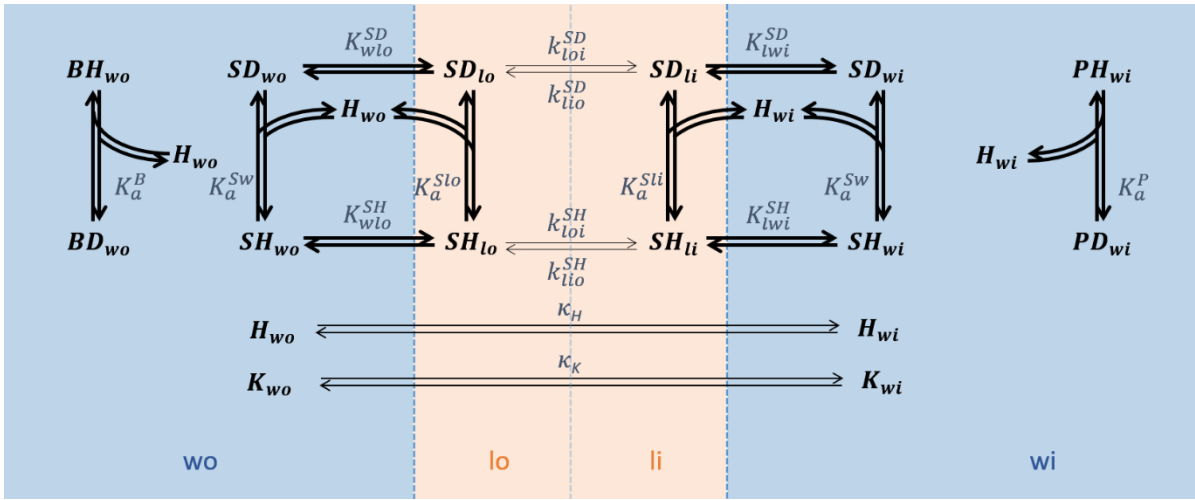
Figure 20. Reaction scheme for the permeation of a weak base through lipid membranes. The translocation of the weak base (*SD*) and that of the conjugated acid (*SH*) between the membrane leaflets are both considered the rate-limiting steps (thin arrows), while protonation/deprotonation and aqueous/membrane partition processes are at quasi-equilibrium (thick arrows).

Since now the ionic species is the conjugated acid, the equations that describe the dynamics of the aggregated variables S_i and H_i were modified accordingly to equations (125) and (126), respectively. Additionally, in the calculation of the amount of the accumulated charged species (Q), the basic species must be substituted by the acid species SH_{li} and SH_{wi} (equation (127)).

$$S_i'[t] = k_{loi}^{SD}\, SD_{lo}[t]\frac{V_{lo}}{V_{wi}} - k_{lio}^{SD}\, SD_{li}[t]\frac{V_{li}}{V_{wi}} + k_{loi}^{SH}\, SH_{lo}[t]\frac{V_{lo}}{V_{wi}} - k_{lio}^{SH}\, SH_{li}[t]\frac{V_{li}}{V_{wi}}\, e^{\,z_{SH}\frac{F\,\Delta\psi[t]}{R\,T}} \quad (125)$$

$$H_i'[t] = \frac{A_T^{io}\,\kappa_H}{V_{wi}}\left(H_{wo}[t] - H_{wi}[t]\, e^{\,z_H\frac{F\,\Delta\psi[t]}{R\,T}}\right) + k_{loi}^{SH}\, SH_{lo}[t]\frac{V_{lo}}{V_{wi}} - k_{lio}^{SH}\, SH_{li}[t]\frac{V_{li}}{V_{wi}}\, e^{\,z_{SH}\frac{F\,\Delta\psi[t]}{R\,T}} \quad (126)$$

$$Q = (\Delta n H_{wi}[t] + \Delta n K_{wi}[t] - \Delta n PD_{wi}[t] + n SH_{li}[t] + n SH_{wi}[t])\, N_A\, e \qquad (127)$$

Equation (127) can be simplified and rewritten in terms of the aggregated variable H_i:

$$Q = \frac{4}{3}\pi\,(r-h)^3\left[z_H\left(H_i[t] - H_{wi}[0] - \frac{H_{wi}[0]\,P_T}{H_{wi}[0] + K_a^P}\right) + z_K\,(K_{wi}[t] - K_{wi}[0])\right] N_A\, e. \qquad (128)$$

These are the biggest modifications to what was defined earlier for the permeation of weak acids. The remaining equations (mass conservations, equilibrium relationships, and initial conditions) are identical to the ones defined in the previous sections.

Chapter 4

Results and Discussion

4.1. <u>Model assessment</u>

A complex kinetic model must be developed step by step, as described in the previous chapter. This strategy allows a faster and easier identification of possible errors in the implementation of the model. Additionally, the self-consistency and plausibility of the models must be systematically assessed. In other words, equations must be dimensionally consistent, respect invariants (mass conservation, and micro-reversibility constraints), and symmetries. Parameter and variable values must respect physical boundaries (for example, the rate constant of bimolecular reactions is limited by the diffusion rate, and concentrations must remain within the solubility and osmolarity limits). Adherence of all the implemented models to these requirements was assessed, and the plausibility of the simulation results was analysed. When something was not correct or in accordance with the observations, the imperfections or possible errors were corrected.

4.2. <u>Model analysis</u>

In this section, all the models will be analysed and explored in order to evaluate the effect of specific parameters on the permeation kinetics of weak acids and bases.

4.2.1. Model I – Permeation of the uncharged species

As a first step towards assuring a reliable modelling and building an understanding of the system, the simplest model (Model I) was numerically integrated with the parameters shown in Table 6 to obtain the time course of the concentrations of all the species in the aqueous and lipidic compartments (**Figure 21A** and **B**, respectively). The parameters considered for the membrane lipids (a_L, and $\overline{V_L}$) were those of 1-palmitoyl-2-oleoyl-sn-glycero-3-phosphocholine, which is the major constituent of most biomembranes and is commonly used in membrane model systems. The membrane is assumed to be dispersed in vesicles with 100 nm radius, and from the lipid parameters, a 3.9 nm lipid bilayer thickness is calculated. The total volume considered for the system is 1 dm³, and the lipid concentration (c_L) is 10^{-3} M, leading to the volumes indicated in Table 6 for all the compartments (V_{wo}, V_{lo}, V_{wi} and V_{li}). The concentration of the solute with respect to the total volume (S_T) is 10^{-6} M, the local concentration of fluorescent the probe (P_T) inside the vesicles is 10^{-6} M, the concentration of the buffer in the

aqueous medium outside the vesicles (B_T) is 0.01 M, and the initial pH is 7 in both aqueous compartments. The rate constant considered for the translocation of the protonated solute from the outer to the inner leaflet is typical for a small noncharged amphiphile ($k_{loi}^{SH} = 1$ s^{-1})[79] and the reverse translocation is calculated from the ratio of the volumes of both membrane leaflets, which yields a slightly higher value (see Section 3.1 for details). For simplicity, in this first model the same 10^2 aqueous/membrane partition coefficients were considered for all species (protonated and unprotonated). The acidity constants were considered close to 10^{-7} M for all ionisable species, with that of the solute being $10^{-6.9}$ M to facilitate the graphical evaluation of the results.

Table 6. Parameters used in the simulation of the simplest model (Parameters Choice 1).

Geometric parameters			*Concentrations* (M)		*Partition coefficients*	
(nm)	r	100	c_L	10^{-3}	K_{wlo}^{SH}	10^2
	h	3.9	S_T	10^{-6}	K_{wli}^{SH}	10^2
Area (dm^2)	a_L	6.40×10^{-17} [113]	P_T	10^{-6}	K_{wlo}^{SD}	10^2
	A_T^o	2.00×10^5	B_T	0.01	K_{wli}^{SD}	10^2
	A_T^i	1.85×10^5	$H_{wo}[0]$	10^{-7}		
Volume (dm^3)	V_T	1	$H_{wi}[0]$	10^{-7}	*Acidity constants* (M)	
	V_{wo}	9.93×10^{-1}			K_a^{Sw}	$10^{-6.9}$
	V_{lo}	3.88×10^{-4}	*Rate constants* (s^{-1})		K_a^{Slo}	$10^{-6.9}$
	V_{wi}	5.92×10^{-3}	k_{loi}^{SH}	1	K_a^{Sli}	$10^{-6.9}$
	V_{li}	3.72×10^{-4}	k_{lio}^{SH}	1.04	K_a^B	10^{-7}
(dm^3 mol^{-1})	$\overline{V}_L$	0.76 [114]			K_a^P	10^{-7}

Figure 21 shows the time evolution of the local concentration of all solute species in the aqueous (plot A) and membrane compartments (plot B). At the beginning of the simulation, the solute is only in the outer compartments, equilibrated between the aqueous medium and the outer membrane leaflet. Over time, the solute permeates into the inner leaflet, and equilibrates with the aqueous media inside the vesicles.
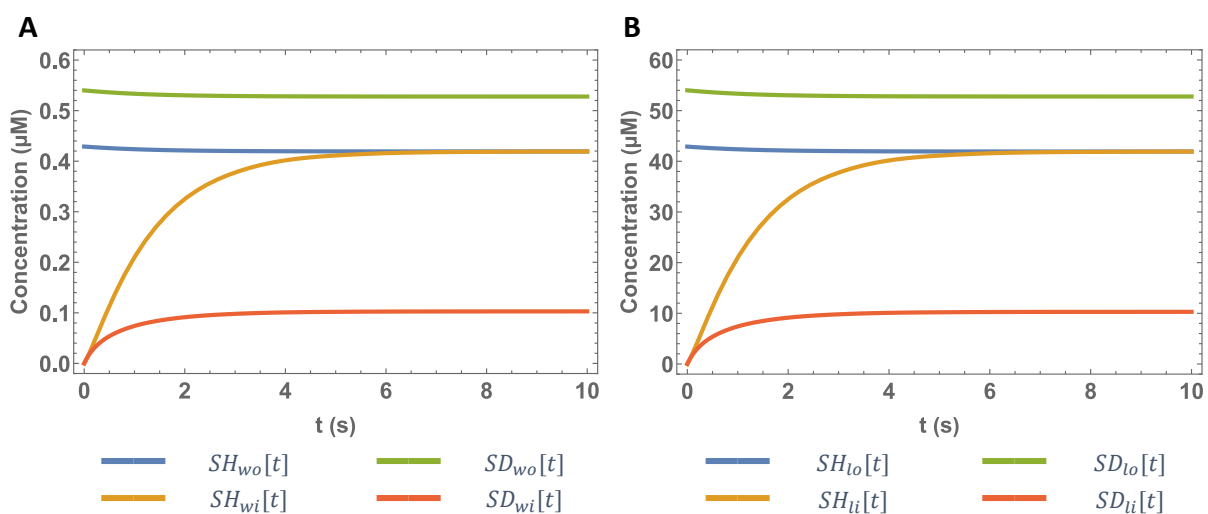
Figure 21. Time evolution of the solute species in the **A)** outer and inner aqueous compartments and in the **B)** outer and inner leaflets. Simulation parameters are shown in Table 6.

In this model, only the (neutral) weak acid is allowed to translocate between the outer and inner membrane leaflets. When it reaches the inner compartments, it deprotonates to yield the anionic *SD* and protons. While *SH* permeates, more SD_{wo} and SD_{lo} bind protons from the outer buffered aqueous compartment to yield additional weak acid. Permeation stops when the concentration of the protonated species in the inner compartments equals the concentration in the corresponding outer compartments. At the equilibrium, the concentrations of *SD* in the inner compartments (SD_{wi} and SD_{li}) are distinct from those in the corresponding outer compartments (SD_{wo} and SD_{lo}, respectively). This is because the permeation of the protonated solute leads to a decrease in the pH of the inner compartment (**Figure 22**), and at the equilibrium, the ratio *SD:SH* depends on the local pH value. That is, at equilibrium, the *SD* concentration gradients between inner and outer compartments are counterbalanced by opposing proton concentration gradients
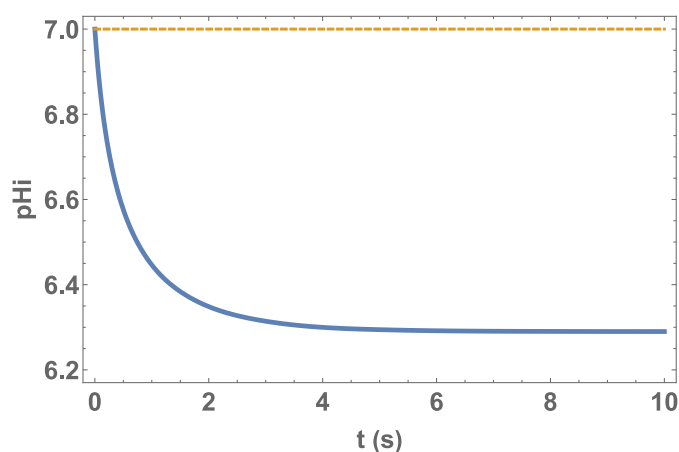
Figure 22. Variation in the pH value in the outer (- - - -) and inner (——) compartments, due to the permeation of a weak acid with the parameters shown in Table 6.

The simulations above yielded results that are consistent with the expected behaviour of the modelled processes given the underlying assumptions, which adds confidence in the correct implementation of the model and in the numerical integration.

The next sections will explore the influence of several parameters of the experimental design with the aim of understanding their effect on the reliability of experimental determinations. Namely, the size of the vesicles that encapsulate the inner compartments (for radius between 25 nm and 5 µm), the relative affinity of the protonated and deprotonated species for the membrane, the total concentration of solute, and the concentration of fluorescent probe in the inner aqueous compartments. The vesicle size was varied for each of the twelve conditions defined by the other studied parameters. In the simulations with **Parameters Choice 1 (C1),** the partition coefficient of all the species between the water and the membrane is 10^2. **Parameters Choice 2 (C2)** depicts a more realistic situation, where the affinity of the charged solute for the membrane is lower than that of the

neutral solute, with K_{wlo}^{SH} and K_{wli}^{SH} equal to 10^3, and K_{wlo}^{SD} and K_{wli}^{SD} equal to 10^2. Consequently, to satisfy the micro-reversibility constraints, the acidity constant of the weak acid in the membrane is one order of magnitude higher than the acidity constant in water. Additionally, the next analysis will be performed using two concentrations of solute and three concentrations of the pH-sensitive probe. A code was defined to facilitate the identification of the different conditions, with the form CX SX PX (**Table 7**). CX denotes the parameter choice (C1 or C2), SX the solute concentration with respect to the total volume (S1 or S2, for $S_T = 10^{-6}$ or 10^{-5} M, respectively), and PX the concentration of fluorescent pH probe in the internal aqueous compartments (P1, P2, or P3, for $P_T = 10^{-6}$, 10^{-5} or 10^{-4} M, respectively). All the other parameters are shown in Table 6.

Table 7. Identification code for sets of simulation parameters.

Code	Parameters			
	$K_{wlo}^{SH}, K_{wli}^{SH}$	$K_{wlo}^{SD}, K_{wli}^{SD}$	S_T (M)	P_T (M)
C1 S1 P1	10^2	10^2	10^{-6}	10^{-6}
C1 S1 P2	10^2	10^2	10^{-6}	10^{-5}
C1 S1 P3	10^2	10^2	10^{-6}	10^{-4}
C1 S2 P1	10^2	10^2	10^{-5}	10^{-6}
C1 S2 P2	10^2	10^2	10^{-5}	10^{-5}
C1 S2 P3	10^2	10^2	10^{-5}	10^{-4}
C2 S1 P1	10^3	10^2	10^{-6}	10^{-6}
C2 S1 P2	10^3	10^2	10^{-6}	10^{-5}
C2 S1 P3	10^3	10^2	10^{-6}	10^{-4}
C2 S2 P1	10^3	10^2	10^{-5}	10^{-6}
C2 S2 P2	10^3	10^2	10^{-5}	10^{-5}
C2 S2 P3	10^3	10^2	10^{-5}	10^{-4}

The simulations C2 SX PX differ from the C1 SX PX also in the parameters K_a^{Slo} and K_a^{Sli}, due to the micro-reversibility constraints. K_a^{Slo} and K_a^{Sli} are 1 order of magnitude lower than the K_a^{Sw} ($K_a^{Slo} = K_a^{Sli} = 10^{-7.9}$ M).

4.2.1.1. Effect of the vesicle size on permeation

In these simulations, the concentration of lipids remains the same and the outer radius of each vesicle varies between 25 and 5000 nm. As expected, when increasing the radius, the curvature of the vesicles decreases, and the volume of both membrane leaflets tends to become equal (**Figure 23A**). The difference between the two is around 4 % at an outer radius of 100 nm and becomes negligible for outer radius larger than 500 nm. The internal aqueous volume increases considerably with the increase in the liposome radius (**Figure 23B**), representing more than 3 % of the total aqueous media for a radius larger than 500 nm.
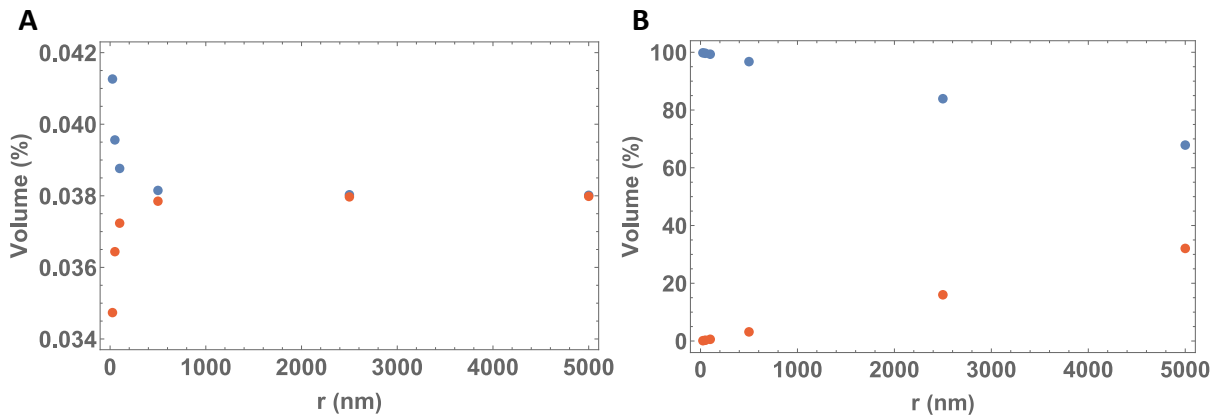
Figure 23. Effect of the size of the vesicles: Percentage of the volume of **A)** the outer (●) and inner (●) lipid membrane leaflets and **B)** the outer (●) and inner (●) aqueous compartments, for a lipid concentration equal to 10^{-3} M, and the lipid parameters as defined in Table 6.

Due to the increase in the relative volume of the inner aqueous compartments when the size of the vesicles increases, more solute molecules cross the membrane, and more time is needed to reach the equilibrium (**Figure 24** and **Table 8**). The volume of the inner aqueous compartments increases with the power of 3 with respect to the radius of the vesicles, but the volume of the inner membrane leaflet does not change significantly. Thus, the proportion of solute molecules in the membrane and aqueous media of the inner compartments changes, decreasing with the increase in the vesicle radius. As a consequence, the concentration of solute molecules in the inner compartments ($nS_i / V_{wi} = S_i$) decreases with the increase in the vesicle radius (**Figure 24A**).

Nevertheless, the mean occupancy numbers still increase with the vesicle radius (**Table 8**).
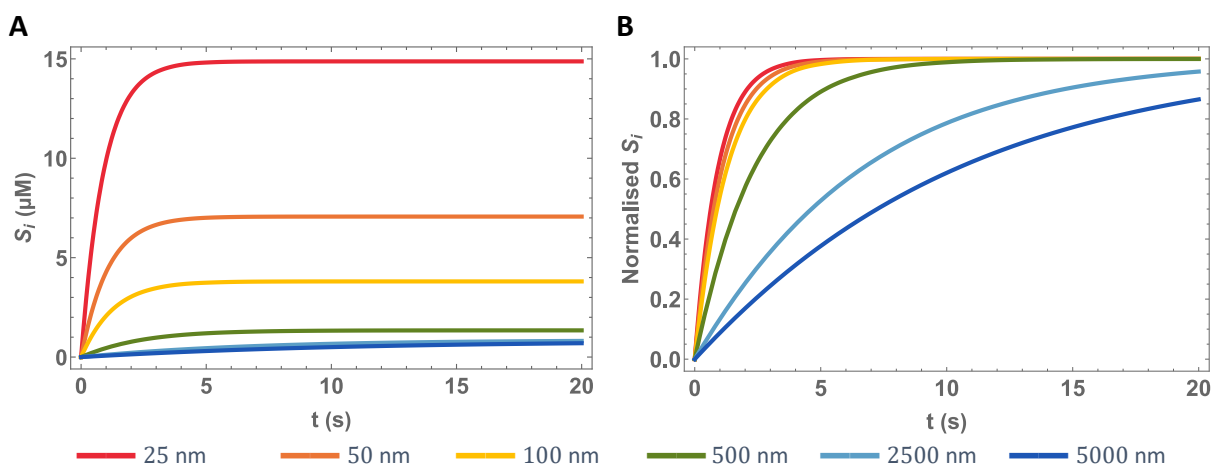
Figure 24. Effect of the size of the vesicles on the kinetics of weak acid permeation into the aqueous media encapsulated by the vesicles. **A)** Concentration of solute in the inner compartments (S_i). **B)** S_i normalised by the concentration at the respective equilibrium (results obtained with the simulation conditions C1 S1 P1).

4.2.1.2. Relationship between vesicle size and the pH gradient generated

In these simulations (Parameters Choice 1), only the protonated solute was allowed to permeate through the lipid membrane, the total solute concentration (with respect to the total volume) was fixed at 10^{-6} M, and the concentration of fluorescent pH probe in the inner aqueous compartments was 10^{-6} M (simulation conditions C1 S1 P1). The corresponding mean occupancy numbers for the solute inside each vesicle (leaflet and vesicle lumen) at equilibrium vary from 0.3 to over 10^5, as the liposome radius increases from 25 to 5000 nm (**Table 8**). As mentioned before (Section 4.2.1), the development of a pH gradient causes the net permeation of the solute to stop before the concentrations equalise between corresponding internal and external compartments. Table 8 also shows the mean occupancy numbers that would be achieved in the absence of this effect. The difference in occupancies between these scenarios is larger the smaller the vesicles are, reflecting a significant variation in the proton concentration (stronger ΔpHi). The effect of increasing the concentration of the fluorescent probe inside the vesicles (C1 S1 P2 and C1 S1 P3) is presented in Table 8 as well. The fluorescent probe captures some of the protons released by the weak acid in the inner compartment, and thus the generated pH gradient decreases with increasing the probe concentration. The mean occupancy numbers thus approach the ones predicted in the absence of a pH gradient.

Table 8. Mean occupancy numbers *per* vesicle, with outer radius r, in the absence of a transmembrane pH gradient and at the attained equilibrium. The concentration of fluorescent probe inside the vesicles considered was 10^{-6}, 10^{-5} and 10^{-4} M (P1, P2 and P3), the concentration of solute was 10^{-6} M (S1), and only the protonated species was allowed to permeate. The values were obtained considering the parameters choice 1 (C1, see Table 7).

r (nm)	No pH gradient	C1 S1 P1	C1 S1 P2	C1 S1 P3
25	0.7	0.3	0.4	0.6
50	3.3	1.7	2.1	2.9
100	15	9	11	14
500	629	413	538	615
2500	45 136	33 259	41 261	44 610
5000	327 209	254 695	304 583	322 834

4.2.1.3. The consequences of microheterogeneity for the kinetics of the approach to the equilibrium

Smaller vesicles have mean occupancy numbers close to 1 or even smaller (**Table 8**). In those situations, stochastic effects are significant making the kinetics of approaching the equilibrium more complicated. More concretely, the variability of the occupancy number *per* vesicle will be high and most vesicles may not have any molecules of solute. For example, considering the simulation C1 S1 P1, 74 % of the vesicles with 25 nm radius lack any molecule. For vesicles with 50 nm radius, having on

average 1.7 molecules, 31 % have 1, 26 % have 2, 14 % have 3 and 18 % have none (percentages were calculated using a Poisson distribution). Even for vesicles with 100 nm radius, stochastic effects may still be relevant. When using a solute concentration of 10^{-6} M, the mean occupancy number is about 9. In this situation, only 13 % of the vesicles contain 9 solute molecules, more than 23 % of the vesicles have less than 6 or more than 12 molecules of solute. Moreover, because the equilibrium is attained faster, important information may be lost during the stopped-flow mixing time. Therefore, small vesicles should not be used in those assays.

4.2.1.4. Implications of microheterogeneity and pH gradients for experimental design

The results above show that by increasing the concentration of the probe, the buffering capacity in the internal aqueous compartment also increases, the variation in the pH decreases, and the occupancy number approaches the equilibrium number (**Table 8**).

Therefore, to prevent the occupancy heterogeneities, bigger vesicles, higher concentrations of the probe and/or solute can be used. [The mean occupancy numbers for simulations of the Parameter Choice 1 considering a higher concentration of solute (10^{-5} M) are shown in Supplementary Material (**Table S1**).] However, care must be taken when using high concentrations of solute, especially if its affinity for the lipid membrane is high. This is because the high local concentrations of solute attained in the membrane may perturb its barrier properties. For the low solute concentration and membrane affinity considered in this work, the local solute concentration in the membrane is around 50 μM at equilibrium (**Figure 21**), corresponding to a solute to lipid molar ratio of around $1 : 10^4$ and very little membrane perturbation. The membrane affinity of drug-like molecules may be as high as 10^4 [Ref. 80], leading to a molar ratio of $1 : 10^3$ at a total concentration of solute equal to 10^{-6} M. In this case, increasing the solute concentration would most likely lead to a significant perturbation of the membrane properties.[80,115]

The pH variation observed at equilibrium is dependent on the extension of the deprotonation process, being larger for smaller vesicles, lower concentrations of the pH fluorescent probe, and higher concentrations of solute (**Table 9**). Despite the low occupation numbers, simulations carried out with vesicles with small radius exhibit higher pH variations. This is because smaller vesicles have smaller aqueous entrapped volumes which result in a higher variation of the concentration of protons when, for example, 1 molecule deprotonates. Upon permeation of the weak acid, the pH-sensitive probe can capture the released protons. Thus, the higher the probe concentration, the greater will be the buffer capacity and the smaller will be the pH variations. Using higher concentrations of solute will lead not only to higher occupancy numbers but also an enhanced pH variation because more weak acid molecules release a proton when they reach the inner compartments.

Table 9. pH variation for Parameter Choice 1 simulations (C1), when varying the concentration of the probe, 10^{-6}, 10^{-5} and 10^{-4} M (P1, P2 and P3), and solute, 10^{-6} and 10^{-5} M (S1 and S2).

r (nm)	C1 S1 P1	C1 S1 P2	C1 S1 P3	C1 S2 P1	C1 S2 P2	C1 S2 P3
25	1.06	0.67	0.19	1.59	1.39	0.70
50	0.87	0.46	0.10	1.41	1.14	0.48
100	0.71	0.32	0.06	1.25	0.92	0.33
500	0.45	0.14	0.02	0.97	0.57	0.14
2500	0.34	0.09	0.01	0.85	0.44	0.09
5000	0.33	0.08	0.01	0.85	0.43	0.09

4.2.1.5. Effect of the membrane affinity of the weak acid

Parameters Choice 2 describes a situation where the uncharged species has a 10-fold higher membrane affinity than the charged ones. This leads to higher mean occupancy numbers at equilibrium (**Table 10**). [The mean occupancy numbers for C2 S2 simulations are shown in Supplementary Material (**Table S2**).]

Table 10. Mean occupancy numbers *per* vesicle as a function of the outer radius r, in the absence of a transmembrane pH gradient and at the attained equilibrium. Simulations were carried out with Parameters Choice (C2), with the concentration of the entrapped fluorescent probe 10^{-6}, 10^{-5} and 10^{-4} M (P1, P2 and P3), and that of solute 10^{-6} M (S1).

r (nm)	No pH gradient	C2 S1 P1	C2 S1 P2	C2 S1 P3
25	2.7	2.4	2.4	2.6
50	12	11	11	12
100	52	48	50	52
500	1 557	1 417	1 503	1 549
2500	62 120	54 560	59 864	61 835
5000	363 044	316 586	350 114	361 462

The interaction of the weak acid with the membrane, which is thermodynamically more favourable, also decreases the tendency of the weak acid to deprotonate in the membrane. As a consequence, the pH decreases slightly less (**Table 11**) than in the C1 simulations (**Table 9**). This occurs despite the larger mean occupancy numbers in C2 simulations.

Table 11. pH variation for the Parameters Choice 2 simulations (C2), when varying the concentration of the probe, 10^{-6}, 10^{-5} and 10^{-4} M (P1, P2 and P3), and the concentration of the solute, 10^{-6} and 10^{-5} M (S1 and S2).

r (nm)	C2 S1 P1	C2 S1 P2	C2 S1 P3	C2 S2 P1	C2 S2 P2	C2 S2 P3
25	1.00	0.60	0.16	1.54	1.31	0.62
50	0.81	0.40	0.08	1.35	1.05	0.42
100	0.65	0.27	0.05	1.20	0.84	0.28
500	0.40	0.11	0.01	0.91	0.50	0.12
2500	0.30	0.07	0.01	0.79	0.38	0.07
5000	0.29	0.07	0.01	0.78	0.37	0.07

4.2.1.6. Fluorescence intensity as a reporter of solute permeation

The previous subsections have shown that i) small vesicle radius may lead to undesired stochastic effects due to small solute mean occupancy numbers; ii) this could be overcome by increasing the total concentration of solute and/or the pH buffer capacity inside the vesicles; iii) the pH variation is larger for smaller vesicles; and iv) it is increased for higher solute concentrations and decreased when the pH buffer capacity inside the vesicles is increased. Although a significant pH variation is necessary when using this methodology, it will be shown in this section that it should not be too large. The size of the vesicles, the solute concentration, and that of the pH probe, should be carefully chosen to avoid stochastic effects and to lead to moderate pH variations.

In the pH variation assay, a fluorescent pH probe is encapsulated in the aqueous compartment inside the vesicles. As only the deprotonated form (PD_{wi}) of the pH probe is fluorescent, variations in fluorescence intensity report changes in the fraction of probe in this form. For pH values near the probe pK_a, the concentration of this species is approximately proportional to the pH, and hence fluorescence can accurately report the pH variation in the inner aqueous compartment (**Figure 25A**). However, this proportionality breaks down as the pH value deviates from the probe pK_a. For instance, 0.4 and 0.5 units below the operating point, the assumption of a proportional response yields 5.3 % and > 10 % errors, respectively. And 0.57 and 0.76 units above the operating point, it yields 5.1 % and 10 % errors, respectively (**Figure 25B**).

A

B
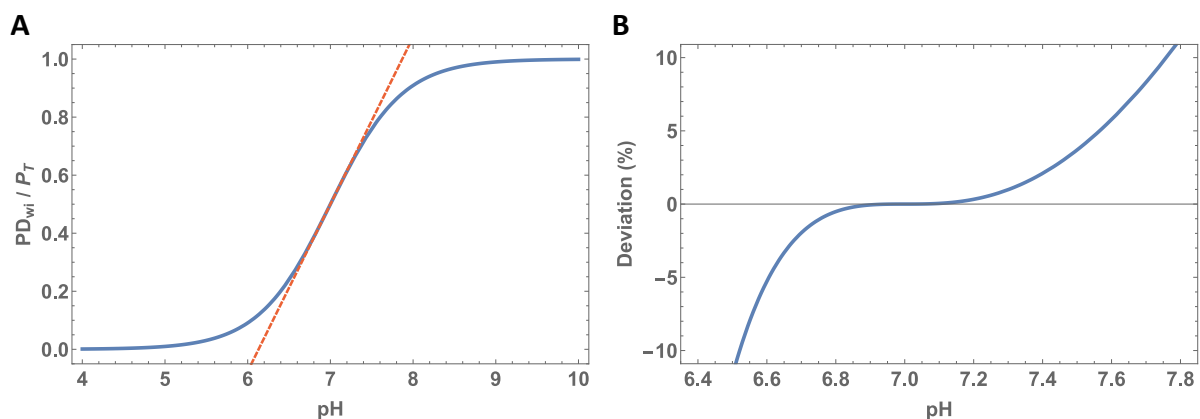
Figure 25. A) Ratio of the deprotonated fluorescent probe (PD_{wi}) with $pK_a = 7$ as a function of the pH, estimated with the Henderson-Hasselbalch equation (——), and linear approximation around the operating point (7.0, 0.5) (----). **B)** Deviation between the linear approximation and the function that describes PD_{wi}/P_T with the pH.

For this method to be sensitive, there must be a significant pH variation in the vesicles' lumen. But as follows from the previous analysis, the pH variation should remain in a limited interval around the probe's pK_a for the fluorescence change to accurately report it. Another important question is whether the pH variation accurately reflects the variation in the amount of solute that has permeated, which is the relevant variable for determining the permeability coefficient. Indeed, this is not the case for a pH variation over 1 unit (**Figure 26A**). Instead, it is the variation in the concentration of protons (H_{wi}) that best tracks the solute accumulation dynamics in the inner compartments (S_i). Already, for a 0.19 units pH variation, the normalised variation of the concentration of the fluorescent probe and the pH variation are nearly equal, and very similar to the variation of the solute and proton concentrations (**Figure 26B**).

A

B
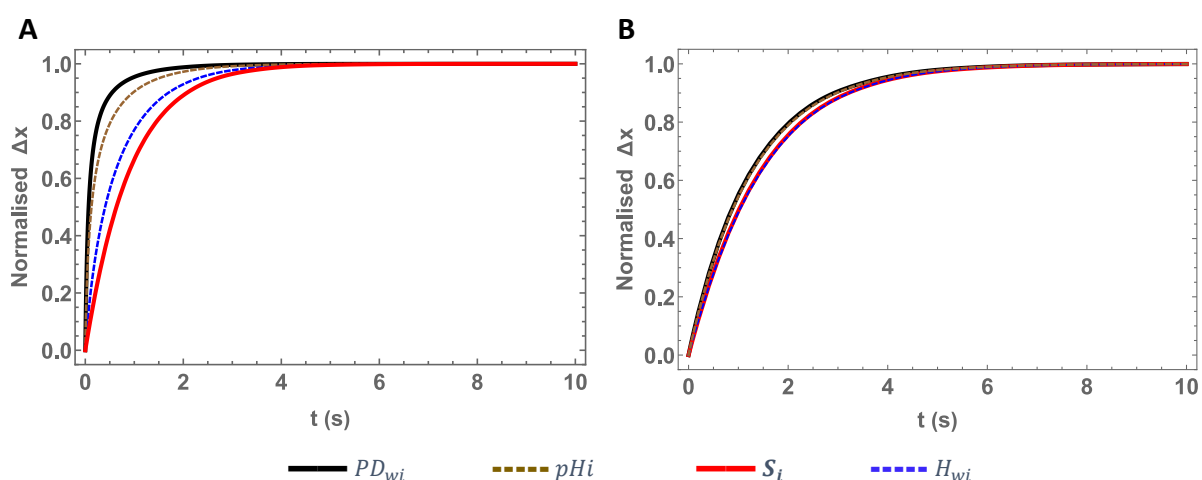
Figure 26. Normalised variations of PD_{wi}, pHi, S_i and H_{wi}. **A)** Simulation conditions: C1 S1 P1, $r = 25$ nm (ΔpHi = 1.06). **B)** Simulation conditions: C1 S1 P3, $r = 25$ nm (ΔpHi = 0.19).

4.2.1.7. Parameter estimation

This section will analyse some of the simulations presented above in further detail to find out (i) what is the maximum acceptable pH variation, and (ii) what should be the experimental settings to obtain the rate of the weak acid permeation with good accuracy from an exponential fit of the fluorescence variation.

In a technique as rigorous as fluorescence, the measurement uncertainty is no higher than 5%. However, in the pH variation assay, the fluorescence of an entrapped probe is used to evaluate indirectly the permeation of weak acids or bases, and the uncertainty can increase depending on the experimental conditions. In the subsequent analysis of the accuracy of fluorescence as a reporter of solute permeation, only simulations that yield a pH variation between 0.05 and 0.40 units will be considered. The former value is limited by the sensitivity of the method and equipment and may thus depend on the experimental settings. In turn, the latter value was chosen according to the deviations (< 5 %) between the actual pH dependence of the fraction of deprotonated probe and its linear approximation around probe's pK_a (**Figure 26B**).

For the selected simulations, the fits of the solute concentration variation will be compared to the time course of the concentration of the fluorescent probe, referred to the total volume ($PD_{wi}*[t]$). The analysis proceeded as follows. First, the time courses of S_i and $PD_{wi}*$ were fitted with a mono-exponential function, equation (129). Here the independent variable is time (t), the dependent variable is the concentration of the species, and the adjustable parameters are the concentration at equilibrium (y_∞), the concentration at $t = 0$ (y_0) and the characteristic constant (β, with units s^{-1}). A bi-exponential function, equation (130), was also fitted to the data obtained in each simulation. y_∞ and y_0 have the same meaning, α_1 and α_2 are pre-exponential factors with respect to the characteristic constants β_1 and β_2, respectively.

$$y[t] = y_\infty + (y_0 - y_\infty)e^{-\beta t} \tag{129}$$

$$y[t] = y_\infty + (y_0 - y_\infty)(\alpha_1 e^{-\beta_1 t} + \alpha_2 e^{-\beta_2 t}), \alpha_1 + \alpha_2 = 1 \tag{130}$$

The best fit of the equations above to the simulated data was obtained by the method of minimum sum of square deviations. The goodness of fit was evaluated and the model that better describes the data was selected according to Akaike's Information Criterion (AIC), a statistical parameter that allows the comparison of models with different number of Best-fit parameters.[116]

Table 12 shows the Best-fit parameters for $S_i[t]$ and $PD_{wi}*[t]$, as well as the relative deviation between the estimates of the characteristic constant of solute accumulation (β_{S_i}) and the closer characteristic constant obtained for the variation of the probe concentration (β_1).

Table 12. Best-fit parameters of the time course of the concentrations of solute ($S_i = nS_i/V_{wi}$) and of the fluorescent probe with respect to the total volume ($PD_{wi}* = nPD_{wi}/V_T$), for the simulations satisfying 0.05 < ΔpHi < 0.40. The relative deviation reflects differences between the characteristic constant obtained by fitting $S_i[t]$ (β_{S_i}) and the characteristic constant (β_1) obtained when fitting $PD_{wi}*[t]$ with a mono- or bi-exponential functions.

Simulation			S_i			$PD_{wi}*$					% Deviation
Descriptor	Radius (nm)	ΔpHi	y_0 (M)	y_∞ (M)	β_{S_i} (s⁻¹)	y_0 (M)	y_∞ (M)	β_1 (s⁻¹)	α_1	β_2 (s⁻¹)	$\frac{\beta_{S_i}-\beta_1}{\beta_{S_i}}\times 100$
C1 S1 P1	2500	0.34	0	8.51×10^{-7}	0.15	8.00×10^{-8}	5.00×10^{-8}	0.16	0.64	0.39	7
	5000	0.33	0	8.12×10^{-7}	0.10	1.60×10^{-7}	1.02×10^{-7}	0.10	0.67	0.26	7
C1 S1 P2	100	0.32	0	4.89×10^{-6}	0.64	2.96×10^{-8}	1.93×10^{-8}	0.71	0.81	1.59	10
	500	0.14	0	1.75×10^{-6}	0.32	1.58×10^{-7}	1.33×10^{-7}	0.35	0.99	1.36	8
	2500	0.09	0	1.05×10^{-6}	0.12	8.00×10^{-7}	7.19×10^{-7}	0.13			5
	5000	0.08	0	9.75×10^{-7}	0.08	1.60×10^{-6}	1.45×10^{-6}	0.08	0.97	0.15	3
C1 S1 P3	25	0.19	0	2.41×10^{-5}	0.70	5.60×10^{-8}	4.40×10^{-8}	0.74	0.80	1.08	6
	50	0.10	0	1.19×10^{-5}	0.55	1.36×10^{-7}	1.20×10^{-7}	0.58			6
	100	0.06	0	6.33×10^{-6}	0.46	2.96×10^{-7}	2.77×10^{-7}	0.47			3
C1 S2 P3	100	0.33	0	4.85×10^{-5}	0.65	2.96×10^{-7}	1.90×10^{-7}	0.71	0.79	1.47	9
	500	0.14	0	1.74×10^{-5}	0.33	1.58×10^{-6}	1.32×10^{-6}	0.33	0.56	0.40	-1
	2500	0.09	0	1.05×10^{-5}	0.12	8.00×10^{-6}	7.16×10^{-6}	0.13			5
	5000	0.09	0	9.70×10^{-6}	0.08	1.60×10^{-5}	1.45×10^{-5}	0.08			4
C2 S1 P1	500	0.40	0	4.60×10^{-6}	1.03	1.57×10^{-8}	9.06×10^{-9}	1.16	0.61	4.36	13
	2500	0.30	0	1.39×10^{-6}	0.76	8.00×10^{-8}	5.37×10^{-8}	0.84	0.71	2.59	10
	5000	0.29	0	1.01×10^{-6}	0.63	1.60×10^{-7}	1.09×10^{-7}	0.68	0.72	1.95	8
C2 S1 P2	100	0.27	0	2.23×10^{-5}	1.12	2.96×10^{-8}	2.07×10^{-8}	1.19	0.72	3.62	6
	500	0.11	0	4.88×10^{-6}	0.96	1.58×10^{-7}	1.37×10^{-7}	1.00	0.88	2.56	4
	2500	0.07	0	1.53×10^{-6}	0.68	8.00×10^{-7}	7.35×10^{-7}	0.71	0.97	2.41	4
	5000	0.07	0	1.11×10^{-6}	0.56	1.60×10^{-6}	1.48×10^{-6}	0.58	0.99	2.54	4
C2 S1 P3	25	0.16	0	1.09×10^{-4}	1.26	5.60×10^{-8}	4.59×10^{-8}	1.30	0.82	3.46	4
	50	0.08	0	4.84×10^{-5}	1.13	1.36×10^{-7}	1.23×10^{-7}	1.16	0.91	2.96	3
C2 S2 P2	2500	0.38	0	1.36×10^{-5}	0.79	7.99×10^{-7}	4.72×10^{-7}	0.87	0.68	2.63	10
	5000	0.37	0	9.79×10^{-6}	0.65	1.60×10^{-6}	9.65×10^{-7}	0.72	0.71	2.09	10
C2 S2 P3	100	0.28	0	2.23×10^{-4}	1.12	2.96×10^{-7}	2.04×10^{-7}	1.19	0.72	3.65	7
	500	0.12	0	4.88×10^{-5}	0.96	1.58×10^{-6}	1.37×10^{-6}	1.00	0.88	2.52	4
	2500	0.07	0	1.53×10^{-5}	0.68	8.00×10^{-6}	7.32×10^{-6}	0.70	0.91	1.34	2
	5000	0.07	0	1.11×10^{-5}	0.55	1.60×10^{-5}	1.48×10^{-5}	0.57	0.97	1.48	3

In all the selected conditions, the concentration of solute in the internal compartments at $t = 0$ obtained from the best fit is always zero and the variation of its concentration was always well fitted with a mono-exponential function. In contrast, the time course of $PD_{wi}*$ was usually better fitted by a bi-exponential function. Also, even in the simulations where the variation of the probe concentration was well fitted with a mono-exponential function, the characteristic constants were not exactly equal to those obtained for the mono-exponential fit of $S_i[t]$. Moreover, when $PD_{wi}*$ was better fitted with a bi-exponential function, the smaller characteristic constant was always closer to and higher than the characteristic constant obtained for the variation in the concentration of S_i [except in the simulation C1 S2 P3 with $r = 500$ nm]. That is, inaccuracies in the description of the solute dynamics by the variations in the fluorescence intensity tend to overestimate the rate of solute permeation. In the Simulation C1 S2 P3 with $r = 500$ nm, the smallest characteristic constant is still the one with the highest pre-exponential factor. These results are consistent with each other and suggest that the permeability of the weak acid must be calculated from the smallest characteristic constant of the fluorescence signal, which is also the one with the highest pre-exponential factor. However, the fastest characteristic constant of the first compartment of the fluorescence variation has been used instead in previous application of this method.[68] According to the published data, this is also the characteristic constant with the highest pre-exponential factor. The reason for this discrepancy is unclear. The choice for the highest characteristic constant is not properly substantiated in the published literature, and so its use may lead to an overestimation of solute permeability coefficients.

From these results (**Table 12**) and as was expected from the discussions above, lower concentrations of the fluorescent probe (10^{-6} M) (S1 P1 simulations) lead to less accurate reporting of the permeation of the weak acid through the membrane, due to the larger pH variations observed. Even for the intermediate probe concentration, the accuracy remains unsatisfactory for a higher concentration of solute (S2 P2 simulations). According to the simulations in Table 12, a 10 to 100 ratio between the concentration of the probe in the inner compartments and the solute concentration is required for an acceptable relative deviation. As the pH variation is dependent on the extent of permeation, the generality of this conclusion should be studied experimentally in the future.

Parameter Choice 2 simulations describe a more realistic situation, and result in a broader pH variation range, allowing a more comprehensive view of the effect of the pH variation in the accuracy of the probe as a reporter of solute permeation. The results show that pH variations lower than 0.25 units lead to deviations ≤ 10 % between the characteristic constants obtained by fitting the solute dynamics and those by fitting the probe concentration (**Figure 27**). Thus, when performing the pH variation assay, pH variation must be under 0.25 units to obtain accurate permeation coefficients.
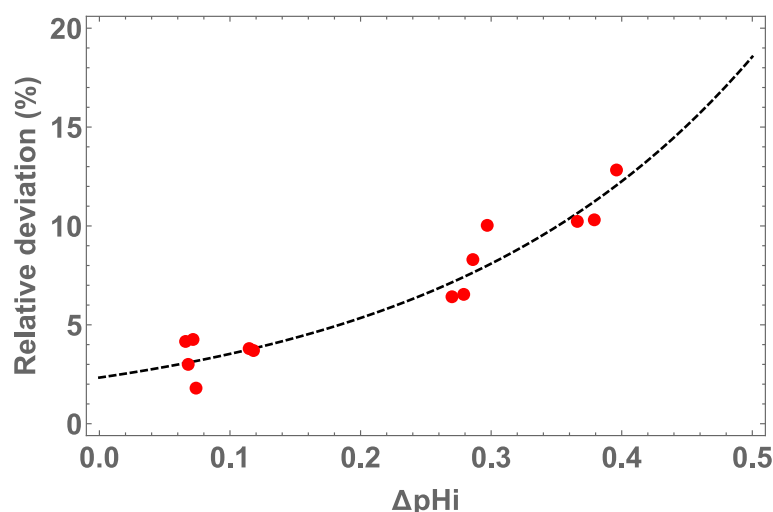
Figure 27. Relative deviations between the characteristic constant obtained by fitting $S_i[t]$ (β_{S_i}) and the lowest characteristic constant attained when fitting $PD_{wi}*[t]$ (β_1) for the selected Parameter Choice 2 simulations. The dashed line is the exponential tendency of the data ($\chi^2=0.92$).

It could be questioned if the optimal range can be improved by making the initial pH higher than the probe pK_a when determining the permeability of weak acids (or lower than pK_a^P when determining the permeability of weak bases). To address this question, simulations were carried out for three of the selected conditions by changing the initial pH around the pK_a^P. It was observed that the pH variation upon weak acid permeation increases by raising the initial pH, and the permeation of the weak acid becomes slower (β_{S_i} decreases) (**Table 13**). Additionally, the relative deviation between the characteristic constants, obtained from fitting the time courses of solute concentration and the fluorescence, is slightly increased.

Table 13. Best-fit parameters of the time course of the concentrations of solute (β_{S_i}) and of the fluorescent probe with respect to the total volume (β_1, β_2 and α_1). The relative deviations reflect the difference between β_{S_i} and β_1.

r (nm)	pH[0]	ΔpHi	β_{S_i} (s⁻¹)	β_1 (s⁻¹)	α_1	β_2 (s⁻¹)	% Deviation
	7.0	0.60	1.31	1.66	0.57	7.86	27
25	7.1	0.62	1.29	1.64	0.58	7.92	27
	7.2	0.65	1.27	1.61	0.59	7.97	27
	7.0	0.27	1.11	1.23	0.76	4.04	10
100	7.1	0.29	1.09	1.21	0.76	4.08	11
	7.2	0.31	1.06	1.19	0.76	4.11	11
	7.0	0.07	0.55	0.58			6
5000	7.1	0.08	0.51	0.54			6
	7.2	0.09	0.46	0.49			8

As expected, the variation of PD_{wi} better reports the variation of the inner pH when the initial pH is increased (**Figure 28**, blue and green lines). However, the variation of H_{wi} tracks that of S_i slightly less accurately (yellow and orange lines). Figure 29A shows the corresponding percent differences and highlights that the deviation between the variation of the PD_{wi} and pHi (dashed lines) decreases and the percent difference between the variation of S_i and H_{wi} (solid curves) increases. Additionally, the deviation between the variation of pHi and the variation of H_{wi} increases with the variation of the inner pH (**Figure 29B**). This justifies why making the initial pH higher than the pK_a^P tends to increase the inaccuracy of the probe as a reporter of the permeation of weak acids.
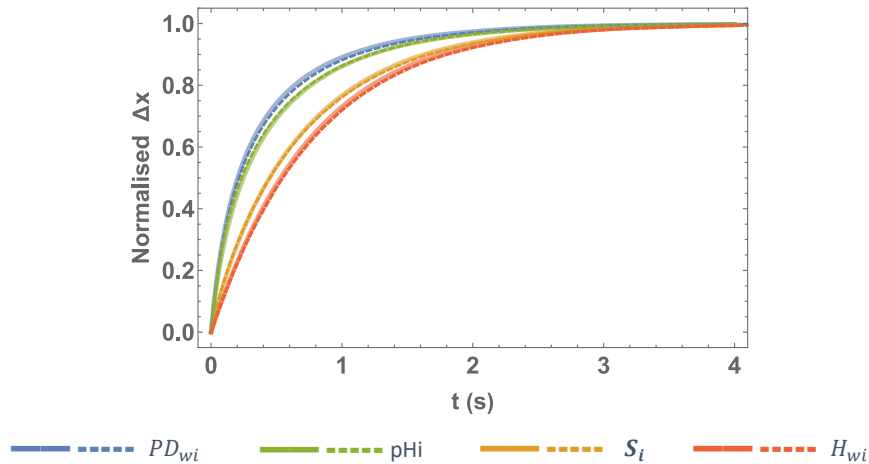
Figure 28. Normalised variations of PD_{wi}, pHi, S_i and H_{wi}. The solid lines are the normalised variations for the simulation with the outer and inner initial pH = 7.0. The dashed lines represent the same variables but for the simulation with an outer and inner initial pH of 7.2. Simulation conditions: C2 S1 P2, and $r = 25$ nm.
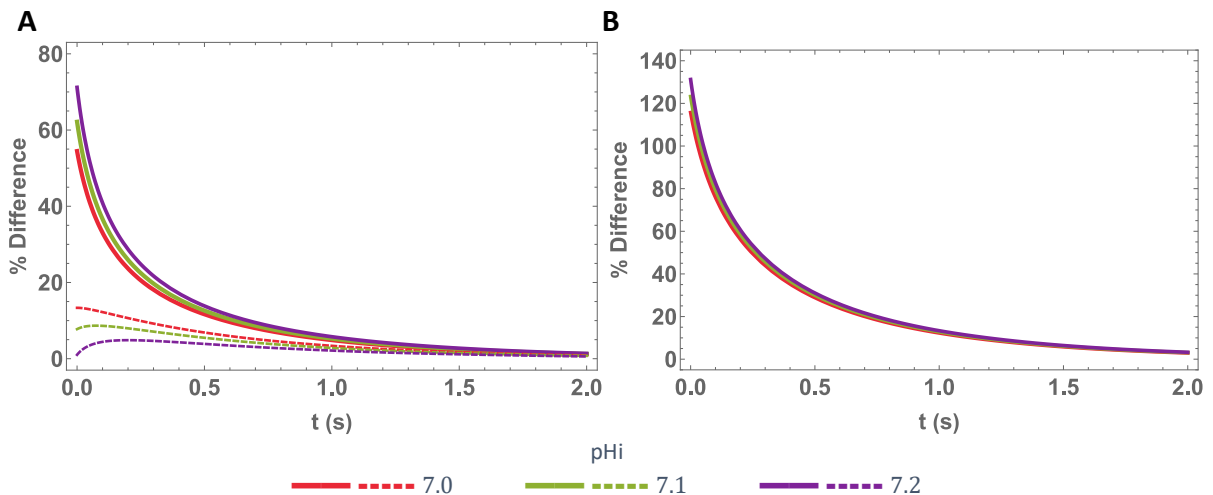
Figure 29. Effect of the initial pH in the accuracy of the fluorescence intensity variation as a reporter of solute permeability. **A)** Percentual difference between the normalised variation of PD_{wi} and pHi (dashed lines) and between the normalised variation of S_i and H_{wi} (solid lines). **B)** Percentual difference between the normalised variation of pHi and H_{wi}.

If the pH variation is too small, then the kinetics of permeation of weak acids cannot be easily measured through this method. In this case, increasing the initial pH can also increase the sensitivity of the method by improving the signal-to-noise ratio, without markedly raising the perceived error.

4.2.1.7.1. <u>Fit quality assessment</u>

When performing data fitting, it is important to repeat the procedure using different starting values for the adjustable parameters. This process decreases the probability of getting trapped in a local minimum and avoids obtaining estimates that albeit can describe the data, are meaningless.

The correlation matrix of the bi-exponential fit of the concentration of the probe (**Table 14**, as an example) of all the simulations analysed shows high correlations (close to 1) between β_1, β_2 and α_1, which means that besides the parameters provided in Table 12, other sets of parameters could lead to an equally good fit. Although correlated, when performing the fit using different initial conditions for these parameters, the parameters have converged to the same solution or a solution slightly different but inside the parameter confidence interval.

Table 14. Correlation matrix for the Best-fit parameters of $PD_{wi}{}^*[t]$ (y_0, y_∞, α_1, β_1 and β_2) with the simulation conditions C2 S1 P2, $r = 100$ nm.

	y_0	y_∞	α_1	β_1	β_2
y_0	1	0.09	0.31	0.34	0.59
y_∞	0.09	1	0.38	0.48	0.30
α_1	0.31	0.38	1	0.97	0.92
β_1	0.34	0.48	0.97	1	0.86
β_2	0.59	0.30	0.92	0.86	1

The best fit (mono- or bi-exponential) was selected using the AIC, however, it does not give an idea of the confidence in those parameters. Determining the confidence interval is essential to evaluate the uncertainty of the parameters. This is done by perturbing one of the Best-fit parameters and evaluating how the sum of squared residuals is affected on fitting the remaining parameters.[117] In all the fits, the confidence interval of the characteristic constants is narrow, being narrower for β_1, which is the parameter used in the next section to estimate the permeability coefficient for being the one that better reports the dynamics of solute accumulation. As an example, in Table 15, the confidence intervals for the Best-fit parameters of the simulation C2 S1 P2 with vesicles with 100 nm radius are presented.

Table 15. 95 % Confidence intervals for the parameters obtained by fitting solute accumulation ($S_i[t]$) and the concentration of the probe with respect to the total volume ($PD_{wi}{}^*[t]$). Simulation conditions: C2 S1 P2, and $r = 100$ nm.

Parameter		Value	95 % Confidence interval
$S_i[t]$	β	1.1160	[1.1156, 1.1164]
$PD_{wi}{}^*[t]$	β_1	1.1877	[1.1854, 1.1899]
	β_2	3.6220	[3.5939, 3.6502]
	α_1	0.7228	[0.7203, 0.7253]

Some authors have questioned the origin of the multi-exponentiality of the experimental data in permeability assays. Indeed, the simulated fluorescence time course obtained with Model I does not exactly follow a bi-exponential function. However, this function is used because it fits the simulated data significantly better than a mono-exponential function in most cases.

In real experiments, deviations of the fluorescence variation from a mono- or bi-exponential function may be masked by noise in the experimental data. This was evaluated by adding noise described by a zero-centred Gaussian distribution with a 1, 5, or 10 % coefficient variation to $PD_{wi}{}^*[t]$. After adding this noise, in the simulations where $\alpha_1 > 0.8$ (in the $PD_{wi}{}^*$ fits) in the previous analysis (**Table 12**), the fluorescence became better described by a mono-exponential function. Even where the noisy data was better described by bi-exponential functions, the characteristic constant closer to the characteristic constant of the dynamics of $\boldsymbol{S_i}$ was the smaller one, which had the highest pre-exponential factor.

4.2.1.7.2. Estimation of the permeability coefficient

The characteristic constants determined in the previous sections are closely related to the permeability coefficient, the relevant parameter, but this relationship is not trivial. For instance, while the characteristic constant that characterises the permeation is very sensitive to the vesicle size (**Table 12**), the permeability coefficient should be invariant. We examine this relationship below.

The permeability coefficient can be used to predict the permeation of compounds in systems that have a lipidic membrane as barriers, as for instance cells or endothelia. When using the pH variation assay with spherical lipid vesicles, the permeability coefficient (P) is usually obtained through the equation

$$P = \beta \frac{r}{3}.$$

We have noticed that in literature, this equation is sometimes used under conditions where its applicability is questionable. During the development of this work, we analysed how this widely used expression (equation (2), Section 1.3.2.4) was derived, what approximations must be assumed, and when can it be correctly used. These issues were analysed in detail in a paper that we recently published.[118] This section presents a summary of the main conclusions from this work.

As shown before, the variation in the concentration of solute in the acceptor compartments follows a mono-exponential kinetics, equation (129), which can be simplified to

$$\boldsymbol{S_i}[t] = \boldsymbol{S_{i_\infty}}(1 - e^{-\beta\,t}) \tag{131}$$

if at $t = 0$ the solute concentration in the acceptor compartment is null.

Differentiating equation (131), one gets

$$\frac{d\ S_i[t]}{dt} = S_{i_\infty}\ \beta\ e^{-\beta\ t}, \tag{132}$$

with $S_{i_\infty}\ \beta$ being the initial rate of increase of the solute concentration. This means that the initial rate depends on the concentration at equilibrium and the characteristic constant β.

In a pH variation experiment, what is usually measured is the rate at which the fluorescence intensity reaches the steady-state value. Although it is in principle possible to calculate the corresponding pH variation, and from it the extent of solute permeation, this is not usually done. In contrast, in permeability assays using cell monolayers, the amount of solute that permeates is measured directly over time, and only the initial rate is considered (for less than 10 % solute permeating).[43] The permeability coefficient (dm s^{-1}) is then determined from the rate of solute accumulation by the equation

$$P_{app} = \frac{\left.\dfrac{d\ nS_A}{dt}\right|_{t=0}}{A\ S_{D_0}}, \tag{133}$$

where $\left.\dfrac{d\ nS_A}{dt}\right|_{t=0}$ is the initial rate of increase of the amount of solute in the acceptor compartment (mol s^{-1}), S_{D_0} is the concentration in the donor compartment (mol dm^{-3}) at $t=0$ and A is the area of the surface dividing both compartments (dm^2).[43] Considering the relationship between the initial rate of solute accumulation in the acceptor compartment and the characteristic constant for solute accumulation (from equation (132)), the equation above can be modified to

$$P_{app} = \frac{nS_{A_\infty}\ \beta}{A\ S_{D_0}} = \frac{nS_{A_\infty}\ \beta\ V_D}{A\ nS_{D_0}}. \tag{134}$$

If transport is irreversible, the equilibrium is achieved only when all the molecules of solute have permeated $(nS_{D_0} = nS_{A_\infty})$ and the permeability coefficients may be calculated from the characteristic constant of the mono-exponential variation in S_A, as

$$P_{app} = \frac{\beta\ V_D}{A}. \tag{135}$$

Applying this expression to solute efflux and expressing V_D and A in terms of the vesicle radius, r, leads to equation (2).[59]

In turn, if the transport is reversible, by replacing nS_{A_∞} into equation (134) by the product $S_{A_\infty}\ V_A$, one gets

$$P_{app} = \frac{S_{A_\infty}\ V_A\ \beta}{A\ S_{D_0}}. \tag{136}$$

If the equilibrium is complete and the volume of the donor compartment is much larger than that of the acceptor compartment, the local concentration of solute in the donor compartment does not change over time, and the therefore $S_{D_0} = S_{A_\infty}$, leading to

$$P_{app} = \frac{\beta\, V_A}{A}.$$

This equation is useful for studies using vesicles but is only valid for the permeation of neutral solutes and when an electrical potential gradient is not created.[119] If V_A and A are expressed in terms of the vesicle radius, one again gets the equation (2).

In the pH variation assay, transport is neither irreversible nor from the inner to the outer aqueous compartments. To identify the most suitable approach under these conditions, permeabilities estimates through equations (2) and (136) will be assessed below for the set of simulations C2 S1 P2.

Permeability coefficients express the ease with which a given compound crosses the membrane and it should be independent of the vesicles size in the case that the curvature is negligible and if the limiting step of the overall permeation is the same. The surface area is essentially invariant, but the entrapped volume increases considerably. Therefore, according to equation (2), the apparent permeability coefficient would only remain invariant with respect to vesicle radius if the characteristic constant changed reciprocally to the ratio $\frac{V_A}{A}$. However, the simulations show a much shallower dependence of the characteristic constant on the radius (**Table 16**), and as a consequence, the apparent permeability coefficients increase steeply with the radius (**Figure 30**, blue dots). In contrast, permeability coefficients obtained using the equation (136) are essentially invariant (**Figure 30**, orange dots). Even when the volume of the inner compartments is substantially smaller than that of the outer ones ($r < 100$ nm), the two approaches yield very different apparent permeabilities.

Table 16. Effect of the radius on the characteristic constant at which the solute accumulates. Simulation conditions: C2 S1 P2.

Radius (nm)	β_{S_i} (s^{-1})
25	1.32
50	1.19
100	1.12
500	0.96
2500	0.68
5000	0.56
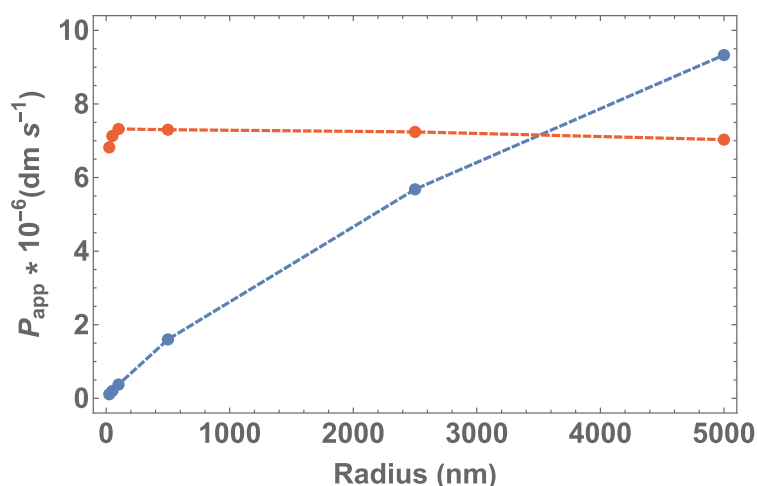
Figure 30. Effect of the radius on the solute permeability coefficient calculated from equation (2) (●) and equation (136) (●), using the Best-fit parameters shown in Table 16. Simulation conditions: C2 S1 P2.

To better understand the source of this discrepancy we first note that equation (136) is equal to equation (2) multiplied by the ratio $\frac{S_{A\infty}}{S_{D_0}}$. Thus, the further away from 1 this ratio is, the stronger will the discrepancy be. This ratio can be strongly influenced by the following two factors whose effects will be examined in turn: i) the volume ratio between donor and acceptor compartments, and ii) the solute's membrane/water partition coefficient.

Even for the largest vesicles considered ($r = 5000$ nm), the outer aqueous (donor) compartment fills most ($\approx 68\,\%$) of the total volume. Therefore, as the total number of moles of solute is equal in all the simulations, S_{D_0} increases just 1.5-fold as the vesicles increase from 25 to 5000 nm radius. However, in Figure 30 the permeability coefficient obtained using equation (2) increases by over one order of magnitude. Therefore, this variation is not highly influenced by the initial concentration of solute in the donor compartment, but by the amount of solute that permeates. As discussed previously, independently of the pH attained, the concentration of solute at equilibrium is higher for small vesicles, thus justifying the greater difference between the values obtained through the two equations.

The set of simulations C1 S1 P2 and C2 S1 P2 (**Figure 31**) shows that a higher partition coefficient of the solute – higher partition to the membrane of the neutral form, in C2 S1 P2 simulations – leads to a higher solute concentration in the acceptor compartments, which include the inner leaflet of the membrane. Therefore, the ratio $\frac{S_{A\infty}}{S_{D_0}}$ can be much higher than 1 for more lipophilic solutes, and significant deviations from the expected behaviour are anticipated. This effect is stronger for smaller vesicles, due to their much larger $\frac{V_{li}}{V_{wi}}$ ratio. Other consequence of the higher lipophilicity of the solute is the larger pH variation inside the vesicles, which leads to more extensive deviations from full

equalisation of the solute concentrations between donor and acceptor compartments. The break-down of the assumption of full equilibration leads to an overestimation of the permeability coefficient by the simplified equation.
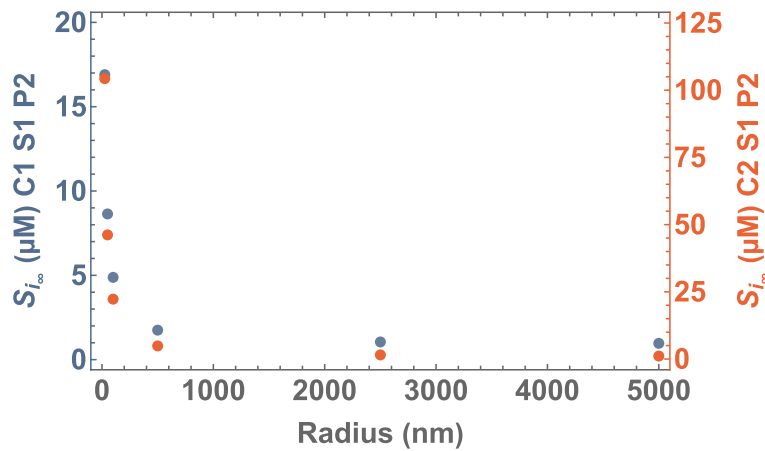
Figure 31. Solute Concentration in the inner compartments at equilibrium for C1 S1 P2 (●) and C2 S1 P2 (●) simulations. Note the different scales.

From this analysis, it is concluded that equation (2) should not be used to estimate the permeability coefficient when performing the pH variation assay. The correct relationship between the experimental parameter and the permeability coefficient is given by equation (136), which depends on the solute concentration at equilibrium. Therefore, it is essential to obtain S_{i_∞} to predict the permeability coefficient of tested solutes with good accuracy. For that, it is necessary to know the pH attained, which is easily achieved by converting the fluorescence signal into pH values. Additionally, it is necessary to know other parameters, such as the volume of each compartment, acidity constant, and solute partition coefficients. Equation (138) defines the concentration of the solute inside the vesicles at equilibrium, and it could be simplified if the barrier is symmetric and considering the typical values of some parameters and details of the experimental design.

$$S_{i_\infty} = \frac{S_T}{\dfrac{V_{wi}}{V_T} + \dfrac{V_{wo}}{V_T} \dfrac{1 + \dfrac{H_{wo}}{K_a^{Sw}}\left(1 + K_{wlo}^{SH}\dfrac{V_{lo}}{V_{wo}}\right)}{1 + K_{wli}^{SD}\dfrac{V_{li}}{V_{wi}} + \dfrac{H_{wi}}{K_a^{Sw}}\left(K_{wli}^{SH}\dfrac{V_{li}}{V_{wi}} + 1\right)}}$$

(138)

For non-lipophilic solutes, if $K_{wlo}^{SH} \ll V_{wo}/V_{lo}$ and $V_T \gg V_{wi}$, equation (138) simplifies to

$$S_{i_\infty} = \frac{S_T}{\dfrac{V_{wo}}{V_T} \dfrac{1 + \dfrac{H_{wo}}{K_a^{Sw}}}{1 + K_{wli}^{SD}\dfrac{V_{li}}{V_{wi}} + \dfrac{H_{wi}}{K_a^{Sw}}\left(K_{wli}^{SH}\dfrac{V_{li}}{V_{wi}} + 1\right)}}.$$

(139)

4.2.2. Model II – Effect of including a binding agent inside the vesicles

When applying the pH variation assay to fast-permeating solutes the informative part of the fluorescence change may largely fall within the dead time of the stopped-flow apparatus. Here we analyse the usefulness of including a binding agent inside the vesicles as a way to overcome this problem. The rationale for this approach is to delay the attainment of the equilibrium by increasing the amount of solute that permeates, which also decreases the stochastic effects.

For this analysis the simplest model was extended with the addition of a reversibly binding agent to the inner aqueous compartment. The latter was considered to be a protein that can interact with the weak acid and its conjugated base to the same extent (K_d^{PSH}, $K_d^{PSD} = 10^{-4}$ M). This study was performed with three different concentrations of entrapped protein ($P_{wi_T} = 0, 100$ and 600 µM), considering the set of parameters of the simulation C2 S1 P2 and vesicles with 100 nm radius. The inclusion of a protein also changes the buffer capacity inside the vesicles as its residues have exposed acidic or basic side chains, but this effect was not considered.

With the inclusion of a protein, the amount of solute that permeates slightly increases from 49 molecules *per* vesicle in the absence of the protein to 51 and 55 molecules for 100 and 600 µM protein, respectively. As expected, as more molecules permeate, the pH variation is larger, and the observed kinetics is slower (β_{S_i} decreases, **Table 17**). The larger pH variation also causes a greater deviation between the characteristic constant of solute accumulation and that for the concentration of the fluorescent deprotonated probe.

Table 17. Best-fit parameters of the time course of the concentration of solute (S_i), and the concentration of the fluorescent probe, considering the total volume ($PD_{wi}*$). Simulations were performed using the parameters defined in C2 S1 P2, considering lipidic vesicles with a radius equal to 100 nm and varying the concentration of the encapsulated protein. The relative deviation between the characteristic constant obtained by fitting $S_i[t]$ (β_{S_i}) and the lowest characteristic constant (β_1) obtained when fitting $PD_{wi}*[t]$ is also indicated.

Simulation		S_i		$PD_{wi}*$					%
P_{wi_T} (µM)	ΔpHi	y_∞ (10^{-5} M)	β_{S_i} (s⁻¹)	y_0 (10^{-8} M)	y_∞ (10^{-8} M)	β_1 (s⁻¹)	α_1	β_2 (s⁻¹)	**Deviation**
0	0.27	2.32	1.12	2.96	2.07	1.19	0.72	3.67	6
100	0.29	2.38	1.10	2.96	2.00	1.18	0.71	3.68	7
600	0.38	2.45	1.03	2.96	1.74	1.13	0.66	3.76	10

The dissociation constants considered for the interaction of the solute to the protein ($K_d^{PSH} = K_d^{PSD} = 10^{-4}$ M $\Rightarrow K_{eq} = 10^4$ M⁻¹) correspond to moderate affinity. Nonetheless, the effect of the entrapped protein on the equilibrium concentrations was surprisingly small. The reasons for the smaller increase are twofold: i) as indicated in section 4.2.1, the development of the pH gradient

prevents the equalisation of the solute concentrations at equilibrium, and the deviation is larger for higher values of ΔpHi; and ii) the presence of the protein only influences the solute concentration in the inner aqueous compartment, not the solute associated with the inner membrane leaflet. In fact, the concentration of solute in the inner aqueous compartment has increased 2 and 7-fold for P_{wi_T} equal to 100 and 600 µM, respectively. Therefore, the smallness of the effect of the inclusion of the protein inside the vesicles was mainly due to the sequestration of the solute in the membrane. For higher concentrations of the binding protein or higher relative affinities of the solute for this protein, a larger effect would be expected. However, concentrated protein solutions tend to be very viscous limiting the concentration that could be used experimentally. The parameters considered in those simulations are representative of the experimental conditions and the properties of drug-like molecules (moderate affinities for both the lipid membranes, $K_{wli}^{SH} = 10^3$ and $K_{wli}^{SD} = 10^2$, and for the protein, $K_{eq} = 10^4$ M^{-1}), which shows that this approach is not promising.

4.2.3. Model III – pH equilibration

A more realistic model of the pH variation assay must account for the equilibration of the pH between the inner and outer aqueous compartments. This equilibration can be achieved by the permeation of the conjugated base into the inner compartments or by the efflux of the extra protons in the inner aqueous compartment, which is indistinguishable from the influx of OH$^-$. Both situations were implemented in Model III, and simulations were performed to analyse the effects of some parameters on the kinetics observed for the solute permeation and pH equilibration.

4.2.3.1. Model IIIa – Permeation of the conjugated base

Model IIIa is an updated version of Model I with minor modifications (for more details see Section 3.2.4.1). In this model, the conjugated base is also allowed to translocate between the two membrane leaflets. The flip-flop process of charged compounds can be very slow due to the thermodynamic constraints of moving charged groups across the hydrophobic bilayer centre. However, the molecular structure of charged drug-like compounds can mask the charge, or the compounds may form more lipophilic complexes with other agents (ion-pair complexes). These phenomena increase the affinity of the charged compounds to the membrane and may raise flip-flop rates to the range observed for neutral molecules, thus increasing their bioavailability.[61,120] This justifies analysing the effect of the translocation of the conjugated base. Thus, the effect of two parameters that characterise solute properties will be analysed: i) the rate of the flip-flop of the conjugated weak base (k_{loi}^{SD} and k_{lio}^{SD}) and ii) the acidity constant of the solute.

4.2.3.1.1. Effect of the flip-flop rate

Numerical integration was performed considering k_{loi}^{SD} equal to 0.1, 0.03 and 0.01 s⁻¹, all other solute parameters as in C2 S1 P2 simulations, and vesicles with a 100 nm radius. The addition of the translocation of the charged solute resulted in equal concentrations of all the equivalent species at equilibrium (**Figure 32**), in contrast to in the previous models (**Figure 21**). The variation of the concentration of the charged species (SD_{wi} and SD_{li}) has clearly a biphasic behaviour, resulting from the quick influx of the weak acid that dissociates when it arrives at the inner compartments, and the much slower influx of the charged conjugated base. Even where the rates of translocation of the neutral and charged species were equal, the net flux of the conjugated base was lower, and the time course of the deprotonated species and the inner pH showed the same profile (not shown). This is a consequence of the higher membrane affinity of the neutral species, leading to a higher concentration of this species in the outer membrane leaflet relative to that of the conjugated base.
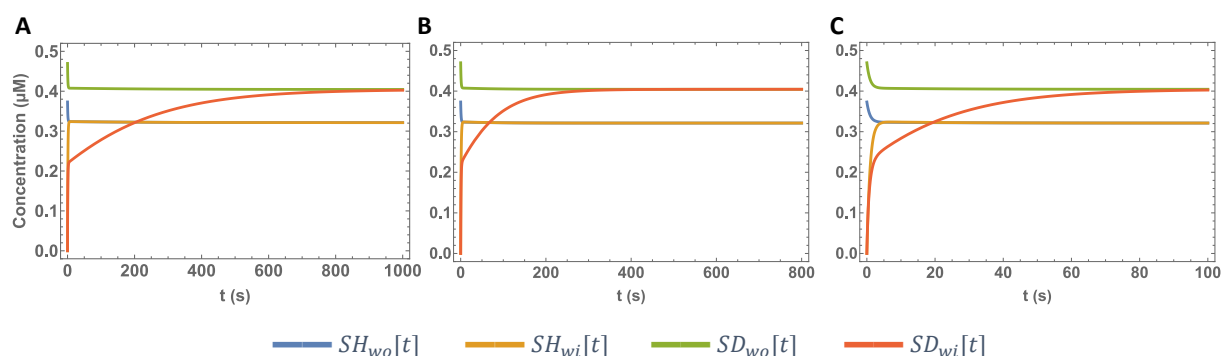
Figure 32. Temporal evolution of the solute concentration in the aqueous compartments varying the rates k_{loi}^{SD} and k_{lio}^{SD}: **A)** $k_{loi}^{SD} = 0.01$ s⁻¹, **B)** $k_{loi}^{SD} = 0.03$ s⁻¹ and **C)** $k_{loi}^{SD} = 0.1$ s⁻¹. Simulation conditions: C2 S1 P2, and $r = 100$ nm.

The biphasic evolution of the concentration of the charged species is not so evident in the profile of the total solute concentration inside the vesicles (S_i) (**Figure 33A**). At the conditions considered in those simulations, 90 % of the solute equilibrates during the fast permeation step, and only 10 % during the slow accumulation phase. The concentrations of the weak acid, conjugated base, and proton are intrinsically correlated according to acidity constants. Thus, by equalling the concentration of the conjugated base inside and outside the vesicles, the inner pH is restored (**Figure 33B**). The speed of the net flux of the charged solute sets the minimum pH attained and the speed of its recovery. The slower the translocation of the charged solute, the greater the separation between the two permeation regimes.
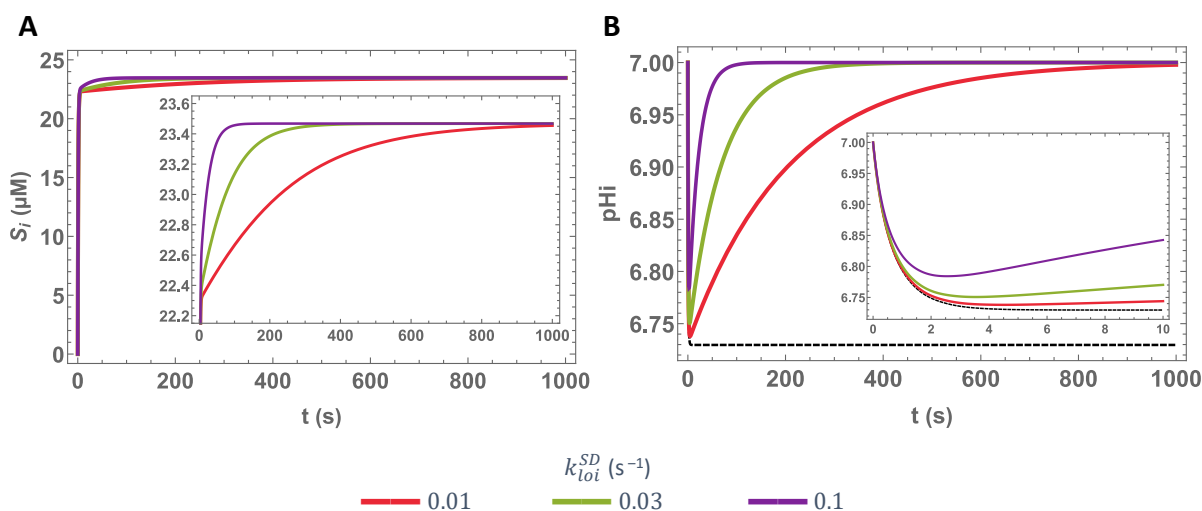
Figure 33. Effect of the rate of translocation: **A)** Total solute concentration in the inner compartments. The inset shows the slower phase of the variation of S_i. **B)** pH of the inner compartment. The dashed line is the inner pH time course when the permeation of the conjugated base is negligible, and the inset shows the pH variation profile in a short time scale. Simulation conditions: C2 S1 P2, and $r = 100$ nm.

4.2.3.1.2. Effect of the acidity constant of the weak acid

This section intends to increase the knowledge of the effect of the charged species on the overall permeation kinetics. This will give an overview of the applicability of the pH variation assay to assess the permeability of different weak acids. pK_a^{Sw} was varied between 4 and 7, while maintaining the translocation rate constant of $0.1\ s^{-1}$ for the conjugated base. The acidity constant determines the degree of dissociation of the weak acids. At the initial pH the concentration ratios of the charged amphiphile to the protonated forms in water are 1000, 100, 10 and 1, for pK_a^{Sw} 4, 5, 6 and 7, respectively. The corresponding ratios for the membrane-associated solute are 10-fold lower because the membrane affinity of the neutral species is considered to be 10-fold that of the charged species. Figure 34 shows the time evolution of the concentration of neutral species (blue), of the charged species (orange), and the sum of both (black). The concentrations were normalised by the value attained at equilibrium to facilitate the analysis of their time evolution. In Figure 34A, the weak acid has a pK_a of 4 when in the aqueous media, 5 when associated with the lipid membrane. Thus, at the initial pH of 7, most of the solute is deprotonated, both in the aqueous media and in the membrane. As a consequence, the fraction of protonated solute that permeates is negligible, and the time evolution of the total solute in the inner compartments follows the curve observed for the deprotonated species. On the other hand, when the pK_a of the solute in the aqueous media is 7 (**Figure 34D**), the concentration of the protonated and deprotonated species in the aqueous medium at the beginning of the simulation is equal, but in the membrane there is a 10-fold excess of the neutral protonated species. Because the flip-flop rate for this species is faster than for the charged one, the solute equilibrates mostly due to the permeation of the neutral species and the time evolution of the

total solute in the inner compartments is very close to that of the neutral species. The two simulation conditions shown in plots B and C correspond to intermediate situations ($pK_a^{Sw} = 5$ and 6). Plot C shows a condition where both the permeation of the protonated and deprotonated species contributes significantly to the overall solute permeation.

The results show some known deviations from the pH-partition hypothesis (Section 1.5.1). Depending on the compounds or the experimental conditions, the overall permeation kinetics may become controlled by the transport of the charged solute. This occurs when the relative abundance of this species in the medium overcompensates for its smaller rate of transport through the membrane (see black and orange curves, **Figure 34A**, **B**).
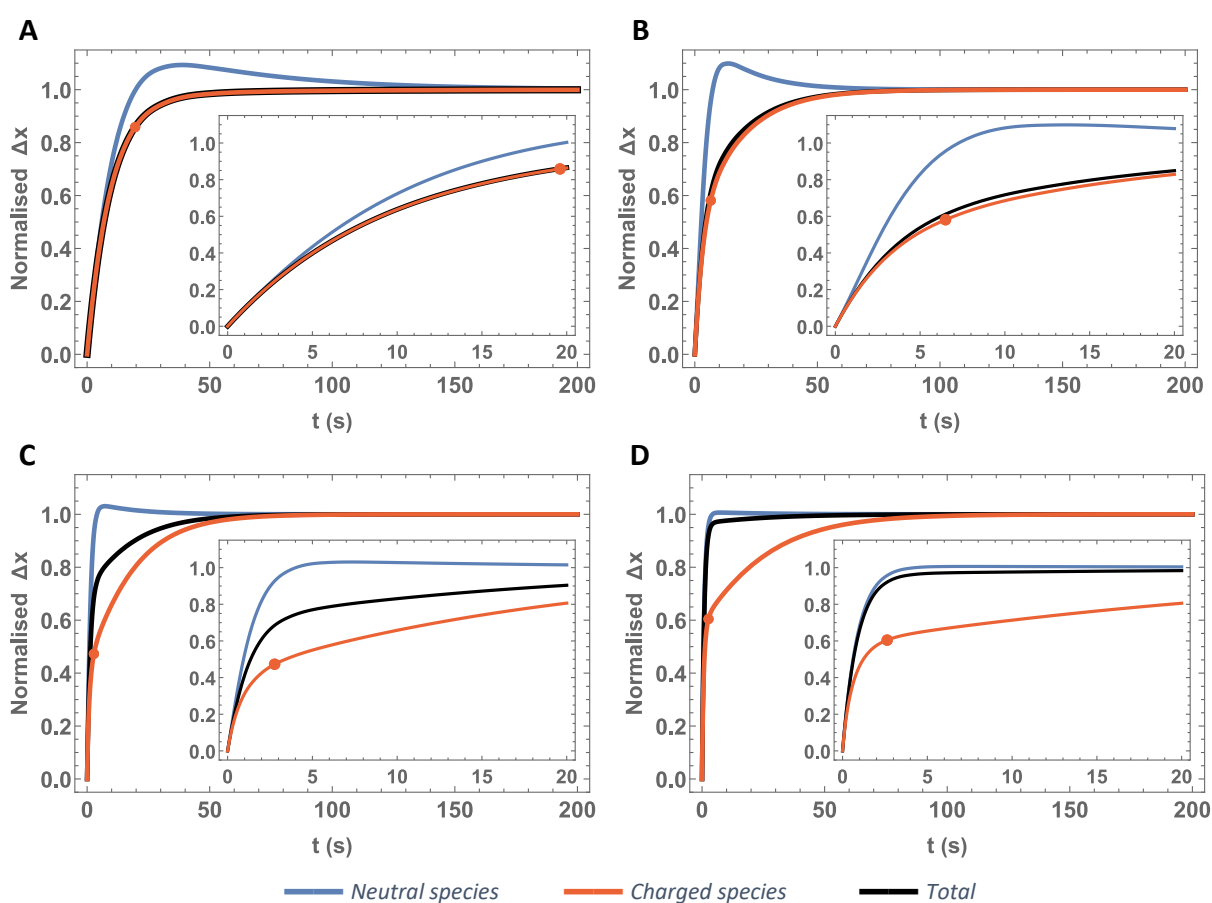
Figure 34. Normalised concentrations of neutral (SH_{li} and SH_{wi}), charged (SD_{li} and SD_{wi}), and total solute in the inner compartments (S_i), for the permeation of a weak acid with pK_a^{Sw} equal to **A)** 4, **B)** 5, **C)** 6 and **D)** 7. The inset graphs show the first 20 seconds and the orange dots in the fraction of the charged species indicate the point at which the pH minimum is observed. Simulation conditions: C2 S1 P2, $r = 100$ nm, and $k_{loi}^{SD} = 0.1$ s^{-1}.

The overshoot of the concentration of the neutral species in the inner compartments (**Figure 34**) is due to the decrease in the pH inside the vesicles, and equilibration between the acid and conjugated base forms of the solute.

The solute acidity has a great influence on the kinetics of permeation as well as in the pH variation. To analyse the latter effect more easily, a brief discussion will be made considering again that the conjugated base is not allowed to permeate − $k_{loi}^{SD} = 0$ s⁻¹ (**Figure 35**). In the conditions considered, solutes with low pK_a^{Sw} are predominantly ionised. Due to the low fraction of the acidic form, the permeation is slow, and the pH decreases slowly (red curve). When the weak acid reaches the inner compartments, it immediately ionises, and the pH significantly decreases. As the pK_a^{Sw} increases, the fraction of the weak acid also increases, the permeation acelerates, and the pH variations decrease due to a low degree of dissociation (purple curve).
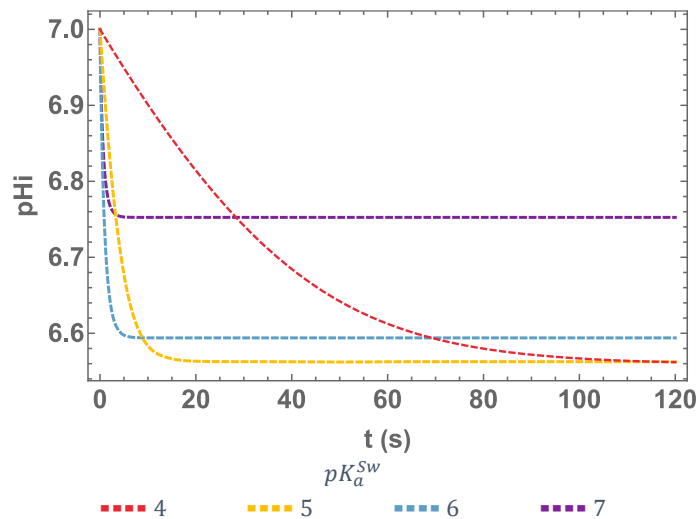
Figure 35. pH dynamics for the permeation of solutes with pK_a^{Sw} between 7 and 4, considering only the permeation of the weak acid as in Model I. Simulation conditions: C2 S1 P2, $r = 100$ nm, and $k_{loi}^{SD} = 0$ s⁻¹.

The decrease in the internal pH is solely due to the permeation and subsequent dissociation of the weak acid. But the permeation of the conjugated base considerably changes the pH time course (**Figure 36A**, compare solid lines with the dashed ones). The large contribution of the conjugated base to the permeation of the solute with lower pK_a^{Sw}, substantially decreases the pH variation. That contribution decreases as the pK_a^{Sw} increases from 4 to 6, leading to a higher transient decrease of pH of the inner aqueous compartment.

The difference between the minimum pH attained when the permeation of the conjugated base is or is not considered tends to decrease as the pK_a^{Sw} increases . Due to the faster permeation of the acid form, a higher concentration of this species leads to a faster decrease in the inner pH value. Therefore, the maximum pH variation is observed at earlier times as the pK_a^{Sw} increases.

The variation in the maximal ΔpHi and the time at which it occurs is represented in Figure 36B for a wider range of solute acidity constants. For pK_a^{Sw} above 6, the maximal ΔpHi decreases and the time at which it occurs increases. This behaviour is not in agreement with the interpretation provided above

for pK_a^{Sw} values between 4 and 6, which was based on the increase in the relative abundance of the protonated form and on its faster permeation. Instead, the decrease in ΔpHi for $pK_a^{Sw} > 6$ is related with the ionisation of the acidic form after permeation into the inner compartments. For pK_a^{Sw} values much lower than the solution pH, solute ionisation is essentially complete and strongly decreases the pH of the inner aqueous compartment. However, as the pK_a^{Sw} approaches the solution pH, the fraction of solute molecules that remain in the acidic form becomes significant. In the extreme, when $pK_a^{Sw} \gg$ pH, all solute is in the acidic form, the extent of the deprotonation reaction is negligible and the permeation of the weak acid does not change the pH of the inner aqueous compartment.

Figure 36 also shows a small increase in the time at which the maximum ΔpHi occurs for $pK_a^{Sw} > 6.5$, in contrast with the behaviour observed for lower values of pK_a^{Sw}. The time at which this minimum occurs is the result of both the rate of ΔpH generation and the rate at which ΔpH dissipates. The variation in t_{min} for $pK_a^{Sw} \leq 6$ was previoulsy interpreted in light of the rate of ΔpHi generation (the higher pK_a^{Sw}, the greater the concentration of the faster permeating protonated species). Instead, for $pK_a^{Sw} > 6.5$ the increase in t_{min} is due to the slower dissipation of the ΔpH as a consequence of the rarity of the charged deprotonated species in the membrane, and to the decrease in ΔpHi, the driving force for the permeation of the conjugated base.
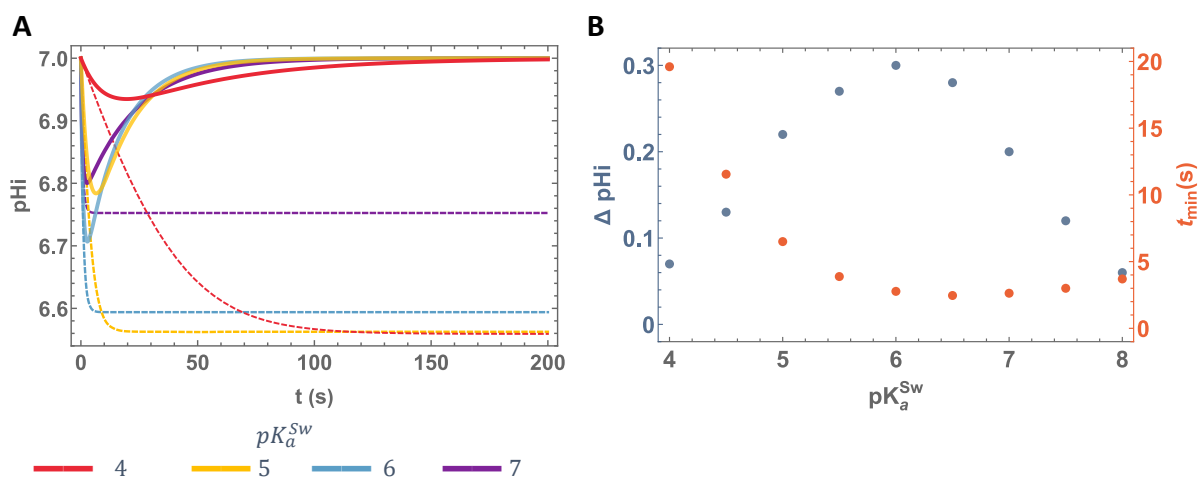
Figure 36. Effect of the solute acidity constant in the pH profile associated with the permeation of a weak acid. **A)** pH dynamics for the permeation of solutes with pK_a^{Sw} 7 to 4. The dashed lines are the pH dynamics in the simulations where only the uncharged weak acid is allowed to permeate. The solid lines represent a situation where both the weak acid and the conjugated base are allowed to permeate. **B)** Maximum pH variation and time at which it is attained. Simulation conditions: C2 S1 P2, $r = 100$ nm, and $k_{loi}^{SD} = 0.1$ s^{-1}.

To help quantify the relative contributions of the neutral and charged species to the overall permeation, Figure 37 shows the fraction of charged species in the internal compartments for the simulations where the conjugated base is (orange dots) or is not (blue dots) allowed to permeate at the moment where the pH attains its minimum in the simulations where both species are allowed to

permeate. The fraction of the charged species that has already permeated (direct or indirectly) has a parabolic behavior with respect to pK_a^{Sw}, with a minimum at $pK_a^{Sw} = 6$. The kinetics of permeation of weak acids with a pK_a^{Sw} of 4 is higly dominated by the direct permeation of the conjugated base, which compensates for the pH variation imposed by the permeation of the weak acid. Consequently, in these circumstances, at the time of the minimum pH, the fraction of conjugated base is maximal and considerably higher than that obtained when the conjugated base does not permeate. Solutes with pK_a^{Sw} of 8 almost do not dissociate in the inner compartments. Since at equilibrium the concentration of the conjugated base is very low, it is not surprising that at the moment of the minimum pH the fraction of the charged solute species is very high.
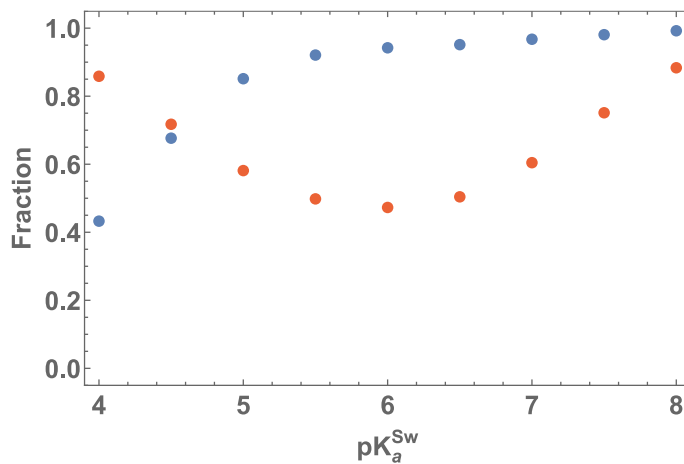
Figure 37. Fraction of charged species in the internal compartments at the time where pH reaches its minimum when the conjugated base is (●) or is not allowed to permeate (●).

Figure 38 shows a schematic summary of the main observations and conclusions about the effect of the acidity constant on the permeation of weak acids.
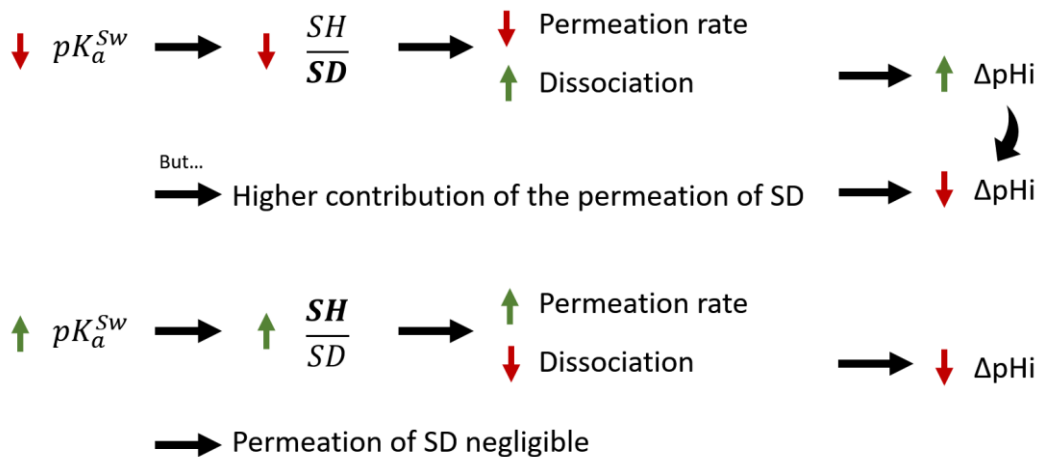
Figure 38. Summary scheme of the effect of the acidity constant on the permeation kinetics of weak acids.

4.2.3.2. Model IIIb – Permeation of the proton

In Model IIIa, the pH gradient generated by the permeation of the neutral acid form was allowed to dissipate due to the permeation of the charged conjugate base. However, the efflux of the proton or influx of the hydroxide ion may also dissipate the pH gradient. Because it is not possible to distinguish between the contributions of proton or hydroxide permeation,[108] pH dissipation will be treated here as being solely due to the permeation of the proton.[108,121] As very distinct values for the proton permeability have been reported in the literature (from 10^{-10} to 10^{-5} dm s^{-1})[122], this section will address the effect of this parameter in the overall solute equilibration kinetics. For the following simulations, κ_H equals 10^{-7}, 10^{-6} or 10^{-5} dm s^{-1}, all the other parameters were set as in C2 S1 P2 simulations, and the lipidic vesicles have 100 nm radius.

Figure 39 shows that proton permeation substantially influences the dynamics of the pH in the inner aqueous compartment. As κ_H increases, the maximum ΔpHi attained due to the permeation of the weak acid decreases, and the dissipation of ΔpHi occurs faster. The maximum ΔpHi observed and the time at which this maximum occurs is determined by the competition between two processes: i) the permeation of the neutral weak acid releasing protons in the inner compartment, and ii) the permeation of the proton leading to the dissipation of ΔpHi. It should be noted that the rate of dissipation of the pH gradient depends not only on the proton permeability coefficient but also on ΔpHi. Thus, the generation of a larger pH gradient between the outer and inner compartments may partially compensate for the rate of dissipation of the pH gradient for lower proton permeability coefficients. Nevertheless, it is evident from Figure 39 that the dissipation rate of the pH gradient is larger for higher κ_H.
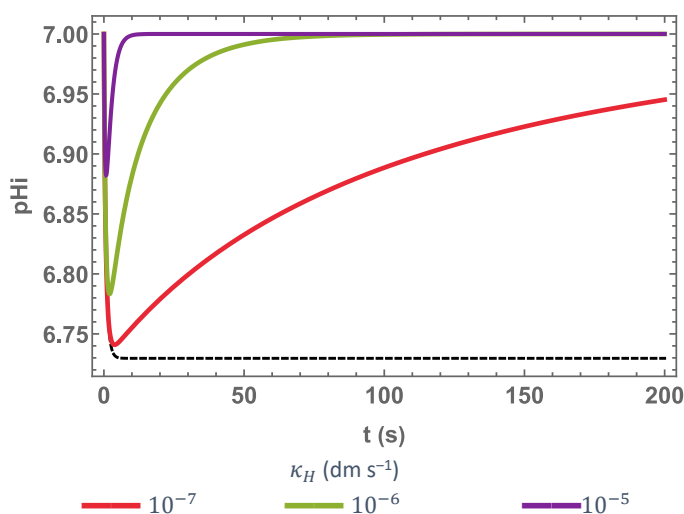
Figure 39. Effect of proton permeability on the dynamics of the pH in the inner compartment. The dashed line is the pH time course in the absence of the permeation of the proton. Simulation conditions: C2 S1 P2, and $r = 100$ nm.

4.2.3.3. <u>Comparison between Model IIIa and Model IIIb</u>

The permeation of the conjugated base and that of the proton have the same effect only with different kinetics. The conjugated base that permeates the membrane into the inner compartments equilibrates with the acid form capturing protons from the aqueous medium. In turn, the efflux of the proton raises the pH of the inner aqueous compartment, which shifts the equilibrium towards the conjugate base. The decrease in the concentration of the acid form is then compensated by the influx of additional solute in this form. In both cases, while the inner pH equilibrates with the external pH after an initial quick undershoot, the concentration gradients of the deprotonated species and the proton vanish (**Figure 40** and **Figure 43**). The permeation of the conjugated base or the proton makes the variation of the concentration of solute in the internal compartments (S_i) biphasic (**Figure 40**, dashed lines) because of the indirect permeation of the neutral and charged species, occurring at two distinct time scales. In a real experiment, both the conjugated base and the proton permeate, and the quicker-permeating of these substances will dominate the kinetics of the slow phase. This is because proton and base concentrations are intrinsically connected by the quick acid-base equilibrium.
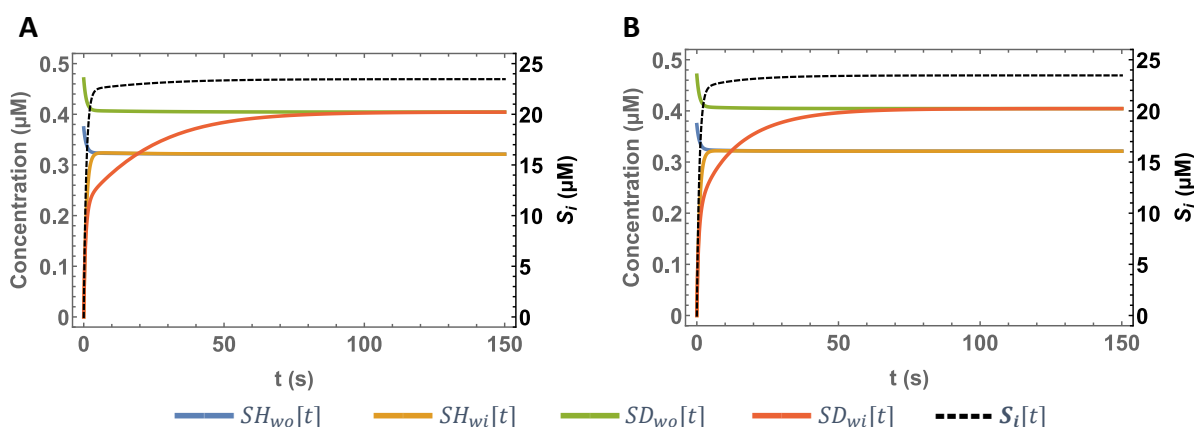
Figure 40. Temporal evolution of the concentration of solute species in the aqueous compartments, considering **A)** the permeation of the conjugated base ($k_{loi}^{SD} = 0.1$ s⁻¹) or **B)** of the proton ($\kappa_H = 10^{-6}$ dm s⁻¹). Simulation conditions: C2 S1 P2, and $r = 100$ nm.

In the pH variation assay, the permeation of the solutes is followed through the variation of the inner pH measured by the fluorescence of an entrapped probe. For the permeation of a weak acid, the dynamics of PD_{wi} translates into an initial decrease of fluorescence intensity due to the pH decrease in the inner aqueous compartment, followed by the slow recovery due to the permeation of the charged species (**Figure 41**). Solute permeation does not stop when the fluorescence intensity ceases to decrease, at the maximal ΔpHi. But most of the solute has already permeated by this time, for the conditions considered: the solute concentrations in the inner compartments are less than 10 % away from those in the corresponding outer compartments (**Figure 41**). This is because with the $pK_a^{Sl} = 7.9$ attributed to the weak acid most of the solute in the membrane is protonated.
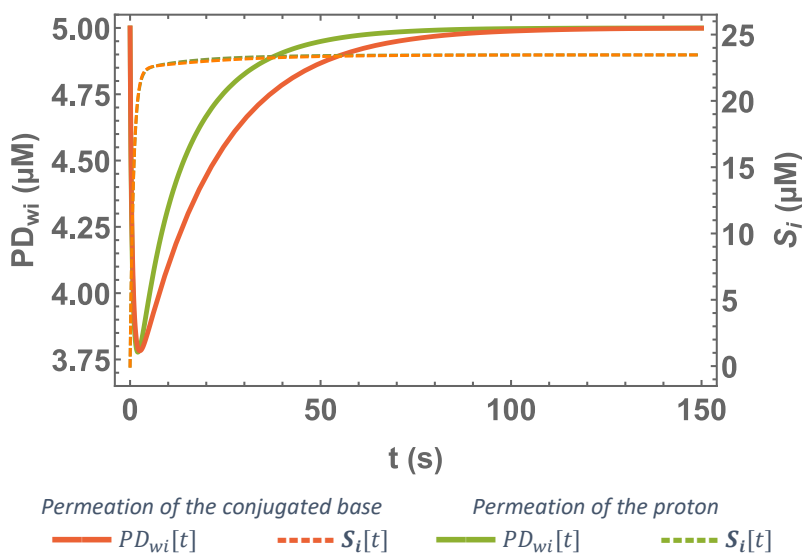
Figure 41. Evolution of the concentration of probe (PD_{wi}) (filled curves) and the solute (S_i) (dashed curves) for the simulations of Model IIIa (orange curves) and Model IIIb (green curves).

As discussed in Section 4.2.3.1.2, a lower pK_a^{Sw} would lead to a larger contribution of the slow phase to the overall solute permeation. Figure 42 shows the variation of the concentrations of probe and solute in the inner compartments upon permeation of a weak acid with $pK_a^{Sw} = 6$. In this case, a significant fraction of the solute permeates during the fluorescence restoration, and this phase will thus give relevant information about the permeation of the conjugated base.
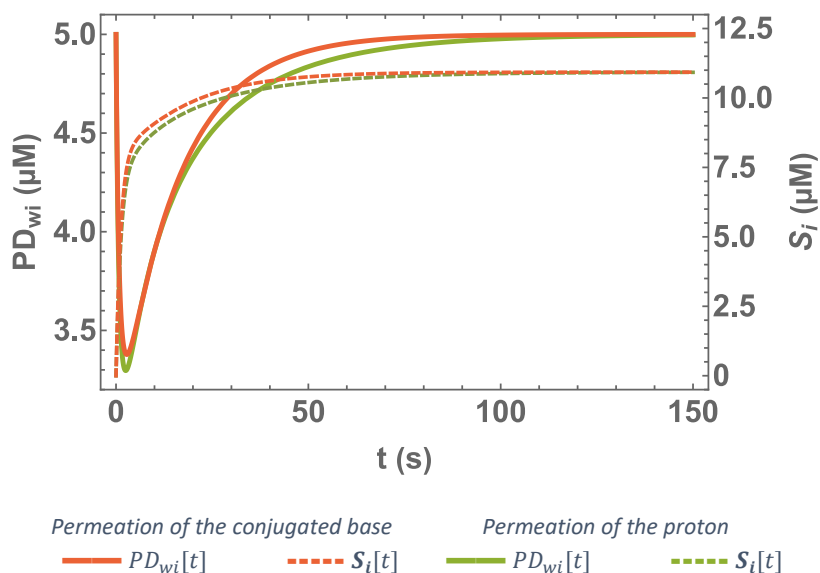
Figure 42. Evolution of the concentration of probe (PD_{wi}) (filled curves) and the solute (S_i) (dashed curves) for the simulations of Model IIIa (orange curves) and Model IIIb (green curves) similar to the ones used in Figure 40, but changing the value of pK_a^{Sw} to 6.

4.2.4. Model IV – Dissipation of the transmembrane potential

The dissipation of the pH gradient (**Figure 43**) requires the transport of charged species (conjugated base influx or proton efflux) across the membrane, creating an excess of negative charges – and thus a negative electric potential – in the internal compartments (**Figure 44**). When considering the permeation of a weak acid with a pK_a^{Sw} of 6, the contribution of the conjugated base to the overall kinetics is significantly increased. Since more molecules of conjugated base are permeating, there is a greater accumulation of negative charges inside the vesicles, leading to a high transmembrane potential (**Figure 44**, dashed curves).
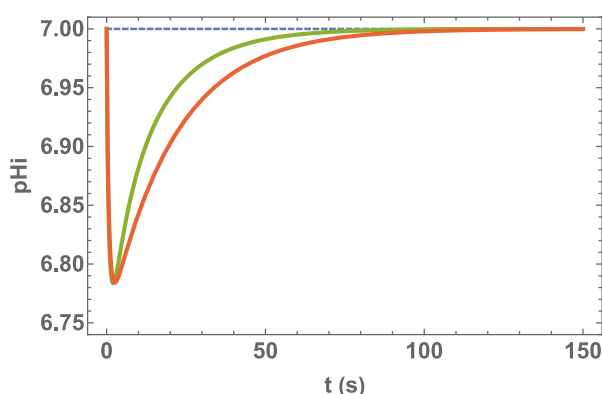
Figure 43. pH evolution when the permeation of the conjugated base ($k_{loi}^{SD} = 0.1$ s⁻¹, ——) or the permeation of the proton ($\kappa_H = 10^{-6}$ dm s⁻¹, ——) are considered. Simulation conditions: C2 S1 P2, and $r = 100$ nm.
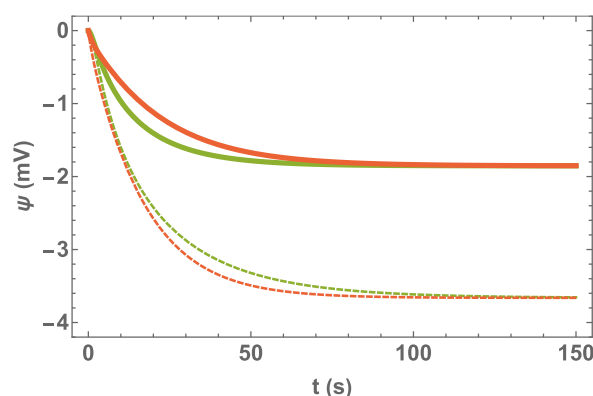
Figure 44. Generated transmembrane potential when the permeation of the conjugated base ($k_{loi}^{SD} = 0.1$ s⁻¹, ——) or the permeation of the proton ($\kappa_H = 10^{-6}$ dm s⁻¹, ——) are considered. Simulation conditions: C2 S1 P2, and $r = 100$ nm. The dashed curves are the transmembrane potential in the same conditions, but when the pK_a^{Sw} is 6.

The dissipation of the electrostatic potential must be done by a very abundant ion, so that it can be achieved through the transport of only a small fraction of the total amount of ions. The salts that are dissolved in the aqueous media to define the ionic strength fulfil this goal, being usually Na⁺, K⁺, and Cl⁻. This section will analyse the influence of the transport of these salts in the pH variation assay using Model IV. In this model, it is assumed that K⁺ is the ion responsible for the dissipation of the electrostatic potential. This ion was selected because its permeability can be modulated by the ionophore valinomycin.

As the permeability of the proton is very uncertain, this section will only consider the permeation of the conjugated base ($k_{loi}^{SD} = 0.1$ s⁻¹ and $\kappa_H = 0$ dm s⁻¹).[122] As done throughout this work, the remaining parameters were defined as in C2 S1 P2 simulations, except pK_a^{Sw} that was considered equal to 6. Here pK_a^{Sw} was changed because this corresponds to a condition in which the conjugated base has a larger contribution for the overall permeation and the developed transmembrane potential is larger.

This section will explore the effects of the ionophore valinomycin on the permeation kinetics of weak acids. Valinomycin presents a high selectivity to potassium and transports these ions down an electrochemical potential gradient. Its effect was simulated changing the permeability coefficient of the potassium ion (κ_K) between 10^{-12} and 10^{-10} dm s^{-1}. The effect on the kinetics of permeation is almost negligible (**Figure 45**) because valinomycin does not directly facilitate the transport of the solute.
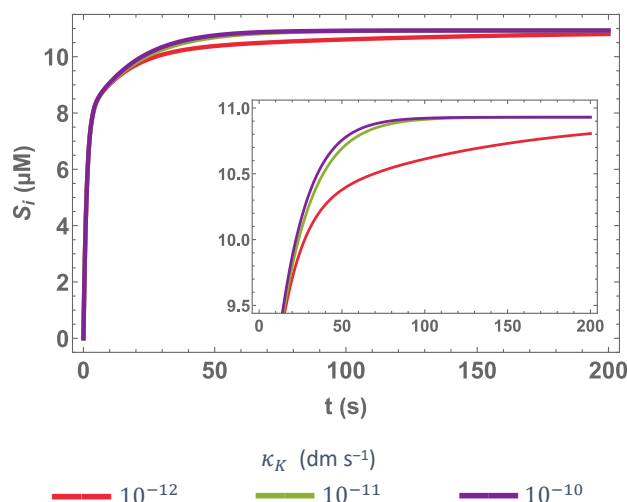
Figure 45. Effect of potassium permeability on the kinetics of solute accumulation. Simulation conditions: C2 S1 P2, $r = 100$ nm, $pK_a^{Sw} = 6$, $k_{loi}^{SD} = 0.1$ s^{-1} and $\kappa_H = 0$ dm s^{-1}.

Additionally, under these conditions, increasing κ_K does not influence the kinetics of the pH decrease nor the minimum pH, but it accelerates the dissipation of the pH gradient (**Figure 46A**). The higher the permeability of potassium, the closer the pH recovery phase becomes monophasic. Additionally, increasing κ_K has a stronger influence on the time course of the transmembrane potential (**Figure 46B**). As the pH in the inner aqueous compartment decreases, the proton concentration gradient also makes the conjugated base to inflow. Generally, the conjugated base and the proton permeate much faster than the potassium ion, and thus a transient negative potential is generated. The higher the permeability of potassium, the lower the developed transmembrane potential and the faster the compensation of the potential difference. Regardless of the potassium permeability, the negative potential is generated with the same kinetics. The minimum potential is not attained simultaneously with the minimum pH, because the negative potential inside the vesicles is generated by the permeation of the conjugated base occurring mostly during the pH recovery.
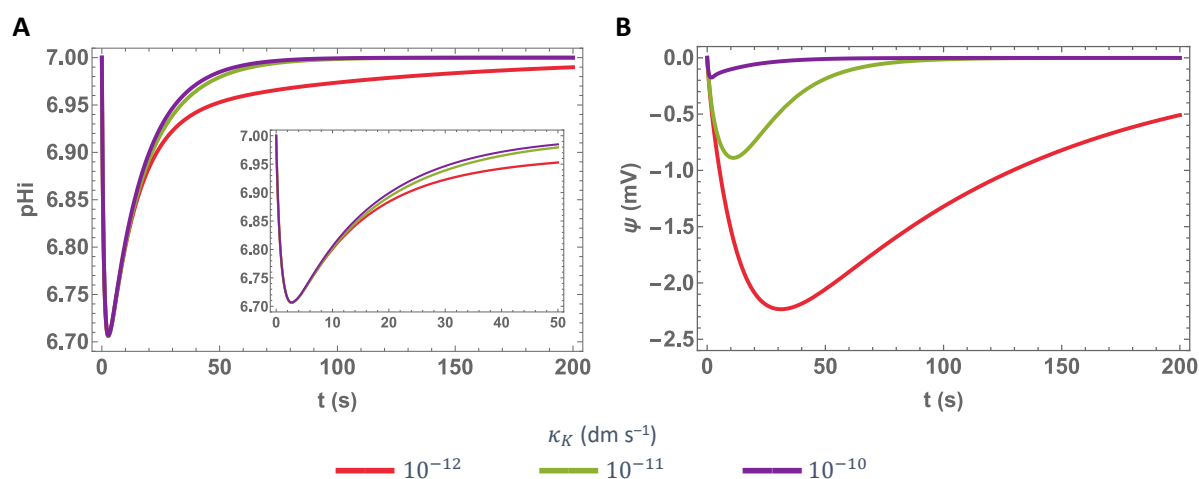
Figure 46. Effect of the potassium permeability coefficient. **A)** pH variation profile with the descending phase being the result of the faster permeation of the solute and followed by a slow ascending phase due to the permeation of the conjugated base and potassium ions. **B)** Evolution of the transmembrane potential. Simulation conditions: C2 S1 P2, $r = 100$ nm, $pK_a^{Sw} = 6$, $k_{loi}^{SD} = 0.1$ s^{-1}, and $\kappa_H = 0$ dm s^{-1}.

In summary, the negative transmembrane potential that develops as the pH gradient dissipates will both limit the influx of the anionic conjugated base and the efflux of the proton. By facilitating the transport of potassium ions down that electrochemical potential, valinomycin attenuates it, thereby facilitating the flux of both conjugated base and protons and accelerating the equilibration of both species across the membrane.

4.2.5. Analysis of the parameter estimation problem using the full model for permeation of a weak acid

Having completed the development, assessment, and analysis of the realistic model (Model IV) we are now in a position to use it for a critical analysis of key issues involved in the estimation of permeability using the pH variation assay. This section will start by analysing how to obtain the permeability of a weak acid from bi-exponential kinetics profiles. In the pH variation assay, the dynamics of the deprotonated fluorescent probe is used to follow the kinetics of solute permeation and estimate the permeability coefficient. In this context, it is important to identify which characteristic constant of the fluorescence profile best describes the permeation kinetics, how it correlates with the intrinsic permeability, and if the fluorescence recovery can give any information about solute permeation. To have a big picture of the permeation of distinct weak acids, it will be reanalysed the influence of the acidity constant on the permeation kinetics, which the study using a simpler model (Section 4.2.3.1.2) highlighted as important.

In the simulations below, potassium permeability coefficient (κ_K) will be kept as 10^{-10} dm s^{-1}.

4.2.5.1. Relationship of bi-exponential kinetic profiles to the apparent permeability

Experimental time courses are often multi-exponential, and questions arise about the meaning of the characteristic constants and their pre-exponential factors, and how these parameters correlate with the physical or chemical properties of interest. As observed in the simulations considering both the permeation of weak acid and the conjugated base or of the proton (Sections 4.2.3.1 and 4.2.3.2), as well as in simulations with the complete description of the pH variation assay, the kinetics of solute accumulation is biphasic. In such a complex system, as is the one we are working with, the kinetics is not bi-exponential, but this function represents relatively well the experimental data. Thus, it is important to understand how the bi-exponential kinetic profiles of solute accumulation relate to the apparent permeability.

Starting with the bi-exponential function that can describe the accumulation of a weak acid within the vesicles, when there is no solute inside at $t = 0$,

$$S_i[t] = S_{i_\infty}\left(1 - \alpha_1\, e^{-\beta_1\, t} - \alpha_2\, e^{-\beta_2\, t}\right), \tag{140}$$

the rate of solute accumulation for a given instant is described by

$$\frac{d\, S_i[t]}{dt} = S_{i_\infty}\left(\alpha_1\, \beta_1\, e^{-\beta_1\, t} + \alpha_2\, \beta_2\, e^{-\beta_2\, t}\right), \tag{141}$$

with $\alpha_2 = 1 - \alpha_1$.

To obtain the apparent permeability is necessary to know the rate of solute accumulation (in mol *per* second) at $t = 0$, as defined explained in Section 4.2.1.7.2. For bi-exponential kinetics, the apparent permeability is obtained from a weighted average of the characteristic constant, through equation (142):

$$P_{app} = \frac{S_{i_\infty}\, V_{wi}\, (\alpha_1\, \beta_1 + \alpha_2\, \beta_2)}{A\, S_{o_0}}, \alpha_1\, \beta_1 + \alpha_2\, \beta_2 = \bar{\beta}. \tag{142}$$

4.2.5.1.1. Effect of the acidity constant of the weak acid

The time course of solute accumulation for the permeation of weak acids with different acidity constants (**Figure 47**) was fitted using a bi-exponential function, equation (140), and the parameters are shown in Table 18. The results show that when the initial pH is 7, the extent of permeation (S_{i_∞}) increases with pK_a^{Sw} (**Figure 47A**). This was already discussed in Section 4.2.3.1.2 and happens because the higher the pK_a^{Sw}, the higher the fraction of the weak acid in solution and the higher the solute concentration in the membrane. Moreover, the faster characteristic constant (β_2) and the respective weighting coefficient (α_2) both increase as the acidity constant decreases from 10^{-5} to 10^{-7} M, also because of the higher fraction of the protonated weak acid. In turn, the slowest characteristic constant (β_1), and most markedly its relative weight, increases from pK_a^{Sw} 4 to 5.5 and decreases from pK_a^{Sw} 5.5 to 7.
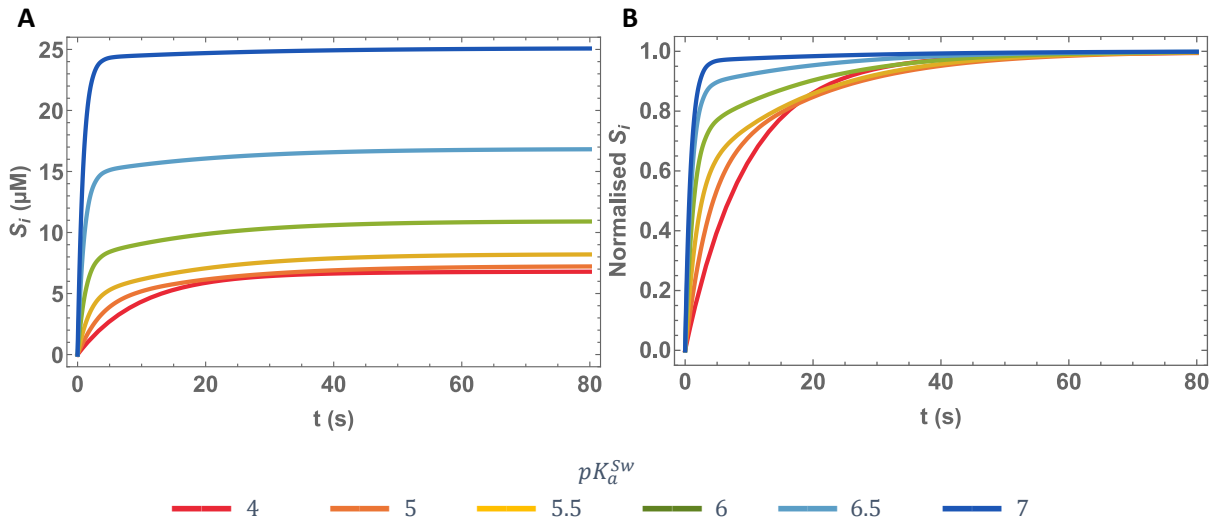
Figure 47. A) Variation of the solute concentration inside the vesicles for the permeation of weak acids with distinct acidity constants. **B)** Normalisation of the data shown in plot A. Simulation conditions: C2 S1 P2, $r = 100$ nm, $pK_a^{Sw} = 6$, $k_{loi}^{SD} = 0.1$ s^{-1} and $\kappa_H = 0$ dm s^{-1}.

Table 18. Best-fit parameters from fitting equation (140) to the simulated time course of the solute, for the permeation of weak acids with different acidity constants. The values marked in blue describes the slowest permeating phase and the values in orange are assigned to the fastest phase. Simulations conditions: C2 S1 P2, $r = 100$ nm, $k_{loi}^{SD} = 0.1$ s^{-1}, $\kappa_H = 0$ dm s^{-1}, and $\kappa_K = 10^{-10}$ dm s^{-1}.

pK_a^{Sw}	ΔpHi	S_{i_∞} (M)	α_1	β_1 (s^{-1})	β_2 (s^{-1})	$\bar{\beta}$ (s^{-1})
7	0.20	2.51×10^{-5}	0.03	0.04	1.14	1.10
6.5	0.27	1.69×10^{-5}	0.13	0.05	1.00	0.87
6	0.29	1.09×10^{-5}	0.28	0.05	0.81	0.59
5.5	0.27	8.24×10^{-6}	0.42	0.05	0.53	0.33
5	0.22	7.26×10^{-6}	0.42	0.05	0.28	0.18
4.5	0.13	6.93×10^{-6}	0.20	0.04	0.14	0.12
4	0.07	6.83×10^{-6}	0.03	0.02	0.10	0.10

The permeation of weak acids with $pK_a^{Sw} \leq 4$ or ≥ 7 is well described by a mono-exponential function. For the initial pH value considered, a weak acid with $pK_a^{Sw} \leq 4$ will be mostly ionised, and the kinetics reflects only the permeation of the conjugated base. The characteristic constant thus tends asymptotically to 0.093 s^{-1}. For a weak acid with $pK_a^{Sw} \geq 7$ the ionisation degree decreases, and the weak acid behaves as a non-ionisable solute. The characteristic constant thus characterises the permeation of the uncharged form and approaches 1.30 s^{-1}. The values 0.093 and 1.30 s^{-1} are the ones predicted for the more abundant forms characterised by $K_{wlo}^{SD} = 10^2$ and $k_{loi}^{SD} = 0.1$ s^{-1} and by $K_{wlo}^{SH} = 10^3$ and $k_{loi}^{SH} = 1$ s^{-1}, respectively. Figure 48 shows the dependence of β_1 and β_2 (blue and orange dots, respectively) with pK_a^{Sw} and the weighted characteristic constant (orange dashed line). The value of the weighted characteristic constant approaches that of β_2 values as the biexponential behaviour decreases.
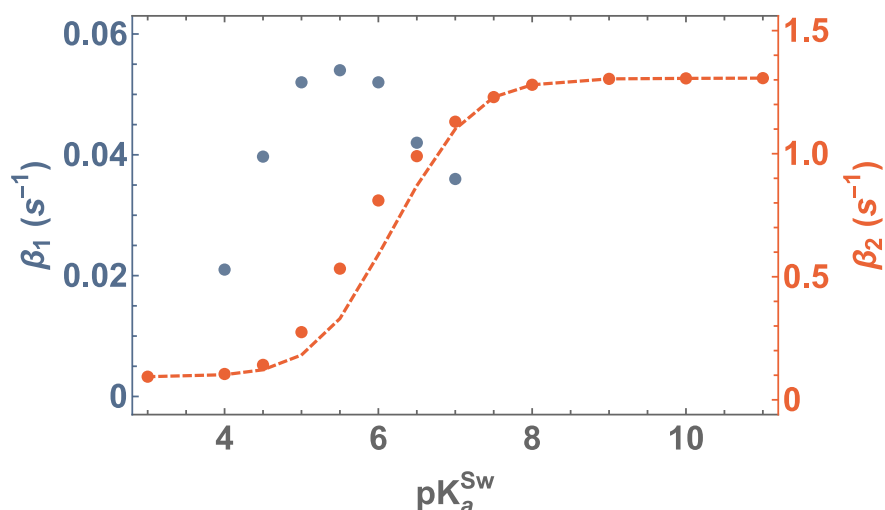
Figure 48. Dependence of the lowest (●) and the (●) highest characteristic constant. Note the different scales. The orange dashed line is the weighted characteristic constant ($\bar{\beta}$).

4.2.5.1.2. Estimation of the apparent permeability from the solute dynamics

Knowing the intrinsic permeability of the neutral and charged forms is useful to evaluate the permeability of ionisable compounds under any condition.

For mono-exponential kinetics, estimating the permeability coefficient is a trivial process. However, when the kinetics is more complicated it is not intuitive how can one obtain the permeability coefficient of the weak acid and the conjugated base. Should we use the highest characteristic constant to calculate the intrinsic permeability of the weak acid and the lowest one for the conjugated base permeability? The dependence of the characteristic constants as a function of the pK_a^{Sw} shows that under several conditions the permeation of the weak acid and the conjugated base are deeply connected by the intrinsic parameters of each species and does not show a simple dependence on the relative abundance of each one. To better distinguish the permeation of the weak acid and that of the conjugated base, we tried to simultaneously fit the data for the simulations shown in the previous section, by fixing β_1 and β_2. The fit quality is not good (data not shown), which shows that α_1 does not directly report the relative abundance of the protonated and deprotonated forms, and thus we cannot directly obtain the rate of the weak acid and base equilibration from the characterisation of a single experiment at a given pH. The overall observed kinetics depends on the kinetic parameters of both species, on their relative rates of membrane permeation and on their affinity for the membrane.

In general, the intrinsic permeability coefficient of weak acids (P_{acid}) at the molar fraction x_{acid} is obtained by neglecting the permeability of the charged conjugated base and attributing the permeation kinetics only to the former, according to equation (143). However, in some conditions the contribution of the conjugated base to the overall kinetics should not be neglected (Section 4.2.3.1.2).

Overlooking the permeation of the weak base can lead to overestimating the intrinsic permeability of the weak acid.

$$P_{app} = x_{acid}\, P_{acid} \;\rightarrow\; P_{acid} = \frac{P_{app}}{x_{acid}} = P_{app}\left(1 + 10^{pH - pK_a}\right) \tag{143}$$

As the system under study does not have an analytical solution, we cannot easily obtain the relationship between the intrinsic parameters and the characteristic constants. Thus, the estimates of the permeability of the weak acid can also be biased by the contribution of the conjugated base to the observed kinetics.

From the weighted characteristic constant and using equation (142) one can obtain the apparent permeability for all the considered weak acids. The apparent permeability is a weighted average of the intrinsic permeabilities of the weak acid (1.45×10^{-5} dm s^{-1}) and the conjugated base (1.93×10^{-7} dm s^{-1}). Figure 49 shows the apparent permeability obtained from equation (142) for a broad spectrum of weak acids (blue dots) and considering only the characteristic constant with the highest pre-exponential coefficient (red dots). The apparent permeability obtained considering the intrinsic permeabilities of the weak acid and the conjugated base and the relative abundance of each one is shown by the black dashed line. This intrinsic permeabilities were calculated using the asymptotic values for the characteristic constants, attributed to the permeation of the weak acid and its conjugated base. If only the characteristic constant with the highest pre-exponential coefficient is considered, the calculated apparent permeability (red dots) moves further away from the expected value, when the kinetics of solute accumulation is biphasic ($4.5 < pK_a^{Sw} < 6.5$).
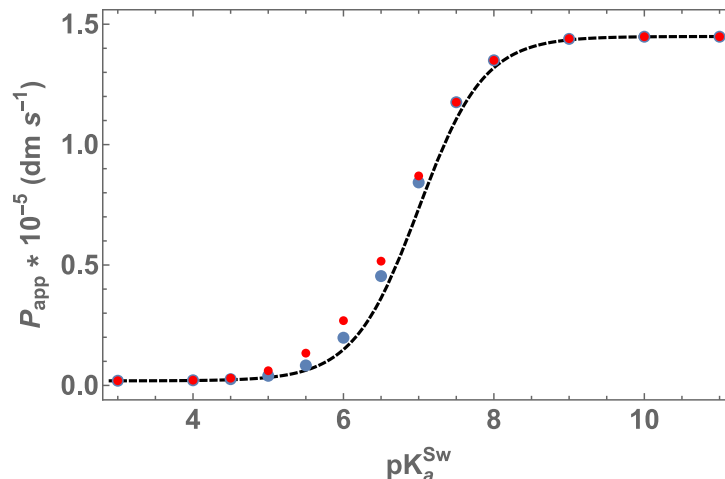
Figure 49. Apparent permeability obtained for weak acids with distinct acidity constants (K_a^{Sw}) calculated through equation (142) (●), equation (136) (●), and considering the intrinsic permeability of the weak acid and the conjugated base, 1.45×10^{-5} dm s^{-1} and 1.93×10^{-7} dm s^{-1}, respectively (-----).

Figure 49 shows some deviations between the apparent permeability calculated through equation (142) and through the intrinsic permeability of the acidic and basic forms (Section 1.5.1). These discrepancies are largest (14 – 33 %) for solutes with pK_a^{Sw} in the 5 – 7 range. The deviations are

smaller for weak acids with pK_a^{Sw} close to 4, because of the low pH variation resulting from the low amount of solute that permeates and of the higher contribution of the conjugated base to the permeation kinetics. They are also small for solutes with pK_a^{Sw} close to 8. For weak acids with $pK_a^{Sw} <$ 4 and > 8, the permeation kinetics results mostly from the permeation of one species, the conjugated base for solutes with $pK_a^{Sw} < 4$, and the acid for $pK_a^{Sw} > 8$. In the latter, it is also important the fact that the acid species has a low tendency to deprotonate when reaching the inner compartments, leading to a small pH variation. The maximum pH variation is observed for pK_a^{Sw} somewhat smaller and closer to pHi[0], due to the higher contribution of the acid form to the overall permeation, and its deprotonation when reaching the inner compartments. Thus, the magnitude of pH variation can influence not only the accuracy of the probe as a reporter of the solute kinetics (Section 4.2.1.6) but also the solute permeabilities.

In summary, the characteristic constant and the permeability of the weak acid and the conjugated base cannot always be unambiguously identified. It is only possible under conditions where the contribution of the weak acid or the conjugated base is negligible, and the kinetics approach a mono-exponential behaviour. It depends on the thermodynamic and kinetic parameters of both species and the conditions at which the method is applied. The model developed in this work and the detailed study performed allows a better understanding of the critical points under this issue. Performing the permeation assay at several different pH is, in practice, the better way to deal with these constraints, and assess the intrinsic permeability of the two forms. It must have to be done with different probes to ensure accurate estimates.

4.2.5.1.3. <u>Estimation of the apparent permeability from the probe dynamics</u>

In a permeability experiment following the pH variation, it is not possible to directly accompany the solute permeation kinetics. Instead, solute permeation is followed through variations in the fluorescence of the pH-sensitive probe. Thus, it is relevant to perform a detailed analysis regarding kinetics of fluorescence variation and compare it with that of the solute.

In experiments, the fluorescence change associated with the permeation of weak acids or bases has two distinct phases. Each of which is the result of different contributions from the permeation of the weak acid, conjugated base, proton/hydroxide ions, and other ions. The fluorescence is usually fitted using a tetra-exponential function, with two exponential terms for each phase (equation (1), Section 1.3.2.4 and presented again bellow):

$$F[t] = F_0 + \alpha_1\, e^{-\beta_1\, t} + \alpha_2\, e^{-\beta_2\, t} + \alpha_3\, e^{-\beta_3\, t} + \alpha_4\, e^{-\beta_4\, t}.$$

At equilibrium, the concentration of the probe is equal to that at $t = 0$, and as such $F_\infty = F_0$ and the pre-exponential factors are interdependent. Therefore, one can eliminate one degree of freedom in the search space when fitting the experimental data, by defining that $\alpha_1 + \alpha_2 + \alpha_3 + \alpha_4 = 0$. This

allows the fitting method to encounter the right solution more easily, with fewer iterations relative to the unconstrained problem.

The dynamics of the deprotonated probe concentration resulting from the permeation of the weak acid at the conditions shown in the previous section were fitted without constraints as performed in the literature for those assays. Table 19 shows the Best-fit parameters from fitting equation (1) to the simulated time course of probe concentration. As the permeation of the protons is not being considered, the kinetics is not too complex, and all the curves, except one, are well fitted by tri-exponential functions. For weak acids with $pK_a^{Sw} < 5.5$, the fluorescence variation associated with the pH recovery phase is best described by two exponential terms. This results from the development of a higher transmembrane potential, that affect the flux of the conjugated base.

Table 19. Best-fit parameters from fitting a tri- or tetra-exponential function to the fluorescent probe concentration time course, for the permeation of weak acids with different acidity constants. β_1 and β_2 are the characteristic constants of the fluorescence decreasing phase and β_3 and β_4 refer to the increasing phase. The values marked in orange refer to the fastest phase of solute permeation and the values in blue are assigned to the solute slowest permeating phase. The bold values are the pre-exponential factor of the characteristic constants highlighted in orange and blue. Simulations conditions: C2 S1 P2, $r = 100$ nm, $k_{loi}^{SD} = 0.1$ s^{-1}, $\kappa_H = 0$ dm s^{-1}, and $\kappa_K = 10^{-10}$ dm s^{-1}.

pK_a^{Sw}	β_1 (s^{-1})	β_2 (s^{-1})	β_3 (s^{-1})	β_4 (s^{-1})	α_1	α_2	α_3	α_4
7	1.18	3.79	0.04		**0.99**	0.33	**-1.32**	
6.5	1.11	3.78	0.06		**1.34**	0.48	**-1.82**	
6	0.91	2.49	0.05	0.07	**1.57**	0.52	-0.28	**-1.82**
5.5	0.48	0.71	0.06		0.34	**1.84**	**-2.19**	
5		0.34	0.06	0.81		**2.44**	**-2.18**	-0.25
4.5		0.17	0.04	0.33		**2.06**	**-1.73**	-0.33
4		0.12	0.02	0.17		**0.92**	**-0.69**	-0.23

The analysis of Model I in Section 4.2.1.7 for solutes with $pK_a^{Sw} \approx 7$ has shown that i) the lowest characteristic constant of the fluorescence change was the one with the highest pre-exponential term, and was always closer to the characteristic constant for the solute accumulation dynamics; and ii) the discrepancy between the characteristic constants obtained from the solute dynamics or from the fluorescence variation increases with the magnitude of the pH variation. Here, the characteristic constant *of the fluorescence decrease phase* with the highest *positive* pre-exponential factor is also the one that better describes the permeation of the solute (characteristic constants in orange in **Table 18** and **Table 19**). Additionally, the relative deviations between the highest characteristic constant of solute accumulation dynamics and the corresponding one for the fluorescence variation does not show a simple dependence on the magnitude of the internal pH variation (**Table 20**). Under these conditions the characteristic constant of the recovery phase with the largest *negative* pre-exponential factor (β_3, **Table 19**) relates with the lowest characteristic constant for the entry of solute into the vesicles (β_1, **Table 18**). In turn, the deviations between this characteristic constant and the characteristic

constant from dynamics of the fluorescence recovery phase increase when the magnitude of the pH variation also increases. The interpretation of these deviations is not straightforward.

Table 20. Relative deviation between the solute best-fit parameters β_1 and β_2 and the equivalent characteristic constants obtained by fitting $PD_{wi}*[t]$.

		% Deviation	
pK_a^{Sw}	ΔpHi	β_1 ($S_i[t]$)	β_2 ($S_i[t]$)
7	0.20	-21	-4
6.5	0.27	-39	-12
6	0.29	-27	-14
5.5	0.27	-19	14
5	0.22	-15	-25
4.5	0.13	-11	-21
4	0.07	> 1	-13

By analysing the fluorescence variation one can thus obtain the rates of the slow and fast phases of solute permeation. As discussed in the previous section, both characteristic constants are needed to estimate the permeability coefficient. However, in the works published in literature only the fast changing phase has been used to estimate the permeability coefficient of weak acids and bases.[68,69] In fact, the pre-exponential factors for each characteristic constant in the dynamics of solute permeation do not depend only on the relative abundance of each species and, therefore, it is not possible to predict them. Under conditions at which the solute kinetics is nearly mono-exponential (determined mostly by one of the solute species), one can obtain accurately the permeability coefficient. This is the case for the simulations with $pK_a^{Sw} = 4$ and 7. However, if the weight of the two exponential terms is not negligible, then estimating the permeability considering only one of the characteristic constants of the fluorescence dynamics becomes inaccurate. The permeability coefficients obtained overestimate the real value, and the deviations increase as the biphasic behaviour of the solute accumulation dynamics (or the corresponding fluorescence variation) intensifies (**Figure 50**).
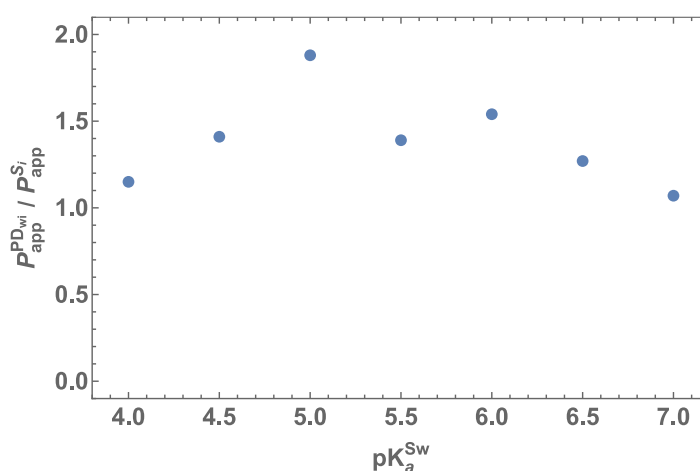
Figure 50. Ratio between the apparent permeability coefficient obtained from the fluorescence dynamics and the real apparent permeability coefficient (obtained from the solute dynamics).

The pH variation assay is an indirect method and the errors in the assessment of the apparent permeability are being added and, in some cases, may lead to significant deviations. Some of the sources for inaccuracy are: i) differences between the characteristic rate of solute accumulation and probe dynamics, ii) failure of the probe as a reporter of the inner pH and solute accumulation as the ΔpHi increases, iii) effect of the ΔpHi on the observed solute apparent permeability, and iv) slowest phase of solute accumulation being non-negligible.

It is important to highlight that, due to the high value of potassium permeability considered in the simulations performed in the previous sections, the developed transmembrane potential is low. In fact, if the permeation of potassium is slower, the dissipation of the charge unbalance will also be delayed, leading to higher transmembrane potentials maintained for longer periods, and to a higher effect on the permeation of the other charged species (conjugated base and protons). Under these conditions, the solute kinetics becomes more complex, and it ceases to be well-fitted by a bi-exponential function. These effects are evident on simulations with a fast and slow value of κ_K and $pK_a^{Sw} = 5$ or 6 (**Figure 51**).
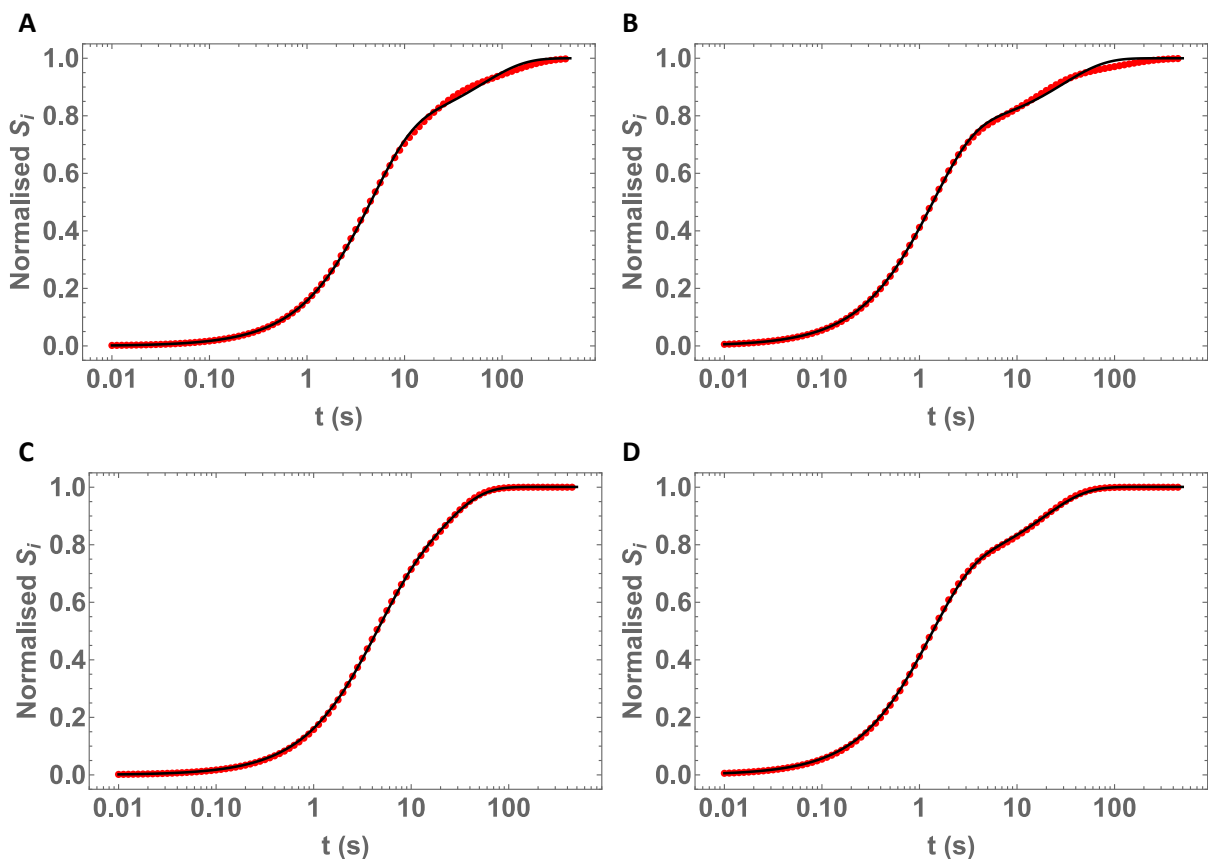
Figure 51. Goodness of the bi-exponential fit of $S_i[t]$ for the simulations **A)** $pK_a^{Sw} = 5$ and $\kappa_K = 10^{-12}$ dm s^{-1}, **B)** $pK_a^{Sw} = 6$ and $\kappa_K = 10^{-12}$ dm s^{-1}, **C)** $pK_a^{Sw} = 5$ and $\kappa_K = 10^{-10}$ dm s^{-1}, and **D)** $pK_a^{Sw} = 6$ and $\kappa_K = 10^{-10}$ dm s^{-1}. The red points are the data, and the black lines is the bi-exponential fit. Note the logarithmic scale of x-axis.

4.2.6. Model V – Permeation of a weak base

The simulations performed to analyse the permeation of the weak bases were designed similarly to the ones done for the weak acids. They were done only for vesicles with 100 nm radius. This was carried out considering the typical values of POPC for a_L, and $\overline{V_L}$, as for the case of weak acids. The thickness and the volume for all different compartments were calculated as explained in Section 3.2.1. As the best experimental conditions have already been analysed, here S_T and P_T were set at 10^{-6} and 10^{-5} M, respectively. All the other concentrations are unchanged, pHo[0] = pHi[0] = 7, and $B_T = 0.01$ M. The kinetic and thermodynamic parameters considered for the charged and uncharged forms of the weak base are equal to the ones defined previously for the respective forms of the weak acid, with $k_{loi}^{SD} = 1 \, s^{-1}$, $K_{wlo}^{SD} = K_{wli}^{SD} = 10^3$, and $K_{wlo}^{SH} = K_{wli}^{SH} = 10^2$. By defining the affinity for the membrane one order of magnitude higher for the neutral weak base, the acidity constant of the charged conjugated acid in the membrane must be set one order of magnitude higher than in water, to satisfy micro-reversibility constraints. All the parameters are listed in Table 21.

Table 21. Parameters using in the simulations of the permeation of weak bases.

Geometric parameters			Concentrations (M)		Partition coefficients	
(nm)	r	100	c_L	10^{-3}	K_{wlo}^{SD}	10^3
	h	3.9	S_T	10^{-6}	K_{wli}^{SD}	10^3
Area (dm²)	a_L	6.40×10^{-17} [113]	P_T	10^{-5}	K_{wlo}^{SH}	10^2
	A_T^o	2.00×10^5	B_T	0.01	K_{wli}^{SH}	10^2
	A_T^i	1.85×10^5	$H_{wo}[0], H_{wi}[0]$	10^{-7}		
Volume (dm³)	V_T	1	$K_{wo}[0], K_{wi}[0]$	0.15	Acidity constants (M)	
	V_{wo}	9.93×10^{-1}			K_a^{Sw}	10^{-8}
	V_{lo}	3.88×10^{-4}	Rate constants (s⁻¹)		K_a^{Slo}	10^{-7}
	V_{wi}	5.92×10^{-3}	k_{loi}^{SD}	1	K_a^{Sli}	10^{-7}
	V_{li}	3.72×10^{-4}	k_{lio}^{SD}	1.04	K_a^{B}	10^{-7}
(dm³ mol⁻¹)	$\overline{V_L}$	0.76 [114]			K_a^{P}	10^{-7}

At $t = 0$, the solute is distributed between the outer aqueous compartment and the outer membrane leaflet. When the membrane is considered impermeable to the charged species (conjugated acid and proton), the net flow stops before the concentrations of the solute equalise between donor and acceptor compartments. Therefore, at equal concentrations of the uncharged base species in donor and acceptor compartments, the concentration of the charged conjugated acid is lower in the acceptor than in the donor compartments (**Figure 52**). As the acidity constant of the conjugated acid in the membrane is equal to the outer concentration of protons, the concentration of the weak base and the conjugated acid in the outer leaflet is always equal (**Figure 52B**).
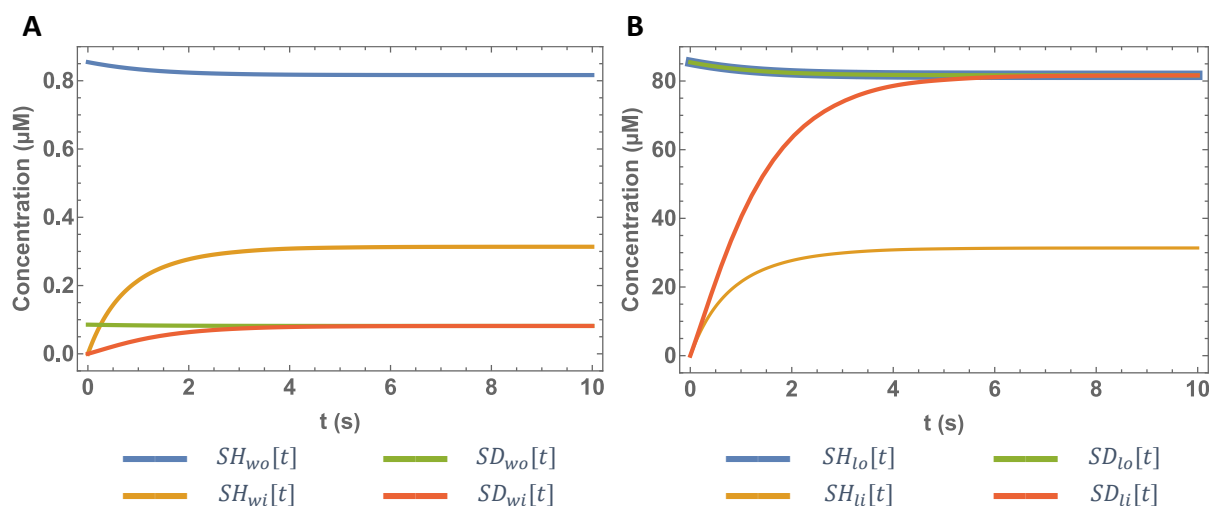
Figure 52. Time evolution of the concentration of the solute species in the **A)** aqueous and **B)** membrane compartments. Simulation conditions: Table 21.

The inflow of the weak base is accompanied by the capture of protons inside the vesicles to ensure the equilibration with the conjugated acid, leading to an increase in the inner pH. The resulting pH gradient across the membrane at equilibrium (**Figure 53**) is counterbalanced by a concentration gradient of the conjugated acid (**Figure 52**).
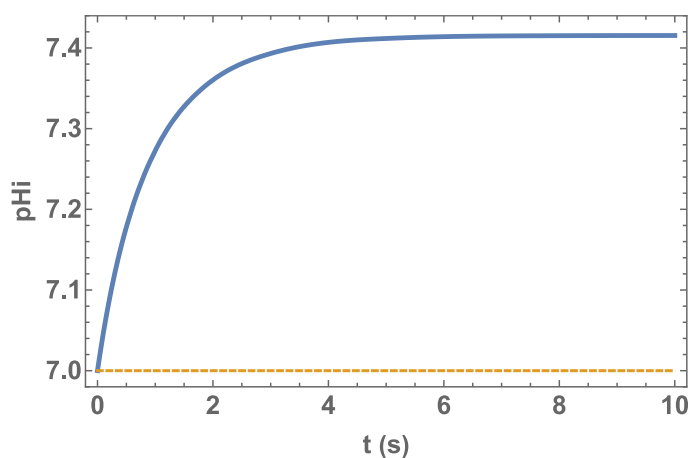
Figure 53. Variation of the pH in the outer (- - - - -) and inner (——) aqueous compartments, due to the permeation of a weak base. Simulation conditions: Table 21.

The next simulations seek to analyse in detail the kinetics of permeation of different weak bases and help understanding the relative contributions of the uncharged and charged species to the overall process. For that, the basicity constant was varied between 10^{-7} and 10^{-4} M, and the time courses for permeation were compared to those for ion-impermeable membranes. The model is however defined in terms of the acidity constant of the conjugated acid and, as such, pK_a^{Sw} was varied between 7 and 10.

If the membrane is considered ion-impermeable, the permeation of a stronger weak base ($pK_b^{Sw} = 4$, $pK_a^{Sw} = 10$) causes a larger pH variation. Under these conditions, the concentrations of the conjugated acid in the aqueous and lipid media are respectively 1000 and 100-fold higher than those of the weak base. Therefore, when the weak base reaches the acceptor compartments, it must capture protons to re-establish the equilibrium with SH_{wi}, SH_{li} and H_{wi}. This causes a large increase in the inner pH, because of the low buffer capacity inside the vesicles (**Figure 54**). Since the concentration of the weak base in the donor compartments is low, the permeation process is very slow. On the other hand, for weak bases with $pK_b^{Sw} = 7$, the balance between the base and the conjugated acid is attained when the concentration of the weak base in the membrane is 10-fold higher. As the weak base is the most abundant species, the degree of ionisation when reaching the donor compartment is low, and the pH variation is small. In this case, the equilibrium is attained rapidly due to the high relative concentration of the permeating species, the neutral weak base. Intermediate strengths of the weak base lead to intermediate rates of equilibration and ΔpHi. A non-linear dependence is however observed for the variation of ΔpHi which is almost the same for $pK_b^{Sw} = 6$ or 7. An equivalent behaviour was observed for the permeation of weak acids (Section 4.2.3.1.2) and is due to the effect of pH in the extent of ionisation of the permeating uncharged weak base to give the conjugated acid.
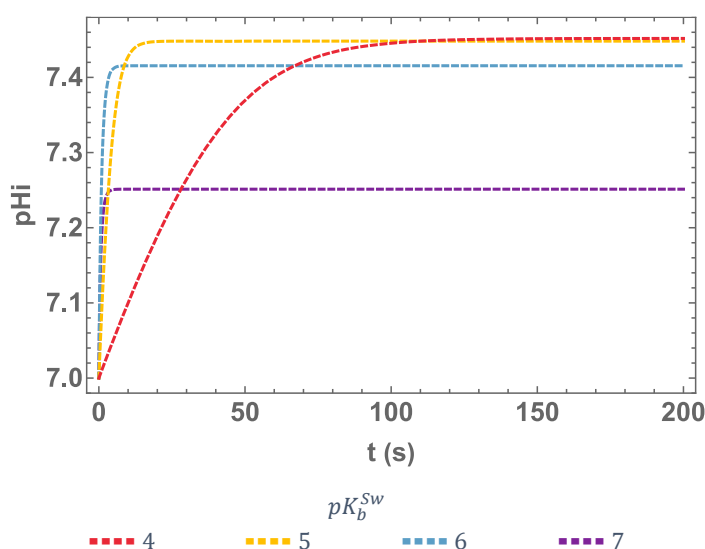
Figure 54. pH dynamics for the permeation of solutes with pK_b^{Sw} between 7 and 4, considering only the permeation of the weak base. Simulation conditions: Table 21.

If the membrane is considered permeable to charged species (protons and/or to the conjugated acid), the concentration gradients of these substances can partially dissipate. In this case, if the contribution of the conjugated acid to the overall permeation is not negligible, the pH variation profile is considerably changed when compared to the case where the membrane was considered impermeable to charges. For example, for solutes with $pK_b^{Sw} = 4$, at pH 7, the concentration of the

conjugated acid is much higher than that of the weak base, and as such, the equilibration of the solute through the membrane is dominated by the permeation of the charged species in spite of its slower translocation rate constant (**Figure 55A**). For solutes with $pK_b^{Sw} = 7$, the overall permeation kinetics is controlled by the permeation of the neutral weak base (**Figure 55B**). Note that in this case, the kinetics of accumulation of the conjugated weak acid is biphasic (orange line) corresponding to the fast permeation of the weak base and the slow permeation of the conjugated acid. However, the slow phase does not contribute significantly to the overall permeation (black lines) due to the relatively small fraction of the conjugated acid.

It is of high relevance to understand the effect of the contribution of the permeation of weak base and its conjugated acid to the overall kinetics. This effect depends on the kinetic and thermodynamic properties of the various species, and the analysis of the simulation results allows anticipating under which conditions the overall permeation is dominated by only one of the species. In this case, the accumulation of solute in the acceptor compartments is well described by a mono-exponential function, and the results obtained from the fluorescence variation profile will be easily analysed.
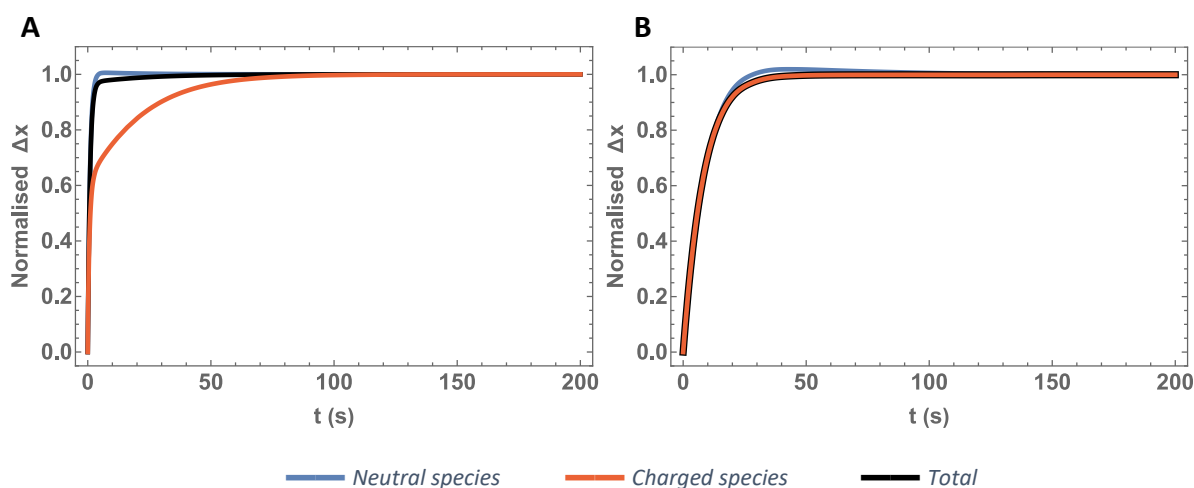
Figure 55. Normalised concentrations of neutral (SD_{li} and SD_{wi}), charged (SH_{li} and SH_{wi}), and total solute in the inner compartments (S_i), for the permeation of a weak base with pK_b^{Sw} equal to **A)** 7 and **B)** 4. Simulation conditions: Table 21, and $k_{loi}^{SH} = 0.1$ s^{-1}.

Although in those simulations the permeation of protons was not considered ($\kappa_K = 0$ dm s^{-1}), the permeation of the solute charged species leads to the dissipation of the pH gradient (**Figure 56**). This have been discussed in detail in Section 0 for the case of permeation of weak acids. Here, it should be noted that in none of the simulations, the pH is fully dissipated. This is because the permeation of the charged species leads to the development of a charge unbalance, and the corresponding electrostatic potential counterbalances the concentration gradient of the charged species.
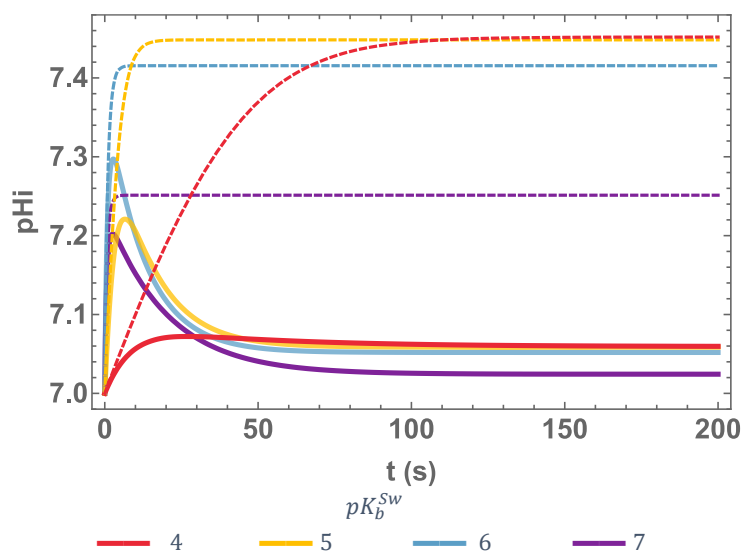
Figure 56. pH dynamics for the permeation of solutes with pK_b^{Sw} between 7 and 4. The dashed lines represent the pH dynamics in the simulations where only the uncharged weak base is allowed to permeate. The solid lines represent a situation where both the weak base and the conjugated acid are allowed to permeate. Simulation conditions: Table 21 and $k_{loi}^{SH} = 0.1$ s⁻¹ if the permeation of the conjugated acid is considered.

The time evolution of the electrostatic potential is shown in Figure 57. The larger the contribution of the conjugated acid to the overall permeation, the higher the magnitude of the transmembrane potential.
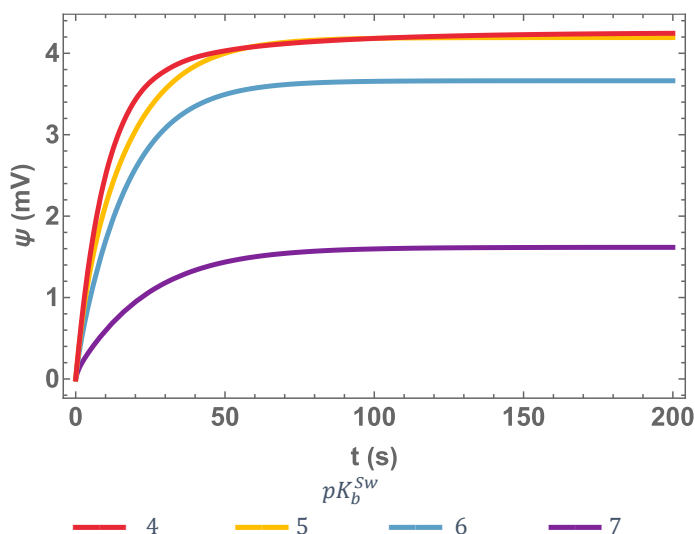
Figure 57. Evolution of the transmembrane potential created by the permeation of the charged conjugated acid. Simulation conditions: Table 21 and $k_{loi}^{SH} = 0.1$ s⁻¹.

The dissipation of the transmembrane potential by the efflux of potassium will allow the system to attain an equilibrium, without significant electrochemical gradients. This is ensured by the efflux of potassium for the permeation of weak bases and the influx of potassium for the permeation of weak acids. The potassium pool inside the vesicles is more limited. Thus, it is necessary to assess whether the amount of potassium inside the vesicles is sufficient to allow the dissipation of the transmembrane

potential generated, without creating a very significant variation in its concentration. There are 335 337 potassium ions inside each vesicle and transmembrane potentials of 4 and 10 mV correspond to an accumulation of respectively ≈ 15 and ≈ 36 positive charges inside each vesicle. These numbers are negligible when compared to the total of potassium ions inside a vesicle. In conclusion, under the simulated conditions, the dissipation of the transmembrane potential will not induce a significant potassium concentration gradient.

4.2.7. Conclusion

Because the pH variation assay is an indirect method, it may not always yield accurate estimates of the apparent permeability of the solute, and inaccuracy can come from different types of sources.

All the simulations presented before gave new useful insights about the pH variation assay and the effect of some parameters on the kinetics of solute permeation and the corresponding variation of the inner pH and fluorescence intensity.

This detailed analysis allowed us to identify that the simplified equation (2) used frequently to calculate the apparent permeability coefficient from the solute equilibration dynamics can in some cases underestimate or overestimate the permeability coefficient by several orders of magnitude. This is a result of the breakdown of several assumptions or approximations. To calculate the solute's permeability coefficient, it is necessary to know the extent of solute equilibration. The amount of solute associated with the membrane contributes significantly to the dynamics of solute equilibration and to the corresponding pH variation. An accurate analysis of the results obtained from the pH variation assay will therefore yield quantitative information not only about the solute that permeated the membrane into the vesicles' lumen, but also on the sequestration by the membrane. The higher the solute lipophilicity, the higher the discrepancies between the apparent permeabilities estimated by the simplified equation (2) and those obtained when taking the extent of permeation into account, equation (136). These aspects have been extensively analysed in a manuscript that was recently published.[118]

In Section 4.2.5.1 it was discussed how to estimate permeability coefficients from bi-exponential fits to the time courses. The permeation of weak acids and bases is commonly biphasic because of a faster permeation of the uncharged species. When fitting the fluorescence variation of the pH-sensitive probe some information is lost. Although some of the characteristic constants of the fluorescence variation approach the ones characterising solute permeation, the pre-exponential coefficients of these fits are not very informative about those of the solute accumulation. Additionally, the prediction of these pre-exponential coefficients is not straightforward, as it will not depend only on the fraction of each species. Here, some questions appear: How is it possible to estimate the solute

permeability more accurately? How to make the best use of the parameters estimated from the fit of the fluorescence time courses?

The analysis performed so far permitted identifying the following experiment design principles to minimise inaccuracies:

i) using larger vesicles avoids complicated kinetics associated with stochastic effects;

ii) the maximum pH variation must be as low as possible, within the limits of the assay sensitivity;

iii) ideally, the assay should be done in conditions where one of the solute species dominates the overall kinetics of solute equilibration, leading to mono-exponential behaviour. This may be achieved when the slowly-permeating charged species is strongly dominant, or when the fraction of the fast-permeating neutral species is significant. Moreover, in cases where there is a significant contribution from both species, a good separation of the fast and slow processes (corresponding to the establishment and dissipation of the pH gradient) provides information on the rate of permeation of both neutral and charged species. The extraction of quantitative information is not straightforward due to contribution from factors such as the rate of permeation of other charged species and would require the execution of the assay in distinct conditions. Nevertheless, this would add significant value to the pH variation assay.

4.3. <u>Determination of the acidity constant of HPTS</u>

The pH-sensitive probe HPTS is commonly used in the pH variation assay to assess the permeation of weak acids and bases. Before its use to characterise quantitatively the permeation of the solutes, it is necessary to know its fluorescence properties.

At very acidic pH values, HPTS absorbs radiation with a maximum at a wavelength equal to 405 nm. When the weak acid converts into its conjugated base, a phenolate is formed (**Figure 58**) which absorbs radiation with a maximum at 455 nm (**Figure 59**). These observations are in accordance with what is known for this fluorophore.[123]
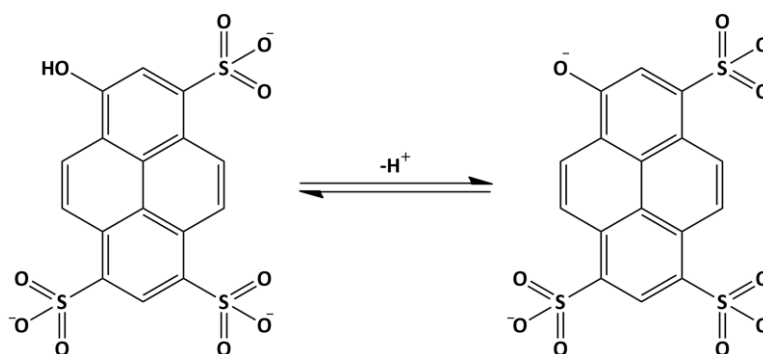
Figure 58. Acidic/phenolic and basic/phenolate forms of the probe HPTS.
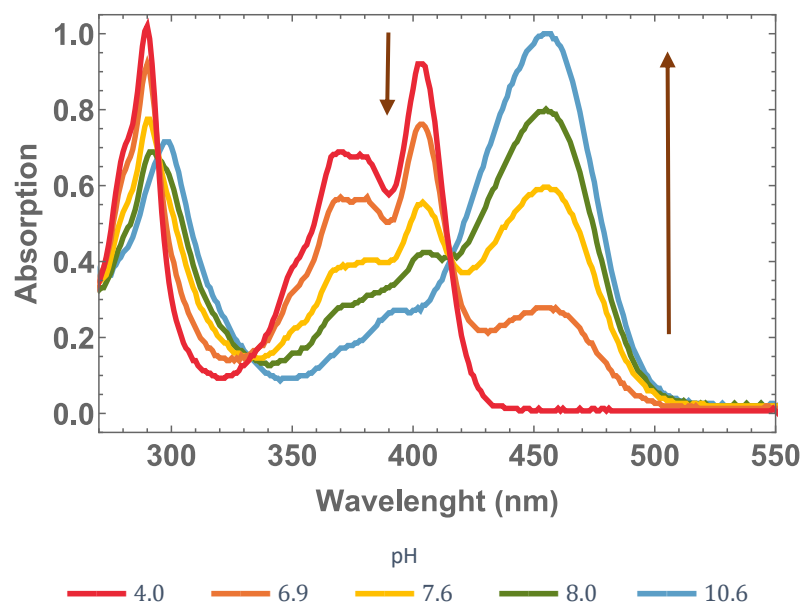
Figure 59. Absorption spectra of HPTS at different pH values reflecting the variation in the proportion of the acid and base forms. The spectra are relative to that of the conjugated base which shows a maximum at 455 nm.

The same samples were excited at the wavelength of the isosbestic point (416 nm) and the fluorescence spectra was collected (**Figure 60**). Pyranine is a fluorophore that undergoes proton transfer upon excitation and has a pK_a in the excited state ($pK_a^* < 2$) much lower than in the ground state.[123] For pH values above 2, after being excited, the weak acid loses a proton, and the emitting form is always the phenolate (excited-state deprotonation upon excitation of the acidic form). This justifies why the fluorescence signal (with a maximum at 512 nm) is not greatly influenced by the solution pH when exiting the sample at the wavelength of the isosbestic point.
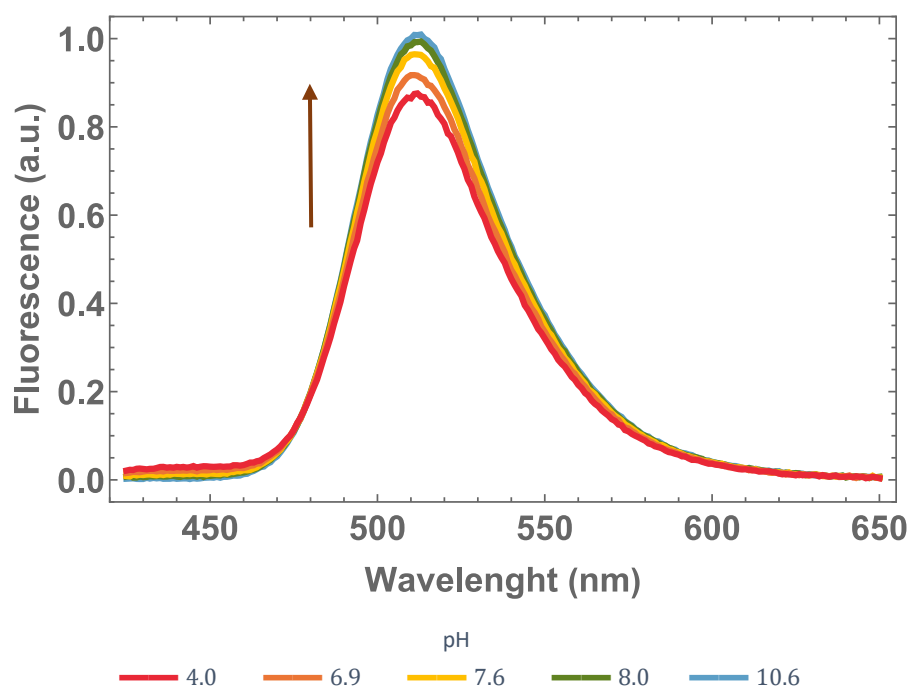
Figure 60. Fluorescence spectra of HPTS at different pH values. The fluorescence intensity was normalised by the maximum emission when the phenolate is the only species (pH=10.6), and the samples were excited at the isosbestic point (416 nm).

If the excitation wavelength is 455 nm, only the conjugated base (phenolate) absorbs and the fluorescence signal depends strongly on the pH, reflecting the concentration of this species in the ground state (**Figure 61**). At those conditions HPTS is useful as a fluorescent pH sensor.

The acidity constant, in the logarithmic form (pK_a) was obtained by fitting the experimental data to the equation (144), derived from the Henderson-Hasselback equation (**Figure 61**). C_T is the total concentration of HPTS and S_{acid} and S_{base} are the Best-fit parameters, which correspond to the fluorescence signal of the acid and base, respectively.

$$Signal\,[pH] = C_T \left(\frac{10^{pK_a - pH}}{1 + 10^{pK_a - pH}}\, S_{base} + \left(1 - \frac{10^{pK_a - pH}}{1 + 10^{pK_a - pH}} \right) S_{acid} \right) \qquad (144)$$
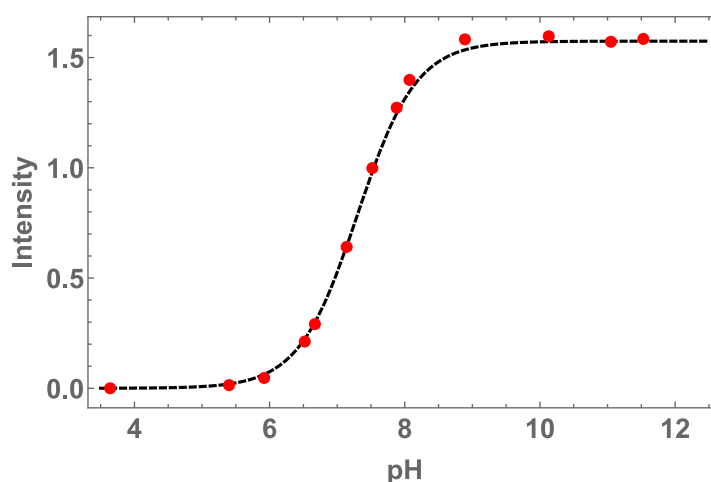
Figure 61. Fluorescence signal of the probe HPTS (●) and respective fit (▪▪▪▪), as a function of pH. The concentration in solution is 0.8 µM and the samples were excited at 455 nm.

The best fit of the fluorescence obtained by excitation at 455 nm resulted in a pK_a equal to 7.3. The pK_a obtained by absorption titration, using a Unicam UV530 UV/Vis spectrophotometer, is also consistent with this value (data not shown) and with the reported values.[123] There are also some different values (between 7 and 7.3), but it could be the consequence of different measurement conditions, as HPTS properties depend a lot on the ionic strength of the medium.[68,123]

4.4. <u>Characterisation of the vesicle size and zeta potential</u>

As shown in Sections 4.2.1.1 to 4.2.1.7, the size of the vesicles has a strong influence on the rate at which the solute equilibrates between the outer and inner compartments. This parameter must therefore be known with accuracy and preferably the sample should be monodisperse. The size distribution of the vesicles (POPC : POPS, 9 : 1) was measured by dynamic light scattering for a sample at pH 7 and 25 °C (**Figure 62**). The vesicles were prepared by extrusion through two stacked 200 nm pore size polycarbonate filters (with 13 passes in total at a pressure of 5 to 10 bar). It is observed that the samples are monodisperse and that the average size obtained is somewhat smaller than the pore size of the filters, 156.1 ± 2.1, or 136.3 ± 0.4 nm, when evaluated from the size distribution by scatter intensity (plot A) or from the size distribution by particles volume (plot B), respectively. The higher average diameter obtained when calculated from the distribution of the scatter intensity is due to supra-linear dependence of the scatter efficiency with the particle size, with larger vesicles contributing more than expected from their abundance in the sample. The average size calculated from the distribution of particles volume is weighted by the volume occupied by particles with a given size and is thus a better descriptor of the sample. The observation that the value obtained is significantly smaller than the filter's pore size suggests that small MLVs were formed upon lipid hydration and/or during the freeze/taw steps. This may be due to the presence of 10 % negatively

charged lipids in the membrane, that leads to electrostatic repulsion and favours the formation of smaller vesicles.

A

B
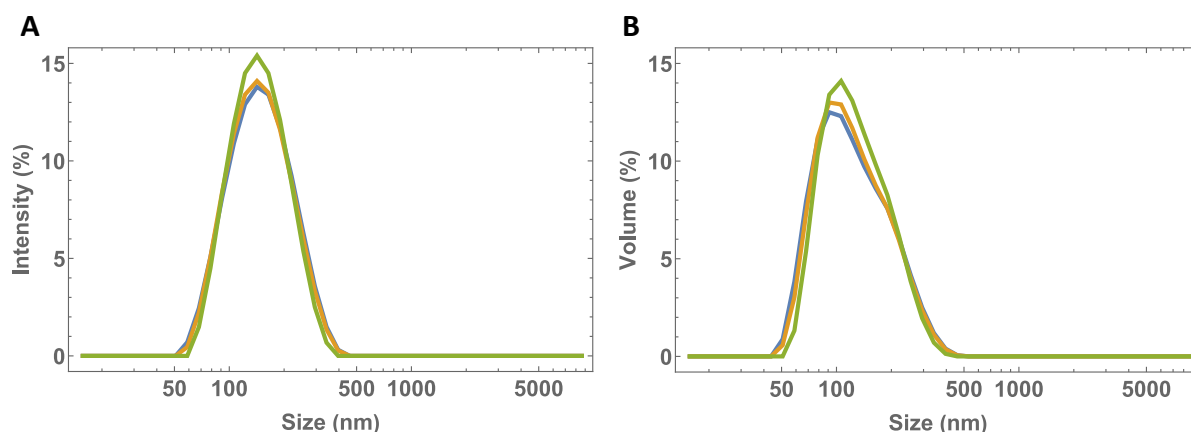
Figure 62. Size distribution of the membrane vesicles prepared by extrusion of POPC and POPS (9 : 1) MLVs. Scatter intensity **A)** and volume **B)** distributions. The curves are replicated measurements.

The zeta potential obtained for the vesicles in the saline buffer was equal to -12.3 ± 1.7 mV. This moderate surface potential increases the stability of the vesicles, preventing their aggregation. Also, the electrostatic repulsion that would occur between membrane multilayers in the same vesicle facilitates the generation of the unilamellar vesicles, which are required in permeability assays.[124]

4.5. <u>Dissipation of the proton gradient</u>

The simulations presented in Sections 4.2.1 to 4.2.1.7.2 showed that the generation of the pH gradient, although necessary to allow following the solute permeation from the variations in the fluorescence of the probe, prevents equalisation of the solute concentration in the donor and acceptor compartments and thus, leads to deviations to the real apparent permeability when using the simplified equation (2). It was also shown that dissipation of the pH gradient may provide information regarding the permeability of the solute charged species. To dissect the observed pH restoration kinetics into the contributions of the solute and proton permeation, it is therefore of high importance to characterise quantitatively the permeability of H^+/OH^- in the absence of the solute.

The simulations also showed that permeation of charged species lead to the generation of an electrostatic potential difference between the donor and acceptor compartments. This potential will compromise the equalisation of the concentration of charged species (solute and H^+/OH^-) in the donor and acceptor compartments. The dissipation of this electrostatic potential may be efficiently achieved by the presence of high concentrations of charged species with fast membrane permeability in both donor and acceptor compartments.

In this experimental section, a pH gradient was generated by the variation of the proton concentration in the outer aqueous compartment, and the rate of the dissipation of this gradient was characterised to estimate the H^+/OH^- permeability (hereafter identified simply as H^+ permeability). Different concentrations of valinomycin were first equilibrated with the lipid vesicles, to characterise the effect of K^+ permeability on the observed dissipation of the pH gradient and identify the most suitable experimental conditions to use in a pH variation assay. In other words, the aim of this experiment was to characterise quantitatively the permeability of protons, and to understand if valinomycin can take a fundamental role in the complete equalisation of the concentration of tested compounds.

Five concentrations of valinomycin and their effect on different pH gradients were tested. The equilibrium was perturbated by decreasing or increasing the outer solution pH with the addition of a more acidic or alkaline buffer, respectively, at a ratio of $1 : 1$. Variations in the fluorescence of the pH probe encapsulated in the vesicles were followed on a stopped-flow and on plate reader, to allow the characterisation of fast and slow processes, respectively.

4.5.1. Plate reader experiments

After imposing a proton gradient between the outer solution and the vesicles' lumen, the system will tend to adjust to a new equilibrium. The pH inside the vesicles at the beginning is always equal to 7. When the pH outside the vesicles is changed to acidic values, the protons will enter the vesicles and the inner pH will decrease until it equilibrates with the outer pH. In these circumstances, the fluorescence of the entrapped fluorophore decreases (**Figure 63**).

As the concentration of valinomycin increases, the pH gradient is dissipated faster. This may be due to a faster dissipation of the electrostatic potential generated in the initial phase of pH equilibration, or due to an increase in the intrinsic permeability of H^+ due to the presence of valinomycin. The presence of a high concentration of K^+ on both aqueous compartments should prevent the transport of H^+ by valinomycin, but the distinction between both possible effects of valinomycin requires a quantitative analysis of the results.
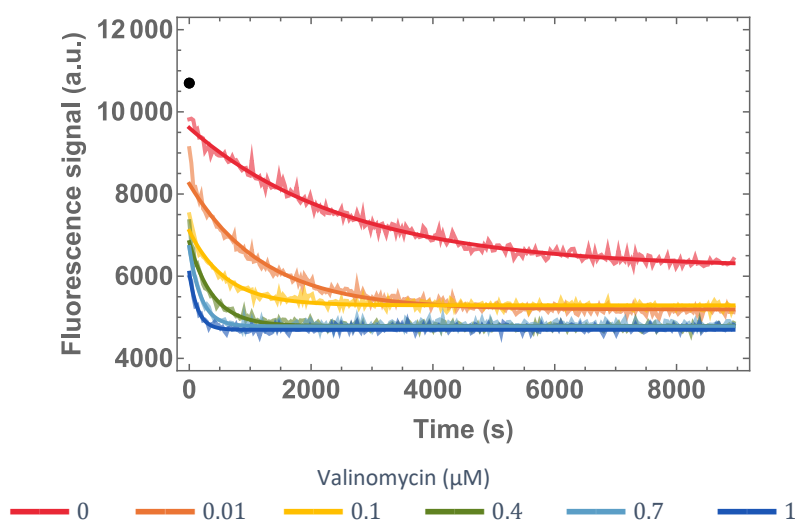
Figure 63. Effect of the concentration of valinomycin on the kinetics of pH equilibration: Experimental results obtained for the dissipation of a pH gradient of 0.5 units (lower pH outside, pHo $\approx$ 6.5). The darker curves are the best mono-exponential fit to the HPTS fluorescence. The black point at $t = 0$ is an estimate of the fluorescence immediately after the injection.

The outer pH was also decreased by approximately 1 unit (data not shown). All the curves are reasonably well described by a mono-exponential function (**Figure 63**) from which a characteristic constant is obtained. Figure 64 shows the characteristic constant obtained when the outer pH was decreased by 0.5 and 1 units. It is observed that the characteristic constant increases approximately linearly with the concentration of valinomycin, not being significantly affected by the magnitude of the pH gradient.
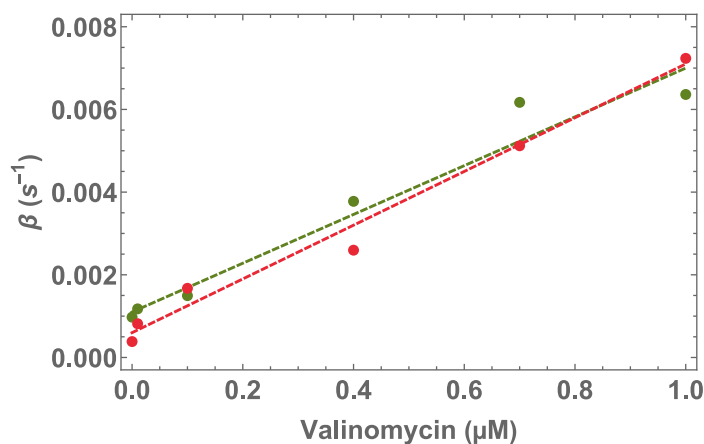
Figure 64. Characteristic constant of the kinetics of fluorescence variation when imposing a pH gradient across the vesicle membrane. The pH in the outer medium was decreased by 0.5 ($\bullet$) and 1 ($\bullet$) units (pHo $\approx$ 6.5 and 6, respectively).

If, on the other hand, the outer pH is increased, the protons inside the vesicles' lumen will exit and the pH and the fluorescence of the HPTS will both increase (**Figure 65A**). The external pH was decreased by approximately 1.5, 1, and 0.5 units, and the characteristic constants obtained from the mono-exponential fits are shown in Figure 65B. It was also observed a linear increase in the characteristic constant with the concentration of valinomycin, but in this case the characteristic constant is higher for larger pH gradients (most significant when comparing 0.5 and 1 pH units).
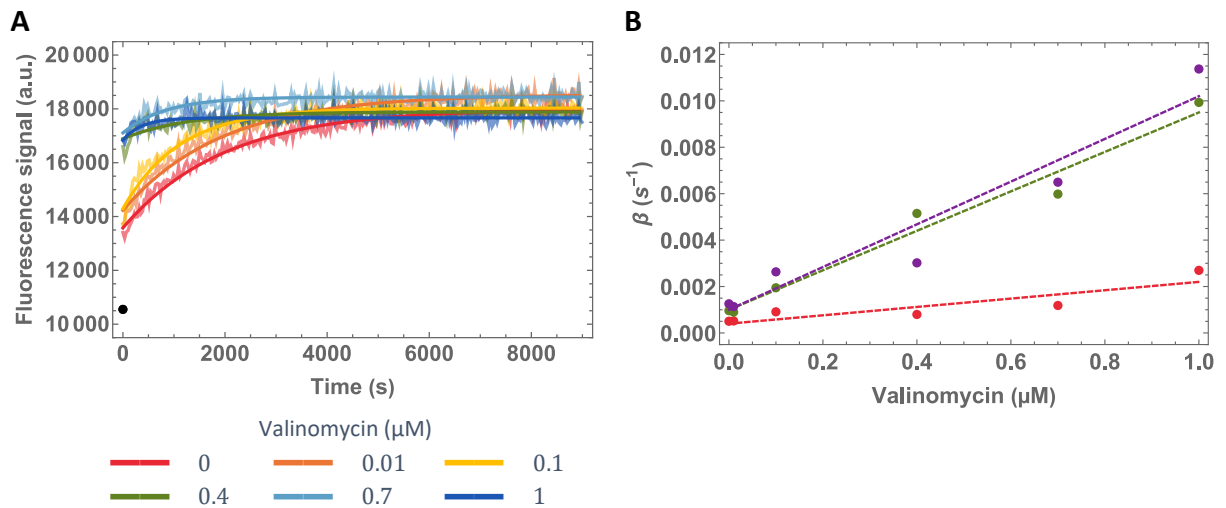
Figure 65. Effect of the concentration of valinomycin on the kinetics of pH equilibration. **A)** Fluorescence of the HPTS when imposing a pH gradient of 0.5 units: higher pH outside (pHo $\approx$ 7.5). The darker curves are the best mono-exponential fit to the HPTS fluorescence. The black point at $t = 0$ is an estimate of the fluorescence immediately after the injection. **B)** Characteristic constant of the kinetics of fluorescence variation when imposing a pH gradient across the vesicle membrane of 0.5 (●), 1 (●), and 2 (●) units (pHo $\approx$ 7.5, 8, and 9, respectively).

It should be highlighted that the fluorescence signal should start approximately at the same value for the different conditions, as the pH inside the vesicles is always the same (pH $\approx$ 7, black points in **Figure 63** and **Figure 65. A**). This is not observed because, at the first measured time, some protons have already permeated and, in some situations, the system is almost at the new equilibrium. The exact delay between the change in the pH in the outer aqueous compartment and the first fluorescence reading is not well known. However, the maximum delay is known because the samples were sequentially diluted with the new buffer using the injectors in the plate reader, and after this step, the fluorescence of all samples was recorded. To evaluate if this delay was responsible for the observed fluorescence intensity at the first time point the fitting was also performed by adding a delay parameter (the same delay for all samples) and fixing the initial fluorescence at the expected value before the pH variation (considering the signal before the injection and the dilution factor). The fit with a mono-exponential function required a delay larger than 500 seconds, which is substantially higher than the time between the beginning of the injection and the measurements (60 seconds maximum). This means that the dissipation of the pH gradient is not a monophasic process, with a faster process occurring during the time not recorded in these experiments.

While the protons enter the vesicles, a positive potential is generated which opposes the driving force for protons permeation generated by its concentration gradient. Further dissipation of the pH gradient requires the vanishing of the electrostatic potential by the permeation of additional charged species. In the presence of valinomycin, it is anticipated that potassium will be the charged species in solution with a higher membrane permeability and thus responsible for the vanishing of the transmembrane potential that allows the full dissipation of the pH gradient. The higher the

concentration of valinomycin, the faster the permeability of potassium ions leading to a smaller transmembrane potential (absolute value), a larger driving force for proton permeation, and thus a faster dissipation of the pH gradient.

The observation that the dissipation of the pH gradient is characterised by a fast partial variation followed by a slow approach to equilibrium, and the direct dependence of the rate of the slow process with the concentration of valinomycin supports the interpretation that the slow step of pH equilibration is being controlled by the developed transmembrane potential. In the absence of valinomycin, the transmembrane potential is dissipated very slowly and only a small number of excess protons permeates during the fast process. Therefore, the fluorescence intensity recorded at the first time point is similar to that expected at the beginning of the experiment (**Figure 63** and **Figure 65**, beginning of the red curves closer to the black points).

For each concentration of valinomycin, the characteristic constant follows a V shape tendency with the pH (**Figure 66**). This dependence with the pH shows that the minimum rate of pH equilibration is attained around pH 7 and the maximum is attained when the outer pH is decreased or increased by 1 and 2 pH units, respectively. This was expected because the driving force increases by increasing the pH gradient, and the observed kinetics is faster. The variation of the characteristic constant at $pH < 7$ seems to be different from the dependence observed at $pH > 7$. At $pH < 7$, the concentration of protons is higher than that of hydroxide ion and if the permeability of both ions is similar, one would expect that proton permeation contributes more to pH dissipation. On the other hand, at $pH > 7$ it would be due to the permeation of the hydroxide ion.[108] It will be necessary other experiments to properly analyse the proton and hydroxide permeability coefficients and analyse if the proton/hydroxide permeability is higher under acidic or alkaline conditions. In fact, membranes are more permeable to anions than cations, and as such, it would be expected that the hydroxide permeability would be bigger than the proton permeability.[122,125] However, it is also found that the permeability of the proton is higher than the hydroxide permeability.[122] The observed saturation of the characteristic constant at higher pH gradients (pHo between 8 and 9) can be assigned to pH probe sensitivity issues.
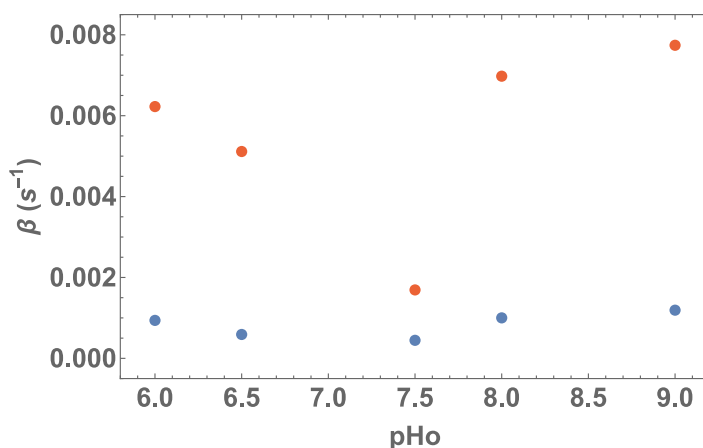
Figure 66. Characteristic constant obtained from a mono-exponential fit of the HPTS fluorescence on the pH equilibration experiments on a plate reader in the absence (●) and with 0.7 µM valinomycin (●) as a function of the outer pH. The values are the ones predicted by the linear tendency shown in Figure 64 and Figure 65B.

Figure 67 shows the percentual variation between the fluorescence signal at $t = 0$ (obtained considering the dilution of the sample with buffer at the same pH) and the fluorescence attained at equilibrium. As expected, the greater the imposed pH gradient, the greater the magnitude of variation in the fluorescence signal. For $6.5 <$ pHo < 8, the observed fluorescence variation varies approximately linearly with the pH. This proportionality breaks down as the pH gradient increases because the outer pH deviates from the pK_a^P (7.3). From this observation, one can conclude that for the highest pH gradients imposed, the fluorescence stops being sensitive to the inner pH before the equilibrium is attained. Another limitation observed for higher pH gradients is that the kinetics of the variation in the pH variation is not equivalent to the concentration of protons inside the vesicles (Section 4.2.1.6). Therefore, to characterise the proton permeability, the pH gradient imposed should be small (0.5 units or less) and the initial pH should be close to pK_a^P.
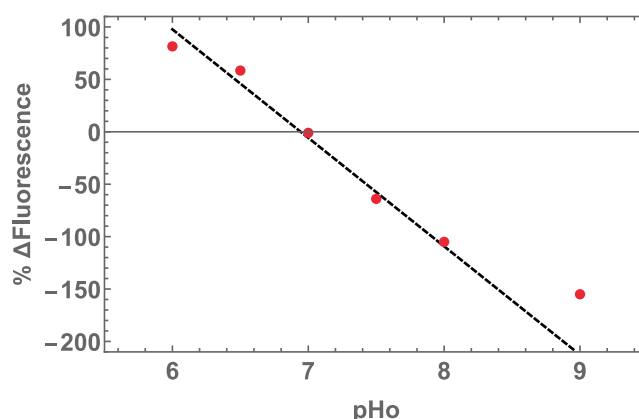
Figure 67. Percentual variation of the fluorescence as a function of the outer pH.

In an attempt to characterise the fastest step in the dissipation of the pH gradient, the experiments have also been performed in a stopped-flow equipment. The results obtained are shown in the next section.

4.5.2. Stopped-flow experiments

As observed on the plate reader, the fluorescence intensity does not start in the same value for all pH gradients imposed (**Figure 68**) and the difference to the condition of absence of a pH gradient is higher for the experiments where the outer pH was increased. This shows that some fluorescence variation occurs during the mixing time in the stopped-flow equipment ($\approx$ 20 ms). A very fast change would be expected if some pH probe is present outside the vesicles. However, if this is the case it should not be affected by the presence of valinomycin. Thus, the very fast fluorescence variation should be due to changes in the pH inside the vesicles. One possible very fast process is the dissipation of the pH gradient due to translocation of small amounts of fatty acids present in the membrane, but again, this process should not be affected by valinomycin. One final possibility is that H$^+$ permeation is very fast but the extent of dissipation of the pH gradient is limited by the development of the transmembrane potential. In this case, the presence of valinomycin decreases the potential generated and thus allows a more extensive dissipation of the pH gradient during the fast H$^+$ permeation phase. This interpretation is supported with the larger deviation from the initial signal as the concentration of valinomycin increases. What is strikingly evident when comparing the results shown in Figure 68 is the rate of the slower step, which is much faster in the presence of valinomycin (plot B *vs* plot A).
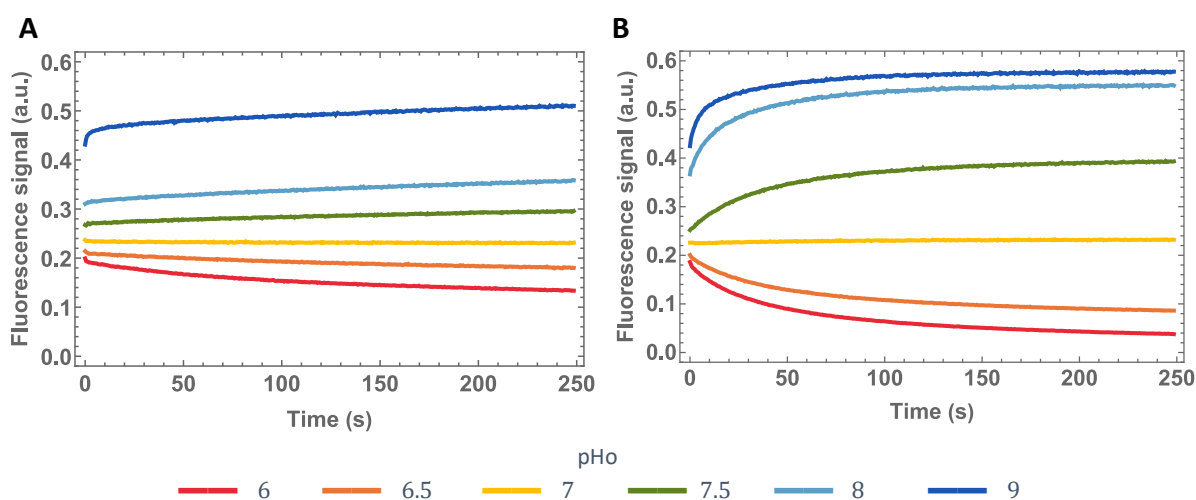
Figure 68. Kinetic profile of the pH equilibration when imposing different proton concentration gradients **A)** in the absence of valinomycin, and **B)** with 0.7 µM valinomycin.

The data were analysed by fitting simultaneously the same condition curves of the plate reader and stopped-flow experiments to bi-exponential functions and imposing that the characteristic constants are the same (β_1 and β_2). The remaining adjustable parameters are the signal at $t = 0$ and ∞, and the pre-exponential terms linked to the two data sets [α_1^{PR} and α_1^{SF} for plate reader (PR) and stopped-flow (SF) experiments]. The values obtained for the characteristic constants and the relative weight of the two processes are shown in Table 22. The quality of the fit can be assessed in the Supplementary Material (**Figure S1** and **Figure S2**).

Table 22. Best-fit parameters from fitting the kinetic profiles acquired on the plate reader (PR) and stopped-flow (SF) with a bi-exponential functions.

Valinomycin		pHo				
		6	6.5	7.5	8	9
0 µM	β_1	0.0007	0.0004	0.0005	0.001	0.003
	β_2	0.015	0.010	0.005	0.029	0.179
	α_1^{PR}	1.00	1.00	1.00	1.00	1.00
	α_1^{SF}	0.89	0.91	0.56	0.05	0.25
0.7 µM	β_1	0.010	0.007	0.001	0.021	0.022
	β_2	0.049	0.037	0.028	0.119	0.220
	α_1^{PR}	1.00	1.00	1.00	1.00	1.00
	α_1^{SF}	0.58	0.53	0.47	0.58	0.51

The faster characteristic constant is not as dependent on the concentration of valinomycin as the slowest one. With 0.7 µM valinomycin, β_1 increases between 13 to 21-fold, while β_2 is only around 3 to 6-fold of that in the absence of the ionophore. This was somewhat expected since the protons are not supposed to be transported by valinomycin under these conditions $(K_{wo}[0], K_{wi}[0] \gg H_{wo}[0], H_{wi}[0])$. However, the fastest characteristic constant also seems to vary linearly with the concentration of valinomycin (**Figure 69A**). The tendency observed for β_2 as a function of the outer pH (**Figure 69B**) is the same as that for the slower one (**Figure 66**). This is also explained by the increase of the driving force as the pH gradient increases. However, the characteristic constant is much higher for pH > 7, which suggests a faster permeability of the hydroxide ion.
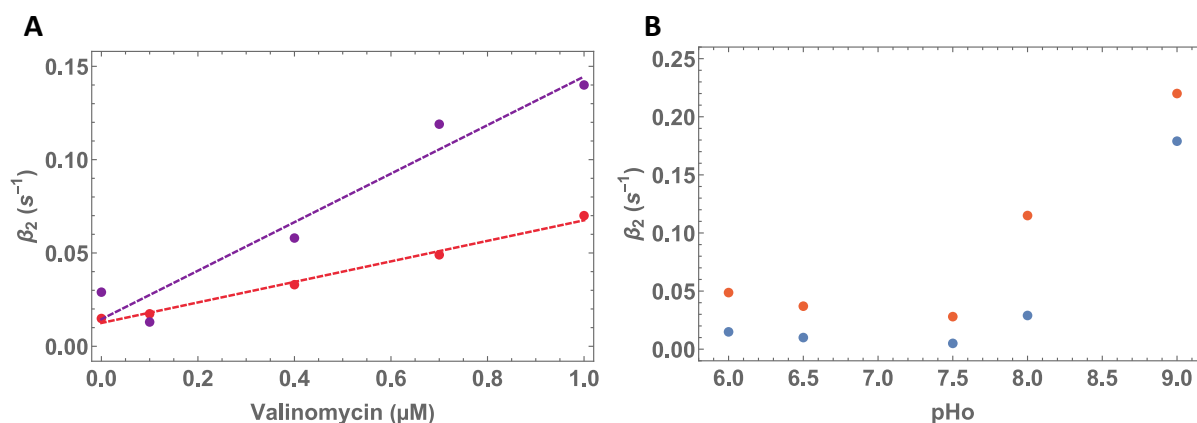
Figure 69. Effect of valinomycin in the characteristic constant of the fastest step (β_2). **A)** Characteristic constant obtained from the bi-exponential fits of the plate reader and stopped-flow experiments, when imposing a pH gradient of 1 unit: lower (●) and higher (●) pH outside. **B)** Characteristic constant in the absence (●) and with 0.7 µM valinomycin (●), as a function of the outer pH. The values represented correspond to the linear Best-fit of the dependence of β_2 with the concentration of valinomycin (Plot A).

Not much emphasis should be given to the results obtained by this analysis because the system is too complex. It is not clear for example if the two characteristic constants obtained from the bi-

exponential fits directly represent the permeability of H⁺/OH⁻ and K⁺ or if the two processes overlap to some extent and influence the obtained parameters. Therefore, some simulations have been performed to gain a better understanding of the processes involved in the dissipation of the pH gradient, and on the effect of changing independently the permeability of protons and potassium ions.

4.6. <u>Exploratory analysis using the kinetic model</u>

Using mechanistic models to predict the parameters that describe the observed behaviour is in some cases better than estimating them through a linear combination of exponential functions. This is useful to analyse the data of complex and non-intuitive systems and interpret them mechanistically. The fitting of non-linear models to the experimental data can be challenging, with a high probability of getting stuck in local minima or the parameters not being identifiable. Therefore, it is essential to perform an exploratory analysis before fitting the data with the kinetic model, to gain insight into how the parameter values relate to the shape of the fluorescence time courses.

Through the quantification of phosphates, the lipid concentration in the samples used for pH equilibration experiments was estimated as 8.50×10^{-5} M. The average diameter of the vesicles was 136 nm and the size distribution was monodisperse, with a polydispersity index of 0.125. The vesicles were prepared in the presence of 10^{-4} M HPTS, and this is the expected local concentration of the pH probe encapsulated in the vesicles. These parameters were considered in a simplified version of Model IV, where only protons and potassium permeate, to simulate the experimental kinetic profiles for the variation in the fluorescence intensity.

First, considering the situation where the outer pH equals 6, the kinetics of pH variation and probe concentration were simulated neglecting the permeability of potassium and varying the permeability of proton between 10^{-8} and 10^{-6} dm s⁻¹ (**Figure 70**). As expected, the pH in the inner aqueous compartments decreases with time, and this is faster for larger values of proton permeability. However, the pH tends towards 6.2 and not to the pH outside the vesicles (pHo = 6) this is due to the establishment of a transmembrane potential of around 11 mV (positive inside the vesicles), which balances the driving force for the influx of protons due to the concentration gradient. Under these circumstances and during the timescale of the experiment, neither the inner pH equilibrates with the outer nor the potential dissipates. The fluorescence seems to report the variation of the pH relatively well (**Figure 70B**).
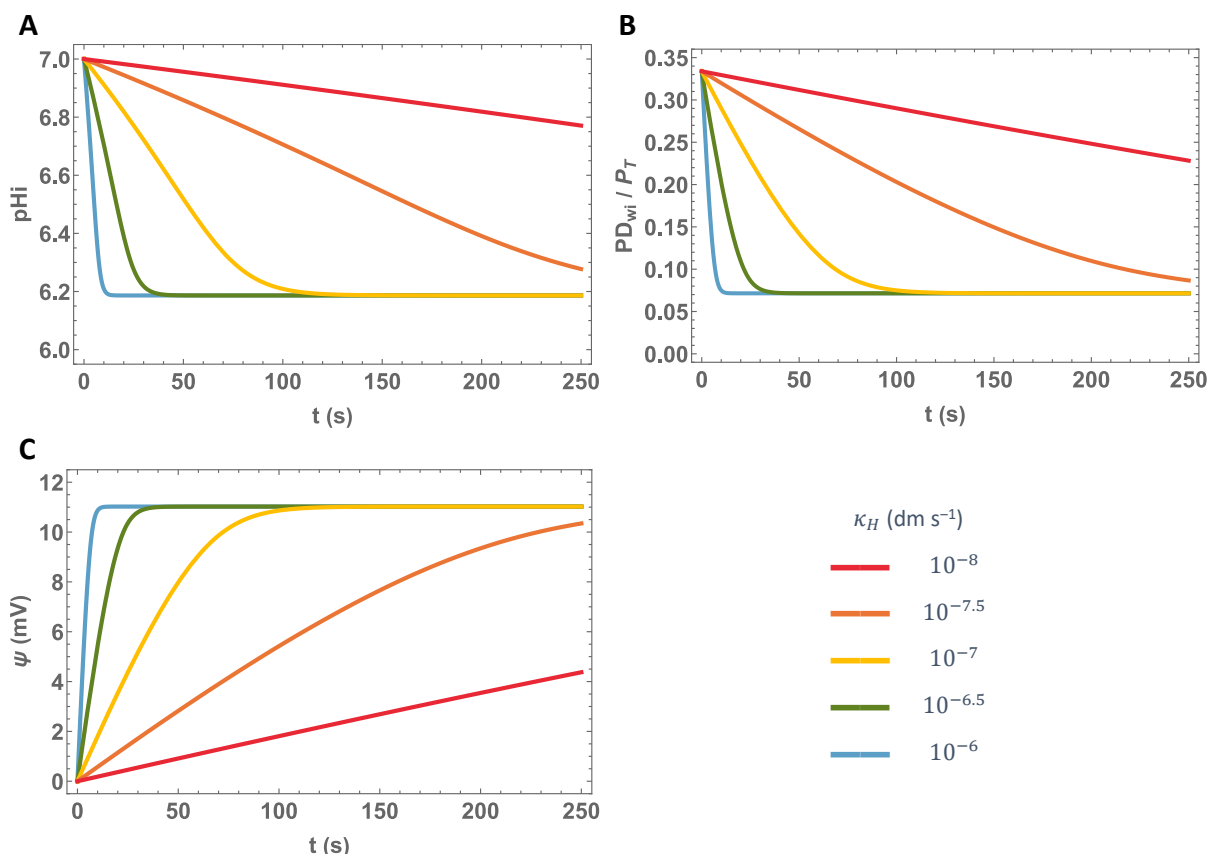
Figure 70. Effect of the proton permeability when the potassium permeability is negligible on the **A)** inner pH, **B)** fraction of the fluorescent probe, and **C)** transmembrane potential. Simulation conditions: $H_{wo}[0] = 10^{-6}$ M, $c_L = 8.50 \times 10^{-5}$ M, $P_T = 10^{-4}$ M, and $r = 68$ nm.

At a 10^{-12} dm s^{-1} potassium permeability, the pH variation becomes biphasic in the timescale of the stopped-flow experiments (**Figure 71A**). This is not so evident in the variation of the molar fraction of the probe (**Figure 71B**) due to the depletion of this specie at low pH values, and it is no longer in the linear range of variation of the fraction of deprotonated species with pH (**Figure 61**). Under these conditions, the fluorescence would not be able to accurately report the variations of the pH inside the vesicles. The transmembrane potential attains higher transient values the more permeable the membrane is to protons (**Figure 71C**). This is because more protons enter the vesicles before charge compensation by the counterflow of potassium ions. As the permeability of protons approaches that of potassium ions, the excess charge accumulated inside the vesicles becomes negligible and no transmembrane potential is generated.
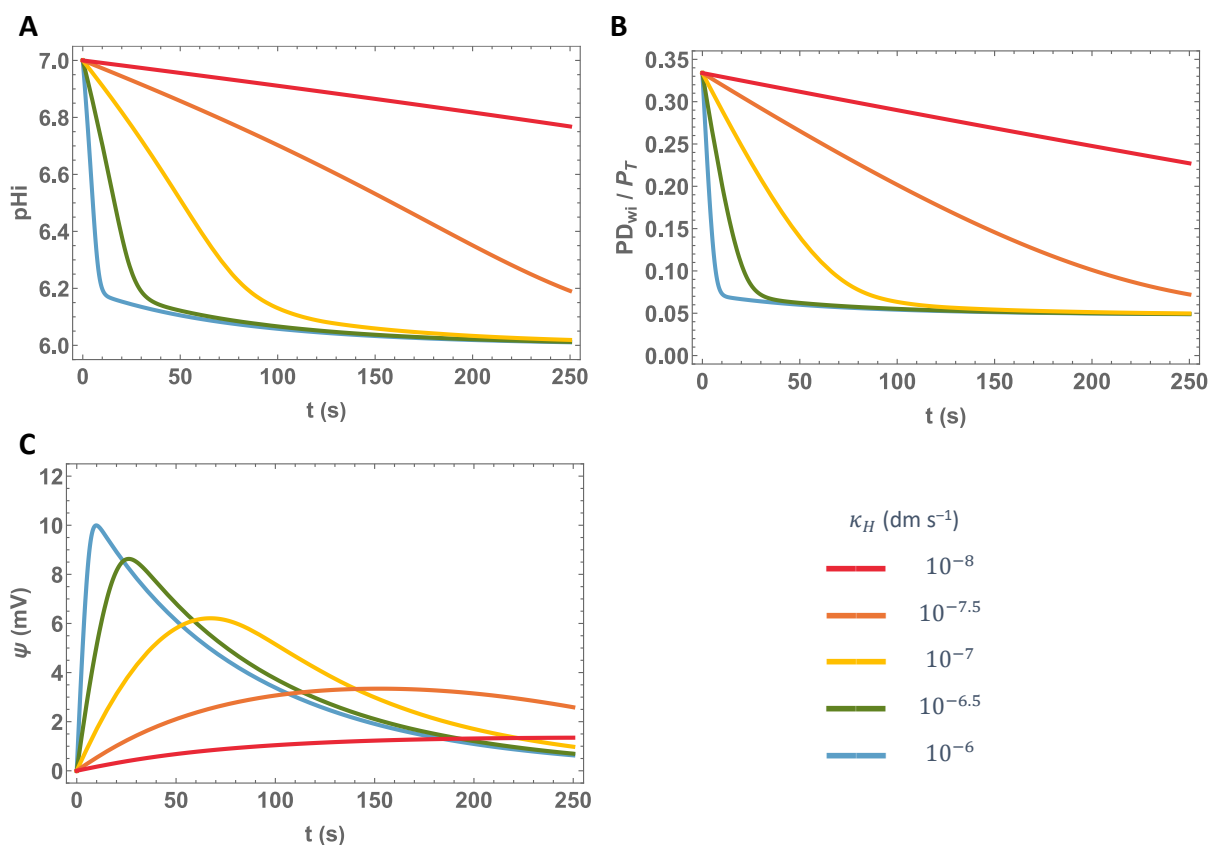
Figure 71. Effect of the proton permeability on the **A)** inner pH, **B)** fraction of the fluorescent probe, and **C)** transmembrane potential. Simulation conditions: $\kappa_K = 10^{-12}$ dm s^{-1}, $H_{wo}[0] = 10^{-6}$ M, $c_L = 8.50 \times 10^{-5}$ M, $P_T = 10^{-4}$ M, and $r = 68$ nm.

If the permeability of potassium is increased at a fixed value of proton permeability ($\kappa_H = 10^{-6}$ dm s^{-1}), the rate of the slow step in the pH equilibration increases (**Figure 72A**). In the limit of very high membrane permeability to potassium ions, no significant transmembrane potential is generated, and the pH variation becomes monophasic. Additionally, as mentioned before, the sensitivity of the fluorescence intensity variation to this slow step in the pH equilibration is very low (**Figure 72**). Experimentally, it is observed that the fluorescence variation is much more affected by the presence and the amount of valinomycin (see **Figure 65** and **Figure 68** on Sections 4.5.1 and 4.5.2) than predicted by the model considering the parameters representative of the experimental conditions.

A

B

κ_K (dm s^{-1})

10^{-13}	$10^{-12.5}$	10^{-12}	$10^{-11.5}$	10^{-11}	$10^{-10.5}$	10^{-10}

Figure 72. Effect of the potassium permeability on the **A)** inner pH and **B)** fraction of the fluorescent probe. The inset graph on plot B shows in detail the first 30 seconds. Simulation conditions: $\kappa_H = 10^{-6}$ dm s^{-1}, $H_{wo}[0] = 10^{-6}$ M, $c_L = 8.50 \times 10^{-5}$ M, $P_T = 10^{-4}$ M, and $r = 68$ nm.

The differences between the experimental observations and the simulations, and the difficulty to fit the data with the kinetic model can have various sources. On one hand, the vesicles are relatively small and thus more prone to stochastic effects. The aim to prepare liposomes with a 200 nm diameter was not accomplished: although the polydispersity index was low, the liposomes had only a ≈ 140 nm diameter. For those small sizes, at a pH of 7, there are on average only 0.07 free protons inside each vesicle and this increases to 0.7 at pH 6. The presence of the fluorescent probe increases the total number of protons (free and associated with probe) to around 44 and 64 at an inner pH of 7 and 6, respectively. The pH equilibration from 7 to 6, requires the entry of 20 protons into the vesicles. Under these conditions, stochastic effects should not be very significant, and the average of the behaviour observed for all vesicles should be similar to that of an average vesicle. Nevertheless, vesicles with larger sizes are preferable and they may be prepared by methods other than extrusion. Unfortunately the polydispersity index obtained by those methods is usually large and multilamelarity may also be a problem.[124,126] Both factors will complicate the estimation of the entrapped volumes, the barrier area and the kinetic analysis.[119]

Uncertainty about the true buffer capacity inside the vesicles may also contribute to these discrepancies. In the simulations the inner aqueous compartment of the vesicles is only buffered by the probe, which is present at a relatively low concentration (10^{-4} M). However, in the real system, other species may contribute to the buffer capacity. Carbon dioxide can easily dissolve in air-exposed solutions, and its solubility of carbon dioxide is pH-dependent, which further complicates the analysis. Carbonic acid has two ionisation equilibria ($pK_{a_1} = 3.5^{127}$ and $pK_{a_2} = 10.3^{128}$) and will contribute to the pH buffer capacity inside the vesicles. To explore this hypothesis, the model could be modified to

119

include other species with pH buffer capacity inside the vesicles. But, for simplicity, in the simulations shown below, the concentration of the probe was increased 10-fold ($P_T = 10^{-3}$ M).

In these simulations, potassium permeability was fixed at 10^{-13} dm s^{-1} to enhance the biphasic behaviour of the pH variation and the permeability of proton was varied between 10^{-8} and 10^{-6} dm s^{-1} (**Figure 73**). When the buffer capacity in the vesicles' lumen is increased, more protons must cross the membrane to equilibrate with the concentration outside. This is because inflowing protons are captured by the weak base of the buffer, which dampens the pH change. Concomitantly, under these conditions, a higher transmembrane potential is developed (**Figure 73C**) in comparison to the conditions described before, and it does not dissipate during the timescale of the plate reader experiments. The amount of protons that must permeate during the slower phase (limited by the dissipation of the transmembrane potential) increases, and therefore, the variation in the internal pH and fluorescence has a higher contribution of the slowest phase for the overall kinetics (**Figure 73A and B**). Also, under these conditions, it takes longer to reach the equilibrium (1 to 2 hours, see Section 4.5.1). Both changes approach the behaviour observed experimentally, suggesting that an increased buffer capacity inside the vesicles is one of the reasons for the mismatch between simulations and experimental results.
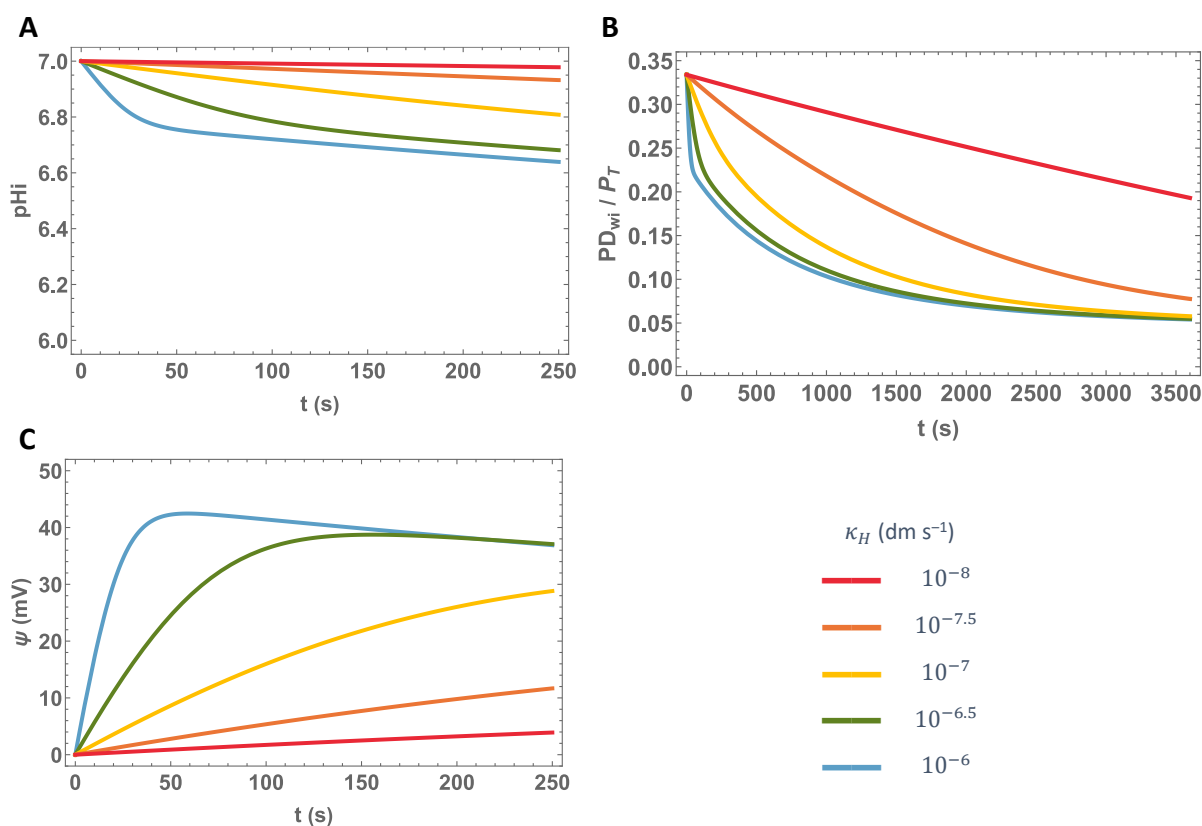
Figure 73. Effect of the proton permeability on the **A)** inner pH, **B)** fraction of the fluorescent probe (simulation time: 1 hour) and **C)** transmembrane potential. Simulation conditions: $\kappa_K = 10^{-13}$ dm s^{-1}, $H_{wo}[0] = 10^{-6}$ M, $c_L = 8.50 \times 10^{-5}$ M, $P_T = 10^{-3}$ M, and $r = 68$ nm.

As done before, and because the intensity of fluorescence has a biphasic behaviour (changes too quickly in the beginning but takes between 1 to 2 hours to equilibrate), the permeability of the proton was fixed at 10^{-6} dm s^{-1} and the permeability of potassium was changed between 10^{-11} and 10^{-14} dm s^{-1}. These simulations show that the increased buffer capacity makes the pH (**Figure 74A**) and the fluorescence (**Figure 74B**) much more sensitive to the permeability of potassium as enhanced by valinomycin, approaching the experimental observations. This indicates that the observed discrepancies between simulations and experiments may be due in part to the buffer capacity having been underestimated in the former. As the excess buffer capacity is most likely due to the dissolution of atmospheric CO_2, it would be necessary to deaerate the solutions and perform these experiments under very controlled conditions.

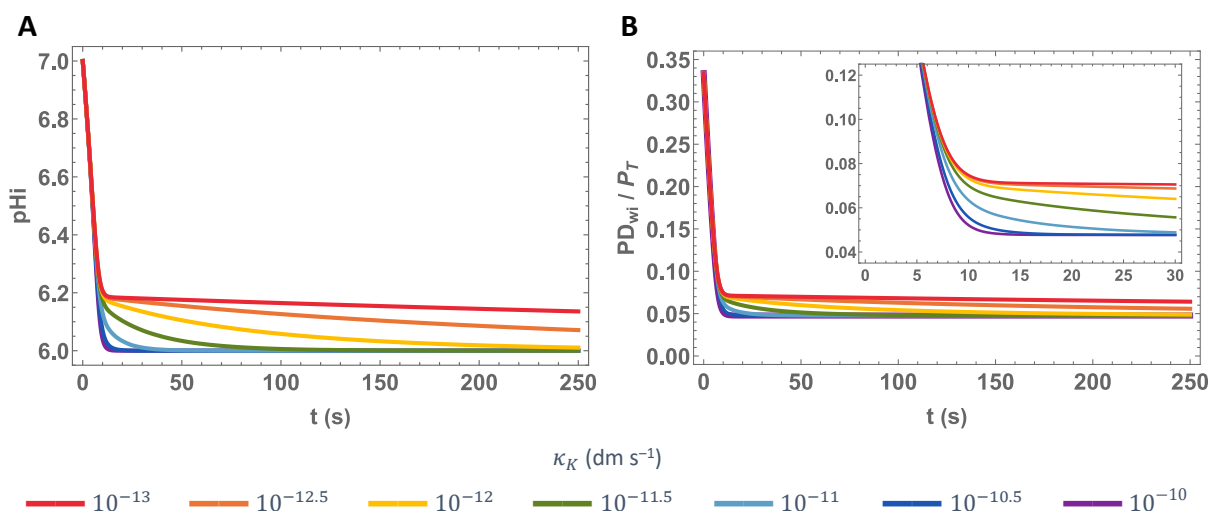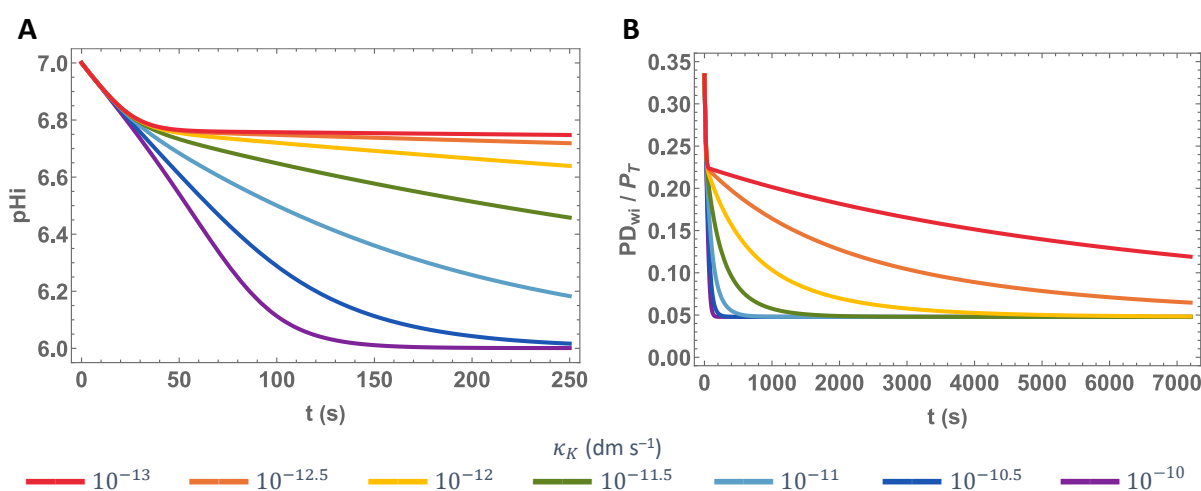**Figure 74.** Effect of the potassium permeability on the **A)** inner pH and **B)** fraction of the fluorescent probe (simulation time: 2 hours). Simulation conditions: $\kappa_H = 10^{-6}$ dm s^{-1}, $H_{wo}[0] = 10^{-6}$ M, $c_L = 8.50 \times 10^{-5}$ M, $P_T = 10^{-3}$ M, and $r = 68$ nm.

Although a calibration between signal and pH was not done, the simulations with a higher buffer capacity suggest that κ_H between 10^{-6} and $10^{-6.5}$ dm s^{-1} and κ_K between 10^{-12} and 10^{-13} dm s^{-1} produce curves of the fraction of the fluorescent probe similar to that observed experimentally in the plate reader (long timescale) and stopped-flow (short timescale). Thus, we used these values as initial guesses to fit the kinetic model to the stopped-flow data for the pH equilibration when the outer pH was jumped to 6, for several valinomycin concentrations. In one series of fit the concentration of carbonic acid was arbitrary fixed at 10^{-3} M, and in another the buffer capacity was solely due to the pH-sensitive probe. The latter fits were considerably worse (**Figure 75**). The former fit yielded narrow confidence intervals for both κ_H and κ_K, and both estimates increase with the concentration of valinomycin (**Figure 76**). The effect is stronger on potassium than on proton permeabilities. By increasing the concentration of valinomycin from 0.01 to 1 μM, proton permeability increases 4.8 ± 0.3-fold and potassium permeability increases 6.9 ± 0.9-fold (**Table 23**). This is somewhat expected and according to information found in the literature. In a work performed by Johnson and Bangham,

it was verified that the permeability coefficient of potassium increases linearly with the concentration of valinomycin up to $\approx$ 20 µmol per mol of lipid.[129] In this work, the lipid concentration was 1 mM, and the ratio is 10 µmol valinomycin *per* mol of lipid (when the concentration of valinomycin is 0.01 µM). It is not surprising that the proton permeability is also affected by the presence of valinomycin. This hypothesis had already been suggested when it was observed that the higher characteristic constant, obtained in the analysis of the stopped-flow experiments, also increase linearly with the concentration of valinomycin.
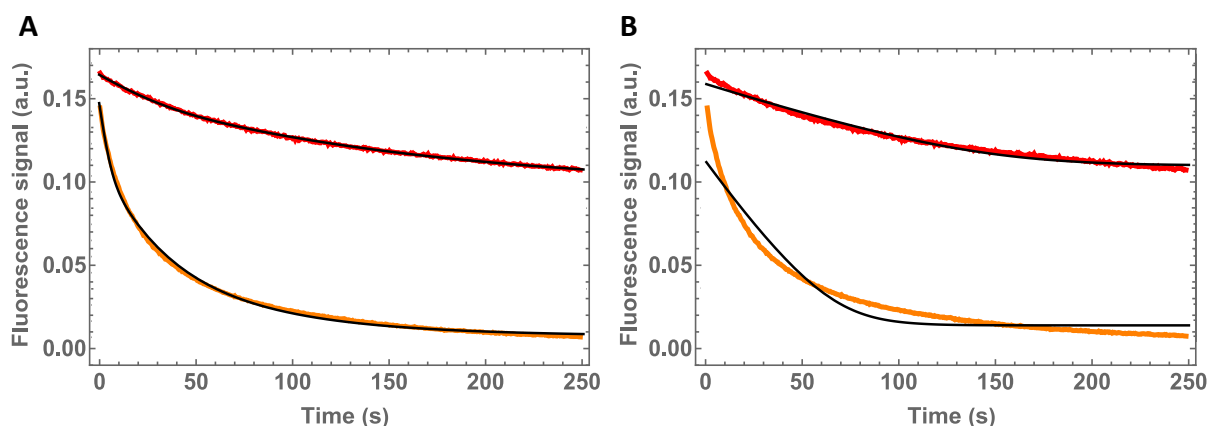
Figure 75. Goodness of fit when considering **A)** $P_T = 10^{-3}$ M and **B)** $P_T = 10^{-4}$ M. Red curves represent the fluorescence variation when imposing a pH gradient of 1 unit in the absence of valinomycin and orange curves when in the presence of 1 µM valinomycin.
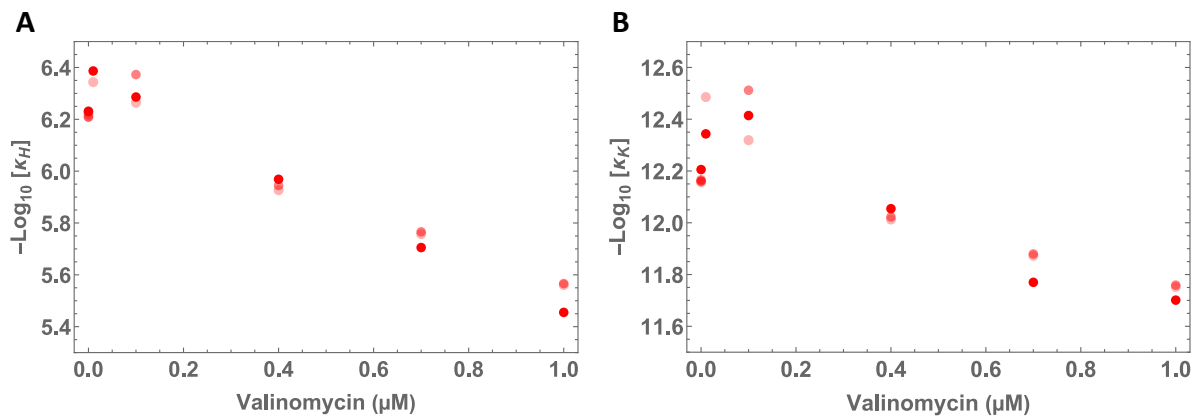
Figure 76. Effect of valinomycin on **A)** proton and **B)** potassium permeabilities. Parameters were obtained by fitting the experimental data (outer pH changed to 6) using a simplified version of Model IV. The points are different replicated.

Table 23. Proton and potassium permeabilities obtained from fitting the stopped-flow data using a simplified version of Model IV, with the parameters $H_{wo}[0] = 10^{-6}$ M, $c_L = 8.50 \times 10^{-5}$ M, $P_T = 10^{-3}$ M, and $r = 68$ nm.

Valinomycin (µM)	κ_H (dm s⁻¹)	κ_K (dm s⁻¹)
0	$(6.01 \pm 0.07) \times 10^{-7}$	$(6.73 \pm 0.17) \times 10^{-13}$
0.01	$(4.32 \pm 0.21) \times 10^{-7}$	$(3.90 \pm 0.63) \times 10^{-13}$
0.1	$(4.95 \pm 0.37) \times 10^{-7}$	$(3.91 \pm 0.50) \times 10^{-13}$
0.4	$(1.13 \pm 0.03) \times 10^{-6}$	$(9.34 \pm 0.27) \times 10^{-13}$
0.7	$(1.81 \pm 0.08) \times 10^{-6}$	$(1.45 \pm 0.12) \times 10^{-12}$
1	$(2.99 \pm 0.26) \times 10^{-6}$	$(1.83 \pm 0.08) \times 10^{-12}$

Chapter 5

General Conclusion

Drug discovery and development is a long, risky and expensive process. It begins with thousands of candidates and only a few of which will enter clinical trials and from those a small fraction reaches the market. Before the clinical trials phase, drug candidates must be characterised in terms of their solubility, stability, toxicity, activity, interaction with different biological entities, and metabolism. The permeability of these compounds through biomembranes is extremely important because it can determine the efficacy of absorption, distribution, and elimination. It is commonly assessed using cell-based (Caco-2, MDCK and brain capillary endothelial cells) or artificial membranes assays (PAMPA and liposome-based assays).

Recently, a pH variation assay has been used to evaluate the permeability of weak acids and bases by monitoring the fluorescence of an entrapped probe.[68] In comparison with the standard protocols used in the pharmaceutical industry, the pH variation assay is not expensive or time-consuming, mimics well the nature of lipid membranes, and the correlation with human absorption data is comparable or better than that of the commonly used assays.[69] However, this assay may be prone to some artefacts, and the permeability coefficients obtained are not always consistent with those from other approaches. With the purpose of identifying these artefacts and understanding how they can be prevented, a kinetic model that includes the permeation of a weak acid/base and its conjugated form, the proton, and potassium was developed. The behaviour of very complex systems is not always intuitive, and these approaches allow a more detailed knowledge of the system.

Using a simple model that only considers the permeation of the uncharged weak acid, we studied the effect of varying the system topology, solute lipophilicity, and solute and probe concentrations. Smaller vesicles lead to faster permeation kinetics, higher pH variations, and lower occupancy numbers. Lower occupancy numbers *per* vesicle increase the experimental noise and make kinetics more complex. The higher the concentration of solute and/or the lower the concentration of the probe, the higher the pH variation. This increases the method's sensitivity but the accuracy of the probe as a reporter of the pH variation and solute accumulation decreases. When the pH variation is less than 0.25 units, the accuracy of the probe is acceptable. Thus, for each set of experiments, a pH calibration must be performed, determining at least the fluorescence signal at very acidic and alkaline pH, and the concentration of solute should be adjusted to lead to a pH variation of about 0.25 units

When the permeation of charged species is not allowed, the variation of the concentration of solute inside the vesicles is well described by a mono-exponential function and the fluorescence (and

probe concentration) is well described by a combination of two exponential functions. The lower characteristic constant, the one with the higher pre-exponential factor, is the one closer to the characteristic constant of solute accumulation. Generally, the characteristic constant is higher when following the probe fluorescence than for following the solute dynamics. Thus, the permeability predicted by fitting the fluorescence will be slightly higher than that obtained directly from the solute accumulation profile.

The analysis of the assumptions underlying the widely used equation $P_{app} = \beta \frac{r}{3}$ showed that it cannot be used to evaluate the permeability of weak acids and bases. It can lead to significantly biased estimates of the ability of compounds to cross membranes because i) the volume inside the vesicles is not always much smaller than the volume outside the vesicles, ii) the pH gradient prevents the equalisation of the solute concentration in the donor and acceptor compartments, and iii) drug-like compounds are usually lipophilic and are sequestrated in the membrane.

The rate at which drug-like molecules permeate lipid membranes is usually fast and requires the use of stopped-flow equipment, which is unavailable in most laboratories. As a way to address this limitation, in this work we have evaluated the effect of including a membrane-impermeable binding agent encapsulated in the vesicles. This results in an increase in the total amount of solute that permeates into the vesicles, which leads to a slower permeation kinetics, and may lead to higher pH variations. However, the simulations performed show that the effects are modest because a large fraction of the permeated solute remains sequestered in the inner leaflet of the membrane barrier.

The permeation of the conjugated base and/or the proton leads to the restoration of the inner pH. The rate of the charged solute flip-flop and the permeability of the protons influence the pH variation profile. The slower the permeation kinetics of the charged species, the less the overlap of the fast and slow processes, the higher the transient pH variation, and the slower the dissipation of the pH gradient. The pH variation profile is also dependent on the fraction of the charged solute in solution. Due to the permeation of this charged species a transmembrane potential is developed. The accumulation of electrical charges (negative for the permeation of weak acids) inside the vesicles prevents the system from having equal concentrations of the charged species in the donor and acceptor compartments. Additionally, the transmembrane potential rises with the increase of the contribution of the charged species to the overall kinetics of solute equilibration. In other words, the permeation of stronger acids (or stronger bases) is accompanied by the development of higher transmembrane potentials.

The dissipation of the transmembrane potential was modelled by the slow counterflow of potassium ions, present at high concentrations. As the membrane becomes more permeable to potassium, the magnitude of the developed transmembrane potential decreases. The transmembrane

potential is an opposite driving force for the ion transport. As such, the higher the permeability of potassium, the faster the solute equilibrium is attained.

The coexistence of various processes with different rates makes the kinetics more complex and harder to analyse. Thus, the use of the ionophore valinomycin could play a leading role in the solute permeation kinetics. The permeation of weak acids and bases exhibits a biphasic behaviour because of the faster permeation of the neutral form and the slower permeation of the charged species (conjugated base and acid, respectively, and proton/hydroxide). The biphasic behaviour is more significant for solutes with pK_a^{Sw} around the solution pH. For bi-exponential kinetics, the permeability should be calculated using the two characteristic constants. These characteristic constants cannot be directly attributed to the permeation of the weak acid/base and its conjugated acid/base. They reflect not only the relative fraction of each one but also their kinetic properties. The weighted characteristic constant shows a high dependence on the solutes' pK_a. It approaches the values predicted for non-ionising solutes as the acid gets weaker, and the value for the permeation of the charged solute as the acid gets stronger.

Experimentally, the permeation of a weak acid or base is followed through the variation in the fluorescence intensity of a pH probe. The fluorescence variation is generally fitted through the combination of four exponential terms, two describing the faster signal variation and two the slower recovery phase. As the pH variation assay is an indirect method to evaluate the permeability coefficient of weak acids and bases, its accuracy may be compromised. Our simulation results have shown that the characteristic constant that best describes a monophasic accumulation of solute is the one with a higher pre-exponential term from the fast phase of fluorescence variation. On the other hand, if solute accumulation is biphasic, the characteristic constant that describes the slower phase is reported in the fluorescence recovery phase, and it is also the term with the highest absolute pre-exponential factor. Depending on the relative rate of permeation of neutral and charged species the two phases may partially overlap. This increases the difficulty and decreases the accuracy of the pH variation assay. An accurate permeability coefficient must be calculated using the weighted characteristic constant obtained from the solute dynamics. However, it is not possible to estimate the weighting coefficients of each characteristic constants. Using only one of the characteristics constants will not be unreliable under conditions at which the solute dynamics is nearly monophasic.

The simulations of the permeation of weak bases corroborate the conclusions taken in the simulations for the permeation of weak acids.

The major goals of our experimental work were the estimation of the permeability of H^+/OH^- and the assessment of the effect of valinomycin on the K^+ permeability coefficient. However, they were not successfully achieved. This information is very important to dissect the contribution of these species to the kinetics of weak acids and bases equilibration, and especially to estimate the permeability of the charged solute. From the global fitting of the data obtained with the plate reader (slow processes) and the stopped-flow (fast processes), it was observed that valinomycin has a higher effect on the slower process, although it also influences the faster one. The characteristic constant of both processes increases linearly with the concentration of valinomycin. The influence on the slower process was anticipated since valinomycin is a potassium ionophore, and this process is attributed to the dissipation of the transmembrane potential. However, the faster process is usually attributed to the transport of H^+/OH^- due to the pH gradient imposed and should not be affected by valinomycin, at least when the concentration of K^+ is high. Additionally, the pH equilibration experiments showed higher sensitivity to the presence of valinomycin than was predicted using a simplified version of the complete kinetic model (Model IV) with a set of parameters representative of the experiment. The hypothesis that the carbonic acid could be responsible for an increased buffer capacity inside the vesicles was evaluated. By increasing the buffer capacity, the pH and the fluorescence profiles become more sensitive to potassium permeability, and they describe considerably better the experimental results obtained. Despite the consistency of the results, it is important to notice that they may not reflect the experimental reality as the carbonic acid concentration is unknown. This study must be performed under more controlled conditions, to confirm if the valinomycin also increases the proton permeability despite the significantly higher concentration of potassium. If this is confirmed, valinomycin will be unsuitable for the desired purpose. This ionophore will not only affect the pH restoration but also the initial pH changing phase, making the analysis more difficult.

Overall, this work gave a better understanding of the permeation of weak acids and bases and how some specific parameters affect the overall kinetics. Additionally, it denotes some important information to be taken in mind for further experiments.

Future Work

This project provides some new insights into the pH variation assay, its strengths, and weaknesses. The kinetic models for the permeation of weak acids and bases were successfully implemented and can be used to answer some future questions.

Some of the questions identified during this work are indicated below, together with a brief description of what has been done and/or a proposal on how they will be addressed in future work.

▪ One of the aims was the preparation of larger vesicles, to increase the amount of solute that must permeate, eliminate stochastic effects and slow-down the equilibration process. By extrusion it is not possible to prepare vesicles much larger than 100 nm in diameter. During the course of this Master thesis, myself and Elsa Loureiro, a Biochemistry student, tried to prepare bigger lipidic vesicles by reverse phase evaporation and we successfully obtained vesicles with 2.5 to 5 μm in diameter. However, the samples are very heterogeneous (higher polydispersity index), and the vesicles present multilamelarity. These characteristics do not satisfy the requirement for a pH variation assay, and no more studies were performed. We also successfully encapsulated bovine serum albumin (BSA), a known binding agent for different compounds, in vesicles prepared by extrusion and reverse phase evaporation. However, as shown in this work (Section 4.2.2), the inclusion of BSA would not have the desired effect in the permeation of weak acids and bases that equilibrate into vesicles with a 100 nm radius. This is a consequence of the low aqueous entrapped volumes. Despite not having been much explored, the inclusion of BSA inside the vesicles could be used to simultaneously estimate protein-ligand affinity and solute permeability coefficients.

▪ Another limitation, when performing kinetics measurements is the delay between the beginning of the reaction or process and the data collection due to limitations of the equipment used. This is a major problem when a plate reader is used, but for very fast processes it may be significant even when using a stopped-flow. This was very evident in the pH equilibration experiments (Section 4.5). During this Master thesis, myself and Anaísa Simões, a Medicine student, evaluated the effect of the membrane lipid composition and the corresponding membrane phase (liquid-disordered or liquid-ordered) on the efflux of fluorescein. We prepared liposomes with POPC, POPC : Cholesterol (1：1), and Sphingomyelin : Cholesterol (6：4), and as expected, the kinetics of fluorescein efflux was strongly affected by the presence of cholesterol in the membrane. The characteristic time for equilibration was 10 min, 30 min, and around 6 hours, respectively, for the POPC, POPC:Cholesterol, and Sphingomyelin:Cholesterol membranes respectively. The use of cholesterol enriched membranes in the pH variation assay may therefore be a promising approach to slow-down the rate of solute permeation.

- The aim of the pH equilibration studies was the measurement of the permeability coefficient of protons and potassium ions. There is a broad spectrum of values on literature and characterising it, in our conditions, would be essential to estimate the permeability coefficient of charged solute species. This was not successfully done, namely due to the dissolution of carbon dioxide in the solution, and it remains an objective in future works. We are considering a different approach to attain this goal, based on the potentialities of photoacids and photobases. These compounds are capable of acidifying or basificating persistently the aqueous environment, when irradiated with a single laser pulse. This would avoid the constraints caused by the exposure of the sample to the air and it would be possible to deaerate the samples before the assay and keep the system closed. The pH-sensitive probe HPTS is also a photoacid, but we will probably have to search for a new compound. It will be necessary to make sure that i) the membrane is impermeable to the photoacid/photobase, and ii) the radiation used for excitation and to create the pH variation is not absorbed by the pH-sensitive probe, since the light exposure could destroy it (photobleaching), and there would be competition for absorption of the incident light leading to difficulties in the calculation of the pH variation generated. Another problem in the design of those experiments was the pH gradient imposed. It was too big, and in those conditions, the fluorescence does not report the variation of the pH nor the variation of the proton concentration. We must redefine conditions and using photoacids/photobases, it will be possible to explore better conditions. Once the proton and potassium permeabilities are determined, the pH variation assay and the model presented here could also be used to estimate the flip-flop rate of weak acids and bases.

References

1. Watson, H. Biological membranes. *Essays Biochem.* **59**, 43–69 (2015).

2. Staverman, A. J. Structure and function of membranes. *J. Memb. Sci.* **16**, 7–20 (1983).

3. Gorter, E., Grendel, F. On bimolecular layers of lipoids on the chromocytes of the blood. *J. Exp. Med.* **41**, 439–443 (1925).

4. Singer, S. J., Nicolson, G. L. The fluid mosaic model of the structure of cell membranes. *Science* **175**, 720–731 (1972).

5. Vaz, W. L. C. Lipid Bilayers: Properties. in *Wiley Encyclopedia of Chemical Biology* 1–15 (John Wiley & Sons, Inc., 2008).

6. Moreno, M. J., Estronca, L. M. B. B., Vaz, W. L. C. Translocation of phospholipids and dithionite permeability in liquid-ordered and liquid-disordered membranes. *Biophys. J.* **91**, 873–881 (2006).

7. Coreta-Gomes, F. M., Vaz, W. L. C., Moreno, M. J. Effect of acyl chain length on the rate of phospholipid flip-flop and intermembrane transfer. *J. Membr. Biol.* **251**, 431–442 (2018).

8. Brown, D. Structure and function of membrane rafts. *Int. J. Med. Microbiol.* **291**, 433–437 (2002).

9. Alberts, B., Bray, D., Hopkins, K., Johnson, A., Lewis, J., Raff, M., *et al. Essential Cell Biology*. *Garland Science* (2014).

10. Seelig, J., Browning, J. L. General features of phospholipid conformation in membranes. *FEBS Lett.* **92**, 41–44 (1978).

11. Phase Transition Temperatures for Glycerophospholipids | Avanti Polar Lipids. *Phase Transition Temperatures for Glycerophospholipids* https://avantilipids.com/tech-support/physical-properties/phase-transition-temps (Accessed on 23-08-2021).

12. Moreno, M. J., Martins, P. A. T., Bernardino, E. F., Abel, B., Ambudkar, S. V. Characterization of the lipidome and biophysical properties of membranes from High Five insect cells expressing mouse P-glycoprotein. *Biomolecules* **11**, 426–442 (2021).

13. Hotchkiss, R. D., Dubos, R. J. Fractionation of the bactericidal agent from cultures of a soil bacillus. *J. Biol. Chem.* **132**, 791–792 (1940).

14. Hladky, S. B., Haydon, D. A. Ion transfer across lipid membranes in the presence of gramicidin A. I. Studies of the unit conductance channel. *Biochim. Biophys. Acta* **274**, 294–312 (1972).

15. Gramicidin S | C60H92N12O10 - PubChem. https://pubchem.ncbi.nlm.nih.gov/compound/Gramicidin-S (Accessed on 24-08-2021).

16. Brockmann, H., Schmidt-Kastner, G. Valinomycin I, XXVII. Mitteil. über Antibiotica aus Actinomyceten. *Chem. Ber.* **88**, 57–61 (1955).

References

17. Shemyakin, M. M., Aldanova, N. A., Vinogradova, E. I., Feigina, M. . The structure and total synthesis of valinomycin. *Tetrahedron Lett.* **4**, 1921–1963 (1963).

18. Neupert-Laves, K., Dobler, M. The crystal structure of a K+ complex of valinomycin. *Helv. Chim. Acta* **58**, 432–442 (1975).

19. Varma, S., Sabo, D., Rempe, S. B. K+/Na+ selectivity in K-channels and valinomycin: Over-coordination Vs cavity-size constraints. *J. Mol. Biol.* **376**, 13–22 (2008).

20. Hughes, J., Rees, S., Kalindjian, S., Philpott, K. Principles of early drug discovery. *Br. J. Pharmacol.* **162**, 1239–1249 (2011).

21. Pankevich, D. E., Altevogt, B. M., Dunlop, J., Gage, F. H., Hyman, S. E. Improving and accelerating drug development for nervous system disorders. *Neuron* **84**, 546–553 (2014).

22. Kamb, A., Wee, S., Lengauer, C. Why is cancer drug discovery so difficult? *Nat. Rev. Drug Discov.* **6**, 115–120 (2007).

23. Comirnaty | European Medicines Agency. https://www.ema.europa.eu/en/medicines/human/EPAR/comirnaty (Accessed on 19-08-2021).

24. Vaxzevria (previously COVID-19 Vaccine AstraZeneca) | European Medicines Agency. https://www.ema.europa.eu/en/medicines/human/EPAR/vaxzevria-previously-covid-19-vaccine-astrazeneca (Accessed on 19-08-2021).

25. Spikevax (previously COVID-19 Vaccine Moderna) | European Medicines Agency. https://www.ema.europa.eu/en/medicines/human/EPAR/spikevax-previously-covid-19-vaccine-moderna (Accessed on 19-08-2021).

26. COVID-19 Vaccine Janssen | European Medicines Agency. https://www.ema.europa.eu/en/medicines/human/EPAR/covid-19-vaccine-janssen (Accessed on 19-08-2021).

27. Campbell, I. B., Macdonald, S. J. F., Procopiou, P. A. Medicinal chemistry in drug discovery in big pharma: past, present and future. *Drug Discov. Today* **23**, 219–234 (2018).

28. Kerns, E. H., Di, L. Pharmaceutical profiling in drug discovery. *Drug Discov. Today* **8**, 316–323 (2003).

29. Wishart, D. S. Improving early drug discovery through ADME modelling: an overview. *Drugs R. D.* **8**, 349–62 (2007).

30. Pocock, S. J. *Clinical trials - A practical approach*. *Wlley* vol. 33 (John Wiley & Sons Ltd,., 2013).

31. Hou, T., Wang, J., Zhang, W., Wang, W., Xu, X. Recent advances in computational prediction of drug absorption and permeability in drug discovery. *Curr. Med. Chem.* **13**, 2653–2667 (2006).

32. Lipinski, C. A., Lombardo, F., Dominy, B. W., Feeney, P. J. Experimental and computational approaches to estimate solubility and permeability in drug discovery and development settings.

Adv. Drug Deliv. Rev. **23**, 3–25 (1997).

33. Krämer, S. D., Aschmann, H. E., Hatibovic, M., Hermann, K. F., Neuhaus, C. S., Brunner, C., *et al.* When barriers ignore the "rule-of-five". *Adv. Drug Deliv. Rev.* **101**, 62–74 (2016).

34. Fogh, J., Fogh, J. M., Orfeo, T. One hundred and twenty-seven cultured human tumor cell lines producing tumors in nude mice. *J. Natl. Cancer Inst.* **59**, 221–226 (1977).

35. Hidalgo, I. J., Raub, T. J., Borchardt, R. T. Characterization of the human colon carcinoma cell line (Caco-2) as a model system for intestinal epithelial permeability. *Gastroenterology* **96**, 736–749 (1989).

36. Hilgers, A. R., Conradi, R. A., Burton, P. S. Caco-2 cell monolayers as a model for drug transport across the intestinal mucosa. *Pharm. Res.* **7**, 902–910 (1990).

37. Schipper, N. G. M., Vårum, K. M., Artursson, P. Chitosans as absorption enhancers for poorly absorbable drugs. 1: Influence of molecular weight and degree of acetylation on drug transport across human intestinal epithelial (Caco-2) cells. *Pharm. Res.* **13**, 1686–1692 (1996).

38. Bourdet, D. L., Pollack, G. M., Thakker, D. R. Intestinal absorptive transport of the hydrophilic cation ranitidine: A kinetic modeling approach to elucidate the role of uptake and Efflux Transporters and paracellular vs. transcellular transport in Caco-2 cells. *Pharm. Res.* **23**, 1178–1187 (2006).

39. Artursson, P., Karlsson, J. Correlation between oral drug absorption in humans and apparent drug permeability coefficients in human intestinal epithelial (Caco-2) cells. *Biochem. Biophys. Res. Commun.* **175**, 880–885 (1991).

40. Bachmakov, I., Werner, U., Endress, B., Auge, D., Fromm, M. F. Characterization of beta-adrenoceptor antagonists as substrates and inhibitors of the drug transporter P-glycoprotein1. *Fundam. Clin. Pharmacol.* **20**, 273–282 (2006).

41. Silva, R., Carmo, H., Dinis-Oliveira, R., Cordeiro-da-Silva, A., Lima, S. C., Carvalho, F., *et al.* In vitro study of P-glycoprotein induction as an antidotal pathway to prevent cytotoxicity in Caco-2 cells. *Arch. Toxicol.* **85**, 315–326 (2011).

42. Chen, J., Lin, H., Hu, M. Metabolism of flavonoids via enteric recycling: Role of intestinal disposition. *J. Pharmacol. Exp. Ther.* **304**, 1228–1235 (2003).

43. Hubatsch, I., Ragnarsson, E. G. E., Artursson, P. Determination of drug permeability and prediction of drug absorption in Caco-2 monolayers. *Nat. Protoc.* **2**, 2111–2119 (2007).

44. Sambuy, Y., De Angelis, I., Ranaldi, G., Scarino, M. L., Stammati, A., Zucco, F. The Caco-2 cell line as a model of the intestinal barrier: influence of cell and culture-related factors on Caco-2 cell functional characteristics. *Cell Biol. Toxicol.* **21**, 1–26 (2005).

45. Sun, D., Lennernas, H., Welage, L. S., Barnett, J. L., Landowski, C. P., Foster, D., *et al.* Comparison of human duodenum and Caco-2 gene expression profiles for 12,000 gene sequences tags and

correlation with permeability of 26 drugs. *Pharm. Res.* **19**, 1400–1416 (2002).

46. Irvine, J. D., Takahashi, L., Lockhart, K., Cheong, J., Tolan, J. W., Selick, H. E., *et al.* MDCK (Madin-Darby Canine Kidney) cells: A tool for membrane permeability screening. *J. Pharm. Sci.* **88**, 28–33 (1999).

47. Di, L., Kerns, E. H., Bezar, I. F., Petusky, S. L., Huang, Y. Comparison of blood–brain barrier permeability assays: in situ brain perfusion, MDR1-MDCKII and PAMPA-BBB. *J. Pharm. Sci.* **98**, 1980–1991 (2009).

48. Hellinger, É., Veszelka, S., Tóth, A. E., Walter, F., Kittel, Á., Laura Bakk, M., *et al.* Comparison of brain capillary endothelial cell-based and epithelial (MDCK-MDR1, Caco-2, and VB-Caco-2) cell-based surrogate blood-brain barrier penetration models. *Eur. J. Pharm. Biopharm.* **82**, 340–351 (2012).

49. Kansy, M., Senner, F., Gubernator, K. Physicochemical high throughput screening: parallel artificial membrane permeation assay in the description of passive absorption processes. *J. Med. Chem.* **41**, 1007–1010 (1998).

50. Sugano, K. Artificial membrane technologies to assess transfer and permeation of drugs in drug discovery. in *Comprehensive Medicinal Chemistry II* vol. 5 453–487 (Elsevier, 2007).

51. Di, L., Kerns, E. H., Fan, K., McConnell, O. J., Carter, G. T. High throughput artificial membrane permeability assay for blood–brain barrier. *Eur. J. Med. Chem.* **38**, 223–232 (2003).

52. Ottaviani, G., Martel, S., Carrupt, P.-A. Parallel artificial membrane permeability assay: a new membrane for the fast prediction of passive human skin permeability. *J. Med. Chem.* **49**, 3948–3954 (2006).

53. Kerns, E. H., Di, L. I., Petusky, S., Farris, M., Ley, R., Jupp, P. Combined application of Parallel Artificial Membrane Permeability Assay and Caco-2 permeability assays in drug discovery. *J. Pharm. Sci.* **93**, 1440–1453 (2004).

54. Hill, W. G., Rivers, R. L., Zeidel, M. L. Role of leaflet asymmetry in the permeability of model biological membranes to protons, solutes, and gases. *J. Gen. Physiol.* **114**, 405–414 (1999).

55. Allen, T. M., Cleland, L. G. Serum-induced leakage of liposome contents. *Biochim. Biophys. Acta - Biomembr.* **597**, 418–426 (1980).

56. Barbet, J., Machy, P., Truneh, A., Leserman, L. D. Weak acid-induced release of liposome-encapsulated carboxyfluorescein. *Biochim. Biophys. Acta* **772**, 347–356 (1984).

57. Chakrabarti, A. C., Clark-Lewis, I., Harrigan, P. R., Cullis, P. R. Uptake of basic amino acids and peptides into liposomes in response to transmembrane pH gradients. *Biophys. J.* **61**, 228–234 (1992).

58. Tejwani, R. W., Anderson, B. D. Influence of intravesicular pH drift and membrane binding on the liposomal release of a model amine-containing permeant. *J. Pharm. Sci.* **97**, 381–399 (2008).

59. Chakrabarti, A. C., Deamer, D. W. Permeability of lipid bilayers to amino acids and phosphate. *BBA - Biomembr.* **1111**, 171–177 (1992).

60. Krämer, S. D., Wunderli-Allenspach, H. No entry for TAT(44–57) into liposomes and intact MDCK cells: novel approach to study membrane permeation of cell-penetrating peptides. *Biochim. Biophys. Acta - Biomembr.* **1609**, 161–169 (2003).

61. Thomae, A. V., Wunderli-Allenspach, H., Krämer, S. D. Permeation of aromatic carboxylic acids across lipid bilayers: The pH-partition hypothesis revisited. *Biophys. J.* **89**, 1802–1811 (2005).

62. Sigler, A., Schubert, P., Hillen, W., Niederweis, M. Permeation of tetracyclines through membranes of liposomes and Escherichia coli. *Eur. J. Biochem.* **267**, 527–534 (2000).

63. Henning, R. pH gradient across the lysosomal membrane generated by selective cation permeability and donnan equilibrium. *Biochim. Biophys. Acta - Biomembr.* **401**, 307–316 (1975).

64. Walter, A., Hastings, D., Gutknecht, J. Weak acid permeability through lipid bilayer membranes. Role of chemical reactions in the unstirred layer. *J. Gen. Physiol.* **79**, 917–933 (1982).

65. Deamer, D. W., Prince, R. C., Crofts, A. R. The response of fluorescent amines to pH gradients across liposome membranes. *Biochim. Biophys. Acta* **274**, 323–335 (1972).

66. Nichols, J. W., Hill, M. W., Bangham, A. D., Deamer, D. W. Measurement of net proton-hydroxyl permeability of large unilamellar liposomes with the fluorescent pH probe, 9-aminoacridine. *Biochim. Biophys. Acta* **596**, 393–403 (1980).

67. Hofmann, M., Schumann, C., Zimmer, G., Henzel, K., Locher, U., Leuschner, U. LUV's lipid composition modulates diffusion of bile acids. *Chem. Phys. Lipids* **110**, 165–171 (2000).

68. Eyer, K., Paech, F., Schuler, F., Kuhn, P., Kissner, R., Belli, S., *et al.* A liposomal fluorescence assay to study permeation kinetics of drug-like weak bases across the lipid bilayer. *J. Control. Release* **173**, 102–109 (2014).

69. Hermann, K. F., Neuhaus, C. S., Micallef, V., Wagner, B., Hatibovic, M., Aschmann, H. E., *et al.* Kinetics of lipid bilayer permeation of a series of ionisable drugs and their correlation with human transporter-independent intestinal permeability. *Eur. J. Pharm. Sci.* **104**, 150–161 (2017).

70. Manallack, D. T., Prankerd, R. J., Nassta, G. C., Ursu, O., Oprea, T. I., Chalmers, D. K. A chemogenomic analysis of ionization constants-implications for drug discovery. *ChemMedChem* **8**, 242–255 (2013).

71. Hannesschlaeger, C., Barta, T., Pechova, H., Pohl, P. The effect of buffers on weak acid uptake by vesicles. *Biomolecules* **9**, 63–79 (2019).

72. Sezer, D., Oruç, T. Protonation kinetics compromise liposomal fluorescence assay of membrane permeation. *J. Phys. Chem. B* **121**, 5218–5227 (2017).

73. Lifnick, R. L. Hans Horst Meyer and the lipoid theory of narcosis. *Trends Pharmacol. Sci.* **10**, 265–

269 (1989).

74.   Verkman, a. S. *Membrane Permeability - 100 Years since Ernest Overton*. *Current Topics in Membranes* vol. 48 (1999).

75.   Paula, S., Volkov, A. G., Van Hoek, A. N., Haines, T. H., Deamer, D. W. Permeation of protons, potassium ions, and small polar molecules through phospholipid bilayers as a function of membrane thickness. *Biophys. J.* **70**, 339–348 (1996).

76.   Krämer, S. D., Lombardi, D., Primorac, A., Thomae, A. V., Wunderli-Allenspach, H. Lipid-bilayer permeation of drug-like compounds. *Chem. Biodivers.* **6**, 1900–1916 (2009).

77.   Filipe, H. A. L., Salvador, A., Silvestre, J. M., Vaz, W. L. C., Moreno, M. J. Beyond Overton's rule: Quantitative modeling of passive permeation through tight cell monolayers. *Mol. Pharm.* **11**, 3696–3706 (2014).

78.   Thomae, A. V, Koch, T., Panse, C., Wunderli-Allenspach, H., Krämer, S. D. Comparing the lipid membrane affinity and permeation of drug-like acids: the intriguing effects of cholesterol and charged lipids. *Pharm. Res.* **24**, 1457–1472 (2007).

79.   Cardoso, R. M. S., Martins, P. A. T., Gomes, F., Doktorovova, S., Vaz, W. L. C., Moreno, M. J. Chain-length dependence of insertion, desorption, and translocation of a homologous series of 7-Nitrobenz-2-oxa-1, 3-diazol-4-yl-labeled aliphatic amines in membranes. *J. Phys. Chem. B* **115**, 10098–10108 (2011).

80.   Martins, P. T., Velazquez-Campoy, A., Vaz, W. L. C., Cardoso, R. M. S., Valério, J., Moreno, M. J. Kinetics and thermodynamics of Chlorpromazine interaction with lipid bilayers: Effect of charge and Cholesterol. *J. Am. Chem. Soc.* **134**, 4184–4195 (2012).

81.   Evans, D. F., Pye, G., Bramley, R., Clark, A. G., Dyson, T. J., Hardcastle, J. D. Measurement of gastrointestinal pH profiles in normal ambulant human subjects. *Gut* **29**, 1035–1041 (1988).

82.   Maex, R. Nernst-Planck Equation. in *Encyclopedia of Computational Neuroscience* 1–7 (Springer New York, 2014).

83.   Hille, B. *Ionic channels of Excitable Membranes*. (Sinauer Associates, Inc., 2001).

84.   Fischer, H. P. Mathematical modeling of complex biological systems: from parts lists to understanding systems behavior. *Alcohol Res. Heal.* **31**, 49–59 (2008).

85.   Torres, N. V., Santos, G. The (Mathematical) Modeling process in Biosciences. *Front. Genet.* **6**, 354–363 (2015).

86.   Wolfram Research Inc. (2021). Mathematica (Version 12). Champaign, IL, U.S.A.: Wolfram Research, Inc.

87.   Hope, M. J., Bally, M. B., Webb, G., Cullis, P. R. Production of large unilamellar vesicles by a rapid extrusion procedure. Characterization of size distribution, trapped volume and ability to maintain a membrane potential. *BBA - Biomembr.* **812**, 55–65 (1985).

88. Stetefeld, J., McKenna, S. A., Patel, T. R. Dynamic light scattering: a practical guide and applications in biomedical sciences. *Biophys. Rev.* **8**, 409–427 (2016).

89. Bartlett, E. M., Lewis, D. H. Spectrophotometric determination of phosphate esters in the presence and absence of orthophosphate. *Anal. Biochem.* **36**, 159–167 (1970).

90. Chance, B. The kinetics of the enzyme-substrate compound of peroxidase. *Adv. Enzymol. Relat. Areas Mol. Biol.* **73**, 3–23 (1999).

91. Powers, R., Copeland, J. C. *Encyclopedia of Biophysics*. *Encyclopedia of Biophysics* (Springer Berlin Heidelberg, 2013).

92. Kuwajima, K., Yamaya, H., Miwa, S., Sugai, S., Nagamura, T. Rapid formation of secondary structure framework in protein folding studied by stopped-flow circular dichroism. *FEBS Lett.* **221**, 115–118 (1987).

93. Chen, C., Li, M., Xing, Y., Li, Y., Joedecke, C.-C., Jin, J., *et al.* Study of pH-induced folding and unfolding kinetics of the DNA i-motif by stopped-flow circular dichroism. *Langmuir* **28**, 17743–17748 (2012).

94. Moody, M. F., Vachette, P., Foote, A. M., Tardieu, A., Koch, M. H., Bordas, J. Stopped-flow x-ray scattering: the dissociation of aspartate transcarbamylase. *Proc. Natl. Acad. Sci. U. S. A.* **77**, 4040–4043 (1980).

95. Grillo, I., Kats, E. I., Muratov, A. R. Formation and growth of anionic vesicles followed by small-angle neutron scattering. *Langmuir* **19**, 4573–4581 (2003).

96. Hannesschläger, C., Barta, T., Siligan, C., Horner, A. Quantification of Water Flux in Vesicular Systems. *Sci. Rep.* **8**, 1–8 (2018).

97. Ali, S. H. Kinetics of the reaction of carbon dioxide with blends of amines in aqueous media using the stopped-flow technique. *Int. J. Chem. Kinet.* **37**, 391–405 (2005).

98. Grimaldi, J. J., Sykes, B. D. Concanavalin A: a stopped flow nuclear magnetic resonance study of conformational changes induced by Mn++, Ca++, and α methyl D mannoside. *J. Biol. Chem.* **250**, 1618–1624 (1975).

99. Filipe, H. A. L., Cardoso, R. M. S., Loura, L. M. S., Moreno, M. J. Interaction of amphiphilic molecules with lipid bilayers: Kinetics of insertion, desorption and translocation. in *Membrane Organization and Dynamics* 49–89 (2017).

100. Abreu, M. S. C., Moreno, M. J., Vaz, W. L. C. Kinetics and thermodynamics of association of a phospholipid derivative with lipid bilayers in liquid-disordered and liquid-ordered phases. *Biophys. J.* **87**, 353–365 (2004).

101. Sampaio, J. L., Moreno, M. J., Vaz, W. L. C. Kinetics and thermodynamics of association of a fluorescent lysophospholipid derivative with lipid bilayers in liquid-ordered and liquid-disordered phases. *Biophys. J.* **88**, 4064–4071 (2005).

References

102. Estronca, L. M. B. B., Filipe, H. A. L., Salvador, A., Moreno, M. J., Vaz, W. L. C. Homeostasis of free cholesterol in the blood: a preliminary evaluation and modeling of its passive transport. *J. Lipid Res.* **55**, 1033–1043 (2014).

103. Gauglitz, G. Photophysical, photochemical and photokinetic properties of photochromic systems. in *Photochromism: Molecules and Systems* 15–63 (Elsevier Inc., 2003).

104. Martins, P. A. T., Domingues, N., Pires, C., Alves, A. M., Palmeira, T., Samelo, J., *et al.* Molecular crowding effects on the distribution of amphiphiles in biological media. *Colloids Surf. B. Biointerfaces* **180**, 319–325 (2019).

105. Estronca, L. M. B. B., Moreno, M. J., Vaz, W. L. C. Kinetics and thermodynamics of the association of dehydroergosterol with lipid bilayer membranes. *Biophys. J.* **93**, 4244–4253 (2007).

106. Sandén, T., Salomonsson, L., Brzezinski, P., Widengren, J. Surface-coupled proton exchange of a membrane-bound proton acceptor. *Proc. Natl. Acad. Sci.* **107**, 4129–4134 (2010).

107. Perkins, W. R., Cafiso, D. S. An electrical and structural characterization of proton/hydroxide currents in phospholipid vesicles. *Biochemistry* **25**, 2270–2276 (2002).

108. Nozaki, Y., Tanford, C. Proton and hydroxide ion permeability of phospholipid vesicles. *Proc. Natl. Acad. Sci.* **78**, 4324–4328 (1981).

109. Deamer, D. W. Proton permeation of lipid bilayers. *J. Bioenerg. Biomembr.* **19**, 457–479 (1987).

110. Hauser, H., Oldani, D., Phillips, M. C. Mechanism of ion escape from phosphatidylcholine and phosphatidylserine single bilayer vesicles. *Biochemistry* **12**, 4507–4517 (1973).

111. Hodgkin, A. L., Huxley, A. F., Katz, B. Measurement of current-voltage relations in the membrane of the giant axon of Loligo. *J. Physiol.* **116**, 424–448 (1952).

112. Singh, A., Marcoline, F. V., Veshaguri, S., Kao, A. W., Bruchez, M., Mindell, J. A., *et al.* Protons in small spaces: Discrete simulations of vesicle acidification. *PLoS Comput. Biol.* **15**, 1–21 (2019).

113. König, B., Dietrich, U., Klose, G. Hydration and structural properties of mixed lipid/surfactant model membranes. *Langmuir* **13**, 525–532 (1997).

114. Greenwood, A. I., Tristram-Nagle, S., Nagle, J. F. Partial molecular volumes of lipids and cholesterol. *Chem. Phys. Lipids* **143**, 1–10 (2006).

115. Moreno, M. J., Bastos, M., Velazquez-Campoy, A. Partition of amphiphilic molecules to lipid bilayers by isothermal titration calorimetry. *Anal. Biochem.* **399**, 44–47 (2010).

116. Yamaoka, K., Nakagawa, T., Uno, T. Application of Akaike's Information Criterion (AIC) in the evaluation of linear pharmacokinetic equations. *J. Pharmacokinet. Biopharm.* **6**, 165–175 (1978).

117. Kemmer, G., Keller, S. Nonlinear least-squares data fitting in Excel spreadsheets. *Nat. Protoc.* **5**, 267–281 (2010).

118. Cordeiro, M. M., Salvador, A., Moreno, M. J. Calculation of permeability coefficients from solute

equilibration dynamics: An assessment of various methods. *Membranes.* **12**, 254–280 (2022).

119. Deamer, D. W., Bramhall, J. Permeability of lipid bilayers to water and ionic solutes. *Chem. Phys. Lipids* **40**, 167–188 (1986).

120. Miller, J. M., Dahan, A., Gupta, D., Varghese, S., Amidon, G. L. Enabling the intestinal absorption of highly polar antiviral agents: Ion-pair facilitated membrane permeation of zanamivir heptyl ester and guanidino oseltamivir. *Mol. Pharm.* **7**, 1223–1234 (2010).

121. Nichols, J. W., Deamer, D. W. Net proton-hydroxyl permeability of large unilamellar liposomes measured by an acid-base titration technique. *Proc. Natl. Acad. Sci. U. S. A.* **77**, 2038–2042 (1980).

122. Deamer, D. W., Nichols, J. W. Proton-hydroxide permeability of liposomes. *Proc. Natl. Acad. Sci.* **80**, 165–168 (1983).

123. Valeur, B., Berberan-Santos, M. N. *Molecular Fluorescence: Principles and Applications*. (Wiley-VCH Verlag GmbH & Co. KGaA, 2012). doi:10.1002/9783527650002.

124. Scott, H. L., Skinkle, A., Kelley, E. G., Waxham, M. N., Levental, I., Heberle, F. A. On the mechanism of bilayer separation by extrusion, or why your LUVs are not really unilamellar. *Biophys. J.* **117**, 1381–1386 (2019).

125. Hannesschlaeger, C., Horner, A., Pohl, P. Intrinsic membrane permeability to small molecules. *Chem. Rev.* **119**, 5922–5953 (2019).

126. Mayer, L. D., Hope, M. J., Cullis, P. R. Vesicles of variable sizes produced by a rapid extrusion procedure. *Bioehimica Biophys. Acta* **858**, 161–168 (1986).

127. Pines, D., Ditkovich, J., Mukra, T., Miller, Y., Kiefer, P. M., Daschakraborty, S., *et al.* How acidic is carbonic acid? *J. Phys. Chem. B* **120**, 2440–2451 (2016).

128. Harned, H. S., Scholes, S. R. The ionization constant of HCO3- from 0 to 50°. *J. Am. Chem. Soc.* **63**, 1706–1709 (1941).

129. Johnson, S. M., Bangham, A. D. Potassium permeability of single compartment liposomes with and without valinomycin. *Biochim. Biophys. Acta - Biomembr.* **193**, 82–91 (1969).

Supplementary Material

Table S1. Mean occupancy numbers *per* vesicle, with outer radius r, in the absence of a transmembrane pH gradient and at the attained equilibrium. The concentration of fluorescent probe considered was 10^{-6}, 10^{-5} and 10^{-4} M (P1, P2 and P3), the concentration of solute was 10^{-5} M. The values were obtained considering the parameters choice 1 (C1, see Table 7).

r (nm)	No pH gradient	C1 S2 P1	C1 S2 P2	C1 S2 P3
25	7.0	3.3	3.3	3.9
50	33	16	16	21
100	152	73	79	108
500	6 292	3 262	3 831	5 357
2500	451 362	257 913	311 885	411 394
5000	3 272 090	2 031 246	2 409 232	3 039 039

Table S2. Mean occupancy numbers *per* vesicle, with outer radius r, in the absence of a transmembrane pH gradient and at the attained equilibrium. The concentration of fluorescent probe considered was 10^{-6}, 10^{-5} and 10^{-4} M (P1, P2 and P3), the concentration of solute was 10^{-5} M. The values were obtained considering the parameters choice 2 (C2, see Table 7).

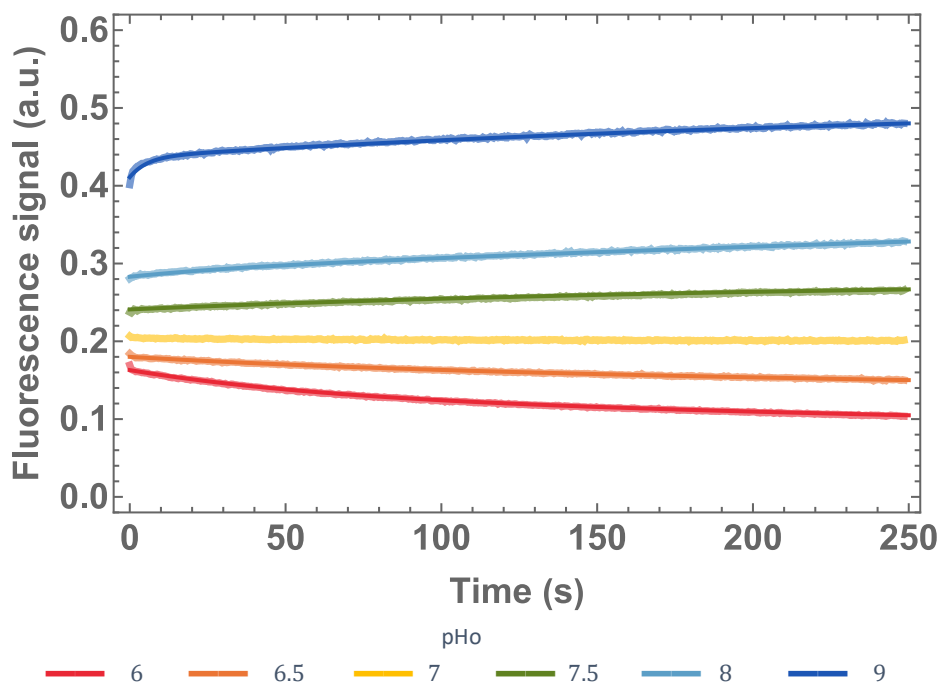| r (nm)	No pH gradient	C2 S2 P1	C2 S2 P2	C2 S2 P3
25	26.5	23.9	23.9	24.5
50	121	109	110	114
100	525	471	475	498
500	15 569	13 499	13 958	15 016
2500	621 197	489 727	531 712	597 920
5000	3 630 440	2 780 739	3 074 011	3 496 908

Figure S1. Goodness of the bi-exponential fit of the fluorescence variation recorded on the stopped-flow, when imposing different protons concentration gradients in the absence of valinomycin. The fluorescence variation recorded on the plate reader under the same conditions was fitted simultaneously.
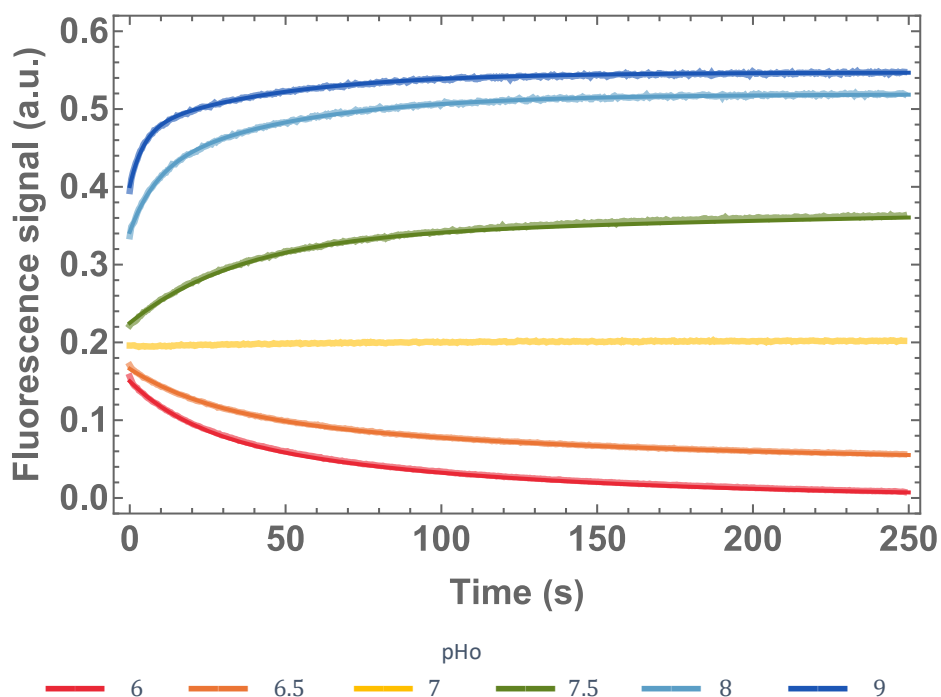

Figure S2. Goodness of the bi-exponential fit of the fluorescence variation recorded on the stopped-flow, when imposing different protons concentration gradients to vesicle samples with 0.7 μM valinomycin. The fluorescence variation recorded on the plate reader under the same conditions was fitted simultaneously.